

2014

Thermal and Hydraulic Conductivity Properties of Geothermal Well Seals Subjected to Cyclic Heating and Cooling

Andisiwe S. Sicwebu
as049@bucknell.edu

Follow this and additional works at: https://digitalcommons.bucknell.edu/masters_theses

Recommended Citation

Sicwebu, Andisiwe S., "Thermal and Hydraulic Conductivity Properties of Geothermal Well Seals Subjected to Cyclic Heating and Cooling" (2014). *Master's Theses*. 119.
https://digitalcommons.bucknell.edu/masters_theses/119

This Masters Thesis is brought to you for free and open access by the Student Theses at Bucknell Digital Commons. It has been accepted for inclusion in Master's Theses by an authorized administrator of Bucknell Digital Commons. For more information, please contact dcadmin@bucknell.edu.

**THERMAL AND HYDRAULIC CONDUCTIVITY PROPERTIES OF GEOTHERMAL
WELL SEALS SUBJECTED TO CYCLIC HEATING AND COOLING**

by

Andisiwe Sicwebu

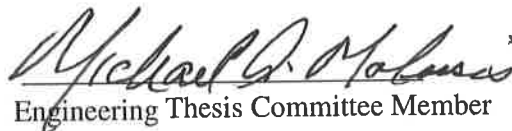
(A Thesis)

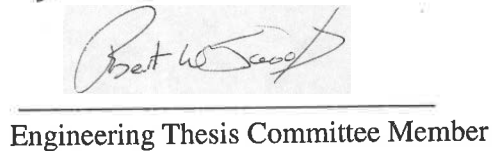
Presented to the Faculty of
Bucknell University
In Partial Fulfillment of the Requirements for the Degree of
Master of Science in Civil Engineering

Approved:


Adviser


Department Chairperson


Engineering Thesis Committee Member


Engineering Thesis Committee Member

May 2014

(Date: month and Year)

I, Andi Sicwebu grant permission for my thesis to be copied.

April 13, 2014

TABLE OF CONTENTS

1. Chapter 1: Introduction	1
1.1 Theoretical Background	1
1.2 Motivation of Study	5
1.3 Research Objectives.....	11
2. Chapter 2: Literature Review	13
2.1 Mineralogical Features of Bentonite.....	14
2.2 Clay Structure	16
2.3 Diffuse Double Layer (DDL) Theory	18
2.4 Effects of Temperature on Molecular Structure of Clay	23
2.4.1 Effects on Thermal Conductivity with Respect to Cohesive Soils.....	25
2.4.2 Effects on Hydraulic Conductivity with Respect to Cohesive Soils....	28
2.5 Case Studies	30
2.5.1 Allan (1997).....	30
2.5.2 Allan and Kavanaugh (1999)	32
2.5.3 Cho <i>et al.</i> (1999)	37
2.5.4 Hueckel and Pellegrini	39
2.5.5 Lee <i>et al.</i> (2010)	41
2.5.6 Park <i>et al.</i> (2011)	43
2.5.7 Philippacopoulos and Brendt (2001)	45
3. Chapter 3: Materials and Methods	48
3.1 Grouting Material.....	48
3.2 Preparation of Slurry.....	49
3.3 Development of Equipment	50
3.4 Thermal Conductivity Tests.....	57
3.5 Hydraulic Conductivity Tests	59
3.5.1 Consolidation Permeability Tests	59

3.5.2	Triaxial Permeability Tests	61
3.5.3	Rigid Wall/Flow Pump Permeability Tests	62
4.	Chapter 4: Data Analysis and Results.....	67
4.1	Thermal Conductivity Results	67
4.2	Hydraulic Conductivity Results	77
4.2.1	Consolidation Permeability Tests	77
4.2.2	Triaxial Permeability Tests	80
4.2.3	Rigid Wall/Flow Pump Permeability Tests	84
4.3	Moisture Content Test.....	91
5.	Chapter 5: Numerical Modeling	97
5.1	Heat Transfer Mechanisms	99
5.1.1	Heat Transfer by Conduction and Convection.....	101
5.2	Boundary and Initial Conditions	102
5.2.1	Convection Heat Transfer	103
5.2.2	Conduction Heat Transfer.....	106
5.3	Finite Element Mesh	107
5.4	Results and Discussion	108
6.	Chapter 6: Performance of Geothermal Heat Pumps.....	117
6.1	Thermal Performance and Efficiency of Geothermal Heat Pump	118
6.2	Hydraulic Performance of Geothermal Borehole	122
7.	Chapter 7: Conclusions and Recommendations	126
7.1	Thermal and Hydraulic Properties of Bentonite Grout.....	126
7.1.1	Thermal Conductivity Results	126
7.1.2	Hydraulic Conductivity Results	128
7.2	Experimental Limitations.....	129
7.3	Recommendations for future research	130

LIST OF FIGURES

Figure 1.1 Cooling cycle of a geothermal heat pump system	4
Figure 1.2 Heating cycle of a geothermal heat pump system	4
Figure 1.3 Geothermal borehole showing acceptable grouting conditions	9
Figure 1.4 Geothermal borehole showing undesirable grouting conditions	9
Figure 1.5 Cracking of neat cement after thermal cyclic testing	11
Figure 2.1 Clay structures of kaolinite, illite, and montmorillonite.....	15
Figure 2.2 Flocculated clay structure.....	17
Figure 2.3 Dispersed clay structure	17
Figure 2.4 Distribution of ions according to the diffuse double layer theory.....	19
Figure 3.1 BENSEAL® granules and EZ-MUD®	50
Figure 3.2 Mixing of BENSEAL/EZ-MUD® slurry.....	50
Figure 3.3 Top and side view of geothermal well model	51
Figure 3.4 Thermocouple placement in the geothermal system model	52
Figure 3.5 Plot of water and ambient temperature over a 24 hour period for a heating cycle	53
Figure 3.6 Plot of grout temperature for twelve thermocouples over a 24 hour period for a heating cycle	53
Figure 3.7 Plot of water and ambient temperature over a 24 hour period for a heating cycle	54
Figure 3.8 Plot of water and ambient temperature over a 24 hour period for a heating cycle	54
Figure 3.9 Schematic of thermal and hydraulic conductivity testing apparatus	56
Figure 3.10 Schematic of falling head permeability setup	60
Figure 3.11 Picture of bentonite slurry in a triaxial cell	61
Figure 3.12 Picture of a PH 22/2000 Programmable Harvard Apparatus flow pump	63
Figure 3.13 Rigid wall permeameter with a bentonite slurry sample	63

Figure 3.14 Infuse and withdraw pumping directions of a Harvard Apparatus flow pump	64
Figure 3.15 Picture of Load Frame-Sigma1 apparatus	65
Figure 3.16 Picture of pressure transducer	65
Figure 4.1 Thermal Conductivity versus Cycle Number for summers 2010 and 2011	68
Figure 4.2 Thermal Conductivity versus Cycle Number for fall 2012	70
Figure 4.3 Thermal Conductivity versus Cycle Number for 2013	71
Figure 4.4 Geothermal Well Model with Cracked Bentonite Grout.....	74
Figure 4.5 Confidence Interval Plot for Thermal Conductivity Results	75
Figure 4.6 Consolidometer Permeability Results	78
Figure 4.7 Changes in Dial Reading versus Time	79
Figure 4.8 Triaxial Permeability Results at Room Temperature	81
Figure 4.9 Triaxial Permeability Results for Cyclic Heating and Cooling.....	82
Figure 4.10 Flow Pump Permeability Results (Hydraulic Conductivity).....	85
Figure 4.11 Flow Pump Permeability Results (Intrinsic Permeability).....	87
Figure 4.12 Confidence Interval for Hydraulic Conductivity Results	89
Figure 4.13 Confidence Interval for Intrinsic Permeability Results	90
Figure 4.14 Locations of Moisture Content Samples	91
Figure 4.15 Bentonite Samples in Moisture Tins	91
Figure 4.16 Moisture Content versus Depth of Geothermal Well Model	94
Figure 4.17 Moisture Content versus Distance from center of Geothermal Well Model..	94
Figure 5.1 Plan view of the geothermal borehole as modeled in COMSOL	98
Figure 5.2 Heat transfer mechanisms and thermal influence factors	100
Figure 5.3 Two Dimensional finite element mesh as modeled in COMSOL	107
Figure 5.4 Case 1 temperature distribution for a heating cycle at 0 hours	110
Figure 5.5 Case 1 temperature distribution for a heating cycle at 72 hours	110
Figure 5.6 Case 1 temperature distribution for a cooling cycle at 0 hours	111
Figure 5.7 Case 1 temperature distribution for a cooling cycle at 72 hours	111
Figure 5.8 Plot of heat transfer rate with respect to time for case 1	113

Figure 5.9 Plot of heat transfer rate with respect to time for case 2	114
Figure 5.10 Plot of heat transfer rate with respect to time for case 3	114
Figure 6.1 Cross section of a geothermal borehole with different soil layers	123
Figure 6.2 Plot of Darcy flow rate with respect to hydraulic gradient	125

LIST OF TABLES

Table 2.1 Dielectric constant values with varying water temperature	22
Table 2.2 Thermal conductivities of neat cementitious grouts	35
Table 2.3 Thermal conductivities of cementitious grouts with different fillers	35
Table 2.4 Thermal conductivities of bentonite-sand grouts	36
Table 3.1 Flow rate data at pump setting of seven	59
Table 4.1 Moisture content results.....	92
Table 5.1 Convective heat transfer values for free convection.....	106
Table 5.2 Steady state temperature results from COMSOL	112
Table 5.3 Steady state heat transfer rate solutions	116

ABSTRACT

Geothermal wells are commonly used in the USA for heating and cooling of both commercial and residential spaces. In these systems, the annulus between the ground and the pipe is filled with a sealant, frequently a bentonite grout which acts as a heat exchange pathway between the earth and the piping material for the thermal conductivity and limits water flow vertically along the well annulus. Due to the grout being subjected to an enormous number of cycles of heating and cooling, it is necessary to understand how, if at all, the thermal and hydraulic conductivity of the bentonite seal changes with cycles of heating and cooling through the life of the geothermal well.

A 150 mm diameter polyvinyl chloride (PVC) that contained a bentonite seal with a 25 mm diameter high-density polyethylene (HDPE) pipe to circulate the fluid was constructed in order to study the thermal and hydraulic properties of bentonite-based seals. After 18 heating and cooling cycles, the bentonite grout used in this research had an average thermal conductivity of 0.64 W/m-K and 0.092 W/m-K for a heating and cooling cycle, respectively. The flow pump permeability results yielded an average hydraulic conductivity of 2.6×10^{-6} cm/s and 1.29×10^{-6} cm/s for a heating and cooling cycle, respectively. The average intrinsic permeability for a heating and cooling cycle was 1.25×10^{-11} cm² and 1.84×10^{-11} cm², respectively. The hypothesis suggested by the data is that the potential formation of an air gap on the grout/pipe interface increases the hydraulic conductivity of the bentonite grout from $\sim 10^{-7}$ cm/s to $\sim 10^{-6}$ cm/s.

Numerical modeling of a geothermal borehole was performed using a computer software package, COMSOL. The three cases that were modeled in COMSOL were: (1) experimental thermal conductivity values from the lab geometry, (2) standard design thermal conductivity values in a model field geometry, and (3) experimental thermal conductivity values considering field conditions. The solutions from COMSOL showed that for a heating cycle, the published thermal conductivity had a heat transfer rate of 27 Watts whereas the experimental thermal conductivity yielded a heat transfer rate of 24 Watts. For a cooling cycle, the heat transfer rate for the published thermal conductivity was nine Watts and the heat transfer rate for the experimental thermal conductivity was one Watt. The conclusion made from the numerical heat flux solutions and analytical solutions was that it is more efficient to use the ground heat exchanging technique for heating rather than cooling. The analysis performed to determine the amount of downward seepage that could be experienced in a geothermal borehole showed that with an increase in hydraulic gradient, the potential for downward seepage also increases. Also, the potential for leakage is the highest during a heating cycle in comparison to a cooling cycle but the quantity of flow is, under all conditions evaluated, rather small.

CHAPTER 1: Introduction

Geothermal heat pumps with heating/cooling loops placed in the earth are used to provide for the heating and cooling of both residential and commercial spaces. Given that ground temperatures are approximately the mean annual temperature (about 12° C in Lewisburg, PA), the use of such heat transfer loops can be cost effective alternatives to conventional heating and cooling systems. The installation of a geothermal heat pump system involves inserting a continuous loop of plastic (HDPE) pipe connected to a heat pump unit into a hole or series of holes in the earth to act as a heat exchanger. A thermally conductive, low permeability grout is then placed in the hole between the pipe wall and the earth. A heat transfer fluid is circulated through the underground heat transfer loop to allow heat to be transferred between the earth and the fluid by means of conduction through the grout and the pipe wall. When the system is operating in a heating mode, a relatively cool heat transfer fluid is circulated through the loop to allow heat to be transferred from the warmer earth into the fluid. Likewise, when the system is operating in a cooling mode, a relatively warm heat transfer fluid is circulated through the loop to allow heat to be transferred from the fluid to the cooler earth.

1.1 Background

During the process of heat exchanging, the ground is used as a heat source during winter and used as a heat sink and as a free cooling source in the summer time. The most common method to exchange heat with the ground is by means of a borehole heat exchanger installed into the ground and connected to a ground source heat pump. Heat

will generally flow from a warmer medium to a colder one and this basic physical law can only be reversed with the addition of energy. A heat pump is a device that transfers heat energy from a heat source to a heat sink under the influence of a temperature gradient. A heat pump uses a refrigeration cycle to transport and intensify the heat provided by the ground loop. The refrigeration process found in a geothermal heat pump is analogous to the refrigeration cycle of a common refrigerator or air conditioner. The one important difference is that the process can be reversed to move heat into or move heat away from residential or commercial spaces. The basic components of a ground source heat pump (GSHP) as stated by Mustafa-Omer (2006) include:

- a. *A ground loop*: This is comprised of lengths of pipe buried in the ground, either in a borehole or a horizontal trench. The pipe is usually a closed circuit and is filled with a mixture of water and/or antifreeze, which is pumped round the pipe absorbing heat from the ground during a heating cycle or heating the ground during a cooling cycle.
- b. *A heat pump*: The heat pump has three main parts:
 - Compressor – The compressor transports the refrigerant around the heat pump and compresses the refrigerant from a gaseous phase to the temperature desirable for the heat distribution circuit.
 - Condenser – The condenser allows the refrigerant to release heat to the surrounding medium as it travels along the coils of the condenser.
 - The evaporator – The evaporator absorbs heat from the warm earth through the ground loop and works by passing warm air over its coils.

The evaporator coils are used to transform the refrigerant from a liquid to a gas. Additionally, the air loses its heat and turns cold.

c. Heat distribution system: This generally consists of under floor heating or radiators for space heating and in some cases water storage for hot water supply.

The abovementioned components are joined to form a continuous system as shown in Figures 1.1 for a cooling cycle and Figure 1.2 for a heating cycle. When considering a cooling cycle, the refrigerant enters the compressor as a low pressure, low temperature saturated vapor and is compressed to the condenser pressure. Thereafter the refrigerant leaves the compressor as a high temperature, high pressure, and superheated vapor and cools down and condenses as it flows through the coils of the condenser by releasing heat to the surrounding medium. Then, it enters an expansion valve or capillary tube where its pressure and temperature decrease drastically due to the throttling effect. The low pressure, low temperature, low quality vapor refrigerant then enters the evaporator, where it evaporates by absorbing heat from the conditioned space. The cycle is completed as the refrigerant leaves the evaporator and reenters the compressor. In the heating cycle, the refrigerant is processed in the reverse order.

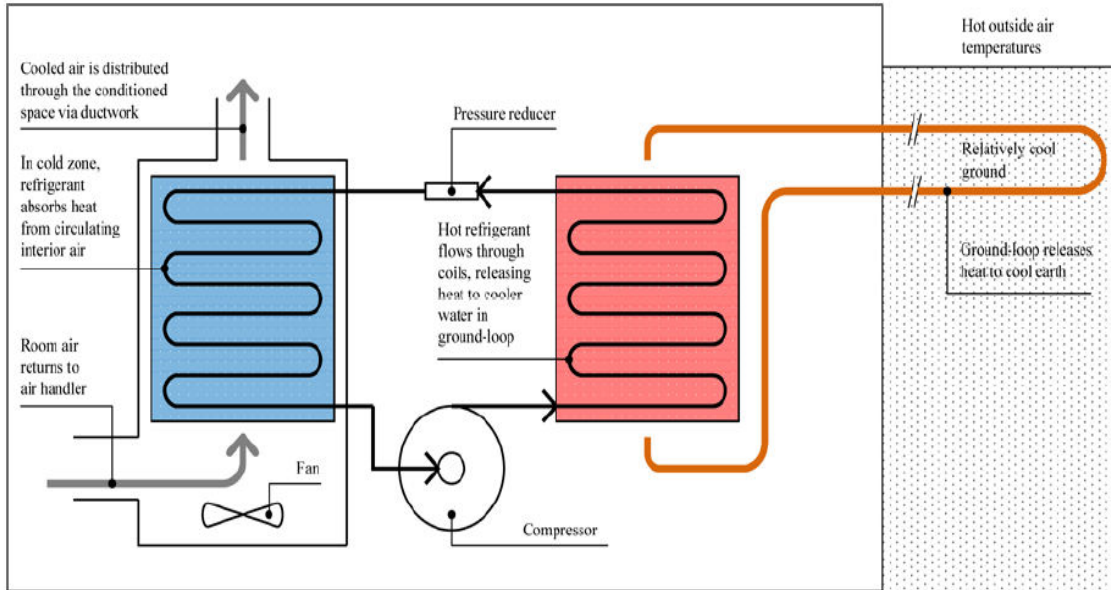


Figure 1.1. The cooling cycle of a geothermal heat pump system [Source: Charoenvisal (2008)]

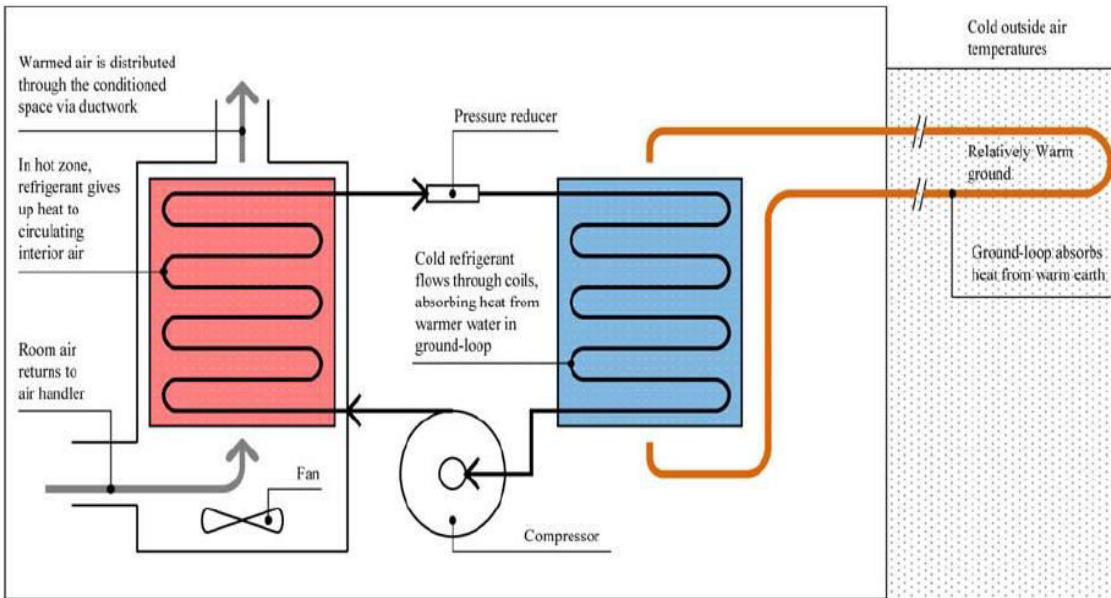


Figure 1.2. The heating cycle of a geothermal heat pump system [Source: Charoenvisal (2008)]

1.2 Motivation for Study

It is important to study and understand the thermal, hydraulic, physical properties of grouting materials for several reasons. First, the efficiency of the heat transfer loop is affected by the grout employed to provide a heat exchange pathway from the surface of the earth along the entire length of the borehole. The grout needs to have a high enough thermal conductivity to ensure that heat is readily transferred between the heat transfer fluid and the earth. Second, the hydraulic conductivity of the grout must be low to provide a hydraulic seal from the ground surface along the entire length of the borehole to provide adequate groundwater protection. A target hydraulic conductivity of 10^{-7} cm/s or less is considered acceptable as a sealant (Skouby, 2010). Third, the grout needs to have a relatively low viscosity to allow for its placement in the space between the heat transfer loop and the earth without leaving voids that could reduce the heat transfer through the grout and provide conduits for leaking fluid to enter groundwater.

The grouting of geothermal systems is a vital component of the installation process because it is critical to protecting groundwater. Although the Federal Underground Injection Control (UIC) and National Pollutant Discharge Elimination System (NPDES) regulations were designed to prevent contamination of groundwater, aquifer, and surface water, the UIC portion of the Safe Water Drinking Act (40 CFR, Parts 144-147) precludes a closed-loop ground source system from being defined as an injection well as it is not used for the emplacement of fluids underground. Similarly, the NPDES portion

of the Clean Water Act (40 CFR, Parts 122-124) which covers surface discharge of fluids, does not include ground-coupled heat pump systems as it is limited to water bodies such as wetlands, ponds, streams, sloughs, and navigable waterways. Federal statutes do not prevent each state or other governing bodies from adopting regulations that are more stringent than those created by the Environmental Protection Agency (EPA) or NPDES. In Pennsylvania, there are currently no state laws pertaining to the grouting of geothermal boreholes. However, Pennsylvania has regulations and guidelines that only exist in the county or township level to encourage the proper construction of geothermal heat pumps. The protection of groundwater quality is a primary concern for many states including Pennsylvania and it is important to understand the performance of geothermal systems and ways to prevent possible contamination of groundwater.

According to (McCray, 1997), the two classes of material that can be used in the space between the heat exchanger pipe and borehole is fill or grout. The common various grouting materials that are typically used in geothermal boreholes are listed below along with their descriptions:

- **Fill (native cuttings):** fill is the use of cuttings or other native materials that can be placed in the borehole under site specific conditions, such as void zones or dry boreholes (when at least 25 ft above the water table) or single, non-flowing aquifer

Advantages: The biggest advantage of using fill is that the material is usually widely available and cost effective

Disadvantages: Even though a particular formation may have a low permeability in its native state, once disturbed the materials from that formation are difficult, if not impossible, to reconstruct at the same permeability coefficient. When using fill, there is no way to guarantee compaction or complete placement from bottom to top. Therefore channels for water migration will most likely occur and allow for unstable conditions (Stitchman, 1990).

- **Bentonite grout:** slurry consisting of sodium montmorillonite, a polymer (which functions as a viscosifier), and water with a solids concentration of not less than 20%.

Advantages: For the most part, bentonite grout seals are effective. Also, the grout is inexpensive, exhibits low permeability, and generally easy to emplace. Both types of pumping systems with low volume/high pressure and high volume/low pressure allow for the bentonite slurry to be pumped from bottom to top in a borehole.

Disadvantages: The larger percentage of the slurry is made up of water; therefore there is a risk of movement of free water surrounding formations due to the potential for drying and cracking. If the bentonite slurry has 10% solids or less, the grout could possibly not perform effectively since the polymer used in the slurry tends to break down over time. Also, pure bentonite slurries tend to settle out and the water dissipates over time because the bentonite molecular forces are overpowered by capillary tensions in surrounding formations which then draw the water away (Stitchman, 1990).

- **Thermally enhanced bentonite grout:** bentonite grout, into which silica sand or other materials such as graphite are added to improve the thermal characteristics for geothermal applications. This grout typically has a minimum solids content of 60%.

Advantages: Thermally enhanced bentonite grouts provide similar advantages to regular bentonite grouts, but with increased thermal conductivity values for better heat transfer between the ground loop and the earth. Also, the addition of sand to the grout is important because it may reduce the number of boreholes needed to run a geothermal system and reduce the power to operate the system. This reduction of costs gives a faster pay-back on the initial installation costs.

Disadvantage: The biggest limitation of thermally enhanced bentonite grouts is the high cost in comparison to regular bentonite grout (Stitchman, 1990).

- **Neat cement grout:** a mixture of one bag of Portland cement (94 pounds) and not more than six gallons of fresh water. Drilling fluid bentonite that is not more than five percent by weight of cement and additional water that is not more than 0.6 gallons for each one percent of bentonite may be used as the fluid to prepare neat cement grout.

Advantages: Portland cement can be easily mixed and is a readily available material. The grout creates a rigid column and can be easily pumped to significant depths. The weight of cement grouts can easily displace other fluids in the borehole and can also be made lighter and smoother through the addition of bentonite.

Disadvantages: Since bleed occurs at the cement particles prior to setting and shrinkage occurs as the cement sets as a result of hydration and heat generated during the curing process, there is likelihood that a “micro-annulus” generates a conduit for water to seep into the surrounding formation. The time needed for the curing process could also be a limitation. Additionally, the heat of hydration can possibly damage the Polyvinyl chloride (PVC) casing.

Although the various types of grouting materials have been documented above, this research project only focuses on bentonite grout. In a geothermal borehole, adequate heat transfer also requires complete thermal contact at all interfaces. The formation of gaps at the grout/U-loop and grout/formation interfaces due to either grout shrinkage, thermal contraction of high density polyethylene (HDPE) U-loop, or external conditions leads to an appreciable reduction of the overall thermal conductivity of the system as shown in Figures 1.3 and 1.4.

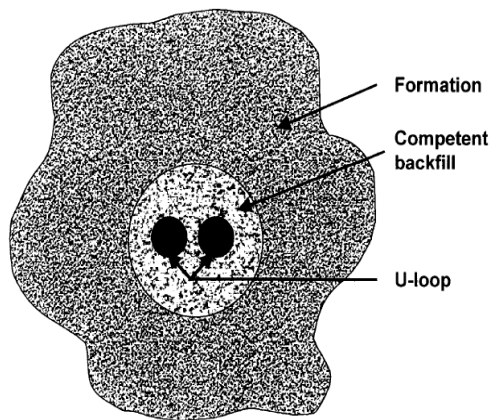


Figure 1.3. Section of geothermal borehole showing acceptable grouting conditions. [Source: (Allan and Philappacopoulos, 1999)]

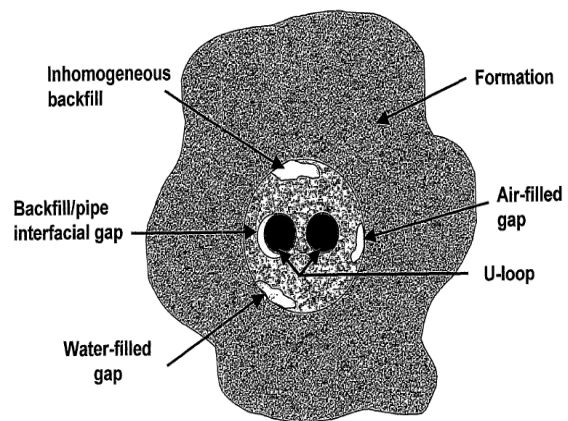
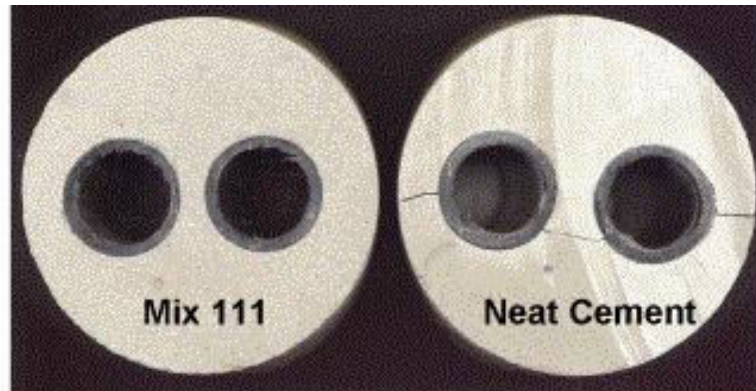


Figure 1.4. Section of geothermal borehole showing undesirable grouting conditions. [Source: (Allan and

An air gap in a geothermal borehole causes a reduction in the thermal conductivity of the system because air has a lower thermal conductivity ($0.027 \text{ W/m}^\circ\text{C}$) than bentonite grouts ($0.74 \text{ W/m}^\circ\text{C}$) and therefore heat will not be conducted quickly as in the case of higher grout thermal conductivity (Mills, 1992). The low hydraulic conductivity of grout/pipe system can be compromised by poor bonding between the grout and the borehole or poor bonding between the grout and the heat conductor pipe (Allan and Philappacopoulos, 1999). Also the decrease in soil moisture content associated with heat rejection and subsequent shrinkage may result in loss of bonding to the grout and consequently reduce the effectiveness of the geothermal heat pump. Therefore, favorable heat transfer in the system requires that the issues of system component bonding and proper grouting techniques as well as the possibility of interfacial gaps are addressed by geothermal installers.

Since the grout and pipe have significantly different coefficients of thermal expansion, the conductor pipe can contract from the grout at low temperatures, forming a conductive pathway for contaminant transport as shown in Figure 1.5. A study conducted by Allan and Philappacopoulos (1999) illustrated that neat cement grouts with water/cement ratios of 0.4 to 0.8 failed in the aforementioned manner during lab experiments where low temperature fluids were pumped through the pipe. A thermally enhanced grout (Mix 111) did not fail, maintaining hydraulic conductivities of less than 10^{-7} cm/sec during these experiments. Mix 111 is a mixture of cement, water, silica sand, and small amounts of superplasticizer and bentonite and has high thermal conductivity (2.42 W/m-K). The

results from the research conducted by Allan and Philappacopoulos (1999) indicated that bentonite based grouts appear to be a better alternative to neat cement grouts.



Grout/U-loop Specimens after Thermal Cycling

Figure 1.5. Cracking of neat cement grout after thermal cyclic testing of grout and U-loop pipe samples. [Source: Allan and Philappacopoulos (1999)]

1.3 Research Objectives

The following objectives, stated as testable questions, form the basis for the proposed research:

1.3.1 What are the long and short term implications imposed to the bentonite grout due to the cyclic heating and cooling?

The main objective of this research project was to evaluate the integrity of a bentonite grout, BENSEAL/EZ-MUD®, over time considering heating and cooling cycles in geothermal heat pumps. This objective was carried out by determining the variation of

the hydraulic and thermal properties of the bentonite grout over time in order to identify any degradation of the grout.

1.3.2 How does the implication of heating and cooling affect the thermal and hydraulic performance of the bentonite grout?

If indeed there is some form of degradation of the bentonite grout over time, it is worth determining how the implications of heating and cooling affect the thermal and hydraulic performance of the geothermal borehole.

CHAPTER 2: Literature Review

Grim (1968) defines clay as a natural, earthy occurring fine-grained mineral that develops plasticity in the presence of limited amount of water. Clay minerals are crystalline substances that are formed from chemical weathering and belong to a class of minerals referred to as phyllosilicates. The two fundamental crystal sheets that form common silicate structures is a combination of tetrahedral (or silica) and octahedral (or gibbsite) sheets (Holtz and Kovacs, 1981). A single tetrahedron unit consists of four oxygen atoms surrounding a silicon atom. The combination of the tetrahedral silica units yields a silica sheet. Conversely, gibbsite sheets are formed by combining octahedral aluminum hydroxyls, which consists of six hydroxyls surrounding an aluminum atom. The differences among clay minerals result from the substitution of different cations in the octahedral sheet. Different clay mineral groups are characterized by the varying stacking arrangements of the tetrahedral and octahedral sheets. If the mineral consists of one octahedral and one tetrahedral sheet, the term given to this clay structure is a 1:1 clay mineral. Similarly if a clay mineral consists of two tetrahedral sheets and a single octahedral sheet, the clay structured is termed a 2:1 clay mineral. The most common clay groups include 1.) kaolinite: a type of clay that forms part of the family of 1:1 minerals. The single octahedral and tetrahedral are held by hydrogen bonds; 2.) montmorillonite (also known as smectite): is a 2:1 clay mineral, the successive octahedral and tetrahedral sheets are bonded by Van der Waals forces. Additionally, this clay structure always consists of exchangeable cations such as magnesium or sodium; 3.) illite: similar to

montmorillonite, the illite clay group is also a 2:1 clay mineral. However, the three sheets are held together by potassium ions. The negative charge to balance the potassium ions comes from the substitution of cations such as aluminum or silicon (Evans *et al*, 1985). This literature review chapter will only examine clay mineralogy pertaining to the montmorillonite clay group. An understanding of the mineralogy of this clay group will help provide a fundamental basis on how the clay properties of the bentonite grout used for this research project will change as a result of cyclic heating and cooling. Additionally, similar peer-reviewed articles on cyclic heating and cooling of bentonite grouts will also be examined in order to compare the results obtained from this research project to that obtained by other researchers.

2.1. Mineralogical Features of Bentonite

The main constituent of bentonite is montmorillonite, which is derived by weathering of volcanic ash. As described above, montmorillonite forms part of a family of expandable 2:1 phyllosilicate. A figure of the montmorillonite clay structure is illustrated in Figure 2.1. The silica and gibbsite sheets are combined in such a way that the tips of the tetrahedrons of each silica sheet and one of the hydroxyl layers of the octahedral sheet form a common layer. The atoms common to both the silica and gibbsite layer are oxygen instead of hydroxyls.

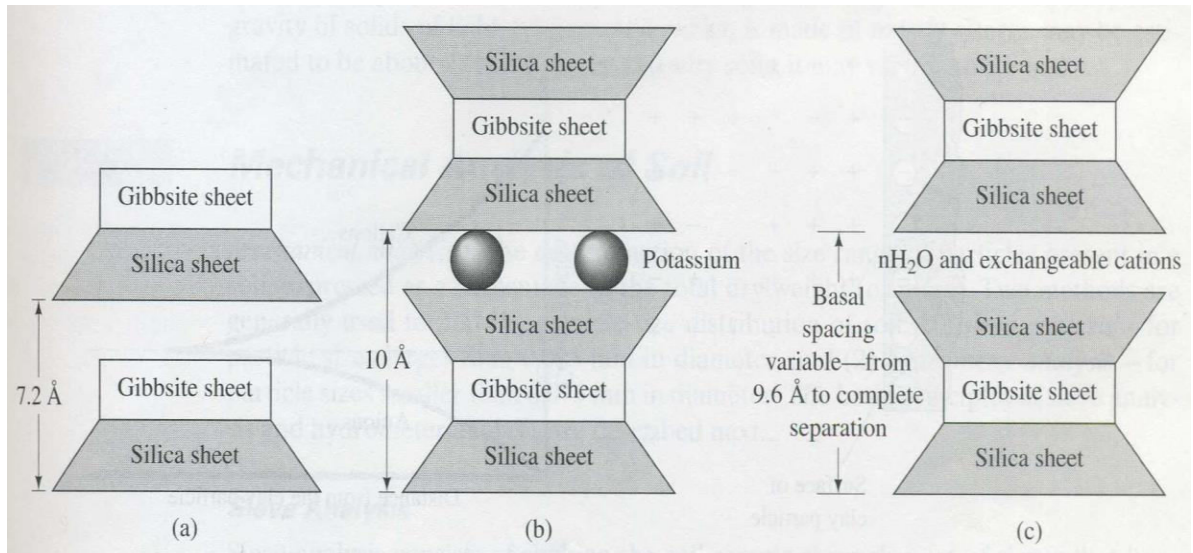


Figure 2.1. Structure of a.) kaolinite; b.) illite; c.) montmorillonite layer with successive layers of silica and gibbsite sheets (Source: Das, 2010).

By stacking the combined octahedral and tetrahedral sheets one above the other, oxygen layers of each unit are adjacent to oxygen of the neighboring units. Therefore, the weak Van der Waals bonds holding the three sheets together can be easily separated by adsorption of water. According to Grim (1968) when montmorillonite is subjected to uniform moisture conditions, the clay particle will develop hydration characteristics of considerable stability. But when the hydration is altered even to a very slight degree, the stability is completely lost. This means that when water enters the montmorillonite structure, the silica-gibbsite sheets expand. Conversely when the water content is reduced, the clay particle also experience considerable shrinkage. The volume change in the clay structure is related to the thickness and mobility of the water film adsorbed onto or surrounding the montmorillonite particle, being increased or decreased relatively easily during wetting and drying conditions (Grim, 1968).

The montmorillonite clay structure has a permanent layer charge because of the isomorphous substitution in the octahedral sheet. Evans *et. al* (1985) describes isomorphous substitution as the replacement of cations within the basic structure, which often results in charge deficiencies. The cation exchange capacity is a measurement of the propensity of cations within a clay mineral structure to be substituted. The substitution of cation exchange capacity can result from 1.) broken bonds within the clay mineral structure; 2.) substitutions within the lattice structure; and/or 3.) replacement of the hydrogens which are part of the exposed hydroxyls. Substitution within the lattice structure is the major contributor to the total cation exchange capacity whereas replacement of the hydrogens is the secondary cause of cation exchange (Evans *et. al*, 1985).

2.2. Clay Structure

The structure of a fine-grained cohesive soil can be defined with the understanding of interparticle forces and the geometrical arrangement of the particles. Lambe (1953, 1958) delineated the structures of cohesive soils into two extreme groups: flocculated and dispersed as shown in Figures 2.2 and 2.3. If two clay particles approach each other in suspension, attractive forces due to Van der Waals forces and repulsive forces due to positively ionized adsorbed layers come into action. At lesser separation, Van der Waals forces dominate and so particles adhere. However, there is a decrease in Van der Waals forces with an increase in separation. If the adsorbed layer is thin, the repulsive force will be negligible and the random movement of particles will bring them into contact.

The net repulsive forces will be greatest when a particle face approach is closer. As a result, the flocculating particles form an edge-to-face arrangement, thus resulting in a flocculated structure (Lambe and Witman, 1979). Conversely, if clay particles have a thick adsorbed layer, the repulsion is greater and the particles are led to a slow independent settlement, after which they remain dispersed. A dispersed structure is one that had face-to-face orientation of the particles.

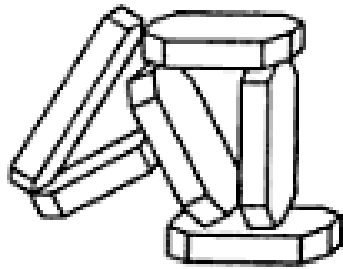


Figure 2.2. Flocculated clay structure illustrating edge-to-face contact (Source: Lambe and Witman, 1979).

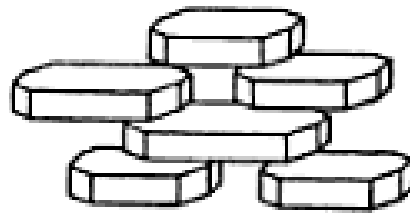


Figure 2.3. Dispersed clay structure illustrating face-to-face contact (Source: Lambe and Witman, 1979).

The engineering behavior of a soil element is highly dependent on the existing structure. According to Lambe and Whitman (1979), an element of flocculated soil has a higher strength, lower compressibility, and higher permeability than the same element of soil at the same void ratio but in a dispersed state. The higher strength and lower compressibility in a flocculated structure result from the interparticle attraction and the greater difficulty of displacing particles when they are in a disorderly array. The higher permeability in the flocculated soil structure is a consequence of the larger channels available for flow. A flocculated and a dispersed element at the same void ratio have approximately the same

total cross-sectional area available for flow. However in the flocculated structure, the flow channels are fewer in number and larger in size therefore less resistance to flow than through a dispersed structure.

2.3. Diffuse Double Layer (DDL) Theory

As noted by Mitchell (1993), the interparticle attractive and repulsive forces influence the flocculation-deflocculation behavior of clays in suspension and the volume change and strength properties of clay at void ratios common to natural soil deposits. Since the soil fabric of clays has a profound influence on its subsequent engineering properties, an understanding of factors that influence the flocculation-deflocculation behavior is of considerable value. The clay-water electrolyte system can be explained using the Gouy-Chapman theory of the diffuse double layer (Gouy, 1910; Chapman, 1913). The Gouy-Chapman theory is formulated from colloidal chemistry, where the colloidal particles are assumed to be infinitely long sheets that are negatively charged. In a dry clay, the negative surface charge is balanced by exchangeable cations such as Ca^{2+} , Mg^{2+} , Na^+ , and K^+ , which surround the particles and are held by electrostatic attraction. Conversely when water is added to clay, the cations will diffuse away due to the requirement for electro-neutrality leaving the liquid layer surrounding the clay particle contained with a net positive charge. Diffusion is due to the high concentration of cations near the particle surface relative to the water outside the realm of influence of the particle, which creates a concentration gradient and ideal diffusion conditions. The ion distribution such as shown

in Figure 2.2 is formed. These counter influences of electrostatic attraction and diffusion result in a distribution of cations referred to as the diffuse double layer (DDL).

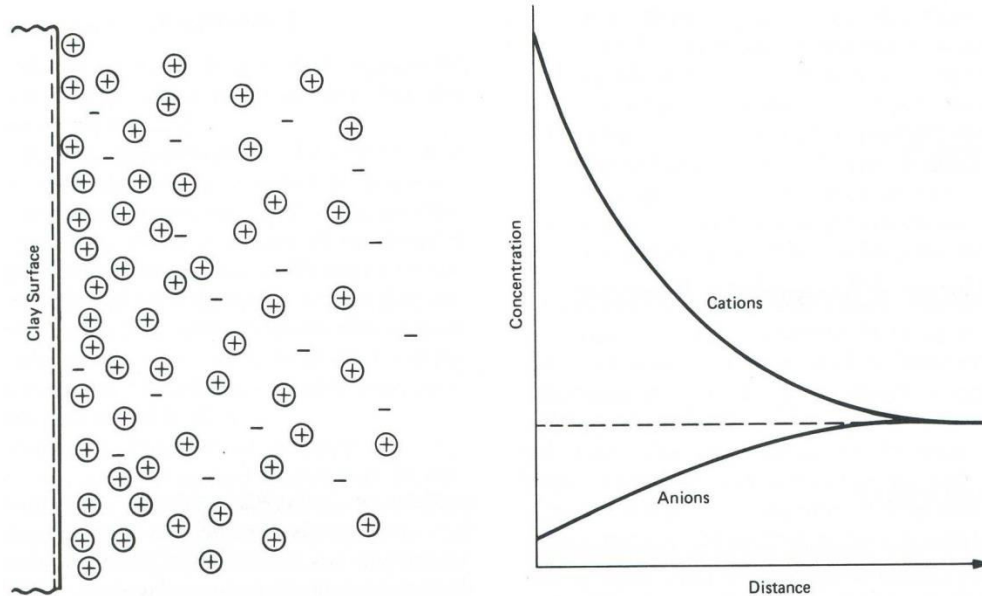


Figure 2.4. Distributions of ions adjacent to a clay surface according to the concept of the diffuse double layer (Source: Mitchell, 1993).

Although the Gouy-Chapman theory is widely accepted for the quantitative description of ion distributions adjacent to charged particles, it has been modified by Stern (1924) to take into account the finite ion size. The Stern model also takes into account that there is a closest layer of cations adjacent to the clay surface, and in this layer certain cations may become selectively absorbed to the clay surface such that they are not effectively part of the diffusing cations. Even though the Gouy-Chapman theory was modified, it has been shown to accurately describe the actual distribution of ions for smectite particles suspended in monovalent electrolyte solutions at low (less than 100 mole/m^3) concentration (Mitchell 1993).

The counter influences of electrostatic attraction and diffusion results into a distribution of cations also known as the DDL. The thickness of the DDL can be calculated from the Gouy-Chapman using Equation 1 [van Olphen (1963); Mitchell (1993)]:

$$D = \sqrt{\frac{\varepsilon kT}{8\pi \eta e^2 v^2}} \quad (1)$$

where ε is the dielectric constant, k is Boltzmann's constant, T is the absolute temperature, η is the concentration of the cations per cm^3 , e is a unit electronic charge, and v is the valence of the cation. The relationship shown in Equation 1 illustrates that the thickness of the DDL is directly proportional to the square root of the dielectric constant and temperature and varies inversely to the square root of the valence and concentration whereas the other factors in the equation remain constant. From the Gouy-Chapman theory, Shackelford (1994) categorizes factors that cause a decrease in the thickness of the DDL and the fabric of clay soils as ones that promote flocculation whereas an increase in the DDL promotes a dispersed structure. The influences of the variables that appear in Equation 1 on the DDL are documented in detail below:

- *Effect of Electrolyte Concentration:* The increase in electrolyte concentration reduces the surface potential for the condition of constant surface charge and also reduces the decay of potential. As electrolyte increases, the electrical potential for interacting parallel plates decrease thereby decreasing the repulsive forces (Mitchell and Soga, 2005). As a result, these conditions promote flocculation as the thickness of the DDL is reduced in size.

- *Effect of cation valence:* When considering solutions of the same molarity and a constant surface charge, a change in cation valence affects both the surface potential and the thickness of the DDL. An increase in the cation valence results in a decrease in thickness of the DDL thereby promoting flocculation. Additionally, an increase in cation valence suppresses the midplane concentrations and potential between interacting plates, thereby resulting in a decrease in interplate repulsion (Mitchell, 1993).
- *Effect of dielectric constant:* The dielectric constant influences both the DDL thickness and surface potential. A study by Kaya and Fang (1995) using the Atterberg limit of solvents as a function of dielectric constant found observations that are consistent with the observations of Mesri and Olson (1971) and Fernandez and Quigley (1985), in that the dielectric constant affects the flocculation and channelization of a soil structure. A decrease in dielectric constant causes aggregation and channelization within a soil mass thereby creating an increase in the flow area.
- *Effect of temperature:* As illustrated in Equation 1, an increase in temperature should cause an increase in the thickness of the DDL. However, an increase in temperature also results in a decrease in dielectric constant. The variation for water is shown in Table 2.1 as specified by Mitchell (1993):

Table 2.1. Dielectric constant values with varying water temperature

T (°C)	T (°K)	Dielectric Constant	
		(ϵ)	$\epsilon \cdot T$ (°K)
0	273	88	2.4×10^4
20	293	80	2.34×10^4
25	298	78.5	2.34×10^4
60	333	66	2.2×10^4

* (Source: Mitchell, 1993)

As shown in Table 2.1, there is very little variation of the term $\epsilon \cdot T$ with change in temperature. Therefore, this means that the DDL should not be greatly influenced. In addition to the factors that appear in Equation 1, other factors that affect the thickness of the DDL include cation size, pH, and anion adsorption (Shackelford, 1994). Descriptions of these properties have are provided below:

- *Effect of ion size:* When considering a small ion, it can closely approach the colloidal surface of the clay particle. Therefore, the smaller the ion, the smaller the diffuse ion layer (Evans *et al*, 1985). Also research conducted by Low (1987) found that there is little dissociation of exchangeable cations from clay particle surfaces due to small and poorly developed diffuse layers. The conclusion from this study was that the swelling of the clay is primarily due to the water hydration of particle surfaces.
- *Effect of pH:* The dissociation of hydroxyls in water is greatly influenced by pH. An increase in pH creates a greater tendency for H^+ from the hydroxyls to go into solution and the greater the effective negative charge of the particle. The pH

influences interparticle repulsions due to the effects of the clay particle surface charge. According to Mitchell and Soga (2005), positive edge charges can exist in low pH environments and these effects are of greatest importance in kaolinite, lesser importance in illite, and relatively unimportant in smectite. A low pH promotes positive edge to negative surface interaction, which leads to flocculation from suspension. In order for clay particles to be dispersed, a high pH is often required (Mitchell, 1993).

- *Effect of anion adsorption:* Certain anion types such as phosphate, arsenate, and borate are attracted to and become part of particle surfaces or edges. This results in an increased electronegativity and the diffuse ion layer. Phosphates strongly attracted to other particles and are amongst the most effective deflocculating agents for soil suspensions (Mitchell, 1993). According to van Olphen (1977), tannate ions are adsorbed at particle edges and form a compound with the exposed octahedral aluminum ions thereby resulting in a negative edge charge that prevents edge-to-face flocculation.

2.4 Effects of Temperature on the Molecular Structure of Clay

When montmorillonite clay particles are exposed to thermal conditions, the effects on the clay particles can include changes in physiochemical properties such as strength, swelling, plasticity, cohesion, compressibility, particle size, pore structure, cation-

exchange capacity as well as chemical composition (Bradley and Grim, 1951). Clay undergoes two main reactions when subjected to heat: 1.) the removal of physical water (dehydration) when subjected to a temperature of 100 °C and 2.) the neoformation with the depleting of chemically bound OH⁻ groups (dehydroxylation) in the temperature range 100 to 500 °C (Yilmaz, 2011). For the research project presented in this thesis, both reactions do not occur because the maximum temperature to which the bentonite grout is subjected in the laboratory is 49 °C. Heating of clays has a positive effect on the degree of cohesion between the clay particles resulting in an increase of the angle of shear resistance (Litvinov, 1960) and in compressive strength, especially for high plasticity clay based soils. However for some clays, temperature may cause dispersion and/or flocculation depending on the clay mineral and type of exchangeable ion. For temperatures above dehydration but below dehydroxylation: that is when the temperature is raised from ambient to that prior the onset of dehydroxylation, clay loses absorbed and hydration water. Loss of absorbed water modifies both the macro and micro porosity of the clay mineral and its plasticity. For temperatures above dehydroxylation, but below the temperature that destroys the clay structure: the changes that occur vary for different clay mineral groups (Yilmaz, 2011). Dehydroxylation destroys the layer structure of trioctahedral, 2:1 type minerals, whereas that of their di-octahedral counterparts is preserved (Heller-Kallai, 2006). Temperature changes influence the liquid and plastic limit proportional to the change with the thermal treatment in the viscosity of water (Fang and Daniels, 2006). Laguros (1969) conducted tests on kaolinite, illite, and montmorillonite clays and established that their liquid and plastic limit decreased with an

increase in temperature, with the greatest effect observed for montmorillonite. The extreme temperature effects that could be imposed on a clay structure would be freezing the clay minerals, which will not be covered in this thesis. The reason for disregarding freezing is because the geothermal systems are designed such that the grout in the borehole does not freeze and anti-freeze solutions are usually circulated in these systems as needed. Hence, the lowest temperature that was considered was 5°C, which was the temperature at which the cooling cycle tests were conducted.

2.4.1 Effects on Thermal Conductivity with Respect to Cohesive Soils

Soil thermal properties are of great importance in a geothermal borehole because the emplaced bentonite grout functions as a heat pathway between the circulating fluid and the earth. Thermal conductivity is a measure of a material's ability to transmit heat. The thermal conductivity of soil is significantly influenced by its saturation and dry density. Other secondary soil properties that have an effect on soil thermal conductivity include mineral composition and temperature (Kersten 1949; Salomone *et al.* 1984; Salomone and Kovacs 1984). The aforementioned soil properties are further explained in detail below:

- *Soil Moisture Content:* According to Salomone *et al.* (1984), moisture content of the soil has the most prominent effect on thermal conductivity. Moisture content has a most notable effect upon soil thermal conductivity. The results from the research conducted by Salomone *et al.* (1984) showed that a silty clay sample

with a moisture content of 9.5% had a thermal conductivity of 0.92 W/m°C and at a moisture content of 27%, the sample had a thermal conductivity of 1.9 W/m°C. Upon adding moisture to a soil, a thin water film develops around the soil particles, which bridges the gaps between the soil particles. The “bridging” behavior results in an increased effective contact area between the soil particles, thereby also increasing the heat flow and resulting in a higher thermal conductivity. As more moisture is added, the voids between the soil particles become completely saturated and the soil thermal conductivity will no longer increase (Salomone *et al.* 1984; Salomone and Kovacs 1984; Salomone and Marlowe 1989).

- *Dry Density*: An increase in dry density of the soil also results in an increase in soil thermal conductivity. When the soil dry density increases, soil particles are packed more closely into a unit volume, which in turn increases the number of contact points between the particles. The increase in contact points facilitates a larger heat flow path resulting in higher soil thermal conductivity (Salomone *et al.* 1984; Salomone and Marlowe 1989).
- *Mineral Composition*: The matrix configuration is responsible for affecting the thermal conductivity of a particular soil. Thermal conductivities measured on fine grained soils exhibited lower thermal conductivity values than coarser soils, and these low values have been related to high clay content (Demongodin *et al.* 1991).

Also, observations made by Salomone *et al.* (1984) confirm that fine-grained soils exhibit higher thermal resistivities than granular soils at given moisture contents. Thermal conductivity depends on grain size and grain size distribution, where coarse materials have higher thermal conductivity than finer materials. This effect is due to resistance between the grains, where the resistance decreases with increasing particle size because the number of contact point is also reduced. (Beziat *et al.* 1992).

Temperature: Studies by Kersten (1949) and Penner *et al.* (1975) specify a drastic change in soil thermal conductivity occurs at the freezing point when considering the heat transfer mode from convection to conduction. However according to Brandon and Mitchell (1989), in other temperature ranges the variation of soil thermal conductivity with temperature is minimal. According to Kersten (1949), an average variation of 4% in soil thermal conductivity of clays when considering the temperature range between 4.4 to 21 °C. The thermal conductivity of water increases with increasing temperature, whereas the thermal conductivity of most minerals decreases with increasing temperature (Midttømme *et. al* 1999). Since changes in pressure and temperature induce volume changes of the pore fluid and the matrix, Midttømme *et. al* (1999) reasons that the uncertainties related to the effects of temperature on thermal conductivity are due to the determination methods, which need to take into account the volume changes of the samples. The effects of temperature on soil plasticity is an under researched subject

considering how useful Atterberg limits are for clay particles. However, Laguros (1969) and Ctori (1989) have observed a reduction in liquid limit with increasing temperature. Youssef *et. al* (1961) and Ctori (1989) conducted their tests within the temperature range of 15 to 35 °C and 6 to 35 °C, respectively. According to Reeves *et. al* (2006), the effect of temperature on liquid limit also applies to other parameters such as the decrease in strength with increasing temperature resulting in a reduction in optimum moisture content for maximum dry density. Conversely, there is an increase in permeability and the coefficient of consolidation with increasing temperature.

2.4.2 Effects on Hydraulic Conductivity with Respect to Cohesive Soils

Hydraulic conductivity (also referred to as permeability) is a measurement of the ease with which a permeant liquid is able to flow through a porous medium. According to Darcy's Law, hydraulic conductivity, k , is a property of both the soil and the fluid. Factors that are known to affect hydraulic conductivity include water content (Lambe 1954; Mitchell *et. al* 1900), degree of saturation (Mitchell *et. al* 1900; Olson and Daniel 1981), void ratio (Bjerru and Huder 1957; Mitchell *et. al* 1900), as well as the size of the clay clods (Daniel 1984; Olsen 1962). However the aforementioned factors in this research project were kept constant, hence the factor under study in the cyclic heating and cooling tests was temperature. As explained in Section 2.3, the diffuse double layer theory indicates that temperature should have a negligible effect on the electrokinetic potential of the colloid system due to counteracting changes as temperature is changed.

As the temperature of the permeant liquid is altered, the viscosity and density of the liquid also changes. Therefore, since temperature affects the viscosity of liquids, the hydraulic conductivity should be sensitive to temperature. Conversely intrinsic permeability (K in m^2), which is a property of the soil only, does not change with viscosity. The relationship between intrinsic permeability and hydraulic conductivity is shown in Equation 2:

$$K = \frac{k\gamma}{\mu} \quad (2)$$

where γ is the volumetric weight of the fluid and μ the dynamic viscosity of the fluid. For this research project, it was more appropriate to investigate the intrinsic permeability values rather than the hydraulic conductivity values because intrinsic permeability is independent of the density and viscosity of the fluid whereas hydraulic conductivity is not. Therefore by evaluating intrinsic permeability, this minimizes the possibility of misinterpreting the changes in hydraulic conductivity as being changes in the clay fabric, when in fact the changes in hydraulic conductivity are influenced by a change in viscosity and/or density of the fluid. Therefore, the subject of interest is to understand to what extent, if any does the cyclic heating and cooling result in changes in the clay fabric without the influence of the permeant fluid. From Equation 2, differences in hydraulic conductivity, k , can result from differences in the intrinsic permeability, K , or from differences in the ratio of unit weight to viscosity of the fluid. For instance, a decrease in K and, therefore k may occur from external forces such as externally applied loads resulting in consolidation or compression of the soil with a subsequent decrease in the

pore space available for flow Shackelford (1994). Also Shackelford (1994) assesses that internal interaction between the liquid in the pore spaces of the soil and the solid soil particles may result in structural changes in the soil which alter the intrinsic permeability of the soil. However, such structural changes typically occur when soils are permeated with liquids that have significantly different chemical properties which is not the case for this research project.

2.5 Case Studies

This section is a presentation and review of studies from the available literature that are related to the cyclic heating and cooling of grout used in geothermal boreholes. Although this research project pertains just to bentonite grouts, some case studies where cement-bentonite grouts have been experimentally tested were also evaluated. The evaluation of cement grouts was investigated in order to understand the benefits of using bentonite based grouts over cement grouts and vice versa. Studies relating to how temperature affects hydraulic conductivity were also been reviewed. The case studies are presented below:

2.5.1 Allan (1997)

The thermal conductivity of cementitious grouts was investigated in order to determine suitability of these materials for grouting vertical boreholes used with geothermal heat pump systems. In addition, other relevant physical and mechanical properties were

determined. Emphasis was placed on evaluation of cement-sand grouts to take advantage of availability, simplicity, low cost, widespread use for other applications and good thermal properties. Different sand gradations were tested to determine effects on thermal conductivity and compatibility with pumpability requirements. The roles of mix variables such as water/cement ratio and sand/cement ratio were then measured. Superplasticizers were used to improve flow characteristics and supplementary cementing materials (fly ash and ground granulated blast furnace slag) were used to improve durability. The cement-sand grouts were tested for rheological characteristics, permeability, bond to HDPE pipe, shrinkage, coefficient of thermal expansion, exotherm, durability and environmental impact. Comparisons were made with conventional neat cement grout to quantify the benefit of adding sand to the grout formulations.

The results of the thermal conductivity tests of the cement-sand grouts ranged from 1.731 to 2.644 W/m.K (1.000 to 1.528 Btu/hr.ft. F), depending on the sand/cement ratio and sand type. This compares with 0.803 to 0.868 W/m.K for neat cement grouts, 0.75 to 0.80 W/m.K for conventional high-solids bentonite grout and 1.46 W/m.K for thermally enhanced bentonite. Another observation that was made was that the thermal conductivity of neat cement and bentonite grouts decreases significantly under drying conditions. The measured permeability of the bulk cement-sand grouts was of the order of 10^{-10} cm/s. Permeability tests performed on grout cast around a length of polyethylene pipe showed that increased flow occurred due to a higher permeability pathway at the grout-pipe interface. The magnitude of permeability increase depended on mix proportions at it was found that grouts containing sand had values still of the order of 10^{-10} cm/s whereas flow

in neat cement grout-pipe specimens increased an order of magnitude. Mechanical bond strength results illustrated that the bond between neat cement grout and the pipe was weak. Addition of sand to the grout improved the bond strength significantly. Improved bonding was correlated with decreased shrinkage of the cement-sand grouts as compared to neat cement grouts. After 91 days the linear shrinkage of cement-sand grouts ranged from 0.24 to 0.28%, whereas neat cement grout with a water/cement ratio of 0.8 shrunk 0.59%. The peak temperatures measured in a simulated 4 in. diameter borehole were 5 1.2°C for a Type I cement-sand grout and 36.7°C for a slag-modified grout. Reduction of grout exotherm by addition of blast furnace slag or fly ash did not result in improved bonding. This was explained by the counterbalancing effect of increased initial shrinkage associated with the use of slag or fly ash. Wet-dry cycles also demonstrated that conventional neat cement grouts are prone to severe cracking and that crack resistance is greatly improved by addition of sand. From the results of the conducted tests, the theoretical reductions in bore length would be around 8% by raising thermal conductivity from 1.46 to 2.42 W/m.K.

2.5.2 Allan and Kavanaugh (1999)

The objectives of the work reported here were to: (1) measure the thermal conductivity of cementitious grouts containing different fillers; and (2) calculate the theoretical reduction in heat exchanger length that could be achieved with such grouts. Two strategies to increase the thermal conductivity of cementitious grouts were used simultaneously. The

first of these was to incorporate high thermal conductivity fillers in the grout formulations. The second strategy was to use a superplasticizer to enable reduction of the water content of the grout mix. Superplasticizer is a liquid additive commonly used in the concrete industry to improve the rheological properties, reduce water/cement ratio and enhance durability. Lowering the water/cement ratio of grout through use of a superplasticizer decreases the porosity of the hardened material and shrinkage during curing. This results in higher thermal conductivity and improves other physical and mechanical properties. Type I cement (ordinary Portland, ASTM C 150) was used for the cement grout and fly ash (conformed to ASTM C 618 Class F) and ground granulated blast furnace slag were used as partial cement replacements for the grout formulations. Cement replacement levels of 40, 60 and 75% by mass were used. The superplasticizer used was a sulfonated naphthalene type with a solids content of 42% by mass. Different particulate fillers were investigated for improving the thermal conductivity of cementitious grouts. The fillers were selected for their thermal conductivity and compatibility with producing a fluid grout. The materials included silica sand, alumina grit, silicon carbide grit, and steel grit. Small proportions of bentonite were added to the cementitious grouts to reduce bleeding, promote full-volume set, and reduce settling. The different water/cement ratio used of the grouts tested without fillers was 0.4, 0.6, 0.8, and 4.2. The water/cement ratio of the filled grouts was kept constant at 0.45 (by mass) so that the effect of filler on conductivity could be determined. The exception to this was a cement-sand grout without superplasticizer that had a water/cementitious material ratio of 0.75. Conventional neat cement (cement plus water) grouts and a cement-bentonite grout

were tested to establish a baseline. However, the cement-bentonite grouts did not contain any fillers. A bentonite-sand grout was also tested for comparison. The cementitious grouts were cast as 75 mm x 125 mm x 25 mm (3 in. x 5 in. x 1 in.) blocks, where three specimens per batch were cast. The blocks were sealed, demolded after 24 hours, and placed in a water bath to cure. The hardened grouts were tested for thermal conductivity after 14 days. The grouts were then dried in an oven at 40°C (104°F) over a period of seven days, allowed to cool, and re-tested to determine the effect of loss of moisture. The bentonite-sand grout was cast as blocks with the same dimensions as the cementitious grouts. The specimens were sealed initially to prevent loss of moisture. Thermal conductivity was measured at four and 24 hours. The specimens were then allowed to air dry at 21°C (70°F) and relative humidity of 40 to 50% for 14 days. Thermal conductivity of the grouts was measured using a thermal conductivity meter that uses the hot wire method. The grout specimens were heated from an initial temperature of 21°C to 60°C (70°F to 140°F) over one minute.

The results of the tests have been summarized in Tables 2.2 to 2.4. Since a probe was used to measure the changes in thermal conductivity, the changes reflect changes in the intact material and did not account for shrinkage and cracking.

Table 2.2 Thermal conductivities of neat cementitious grouts (w/c = water/cement ratio)

Grout Type	w/c	Thermal Conductivity, W/(m.K)		% Mass Loss
		Saturated	After Drying	
Neat Cement & superplastizer	0.4	0.868 ± 0.019	0.706 ± 0.010	5.4
Neat cement	0.6	0.836 ± 0.012	0.585 ± 0.008	12.7
Neat cement	0.8	0.803 ± 0.011	0.456 ± 0.009	22.2
Cement & bentonite	4.2	0.655 ± 0.010	(cracked)	68

Table 2.3 Thermal conductivities of cementitious grouts with different fillers (w/c = water/cement ratio; f/c = filler/cement ratio)

Filler Material	w/c	f/c	Thermal Conductivity, W/(m.K)		% Mass Loss
			Saturated	After Drying	
Silica Sand	0.45	1.2	1.731 ± 0.031	1.605 ± 0.037	3.3
Silica Sand	0.45	2	2.394 ± 0.045	2.265 ± 0.043	1.7
Silica Sand	0.75	2	2.161 ± 0.042	1.491 ± 0.048	7.7
Coarse Alumina	0.45	1.9	2.318 ± 0.030	2.128 ± 0.039	2.9
Fine Alumina	0.45	1.3	2.075 ± 0.036	1.794 ± 0.028	3.2
Coarse silicon carbide	0.45	1.4	3.302 ± 0.056	2.493 ± 0.043	2.9
Fine silicon carbide	0.45	1.1	2.725 ± 0.039	2.147 ± 0.031	3.2
Steel grit	0.45	3.8	2.895 ± 0.049	1.920 ± 0.027	3.6

Table 2.4 Thermal conductivities of bentonite-sand grouts

Age/Condition	Thermal Conductivity, W(m.K)	% Mass Loss
4 hours/moist	1.462 ± 0.020	-
24 hours/moist	1.423 ± 0.021	-
2 days/air dried	1.342 ± 0.027	13.8
7 days/air dried	0.658 ± 0.031	32
14 days/air dried	0.502 ± 0.028	33.7

As can be seen from the thermal conductivity results cement-bentonite grout had the lowest values of all the cementitious materials tested in the saturated state. However, the neat cement grouts also had relatively low thermal conductivities. The results obtained for the bentonite-sand grout showed that the thermal conductivity strongly depends on moisture content. Loss of moisture caused a significant decrease in thermal conductivity of the bentonite grout. The thermal conductivity after air drying was similar to that for the oven dried neat cement grouts.

The oven drying tests gave an indication of the material performance under aggressive drying conditions and the cement-bentonite grout exhibited cracking and friability after oven drying and would act as an insulator if similar dehydration occurred during exposure. The neat cement grout with water/cement of 0.8 showed a significant decrease in mean thermal conductivity of 43.2% upon oven drying. Comparison with the superplasticized grout with water/cement of 0.4 demonstrated that the percentage decrease in thermal conductivity on drying was reduced to 18.7% by lowering the water/cement ratio. The conclusions drawn from this study was that lowering the water/cement ratio of the grouts and addition of conductive fillers can increase thermal

conductivity significantly. Silicon carbide gave the greatest benefit with conductivities of 2.725 to 3.302 W/(m·K) (1.575 to 1.908 Btu/h·ft·°F). However, this additive is probably prohibitively expensive and highly abrasive. The use of fillers, particularly silica sand and alumina grit, improves the thermal conductivity under drying conditions. Silica sand is the most economically favorable of the fillers studied. From the results of this study, the researchers concluded that the bore length could theoretically be reduced by 22 to 37% for a 350 kW (100 ton) load test case through addition of sand to cement-based grout.

2.5.3 Cho *et al.* (1999)

This study presents the results of experimental studies to investigate the effect of temperature on hydraulic conductivities of compacted bentonite samples with various dry densities. The tested specimens were calcium bentonite with the following compositions: 70% of montmorillonite, 29% of feldspar, and small amounts of quartz (~1%). The hydraulic conductivities of the water-saturated bentonite samples with the dry densities of 1.4 Mg/m³, 1.6 Mg/m³, and 1.8 Mg/m³ were measured within the temperature range of 20 to 80°C. The bentonite samples were saturated using demineralized water. The apparatus used to measure the hydraulic conductivity was designed to supply demineralized water into the sample at hydraulic pressures of 900 to 2000 kPa depending on the dry density of the bentonite. The cylindrical cell has an inside diameter of 50 mm (~2 inches) and a height of 25 mm (~1 inch) or 10 mm (~0.4 inches) depending on the dry density. The bentonite with initial water content of 14% was uniaxially compacted to the desired

density in the cell. Thereafter the compacted bentonite specimen in the cell was rigidly confined in the chamber by using a restraining ram. The water was supplied from the bottom to the top of the chamber, and the bentonite specimen was saturated in the cell. The results of the study revealed that the hydraulic conductivities of compacted calcium bentonite with dry densities higher than 1.4 Mg/m^3 are lower than 10^{-9} cm/s . The researchers reason that the high swell potential of bentonite contributes significantly to the development of low hydraulic conductivity values. A linear relationship between the logarithm of the hydraulic conductivity and the bentonite dry density was also observed. The hydraulic conductivities of compacted bentonite increase with increasing temperature, and the hydraulic conductivities at the temperature of 80°C increase up to about three times those at 20°C . The intrinsic permeability is nearly constant and the change in viscosity contributes greatly to the increase of hydraulic conductivity with increasing temperature within a temperature range of 20 to 80°C under the experimental conditions. Although the hydraulic conductivity increases with temperature, the experimental results also indicate that the effect of temperature elevation up to 80°C on the hydraulic conductivity is not large, and the hydraulic conductivities of compacted bentonite with dry density of 1.8 Mg/m^3 are still low and are in the order of 10^{-13} m/s even at the temperature of 80°C .

2.5.4 Hueckel and Pellegrini (1992)

In this research, the behavior of clays when subjected to cycles of heating and cooling in undrained conditions was experimentally studied. Two clays were subjected to cyclic heating-cooling tests: Boom clay from 240 m depth at Mol, Belgium; and Pasquasia clay from 160 m depth in Sicily, Italy. Boom clay is relatively soft and highly plastic (22% smectite, 19% illite, 29% kaolinite), with a low water content. Pasquasia clay is a medium plasticity cemented clay, sometimes fissured, with 10-15% kaolinite, <5% smectite, 20-25% calcite, 15-20% quartz, and with a very low (13%) water content and low permeability. The tests were performed at ISMES (Istituto Sperimentale Modelli E Strutture) with a high pressure, high-temperature triaxial apparatus. The experiment consisted in heating/cooling of clay specimens under undrained conditions at a constant total nonisotropic stress state. The temperature range used for heating and cooling was from 22.5 to 60°C. In the case of Boom clay, three total stress states were examined: an anisotropically normally consolidated state and two over consolidated states. Pasquasia clay was investigated in an over consolidated state. After the desired total stress level was attained, the material was allowed to develop undrained creep up to a stabilization of pore pressure at room temperature. Heating was then performed at closed drainage in small temperature steps. Since the testing system, including the cell, water tubings, and porous stones, was subjected to thermal expansion, corrections were applied by a release of calibrated quantities of water. This was adopted to simulate actual undrained conditions in the sample, as an extreme case of in situ conditions.

In drained conditions under constant effective stress, the yield surface of the clays shrinks with increasing temperature until it reaches an immobile stress point. The condition of constant stress excludes any further shrinking of the surface despite the growth of temperature. Plastic strain is then generated to compensate through strain hardening for the thermal softening. During cooling, the yield surface grows back through the whole temperature range. Thus, it may reach a larger size than the original one, at the completion of cooling. In the undrained tests the researchers found that the only difference from the drained conditions tests was that at a constant total stress, the effective stress is not constant. Rather, a water pressure is generated because of higher thermal expansion of water than that of solid. This induces an equal but opposite in sign decrease in effective mean stress. As a consequence, the shrinking yield surface enters in contact with the stress points at a lower stress value that is at higher temperatures than in drained conditions. The analysis based on a thermoplastic model suggests that the negative pressure is caused by a large plastic dilatancy occurring at effective stress states close to the critical state. Therefore, the conclusion drawn from this research is that heating the clay induces a large pore-water pressure increase, which eventually leads to a large irreversible strain and possible mechanical failure. Subsequent cooling of the clay produces a drop in water pressure.

2.5.5 Lee *et al.* (2010)

An increase in thermal conductivity of backfilling grouts leads to considerable reduction in installation cost for ground heat exchanger by shortening the required bore length. Additionally, acceptable pumpability of grouts should be guaranteed during the installation of the heat exchanger in order to fill completely the annulus without any gaps that may cause thermal discontinuity. In this research, the thermal conductivity and viscosity of grout material, which are used for backfilling ground heat exchangers, were investigated. Seven different bentonite grouts were experimentally evaluated in the case of both neat bentonite grouts and thermally enhanced bentonite grouts with addition of silica sand and graphite as a filler. Bentonite 1 is a low grade bentonite used for a casting process, and Bentonite 2 is improved by adding montmorillonite to increase swelling potential. Bentonites 3 and 4 are produced for the purpose of civil engineering construction such as the mixture for a landfill liner or bentonite slurry. Bentonites 6 and 7 are produced for geothermal application. Bentonite 2 has the highest content of montmorillonite and Bentonite 7 has the highest content of quartz. The procedure for the free swell test was performed in accordance to ASTM D5890 standards. The thermal conductivity of grouts was measured using a QTM-500 thermal conductivity meter (Kyoto Electronics), which is equipped with the PD-13 probe whose dimension are 95 mm×40 mm (3.7 in x 1.57 in). The equipment adopts the transient hot wire method to measure the thermal conductivity of the grout. Since the bentonite grout is an amorphous paste, an acrylic container was constructed to fill the grout in it and to permit the measurement of thermal conductivity. The container consisted of a water jacket, a

perimeter passage, which is connected to a water tank to flow water of the controlled temperature through it. The temperature was controlled at 20°C is during the thermal conductivity measurements. The viscosity of bentonite grouts was measured by a vibration type viscometer of which the measuring plate vibrates with a frequency of 30 Hz. The viscosity range measurable in the viscometer is from 0.003 to 120 P (g/cm-s). In order to investigate the isothermal change in viscosity with time after mixing the bentonite grout samples, an acrylic box similar to that used for measuring thermal conductivity was used, which is also equipped with a water jacket to flow water at a room temperature of 20°C.

The observations made from the results of the free swell test was that the swelling indexes of the seven bentonite grout samples ranged from 13.5 to 29 mL/2g. From these results, a correlation between the content of montmorillonite and the swelling index was observed; that is the higher the content of montmorillonite, the greater the swelling potential is expected. In case of the seven neat bentonite grouts with no addition of fillers, two mixtures of 20% and 30% of bentonite by weight showed a range of thermal conductivity in the fully saturated condition of 0.74–0.81 W/mK and 0.76–0.88 W/mK, respectively. Increase in thermal conductivity by the addition of silica sand was not significant, and even the case of 60% of silica sand resulted in the thermal conductivity less than 1.4 W/mK. Enhancement of thermal conductivity by the addition of graphite powder had greater impact than enhancement by adding silica sand to the bentonite grout. The addition of 20% of graphite enhanced the thermal conductivity of the bentonite grout close to the geologic formation usually ranging from 1.7–2.1 W/mK. A change in

viscosity with time was quantitatively investigated for Bentonites 1 and 3 with the bentonite content of 20%. In this comparison, the effect of magnitude of mixed silica sand and graphite was also examined. There was significant increase in viscosity with increasing time. Additionally, the rate of viscosity increased with the increasing amount of additives mixed in the grout. Therefore, care must be taken not to delay the grout pumping process after preparing the grout paste in the field.

2.5.6 Park *et. al* (2011)

In some countries, cement based grout have been considered as an alternative to bentonite grouts due to the high cost of bentonite. Park *et. al* (2011) carried out laboratory experiments, which included testing for thermal conductivity, hydraulic conductivity as well as unconfined compression test to characterize cement grouts. A single temperature cycle was applied for ten days at 50°C and then switched to -5°C for the next ten days. The mixture design of the 15 specimens that were tested was as follows: a.) specimens GEO-1 to GEO-5 are neat cement grouts (neither sand nor bentonite was added) with the water/cement ratios ranging from 0.4 to 0.8; b.) specimens GEO-6 to GEO-10 (no bentonite was added), the water/cement ratio was fixed at 0.6 and the silica sand content was increased from 2 to 2.8 times the cement content; and c.) specimens GEO-11 to GEO-15, the water/cement and sand/cement ratios was fixed at 0.6 and 2.4, respectively, and bentonite was added with the bentonite/cement ratio increasing from 1% to 6%. In order to investigate the influence of seasonal temperature cycling of circulating fluid on

the integrity of interface between the cement grout and the HDPE pipe, a 36 mm (1.5 inch) diameter pipe was embedded at the center of the cylindrical specimens. The thermal conductivity measurements were performed using a QTM-500 (Kyoto Electronics) device. The apparatus adopts the transient hot wire method to measure the thermal conductivity of grout material and is able to make measurements within the range of 0.023 to 12 W/mK (0.013 to 6.96 Btu/hr.ft².°F) and a reproducibility of ±3%. The specimens were placed in a rectangular mold in a wet condition, where the thermal conductivity was measured continuously for 14 days. The hydraulic conductivity of the specimens was measured using a flexible wall permeameter. The flexible wall permeameter was modified so as to measure the equivalent hydraulic conductivity, which measures the overall hydraulic conductivity of a specimen including both interface gap and the grout. The results of the test revealed that increasing the water/cement ratio can decrease the thermal conductivity. The thermal conductivity values ranged from 0.23 to 0.27 W/m.K (0.133 to 0.157 Btu/hr.ft².°F). For the specimens with the fixed water/cement ratio equal to 0.6, increasing the silica sand/cement ratio increased the thermal conductivity by 0.01 to 0.09 W/m.K (0.0058 to 0.052 Btu/hr.ft².°F). In the case where bentonite was added to the cement grout of fixed water/cement (0.6) and silica sand/cement (2.4) ratios, the thermal conductivity of the grout remained unchanged. Moreover, the addition of bentonite decreased the workability of the grout significantly. An increase in the water/cement ratio as well as the addition of silica sand resulted in a reduction of unconfined compression strength of cement grout specimens. The more the number of temperature cycles, the less the unconfined compressive strength is observed.

The results of the hydraulic conductivity tests ranged from 10^{-10} to 10^{-8} cm/s. The hydraulic conductivities of the cement grout specimen without an embedded pipe was approximately 3.57×10^{-10} cm/s, which is smaller than the equivalent hydraulic conductivity of the pipe-embedded cement grout specimen (4.87×10^{-9} cm/s) because of a formed gap at the contact interface of the pipe. However, the results revealed that the interface integrity between the cement grout and the pipe was not considerably influenced by the cycling of fluid temperature after the first cycle of heating- cooling circulation.

2.5.7 Philippopoulos and Berndt (2001)

Debonding between the grout and the borehole or between the grout and the heat conductor pipe may occur for a variety of reasons, such as shrinkage of the backfill materials or surrounding geo-formation, improper grouting and thermal incompatibility. The effect of thermal contact resistance on the heat conduction due to debonding in ground heat exchangers was investigated. This was accomplished by using analytical one-dimensional radial flow models to examine continuous circumferential gaps at the grout/formation interface. Subsequently, solutions of the two-dimensional heat conduction were obtained by finite element analysis to evaluate the spatial distribution of potential interfacial gaps. Two cases of debonding were considered in this study: a.) debonding at the grout/formation interface and b.) debonding at the pipe/grout interface. The one-dimensional model considered a three-component medium to model the grouted borehole of the ground heat exchanger together with the surrounding formation. The

components of the medium consisted of the grout around the U-loop, an interfacial air gap between the grout and surrounding formation and the surrounding formation. Steady-state heat conduction was assumed and the heat rate associated with the model was assumed to be constant while the heat flux varies inversely proportional to the radial distance. A 102 mm diameter borehole containing two high-density polyethylene pipes with inner diameter of 25.4 mm and outer diameter of 33.0 mm was considered. The center-to-center separation of the two pipes was 50 mm. Analysis was performed considering two types of grouts. The first was superplasticized cement–sand grout, which (referred to as Mix 111). Mix 111 is a mixture of cement, water, silica sand, small amounts of superplasticizer, and bentonite. The exact mix proportions and properties of this grout are presented elsewhere (Allan 2000; Allan and Philippacopoulos 1998; Allan and Philippacopoulos 1999). The second grout used in the analysis was high solids bentonite. The temperature for the cooling mode was taken as 3.3°C. This represents an average of the entering (5.0°C) and leaving water temperatures (1.7°C) in the piping loop for this mode of operation. Similarly, the heating mode temperature was taken as 33°C, which also represents the average of the entering and leaving water temperatures 30 and 36°C, respectively. The following values for the thermal conductivities were used for both the one-dimensional and two-dimensional analyses: a.) Mix 111: 2.42 W/mK (1.4 Btu/hr.ft².°F); b.) bentonite: 0.75 W/mK (0.43 Btu/hr.ft².°F); and c.) formation: 1.72 W/mK (0.99 Btu/hr.ft².°F). The grout conductivities are based on experimental results (Allan and Philippacopoulos, 1998). The formation conductivity was chosen to represent what might be expected for a sandy or clayey soil, sandstone or limestone. The

corresponding value for the air-filled gaps was 0.027 W/mK (Mills, 1992). The findings of the study revealed that gaps developed at the grout/formation interface generally caused by: a.) a temperature drop along the interface; b.) reduction of heat flux especially near the borehole; c.) increase of the total resistance of the system; and d.) decrease of the overall heat transfer rate. Two-dimensional finite element analysis of the influence of spatial variation of gaps led to the following conclusions: a.) a 90° debonding at grout/formation interface caused 20% reduction in the overall heat transfer coefficient; b.) a 180° debonding a variation-of-parameter studies conducted using different thermal conductivity ratios (grout-to-formation) showed that better heat transfer rates are associated with grout conductivities close to or higher than that of the formation. The grout/formation interface produced 33% reduction in the overall heat transfer coefficient; c.) a 360° debonding at the grout/formation interface produced 60% reduction of the overall heat transfer coefficient; and d.) a 360° debonding (all around gap at grout/pipe interface) produced 66% reduction of the overall heat transfer coefficient. The final conclusion made was that debonding at the backfill/pipe interface was found to be of greater significance than debonding between grout and formation.

CHAPTER 3: Materials and Methods

To gain insight into the effects of heating and cooling upon the bentonite well seal grouting material used in geothermal heat pump systems, thermal and hydraulic conductivity tests were conducted. These laboratory tests were selected based on the performance requirements of the grout employed in these systems. These performance requirements included the need to control ground water migration along the well annulus between aquifers and to conduct heat to and from the formation materials. Thus, thermal and hydraulic conductivity results for this research provide information on the functionality of the bentonite grout over time. This section provides detailed descriptions of the materials and methods used in this research project.

3.1 Grouting Material

The BENSEAL/EZ-MUD® slurry, which is manufactured by Baroid Industrial Drilling, Inc., was the bentonite grout tested for this research project. The 20% solids bentonite slurry combines two products: the BENSEAL® bentonite granules and a polymer referred to as EZ-MUD®. BENSEAL® is a naturally occurring, bluish/gray granular, Wyoming sodium bentonite. EZ-MUD® is a liquid polymer emulsion containing partially hydrolyzed polyacrylamide/polyacrylate (PHPA) copolymer and is used in the slurry to stabilize the highly reactive BENSEAL® from swelling and sloughing before it is placed in the borehole. This stabilization involves lowering the viscosity of the slurry during the preparation process so as to increase the workability of the grout. According

to the manufacturer of the grout, the combination of these two products provides an economical method to seal and grout boreholes. The thermal conductivity and permeability of the grout as specified by the manufacturer is 0.74 W/m-K (0.43 Btu/hr.ft.°F) and 1.2×10^{-8} cm/sec, respectively. The aforementioned slurry was selected with the help of Mr. William Reichart, president of the Pennsylvania Ground Water Association (www.pwgwa.org) and president of William W. Reichart Inc., a drilling firm active in the installation of geothermal systems. The BENSEAL/EZ-MUD® slurry was chosen because it is commonly used in Pennsylvania for grouting applications including in geothermal heat pump systems. The grout was provided by Mr. Reichart to assure laboratory studies used the same material as is used in the field.

3.2 Preparation of Slurry

The BENSEAL/EZ-MUD® slurry was prepared using the mixture proportions specified by the manufacturer. The slurry mixture procedure was as follows:

- 14.5 mL of EZ-MUD® was added to 5 L of tap water (the electrical conductivity of the tap water was 232 μ S/cm and a pH equal to 6.5)
- Using a Hobart mixer, the EZ-MUD® and water solution was stirred at a fairly slow rate until the EZ-MUD® completely dissolved in the water.
- One kilogram of BENSEAL® was then added to the EZ-MUD®/water mixture, while continuing to stir the mixture gently (no faster than 40 rpm). The manufacturer recommends that the slurry be blended only long enough suspend the BENSEAL® material.

Figures 3.1 and 3.2 illustrate the preparation process of the BENSEAL/EZ-MUD® slurry. During field operations when the slurry preparation is complete, the grout is usually tremied to allow the bentonite granules to hydrate and swell in situ. For this research project, there was no need to tremie the grout because the depth of testing apparatus in the laboratory did not extend to significant depths as compared to the geothermal systems in the field.



Figure 3.1 The constituents of the bentonite grout: BENSEAL® granules and EZ-MUD®



Figure 3.2 The BENSEAL/EZ-MUD® slurry being mixed in the Hobart mixer

3.3 Development of Equipment

In order to test for thermal properties of the bentonite grout, a geothermal well model was constructed of a 152 mm (6 in) diameter, polyvinyl chloride (PVC) outer pipe to contain the bentonite seal with a 25 mm (1 in) diameter, high density polyethylene (HDPE) inner

pipe to circulate the heating and cooling fluid. The geothermal well model is shown in Figure 3.3.



Figure 3.3. Top and side view of geothermal well model

The apparatus has analogous lateral dimensions to that of an actual geothermal system, while the height of the device represents a small portion of the height for an actual system and is approximately 305 mm (1 ft). The piping material that was used is the same HDPE piping used in the installation of geothermal systems. Within the annulus of the device, 15 thermocouples were strategically placed for the calculation of the system thermal conductivity using Fourier's law for heat flux in soils. The thermocouples were numbered according to their channels from 101 to 115 as shown in Figure 3.4. Channel 101 being the thermocouple at room temperature, 102 to 113 are the thermocouples measuring the change in temperature of the grout, 114 and 115 are the thermocouples measuring the drop in temperature of the water circulating the system. An additional

thermocouple, channel 116, was used to measure the temperature of the water in the water bath.

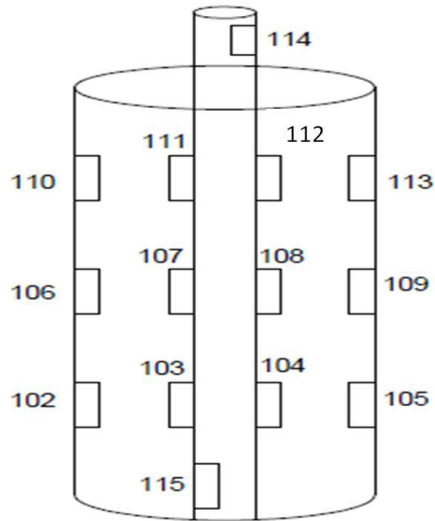


Figure 3.4. Thermocouple placement in the geothermal system model

As shown in Figure 3.4, there was an equal vertical spacing of 76 mm (3 in) between the thermocouples. The replication of the thermocouples across the geothermal model was done so that if there was a malfunction with one thermocouple, the ongoing tests would not need to be terminated. The initial thermal conductivity tests were conducting for 24 hours for each heating and cooling cycle until all the thermocouples reached equilibrium. In order to determine whether equilibrium had been reached, the temperature readings for both the grout and water for a heating and cooling cycle were plotted over a 24 hour period as shown in Figures 3.5 to 3.8.

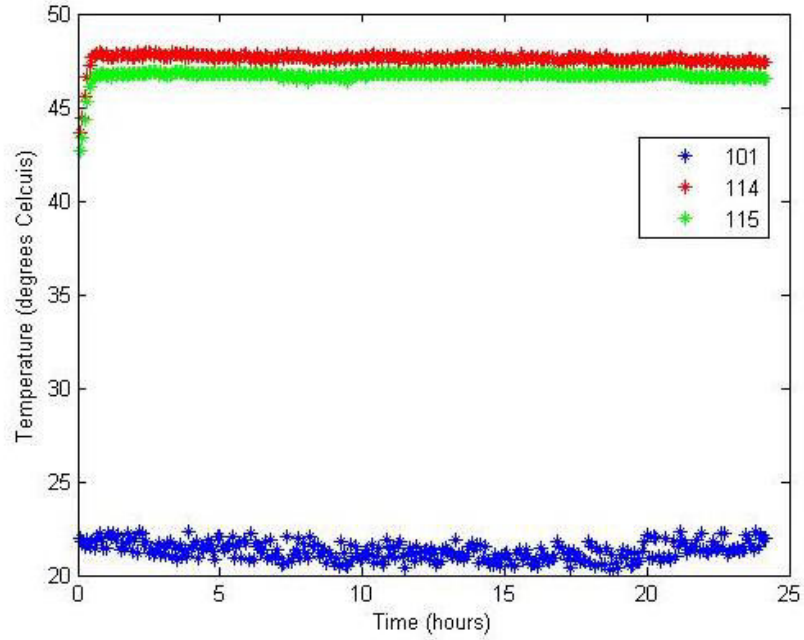


Figure 3.5 Plot of water and ambient temperature over a 24 hour period for a heating cycle

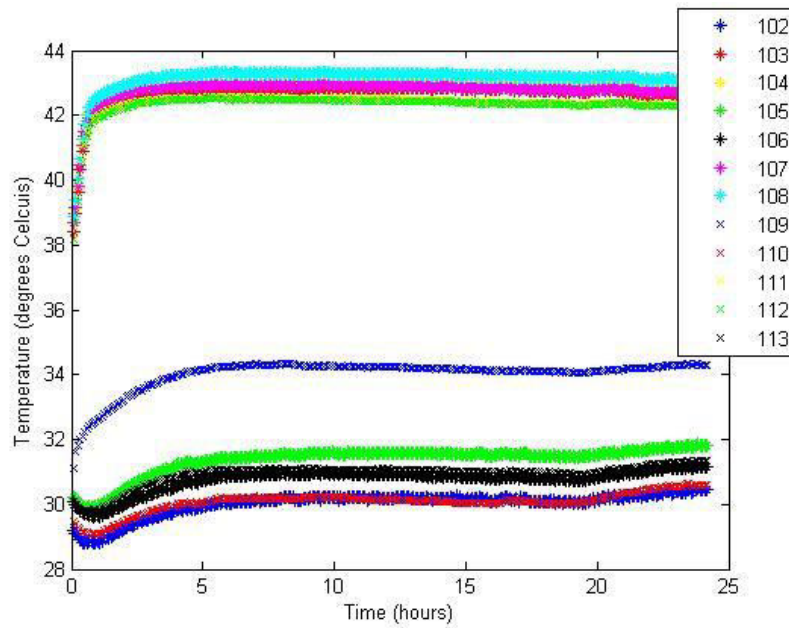


Figure 3.6 Plot of grout temperature for twelve thermocouples over a 24 hour period for a heating cycle

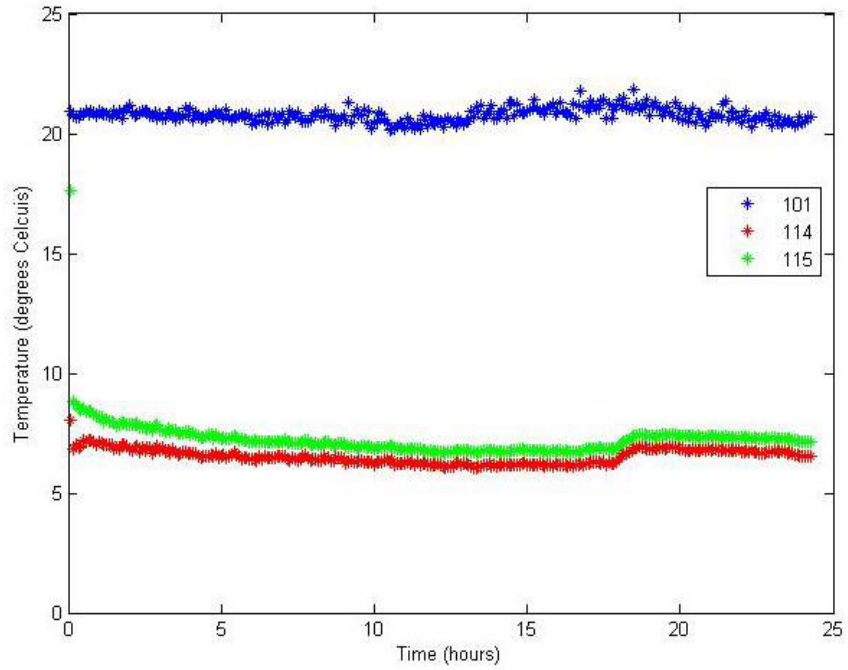


Figure 3.7 Plot of water and ambient temperature over a 24 hour period for a heating cycle

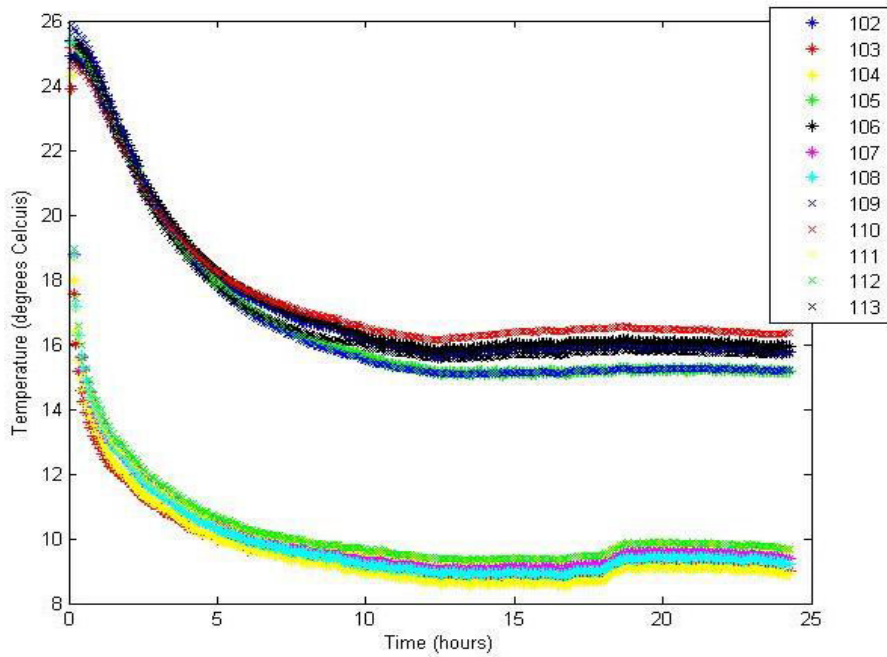


Figure 3.8 Plot of grout temperature for twelve thermocouples over a 24 hour period for a cooling cycle

The thermal conductivity tests in 2010 to 2012 were conducted for 24 hours. However, the thermal conductivity tests in 2013 were conducted for 72 hours in order to accommodate the modified hydraulic conductivity tests. The thermal conductivity of the system was then calculated from the last ten data points because this was when the change in temperature had reached equilibrium; that is the data plateaus and there was little to no variability in the data. The entire system shown in Figure 3.9, had two separate continuous loops (indicated by the red and green flow lines), where water was circulated at a rate of 6825 mL/hr. A peristaltic pump was used to provide a continuous flow through the system. The red flow path illustrates a continuous loop from the electric heating bath through the geothermal model and back into the electric heating bath. The electric heating bath and water chiller were used to regulate water temperatures comparable to those experienced in a geothermal well (0-50 °C). In the red flow path, the direction of the water flow influenced the thermal conductivity values. During the initial system setup, it was observed that when water was flowing upward, the test produced a higher thermal conductivity than when the water was flowing downward in the system. This is because an upward flow eliminates any air bubbles that may be present in the system. Therefore, the water was directed to flow in an upward direction through the geothermal model.

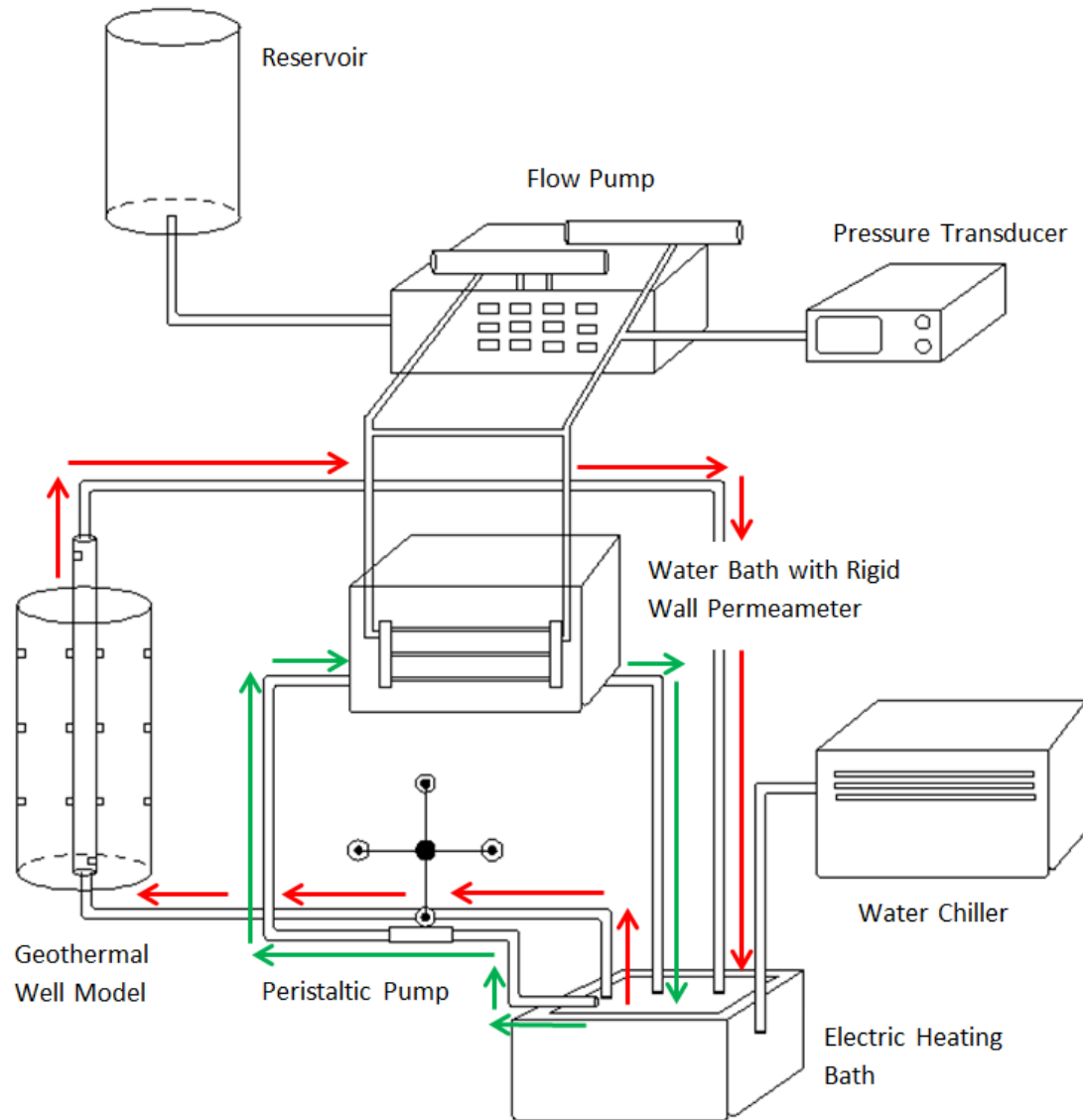


Figure 3.9 Schematic of thermal and hydraulic conductivity testing apparatus

The green flow path illustrates a continuous loop through a water bath which contained a rigid wall permeameter that was used for measuring the hydraulic conductivity of the bentonite grout. When a heating cycle was conducted, the water bath was heated together with the grout and likewise when a cooling cycle occurred. Thus, the hydraulic

conductivity of the grout was tested while being subjected to both heating and cooling cycles. The water bath was insulated and remained closed throughout the testing in order to minimize any heat losses.

3.4 Thermal Conductivity Tests

The instrumentation and data acquisition equipment used to determine thermal conductivity included a flow meter, a watt transducer, thermocouples, and a data logger. To determine thermal conductivity, Fourier's law for heat flux in soils was used. Fourier's law is given in the following form:

$$Q = -k_t A \frac{dT}{dx} \quad (3)$$

where Q is the heat flow per unit column, k_t is the thermal conductivity of the grout slurry, A is the area of the geothermal model, and dT/dx is the temperature gradient. From the geothermal model, the inner and outer surfaces of the cylinder were each at a different uniform temperature. The heat flowed radially through the wall of the cylinder. The cylinder was then considered to be made up of disks that form a series of successive layers. From continuity considerations, the radial heat flow through each of the successive layers in the wall of the geothermal model was assumed to be constant since steady flow conditions were assumed (and shown by the thermocouples in Figures 3.5 to 3.8). Since the area of the successive layers increased with an increasing radius, therefore the temperature gradient had to decrease with increasing radius. A concentric layer (of thickness dR and radius R from the center) in the wall of the cylinder was considered where the area of heat flow was $2\pi R$ for a unit length of cylinder. According

to Fourier's law, the temperature gradient normal to the axis of the cylinder is dT/dR and Equation 3 was then integrated in the following form:

$$Q = -2\pi R k_t \left(\frac{dT}{dR} \right) \quad (4)$$

$$Q \ln \left(\frac{R_2}{R_1} \right) = -2\pi k_t (T_2 - T_1) \quad (5)$$

where R_1 is the inside radius with corresponding temperature T_1 and R_2 is the outer radius corresponding to temperature T_2 . Considering a cylinder of length L and rearranging the integrated equation to eliminate the negative sign formulated Equation 6:

$$k_t = \frac{Q \ln \left(\frac{R_2}{R_1} \right)}{2 \pi L \Delta T_g} \quad (6)$$

where ΔT_g the change in temperature of the grout. The thermocouples measured the temperature difference and a measurement of Q was obtained by using Equation 7:

$$Q = \dot{m} c_p \Delta T_w \quad (7)$$

where \dot{m} is the mass flow rate of water through the inner pipe, C_p is the specific heat capacity of water (1 cal/g°C), and ΔT_w is the drop in temperature of the water from the inlet to the outlet of the geothermal model. In order to obtain a value of \dot{m} , the rate of flow at which the peristaltic pump was moving the water was calculated as shown in Table 3.1.

Table 3.1. Flow rate data at pump setting of seven

Time (s)	Volume (mL)	Flow rate (mL/hr)
33.03	62	6758
44.55	85	6869
51.52	98	6848

The three trials taken at setting seven of the peristaltic pump were averaged to get a final flow rate of 6825 mL/hr. In order to optimize the mechanical mixing within the HDPE pipe, the pipe was filled with six millimeter seamless air soft BBs. Calculations for the thermal conductivity were done by creating a Matlab program (refer to Appendix A for the Matlab code). The Matlab code calculated the thermal conductivity of the system by considering the two thermocouples across from each other as a set. Therefore, the thermocouple setup shown in Figure 3.4 gave a total of six sets. Once the thermal conductivity for each set had been calculated, the Matlab code averaged these six values to obtain an average thermal conductivity of the entire geothermal model.

3.5 Hydraulic Conductivity Tests

3.5.1 Consolidometer Permeability Tests

The initial hydraulic conductivity tests were conducted using the falling head method in a consolidometer apparatus. A schematic of a falling head permeability setup is shown in Figure 3.10. The bentonite grout was placed in a consolidometer ring of cross sectional

area A . The attached standpipe was designated with a cross sectional area of a . Before the commencement of the test, the bentonite grout was consolidated and then saturated by allowing water to flow continuously through the sample from the standpipe. A $\frac{1}{4}$ tsf load was applied. After saturation was completed, the standpipe was filled with water up to a height of h_0 and the initial time recorded and denoted as t_0 . When the water level dropped from h_0 to h_1 the time, t_1 , was noted.

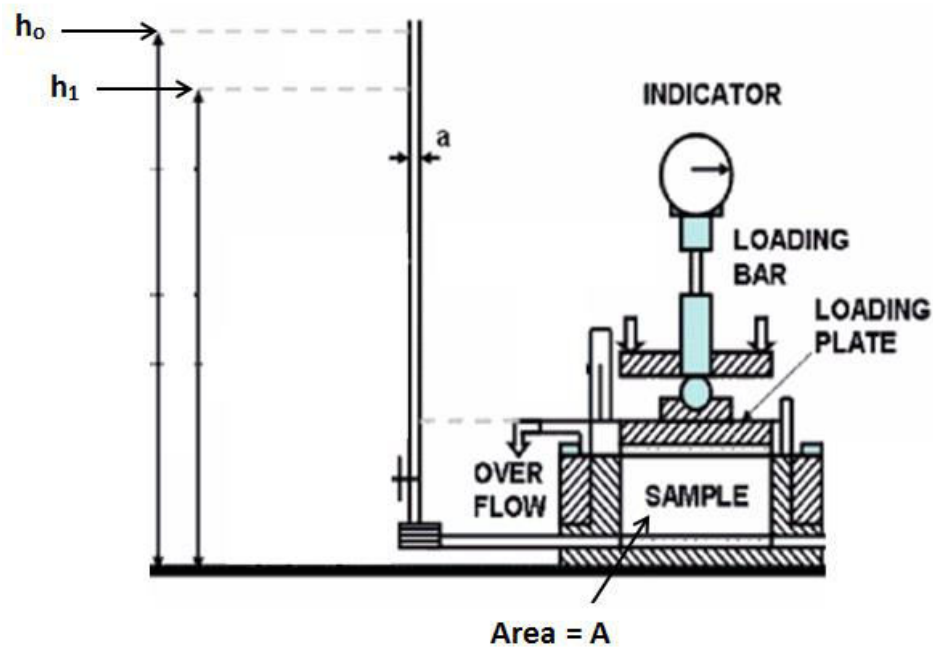


Figure 3.10 Schematic of falling head permeability setup (Source: Barzani, 2010)

The hydraulic conductivity, k , was then determined on the basis of the drop in head ($h_0 - h_1$) and the elapsed time ($t_0 - t_1$) using Darcy's Law in the following equation for falling head with constant tail water:

$$k = \frac{L}{t_1 - t_0} \left(\frac{a}{A} \right) \ln \left(\frac{h_0}{h_1} \right) \quad (8)$$

The testing methodology was extended from the consolidometer test to a triaxial permeability test during the summer of 2011. The experimental modification enabled the bentonite sample being tested to be subjected to both heating and cooling cycles in a similar manner as the thermal conductivity tests.

3.5.2 Triaxial Permeability Tests

The testing entailed incorporating a triaxial water bath in the testing apparatus as mentioned in the materials and methods section. The modified hydraulic conductivity tests were conducted in accordance to ASTM D-5084 standards. A photograph of a prepared sample in a triaxial cell is shown in Figure 3.11.



Figure 3.11 Bentonite slurry sample in a triaxial cell

Since the as-mixed bentonite slurry could not remain in an upright position within the latex membrane prior to consolidation, a plastic proctor was used for support in the

triaxial cell until the sample had consolidated. The dimensions of the slurry sample within the plastic proctor were a height of 102 mm (4 in) and a diameter of 72 mm (2.85 in). The applied pressures on the cell, headwater, and tailwater were 331 kPa (48 psi), 276 kPa (40 psi), and 317 kPa (46 psi), respectively. The tests were also conducted using a hydraulic gradient of 42. Darcy's Law for falling headwater and rising tailwater was applicable and therefore the hydraulic conductivity of the bentonite grout was calculated using Equation 9:

$$k = \frac{aL}{2A\Delta t} \ln \left(\frac{h_1}{h_2} \right) \quad (9)$$

Due to the unexpected significant volume changes (up to 61 cm³) that were experienced as a result of cyclic heating and cooling, the testing method was further modified to a flow-pump permeability method. A detailed description and sample calculations of the volume changes appears in Chapter 4 under the triaxial permeability results and discussion.

3.5.3 Rigid Wall/Flow Pump Permeability Tests

A closed system, flow-pump permeability method enabled better control of the flow of water in and out of the slurry sample by eliminating volume change observed in the open triaxial system. Since the apparatus that contained the bentonite slurry was a rigid wall and allowed virtually no volume changes. The stainless steel piping to and from the system also minimized the expansion of the water lines when subjected to heating cycles.

The type of flow pump that was used for the testing was a PH 22/2000 Programmable Harvard Apparatus as illustrated in Figure 3.12. The rigid wall permeameter is also shown in Figure 3.13.



Figure 3.12 A PH 22/2000 Programmable Harvard Apparatus flow pump that was used for the hydraulic conductivity tests

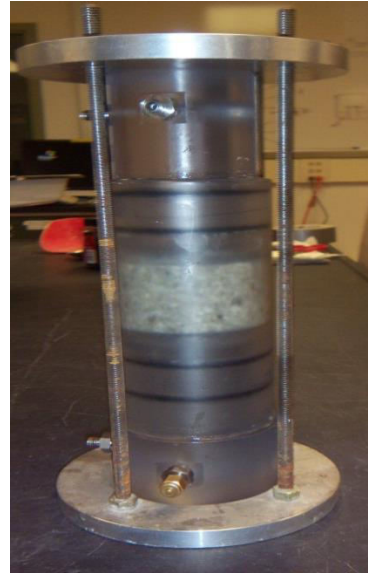


Figure 3.13 Rigid wall permeameter with a bentonite slurry sample

As shown in Figure 3.12, the flow pump consisted of two syringes that were used as a fluid reservoir. The syringe pump motor moved the pusher block forward which depressed the syringe plunger causing fluid to be dispensed. A motor within the pump moved the plunger of the syringe in, pushing the fluid out (in an infuse direction). Reversing the direction of the motor involved moving the plunger back allowing the syringe to be filled (in a withdraw direction) as shown in Figure 3.14.

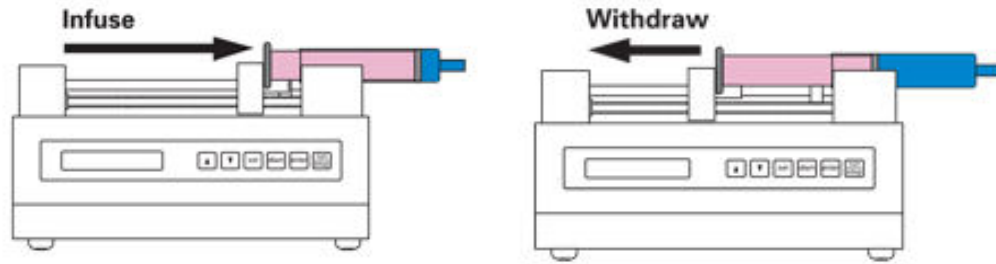


Figure 3.14 Infuse and withdraw directions of the syringes in the Harvard Apparatus flow pump [Source: www.harvardapparatus.com]

The flow rate of the pump was selected based on the observations from the triaxial tests; that is for an applied 14 kPa (2 psi) pressure, the water level in the burettes dropped by 1.4 mL/day which converts to 0.058 mL/hr. When the pump was running at the selected value of 0.058 mL/hr, there was not enough build-up pressure in the system to enable the pressure transducer to take differential pressure readings instead the pressure remained at a reading of zero. Therefore, the flow rate was increased to 0.1 mL/hr in order to allow the system to have sufficient build-up pressure that could be detected by the pressure transducer. By measuring the pressure differential across the specimen, the pressure gradient was also known and the coefficient of permeability was calculated using Darcy's law in the following form: $q = kiA$, where k is the hydraulic conductivity, i is the hydraulic gradient, and A is the area of the sample.

Prior to conducting the hydraulic conductivity tests, the sample was loaded with an applied vertical load of 367 N (82.5 lbs) using the Load Frame-Sigma1 program as shown in Figure 3.15. The applied load was determined by assuming the sample was extracted at a depth of 6 m (20 ft) and its surrounding soil had a unit weight of 15.7

kN/m^3 (100 pcf). Therefore, the vertical stress was calculated as: $6 \text{ m} \times 15.7 \text{ kN/m}^3 = 94.2 \text{ kN/m}^2$ (20 ft \times 100 pcf = 2000 psf). The force thereafter was calculated using the following relationship: $F = \sigma A$ where F is the applied force, σ is the vertical stress, and A is the area of the sample. The application of the force on the sample was done to consolidate the slurry and drain as much water as possible. The sample was loaded until there was no noticeable change in the height of the sample.



Figure 3.15 Load Frame-Sigma1 apparatus that was used to consolidate the bentonite slurry

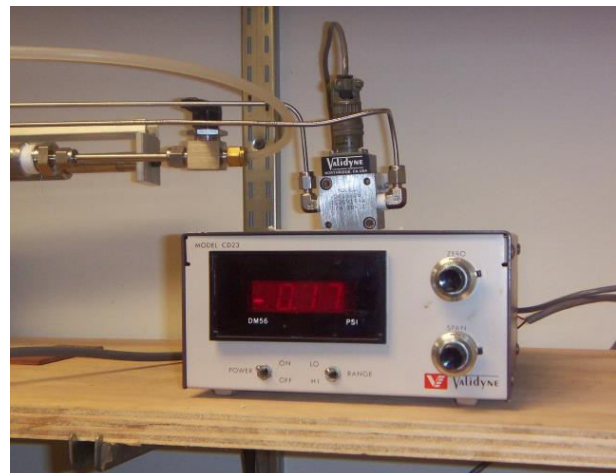


Figure 3.16 Pressure transducer used to measure the differential pressure across the rigid wall permeameter

Once the loading of the sample was completed, the sample was placed in the permeability water bath and subjected to cyclic heating and cooling during both the hydraulic and thermal conductivity tests. Within the water bath, the fixed wall permeameter was laid horizontally instead of vertical because the upward and downward flow was not the same within the specimen. The upward flow produced a negative differential pressure and the

downward flow produced a positive pressure. Laying the apparatus horizontally eliminated the varying differential pressures because the head was equal across the entire sample. A pressure transducer as shown in Figure 3.16 was used to measure the differential pressure during the hydraulic conductivity testing.

CHAPTER 4: Data Analysis and Results

This chapter presents the results from the thermal and hydraulic conductivity laboratory tests. The laboratory testing, data collection and processing was undertaken to determine the long term behavior of the grout as a result of cyclic heating and cooling, the principal objective of this research. The findings presented in this chapter demonstrate the behavior of bentonite based grout in a geothermal borehole and how the changes in temperature influence the properties of the grout, principally the thermal and hydraulic conductivity.

4.1 Thermal Conductivity Results

The thermal conductivity setup as explained in the materials and methods section was first designed, evaluated, and tested during the summer 2010. During the summer of 2010, only four heating and cooling cycles were conducted and the results were analyzed using Microsoft excel spreadsheet. Given the encouraging results from these early experiments, a Matlab® code was developed and used to validate the thermal conductivity data that was collected in summer 2010. The validation of the thermal conductivity results from the Matlab® code was done by recalculating the 2010 thermal conductivity values and comparing the values to those that were calculated in 2010 using an excel spreadsheet as well as with selected manual calculations. The raw data for these tests, which are the temperature values taken by the data acquisition system, have been attached in Appendix A. Also attached in Appendix A are sample calculations for a heating and cooling cycle, which illustrate how the Matlab® code calculates the average

thermal conductivity of the geothermal model. After verifying that the values were identical, a second trial for both heating and cooling tests was conducted on a newly prepared grout mixture and analyzing the data with the newly developed Matlab® code. The goal for the second trial was to study the reproducibility of the data from the summer of 2010. Figure 4.1 presents the thermal conductivity results that were obtained in the summers of 2010 and 2011.

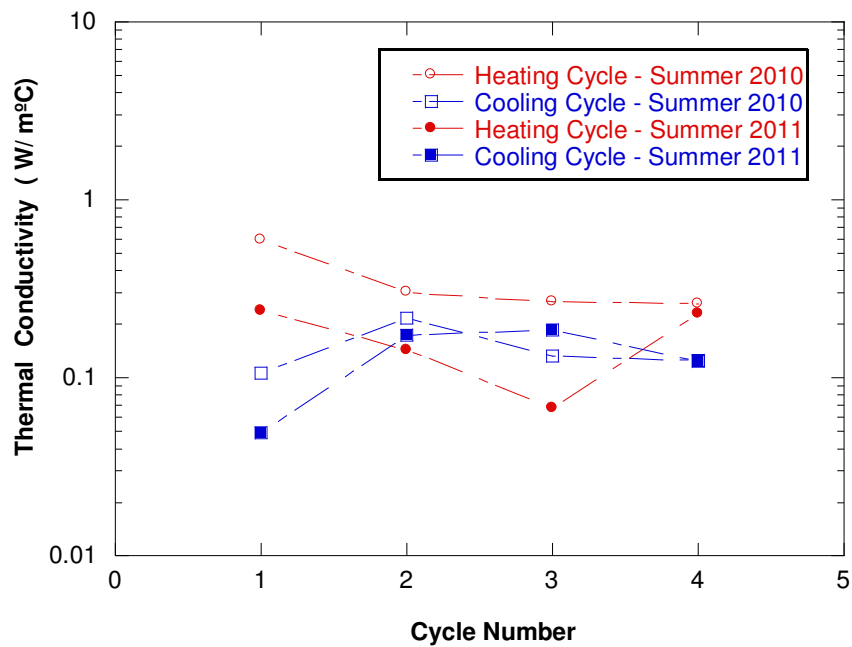


Figure 4.1 Plot of the thermal conductivity versus time after cycle commencement for four alternating heating and cooling cycles

As shown in Figure 4.1, there appeared to be some variability between the two heating cycles whereas the results from the cooling cycle are in close proximity. The variation was possibly due to the uniqueness of each grout mixture even though the procedure for preparing the slurry was exactly the same. The average thermal conductivity for the

heating cycles in 2010 and 2011 was 0.62 W/m-K (0.36 btu/hr.ft.°F) and 0.29 W/m-K (0.17 btu/hr.ft.°F), respectively. For the cooling cycles, the average thermal conductivity observed in 2010 and 2011 was 0.24 W/m-K (0.14 btu/hr.ft.°F) and 0.22 W/m-K (0.13 Btu/hr.ft.°F), respectively. The data show that the thermal conductivity is generally lower for the cooling cycle than for the heating cycle. The results shown in Figure 4.1 were preliminary results and were used as a baseline for the thermal conductivity tests that were conducted thereafter. A new grout mixture was prepared using the same methodology as in the previous two trials and the results for the third trial were plotted as shown in Figure 4.2. The raw data for these tests, which are the temperature values taken by the data acquisition system, have been attached in Appendix A.

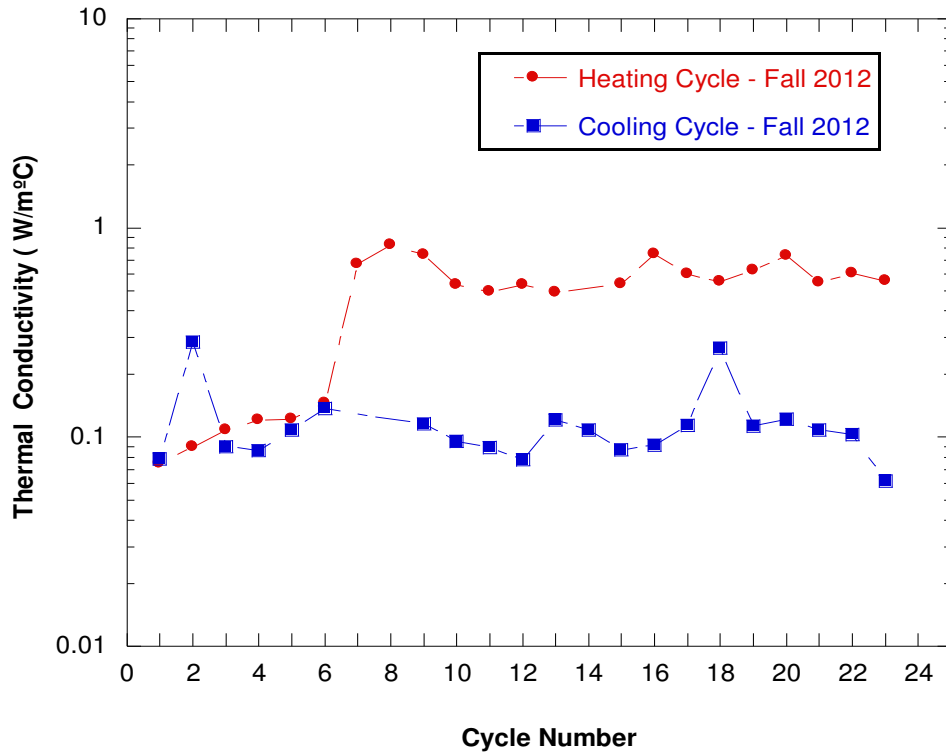


Figure 4.2 Plot of the thermal conductivity versus time after cycle commencement for 23 alternating heating and cooling cycles conducted in 2012

As shown in Figure 4.2, there appeared to be similar difference between the heating and the cooling cycles that was observed in Figure 4.1. The average thermal conductivity for a heating cycle was 0.79 W/m-K (0.46 btu/hr.ft.°F) whereas the average thermal conductivity for a cooling cycle was 0.19 W/m-K (0.11 btu/hr.ft.°F). The obtained thermal conductivity values were consistent but slightly different than the thermal conductivity of 0.74 W/m-K (0.43 btu/hr.ft.°F) published by the manufacturer. In order to validate and assure reproducibility of the results shown in Figure 4.2, a new grout

mixture was prepared and thermal conductivity data was collected following the same procedure. The results from the fourth and final trial have been plotted in Figure 4.3

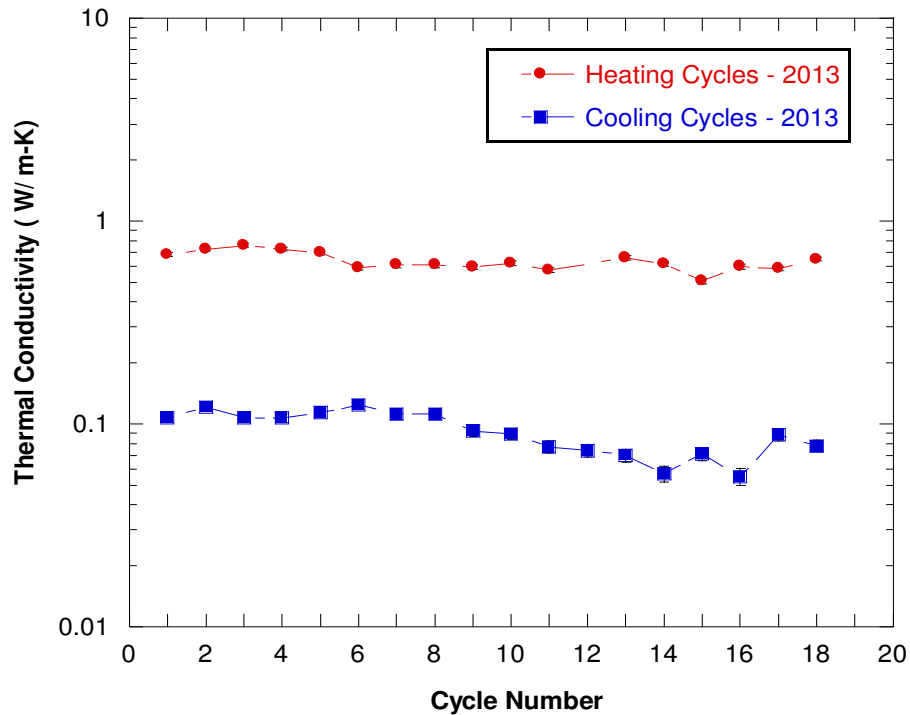


Figure 4.3 Thermal conductivity with respect to cycle number for 18 alternating heating and cooling cycles for the tests conducted in 2013

Figure 4.3 illustrates that after 18 heating and cooling cycles, the average thermal conductivity for a heating cycle was 0.64 W/m-K (0.37 btu/hr.ft.°F) whereas the average thermal conductivity for a cooling cycle was 0.092 W/m-K (0.053 btu/hr.ft.°F). Since the data shown in Figure 4.3 span on several log scales, a log average of the thermal conductivity was taken in order to ensure that the log and arithmetic average yield similar results. The log average value for a heating and cooling cycle was 0.63 W/m-K and

0.089, respectively. While thermal conductivity is a property of the soil and may or may not be expected to remain a constant value between the heating and cooling cycles, Figure 4.3 suggests two hypotheses: 1.) the thermal conductivity is highly influenced by the change in temperature (from a heating to a cooling cycle), and 2.) the cyclic heating and cooling introduces an air gap during the cooling cycles. With respect to the first hypothesis, experimental investigations on thermal conductivity of soils under varying saturation and temperature have also been performed by other researchers (Sepaskhah and Boersma, 1979; Bristow *et al.*, 1998; Campbell *et al.*, 1994; Nassar and Horton, 1997; Hiraiwa and Kasubuchi, 2000; Tarnawski and Gori, 2002). Sepaskhah and Boersma (1979) determined the thermal conductivity of soil samples as a function of water content and temperature by testing samples with 12 different water contents. Their results showed that the thermal conductivity was independent of water content at very low water contents. For the research performed by Sepaskhah and Boersma (1979), the volumetric water content values were 0.03 and 0.05 cm³/cm³ at 45° C and 0.13 and 0.18 cm³/cm³ at 25° C for loam and silty clay, respectively. Campbell *et al.* (1994) also studied thermal properties of soil samples differing in texture, bulk density, water content, and temperature over a temperature range from ambient to 600°C. The results of the study showed that thermal conductivity increases dramatically with temperature in moist soil, reaching values 3 to 5 times the ambient value at 90°C. Thermal conductivity changes with temperature because heat conduction in non-metallic solids is mainly due to lattice vibrations (phonons). As atoms vibrate more energetically at one part of a solid due to high temperatures, heat is transferred to less energetic neighboring atoms. Due to

the material temperature increase, the internal particle velocity increases as well thereby increasing the thermal conductivity. The increased velocity transfers heat with less resistance (Ziman, 1967).

With respect to the second hypothesis, the obtained average thermal conductivity for a cooling cycle (0.092 W/m-K) was considered too low for a bentonite grout that was mainly prepared with water (5:1 ratio of water to bentonite). The decrease from the average thermal conductivity of a heating cycle, which was 0.64 W/m-K to 0.092 W/m-K suggested a 7:1 ratio change in thermal conductivity, which is a rather drastic change. Water has an expected thermal conductivity of approximately 0.6 W/m-K whereas air has an expected thermal conductivity of approximately 0.027 W/m-K (Mills, 1992). The average thermal conductivity of 0.092 W/m-K is slightly higher than the thermal conductivity of air. As mentioned in Chapter 2, Philippacopoulos and Berndt (2001) studied the influence of debonding in a geothermal heat exchanger. The findings of the study revealed that gaps developed at the grout/formation interface are generally caused by: a.) a temperature drop along the interface; b.) reduction of heat flux especially near the borehole; c.) increase of the total resistance of the system; and d.) decrease of the overall heat transfer rate. The authors performed a two-dimensional finite element analysis of the influence of spatial variation of gaps led to the following conclusions: a.) a 90° debonding at the grout/formation interface caused 20% reduction in the overall heat transfer coefficient; b.) a 180° debonding produced 33% reduction in the overall heat transfer coefficient; c.) a 360° debonding at the grout/formation interface produced 60%

reduction of the overall heat transfer coefficient; and d.) a 360° debonding (all around gap at grout/pipe interface) produced 66% reduction of the overall heat transfer coefficient. The final conclusion made was that debonding at the grout/pipe interface was found to be of greater significance than debonding between grout/formation. Figure 4.4 is a picture of the bentonite grout that was taken immediately after the thermal conductivity tests were terminated. As can be seen in Figure 4.4, there were three distinct cracks and some form of irregular debonding at the grout/pipe interface.



Figure 4.4 Picture of the geothermal well model with cracked bentonite grout after the thermal conductivity test were terminated.

If indeed an air gap was introduced during the cooling cycles, the data shown in Figure 4.3 also suggests that the cracking that occurred was a repeatable pattern that occurred throughout the cyclic heating and cooling tests. Since the thermal conductivity tests were

performed while the geothermal well model was vacuumed sealed, it was hard to observe when the crack was formed. An analysis during the transient phase of the thermal conductivity testing needs to be performed to further verify the occurrence of an air gap and the point of its formation.

The reliability of the thermal conductivity results for both the heating and cooling cycles was assessed by conducting a 95% confidence interval. The confidence interval included determining the standard deviation, which is the measure of the variance in the thermal conductivity data, and the upper and lower bound of the data was also calculated. Figure 4.5 is a plot of the average thermal conductivity for a heating and cooling cycle showing the confidence interval error bars with respect to the 95% confidence interval.

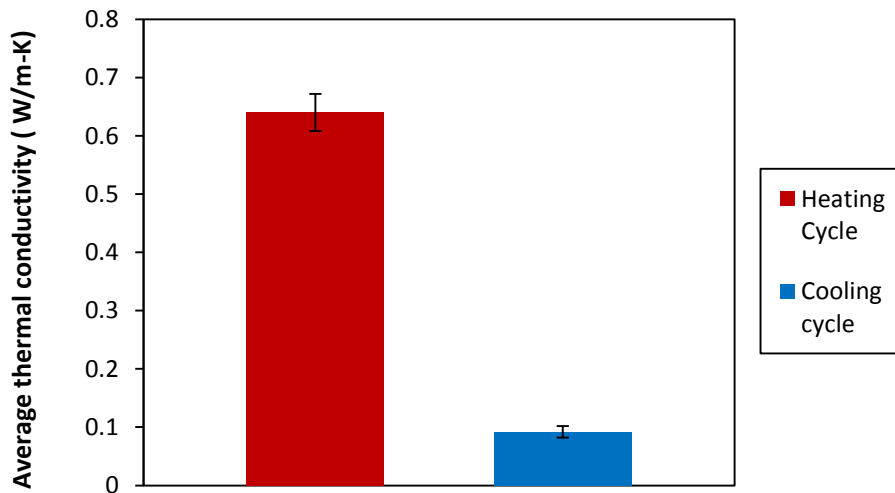


Figure 4.5 Confidence interval plot for the thermal conductivity results

For a heating cycle, the standard deviation was determined to be 0.066 and the data had an upper bound value of 0.667 W/m-K and a lower bound value of 0.604 W/m-K. This means that 95% of the time, the thermal conductivity of a heating cycle will fall between 0.667 W/m-K and 0.604 W/m-K. When considering a cooling cycle, the standard deviation was determined to be 0.021 and an upper and lower bound of 0.102 W/m-k and 0.082 W/m-K, respectively. For both heating and cooling, the standard deviation was low, which was an indication that the thermal conductivity values tend to lie closer to the mean and there was no large variance in the data. However the thermal conductivity values for heating cycles had more variability than the thermal conductivity values for the cooling cycles. Also as can be seen in Figure 4.5, the two different error bars for the average thermal conductivity for a heating and cooling cycle do not overlap, which indicates that the difference between the two mean values was statistically significant.

4.2 Hydraulic Conductivity Results

All the results of the hydraulic conductivity tests appear in this section and the results from the modified permeability tests were merely used as a baseline to compare the hydraulic conductivity values obtained from the flow pump permeability tests. Only the results from the flow pump permeability tests were used to analyze the integrity of the bentonite grout due to cyclic heating and cooling

4.2.1 Consolidometer Permeability Tests

Fixed-wall falling head hydraulic conductivity tests in a consolidometer were conducted as a check of the suitability of the bentonite for long term cyclic thermal and hydraulic conductivity tests. The hydraulic conductivity data for three bentonite samples was collected until the mean hydraulic conductivity of the last four values was within $\pm 25\%$ and there was no observed apparent trend in the data, consistent with ASTM 5084 termination criteria. The hydraulic conductivity termination criterion was reached after five days thereafter the collected data was plotted as shown in Figure 4.6. The raw data collected for the test has been attached in the Appendix B. As shown in Figure 4.6, the hydraulic conductivity for all three bentonite samples was between 10^{-7} and 10^{-8} cm/s. The average hydraulic conductivity for samples one, two, and three was 2.6×10^{-8} cm/s, 1.5×10^{-8} cm/s, and 2.9×10^{-8} cm/s, respectively. According to grouting standards and regulations, a target hydraulic conductivity of 10^{-7} cm/s or less may be used as a sealant (Skouby, 2010). Therefore, the results obtained from all three samples validated that the bentonite grout was well suited to perform as a sealant.

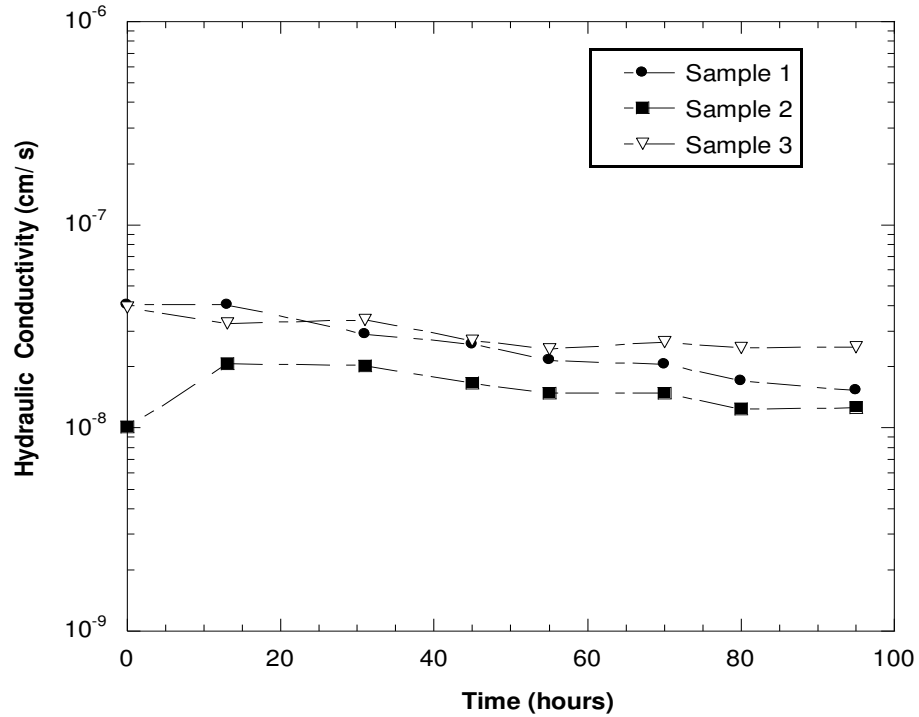


Figure 4.6 Results of the consolidometer permeability tests showing hydraulic conductivity vs. time for three replicate bentonite samples

Also, there was an observed correlation between hydraulic conductivity and the amount of swelling of the bentonite in the consolidometer. The observation made was that the hydraulic conductivity decreased when the bentonite was in its swelling state. This observation was true for all three samples. The observed trend was expected because as bentonite swells, the void ratio of the clay increases. In addition to Figure 4.6, a graph of change in dial reading versus time was plotted as shown in Figure 4.7

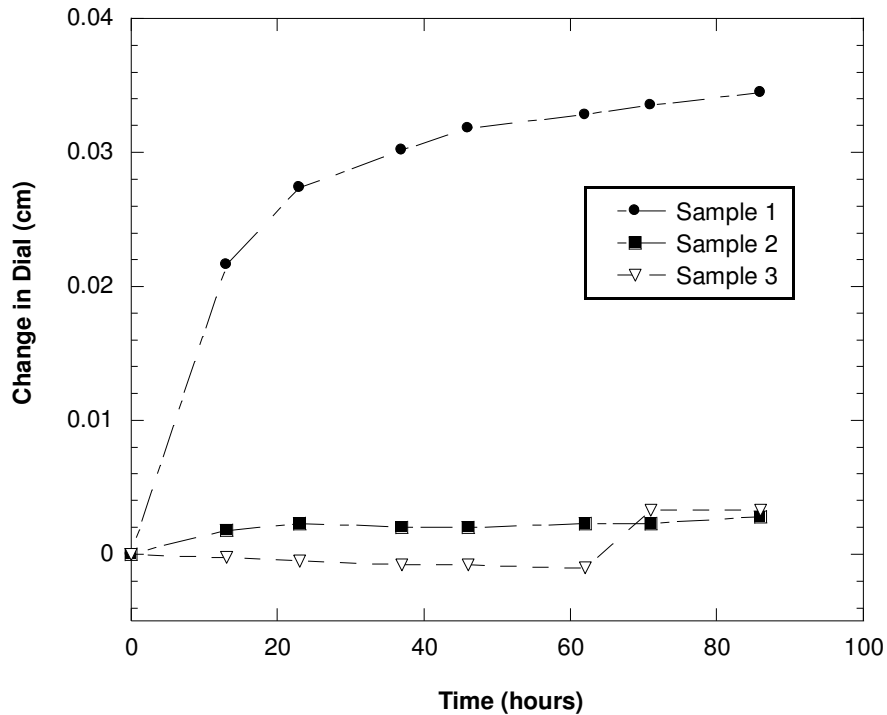


Figure 4.7 Results of consolidation permeability tests showing change in dial reading versus time for three bentonite samples

Figure 4.7 illustrates that the swelling of the bentonite leveled off with time with the exception of sample one. Initially the trend appeared to be curved as the sample was still undergoing consolidation. The completion of consolidation was noted when the dial reading did not provide an increased or decreased deformation. Sample one had a deformation of up to 0.0345 cm (0.0136 in) and the largest deformation of the three samples. Samples two and three had deformation values that were in close proximity, with sample two having a deformation value of up to 0.00279 cm (0.0011 in) and a deformation value of up to 1.3×10^{-5} cm (0.0013 in) for sample three. The main limitation of using the consolidation permeability method was that the samples were not subjected to cyclic heating and cooling conditions in a similar manner with the thermal

conductivity sample but these results confirmed the suitability of the bentonite for the more sophisticated cyclic heating and cooling flow pump permeability tests

4.2.2 Triaxial Permeability Tests

Prior to conducting the triaxial test in the cyclic heating and cooling method, a triaxial test at room temperature was conducted in order to compare with the hydraulic conductivity results that were obtained using the consolidometer permeability device. The results for the triaxial test conducted at room temperature are plotted in Figure 4.8 and the raw data for this test has been included in the Appendix B. As shown in Figure 4.8, the test was terminated when the mean hydraulic conductivity of the last four values was within $\pm 25\%$ of each reading. The average hydraulic conductivity of the sample was determined to be 1.1×10^{-7} cm/s. The hydraulic conductivity of this sample was a magnitude higher than the hydraulic conductivity obtained from the consolidometer permeability tests. This is because the consolidometer permeability tests were performed with an effective stress of 28 kPa (4 psi) whereas the triaxial tests were conducted using an effective pressure of 41 kPa (6 psi). Moreover, the hydraulic conductivity value met the criterion to perform as a sealant.

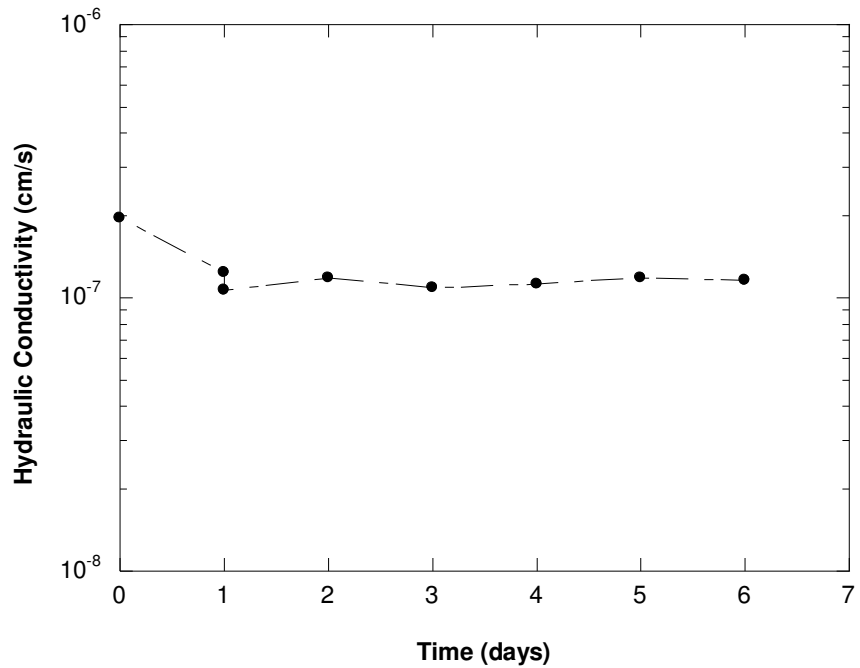


Figure 4.8 Triaxial permeability results for a test conducted at room temperature

Thereafter, the very same sample was then subjected to heating and cooling cycles and the results from the cyclic heating and cooling tests are illustrated in Figure 4.9. The raw data for the cyclic heating and cooling test has also been included in the Appendix B.

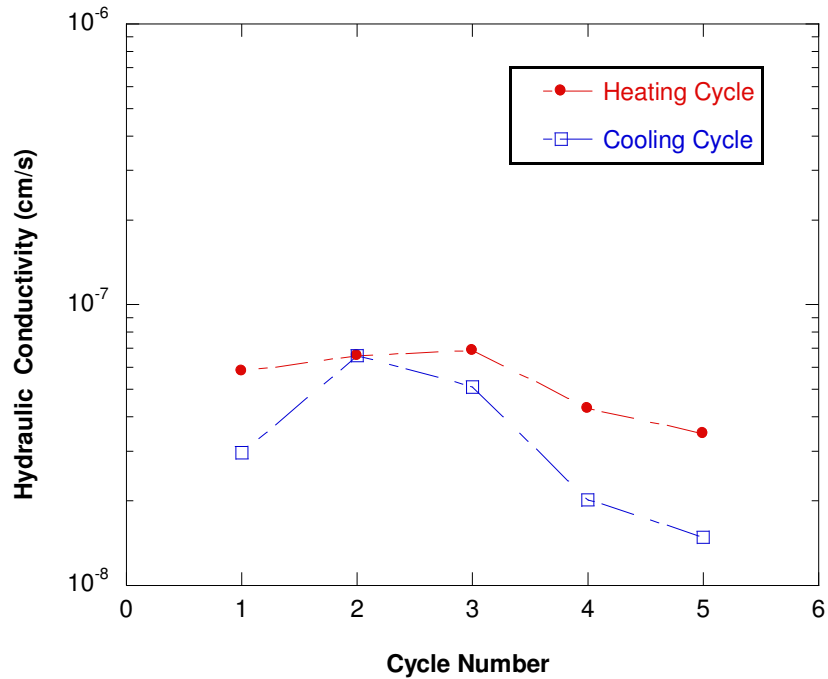


Figure 4.9 Triaxial permeability results for a sample subjected to cyclic heating and cooling

While the results shown in Figure 4.9 should be viewed with some skepticism, the average hydraulic conductivity for a heating and cooling cycle was 5.3×10^{-8} and 3.6×10^{-8} cm/s, respectively. The results shown in Figure 4.9 were conducted as alternating heating and cooling cycles, starting with a heating cycle. From the third to the fifth cooling cycles, there was a decreasing trend in the hydraulic conductivity values after the sample was heated. When the sixth hydraulic conductivity heating cycle was conducted, it was observed that there were discrepancies in the data that pertained to the flow (Q) of the fluid. The discrepancies were that the cell volume did not remain constant but rather decreased and Q_{in}/Q_{out} (the volumetric flux ratio, VFR was not equal to one). For steady flow, the flow in should equal the flow out and $VFR = 1.0$. Observations were that

$VFR_{in,heating} > VFR_{in,cooling}$ and $VFR_{out,heating} \gggg VFR_{out,cooling}$ meaning there was some significant volume changes when switching from a heating to a cooling cycle and then back to a heating cycle again. The volume changes due to expansion and contraction of the pore water that occurred during the test were calculated as follows:

The temperatures considered were 5°C (for a cooling cycle) and 49°C (for a heating cycle). The mass of water, M_w was 5 kg based on the proportion used for the slurry.

At 5 degrees Celsius

$$\rho_w = \frac{M_w}{V_w}$$

$$V_w = \frac{M_w}{\rho_w} = \frac{5 \text{ kg}}{1000 \text{ kg/m}^3}$$

$$V_w = 0.005 \text{ m}^3$$

At 49 degrees Celsius

$$\rho_w = \frac{M_w}{V_w}$$

$$V_w = \frac{M_w}{\rho_w} = \frac{5 \text{ kg}}{988 \text{ kg/m}^3}$$

$$V_w = 0.00506 \text{ m}^3$$

Therefore, $\Delta V_{w(5-49 \text{ } ^\circ\text{C})} = 60.7 \text{ cm}^3$

The very same volume changes that were observed in this test were also observed by Hueckel and Pellegrini (1992). From Hueckel and Pellegrini (1992), the cyclic heating and cooling (temperature range from 22.5 to 60 °C) of boom and pasquasia clay at a constant stress had an effective stress that was not constant. A water pressure was generated because of the higher thermal expansion of water than that of the solid. The conclusion made by Hueckel and Pellegrini (1992) was that the heating of clay induces an increase in pore water pressure. Subsequent cooling of the clay produces a drop in water pressure hence the observed volume changes. In addition to volume changes in the

pore water, the cell water in the triaxial cell was also experiencing volume change. The experimental design resulted in measured flow volumes that were not exclusively due to the applied hydraulic gradient and thus computed values of hydraulic conductivity assuming all flow due to the applied gradient are subject to question. Due to the discrepancies in the data, the test was terminated and an alternative approach was undertaken.

4.2.3 Rigid Wall/Flow Pump Permeability Tests

The results of the flow pump permeability presented in this section were the only hydraulic conductivity results that were used to evaluate the influence of cyclic heating and cooling upon the hydraulic conductivity of the bentonite grout seal. The Raw data and sample calculations have attached in Appendix B. A total of 17 heating and cooling cycles were imposed upon the sample tested in a rigid wall apparatus using a flow pump and the results were plotted as shown in Figures 4.10 and 4.11. Figure 4.10 is a plot of hydraulic conductivity with respect to the number of conducted cycles. The average hydraulic conductivity (all values for each cycle) for a heating and cooling cycle was 2.6×10^{-6} cm/s and 1.29×10^{-6} cm/s, respectively. As shown in Figure 4.10, an increase in temperature caused the hydraulic conductivity to increase as well. The observed fluctuating trend illustrate that during cycles seven to ten, the bentonite grout had a hydraulic conductivity that was greater than 10^{-7} cm/s when considering only a heating cycle. For a cooling cycle, cycles seven and eight had a hydraulic conductivity that was

greater than 10^{-7} cm/s. This means that during the aforementioned heating and cooling cycles, the grout was not performing efficiently as a sealant.

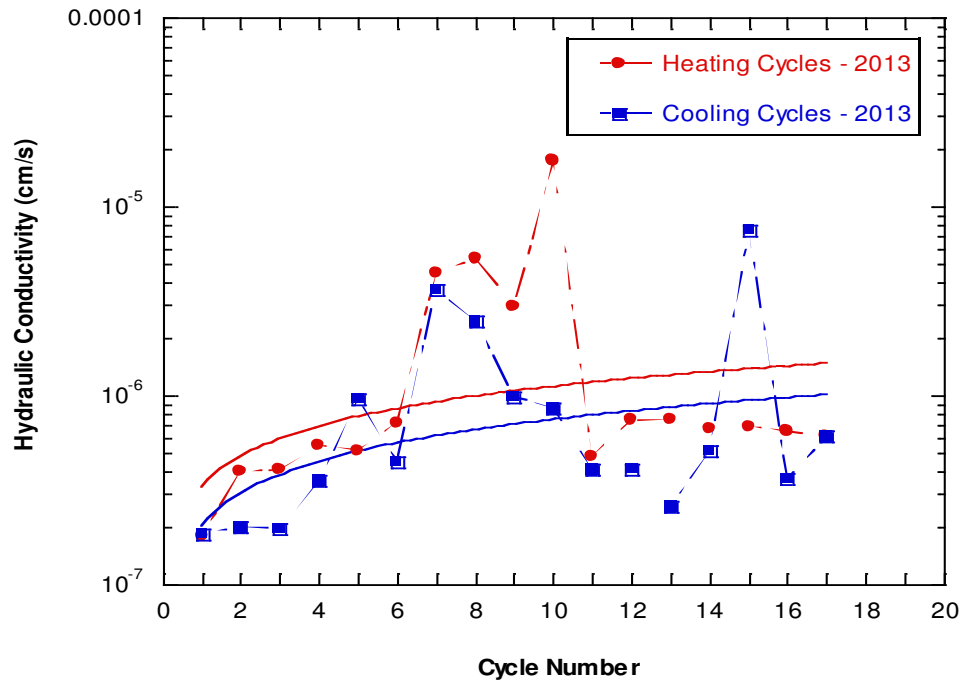


Figure 4.10 Hydraulic conductivity results obtained from the flow pump permeability tests for alternating heating and cooling cycles

The hydraulic conductivity for both heating and cooling cycles decreased to approximately 10^{-7} cm/s during cycle eleven and remained constant. However during the cycles that had a hydraulic conductivity greater than 10^{-7} cm/s, an opportunity for potential contamination would have been created when considering a geothermal borehole in the field because the grout was not performing efficiently as a sealant. As shown in Figure 4.10, a regression analysis was performed by finding a “best fit” curve for a heating and cooling cycle (illustrated by the solid red and blue curves). The selected curve was a power function and was selected because it illustrated a similar increasing

trend when compared to the data. However the power function yielded a coefficient of determination (R^2) that was low (approximately 0.3), which means that it was difficult to determine a specific hydraulic conductivity value with respect to cycle number. The curve lines were used to illustrate that the increase in the hydraulic conductivity for heating cycles was larger in comparison to the cooling cycles. As explained in Chapter 2, the diffuse double layer theory indicates that temperature should have a negligible effect on the electrokinetic potential of the colloid system due to counteracting changes as temperature is changed. However during the cyclic heating and cooling hydraulic conductivity tests, the temperature of the permeant liquid was altered thereby causing the viscosity and density of the liquid to also change. Therefore, since temperature affected the viscosity of the permeant liquid when switching from a cooling to a heating cycle, the hydraulic conductivity was sensitive to the temperature. According to Reeves *et. al* (2006), the effect of temperature on the liquid limit also applies to other parameters such as the decrease in strength with increasing temperature resulting in a reduction in optimum moisture content for maximum dry density. Conversely, there will be increase in permeability and the coefficient of consolidation with increasing temperature.

Since the hydraulic conductivity is a function of both the material and the fluid, and the viscosity and density of the water changes with temperature, the intrinsic permeability as plotted in Figure 4.11 was also assessed to try to distinguish material changes from fluid changes. Intrinsic permeability is independent of the fluid viscosity and density because it is the soil's hydraulic conductivity after the effect of fluid and viscosity has been

removed. As can be seen in Figure 4.11, the intrinsic permeability data had a similar trend as the hydraulic conductivity data that was shown in Figure 4.10. The average intrinsic permeability for a heating and cooling cycle was $1.25 \times 10^{-11} \text{ cm}^2$ and $1.84 \times 10^{-11} \text{ cm}^2$, respectively. Similarly to the hydraulic conductivity data, a power function was selected as the curve fit for both heating and cooling cycles. The power functions helped to illustrate that the cooling cycles had a larger increase in intrinsic permeability in comparison to the heating cycles whereas the opposite was true for the hydraulic conductivity data.

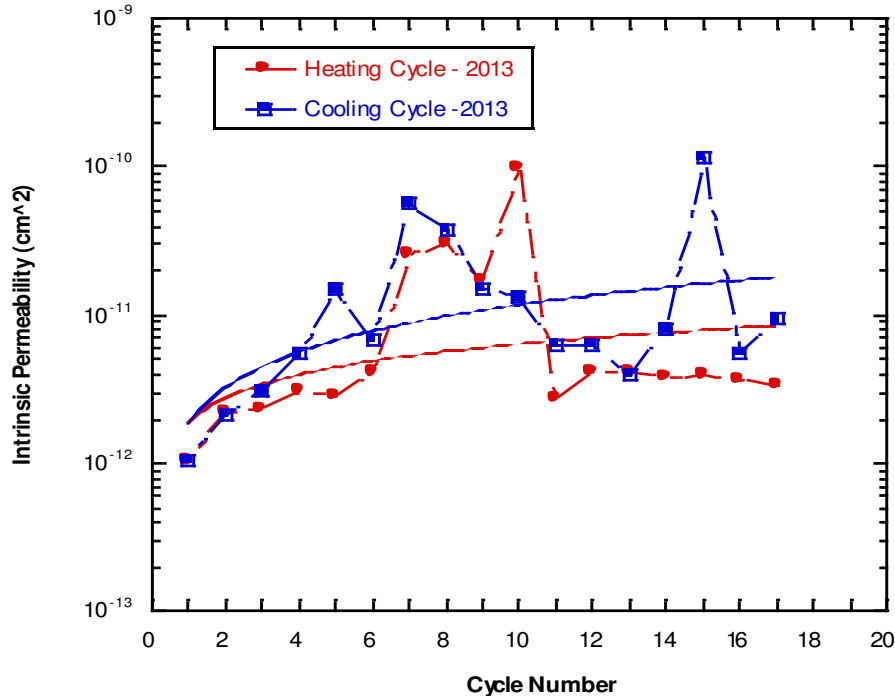


Figure 4.11 Intrinsic permeability results obtained from the flow permeability tests for alternating heating and cooling cycles

Cho *et al.* (1999) conducted an experimental investigation on the effect of temperature on hydraulic conductivity for compacted samples with various dry densities. The

observation made by Cho *et al.* (1999) was that the hydraulic conductivity of compacted bentonite increased with increasing temperature, and the hydraulic conductivities at the temperature of 80 °C increased up to about three times those at 20 °C. The researchers also noticed that the intrinsic permeability of the compacted bentonite samples remained constant, which was not the case for this research project.

The environmental concern about geothermal systems is the ability of the grout used to act as an effective borehole sealant. Therefore, the experimental hydraulic conductivity values were assessed to determine whether the possibility of debonding on the grout/pipe interface had been compromised. As shown in Figures 4.9, the cycles that had a hydraulic conductivity greater than 10^{-7} cm/s suggest that if indeed the formation of an air gap occurred during cyclic heating and cooling, the grout did not perform as an effective borehole sealant. The hypothesis suggested by the data was that the formation of an air gap on the grout/pipe interface increased the hydraulic conductivity of the bentonite grout from $\sim 10^{-7}$ cm/s to $\sim 10^{-6}$ cm/s. Studies of the interfacial microstructure between neat cement grouts and U-loop pipes have revealed gaps up to 0.32 mm wide (Allan, 1998; Allan and Philippacopoulos, 1999). When the same studies were conducted for bentonite grouts, these grouts cracked due to being susceptible to high shrinkage under drying conditions. Allan and Philippacopoulos (1999) examined how the permeability of a grout was affected as a result of debonding. The authors tested an enhanced grout, Mix 111, which was a mixture of cement, water, silica sand, and small amounts of superplasticizer and bentonite. The thermal conductivity of Mix 111 was 2.42 W/m-K. As the fluid

temperature was varied from 3 to 35°C, the authors found that the hydraulic conductivity of Mix 111 remained in the order of 10^{-7} cm/s and did not change.

Similarly to the results of the thermal conductivity, the reliability of the hydraulic conductivity and intrinsic permeability were assessed by conducting a 95 % confidence interval. Figure 4.12 and 4.13 are plots for the standard error for the average hydraulic conductivity and the average intrinsic permeability, respectively.

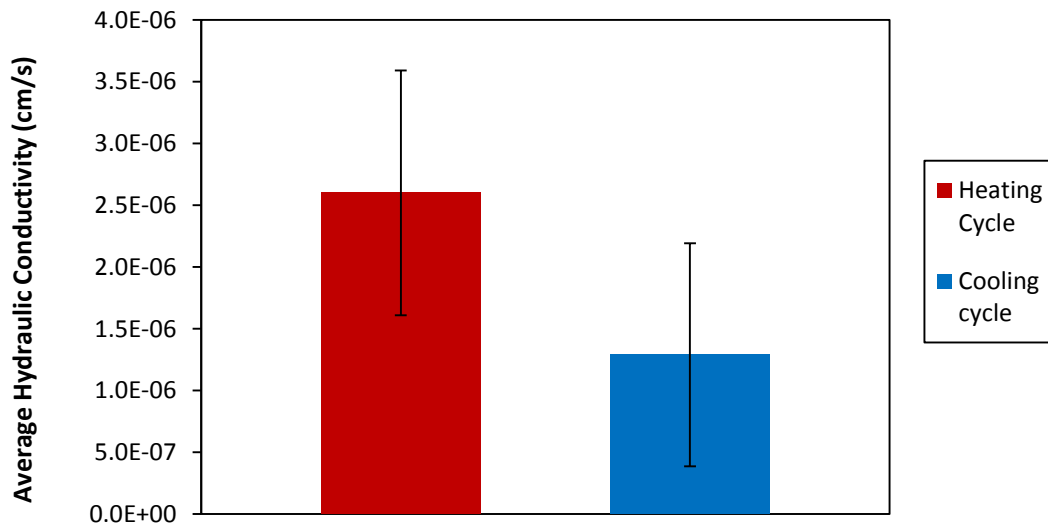


Figure 4.12 Confidence interval plot for the hydraulic conductivity results

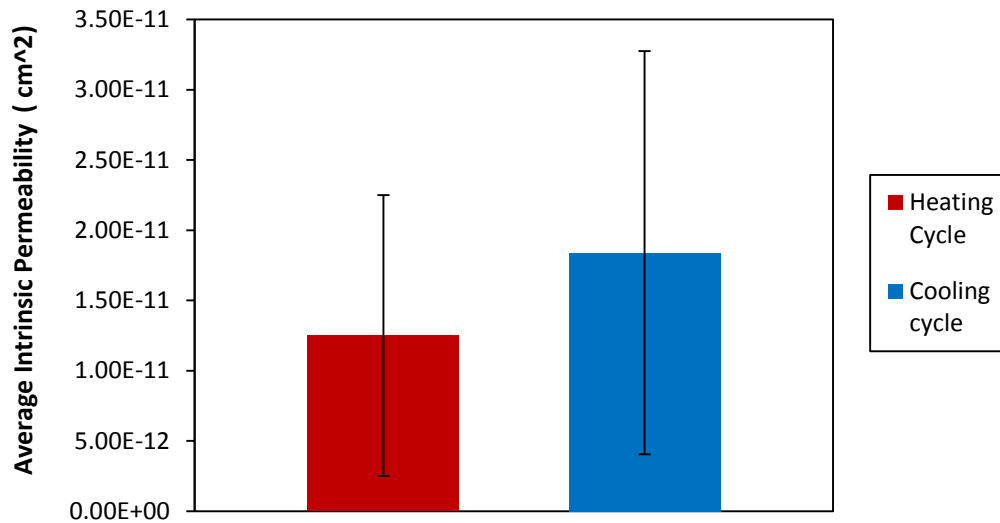


Figure 4.13 Confidence interval plot for the intrinsic permeability results

For the hydraulic conductivity results, the standard deviations for a heating and cooling cycle were determined to be 1.6×10^{-6} and 3.6×10^{-6} , respectively. As shown in Figure 4.12, 95 % of the time the hydraulic conductivity of the bentonite grout would be measured between 4.2×10^{-6} cm/s and 2.1×10^{-7} for a heating cycle whereas it would be measured between 2.1×10^{-6} and 3.1×10^{-7} cm/s for a cooling cycle. For the intrinsic permeability results, the heating cycle had a standard deviation of 2.4×10^{-11} and 2.9×10^{-11} for the cooling cycle. The upper and lower bounds for the average intrinsic permeability of a heating cycle were 2.3×10^{-11} cm² and 1.2×10^{-12} cm². The cooling cycle had an upper and lower bound of 3.2×10^{-11} cm² and 4.6×10^{-12} , respectively. As shown in Figures 4.12 and 4.13, there was a larger variability in the hydraulic conductivity and intrinsic permeability for the heating cycles in comparison to the

cooling cycles. Additionally, both figures illustrate error bars that overlap, which suggests that the difference between the mean of the heating and cooling cycles was not statistically significant.

4.3 Moisture Content Test

At the end of 18 heating and cooling cycles conducted in 2013, the hydraulic and thermal conductivity tests were terminated and a moisture content test was completed using the oven drying method. A total of 18 bentonite grout samples were collected from the geothermal well model in the configuration shown in Figure 4.14.

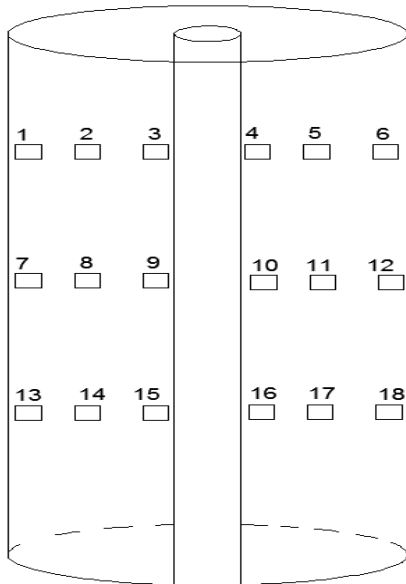


Figure 4.14 Schematic showing where the bentonite samples were taken from the geothermal model

Figure 4.15 Picture of bentonite samples placed in moisture tins before being placed in the oven

location of the thermocouples, where there was an equal vertical spacing of 76 mm (3 in).

Each of the 18 samples was placed in moisture tins as shown in Figure 4.15 and weighed prior being placed in the oven. The samples were then heated at 105 °C and kept in the oven for 24 hours. Thereafter the sample were weighed again after being heated and the final moisture content was calculated using the phase diagram relationships in the following method: moisture content (w) = mass of water (M_w) / mass of solids (M_s). The results of the moisture content test are shown in Table 4.2 and the raw data has been attached in the Appendix B.

Table 4.1 Final moisture content results of 17 bentonite sample after being subjected to heating and cooling cycles

Sample Number	Mass of Solids (g)	Mass of Water (g)	Moisture Content, w (%)
1	2.04	10.7	524.51
2	1.51	7.77	514.57
3	2.66	12.35	464.29
4	1.75	6.38	364.57
5	1.68	8.56	509.52
6	2.06	11.08	537.86
7	2.44	13.38	548.36
8	1.57	8.41	535.67
9	1.07	5.6	523.36
10	1.48	7.9	533.78
11	1.54	8.47	550
12	1.66	8.67	522.29
13	2.69	14.22	528.62
14	2.02	10.6	524.75
15	1.69	9	532.54
16	2.61	13.83	529.89
17	2.11	11.07	524.64
Average Final Moisture Content			516

As can be seen in Table 4.1, 18 moisture content values were calculated and then averaged for a final moisture content of 516%. All the samples had a moisture content of approximately 500% with the exception of samples three and four. When the samples

were collected, samples three and four had a rougher texture than the rest of the grout. These samples had dried out possibly due to the crack that was formed as shown in Figure 4.4. Although the geothermal well model was vacuumed sealed when the thermal conductivity tests were conducted, it appears that there was still a change in moisture content that occurred at the top layer of the grout. According to Roth et al. (2004), heat and moisture in soils due to induced thermal gradients bear a considerable importance in the design of geothermal heat exchangers. As a result, the variance of moisture content with depth within the geothermal model as well the variance with distance from the center of the geothermal model was analyzed by plotting the moisture content values shown in Table 4.1. Figures 4.16 and 4.17 illustrate this variance with moisture content.

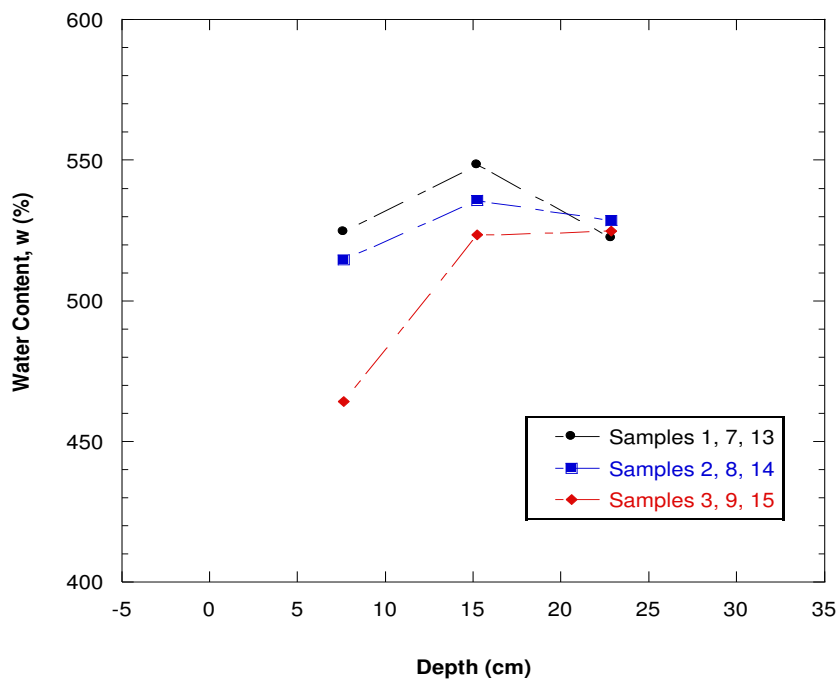


Figure 4.16 Plot of moisture content with respect to the depth within the geothermal model

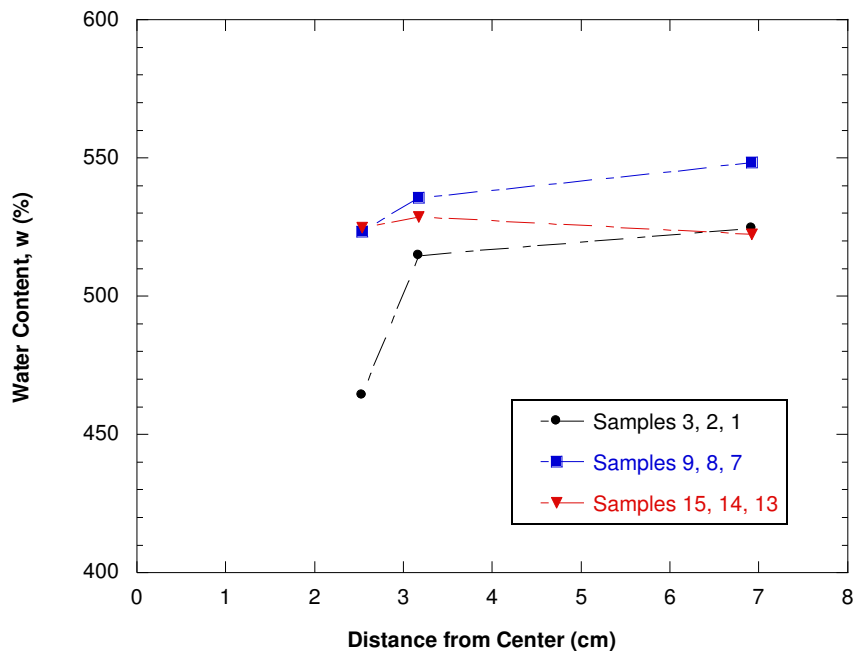


Figure 4.17 Plot of moisture content with respect to the depth within the geothermal model

Figures 4.16 and 4.17 illustrate that the variance of moisture content with depth within the geothermal model and the variance with distance from the center of the geothermal model had a similar trend. The apparent trend was that the samples that were in contact with the 25 mm HDPE pipe had the lowest moisture content. For example considering samples three, nine, and fifteen from Figure 4.16 and samples three, two, and one from Figure 4.17, sample three had the lowest moisture content (464 %) compared to sample nine (523 %) and fifteen (525 %) and likewise for Figure 4.17. Figures 4.16 and 4.17 also show that the moisture content within the geothermal model leveled off with increasing depth and increasing distance away from the center of the geothermal model.

The importance of the final moisture content is because proper design of a geothermal heat pump relies on several factors, which include soil temperature variation, thermal

conductivity of the grouting material as well as the soil porosity and moisture content. As mentioned in Chapter 2, moisture content of the soil has the most prominent effect on thermal conductivity. Upon adding moisture to a soil, a thin water film develops around the soil particles, which bridges the gaps between the soil particles. The “bridging” behavior results in an increased effective contact area between the soil particles, thereby also increasing the heat flow and resulting in a higher thermal conductivity. As more moisture is added, the voids between the soil particles become completely saturated and the soil thermal conductivity will no longer increase. (Salomone *et al.* 1984; Salomone and Kovacs 1984; Salomone and Marlowe 1989). Therefore, the groundwater level should be an important design component of a geothermal heat pump considering that groundwater will add additional moisture to the soil surrounding the geothermal borehole. The interaction of groundwater and the geothermal borehole is further discussed in Chapter 6.

CHAPTER 5: Numerical Modeling

This chapter presents the numerical modeling procedures and results of both the laboratory experiment and a model geothermal borehole in the field. The modeling was done using a computer software package COMSOL. COMSOL is a finite element analysis, solver, and simulation software package used for various engineering and physics applications, including heat transfer and fluid flow. The software facilitates the development of models using partial differential equations that are defined by the user. The coupling between various physical interfaces and/or between entirely different models with varying geometries can also be accomplished. For this research project, COMSOL version 4.3 was used for developing heat transfer models in geothermal boreholes. The three cases modeled were: 1.) experimental thermal conductivity values in the lab geometry, 2.) standard design thermal conductivity values in a model field

geometry, and 3.) experimental thermal conductivity values in a model field geometry. The first case was chosen in order to calibrate the laboratory thermal conductivity tests by comparing the numerical solutions from COMSOL and the hand calculated results to make sure both solutions were the same. The second and third case were chosen to distinguish the thermal performance of the bentonite grout based on the published thermal conductivity (case 2) compared to the experimental thermal conductivity (case 3). It was important to perform separate analyses for case two and case three because the thermal conductivity published by the manufacturer (0.74 W/m-K) was slightly higher than the experimental thermal conductivity obtained from this research project (0.64 W/m-K for a heating cycle and 0.092 W/m-K for a cooling cycle). Additionally, the published thermal conductivity did not vary with temperature. The selected geometry for a 2-dimensional transient thermal analysis is shown in plan view in Figure 5.1

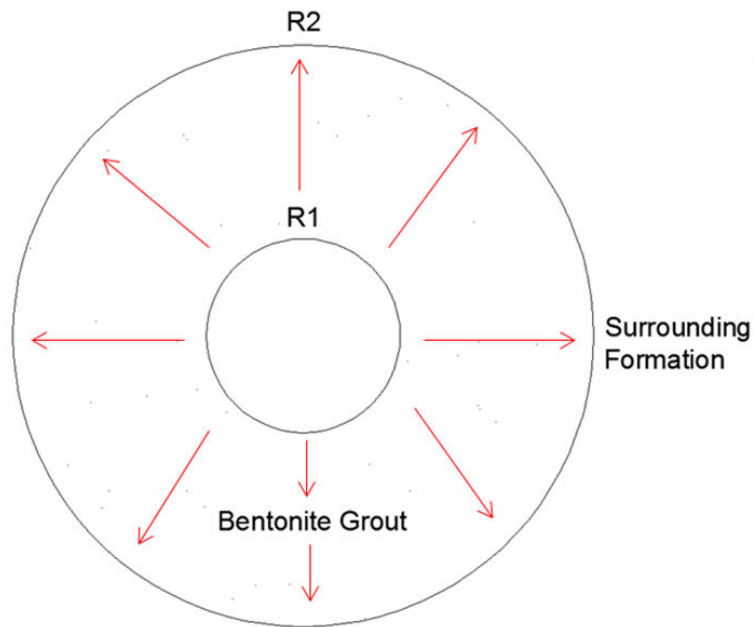


Figure 5.1 Plan view of the geothermal borehole as modeled in COMSOL

The plan view in Figure 5.1 is shown in order to be able to visualize the radial heat distribution with respect to time and position during a heating and cooling cycle. For all three cases that were modeled, the inner pipe with the outer boundary labeled R_1 was 25 mm (1 in) in diameter and the outer boundary labeled R_2 was 152 mm (6 in) in diameter. The differences between the laboratory modeling and modeling the field condition were the properties and temperature of the surrounding formation next to R_2 . For the laboratory modeling the surrounding formation was air whereas for the field conditions the properties and temperature of soil were used. The 152 mm diameter pipe is a PVC pipe and was assumed to have negligible effect between the grout/formation interface when the COMSOL modeling was performed. The red arrows in Figure 5.1 illustrate the heat flux direction as the 25 mm pipe circulated the heated water and had a higher temperature. When considering a cooling cycle, the 152 mm pipe had a higher temperature and therefore the arrows point toward the 25 mm pipe. Typically the piping material in a geothermal borehole forms a U-loop and the modeling in this research project only considered part of the loop with the assumption that the results obtained will be true for the mirror image segment. A time dependent study was chosen on COMSOL in order for the software to be able to report the desired data at a specified time. The objectives of the finite element modeling were twofold: 1.) calibrate the geothermal model that is used for the thermal conductivity tests, and 2.) extend the laboratory data to examine the long term field performance of a geothermal heat exchanger (GHX) from the heat distribution with respect to time and position.

5.1 Heat Transfer Mechanisms

Heat transfer is the process of transmitting energy through materials in response to a temperature gradient. The efficiency of the heat transfer determines the thermal performance of the GHX, and ultimately the thermal performance of the entire geothermal system. The heat transfer mechanisms that occur in the ground in a GHX system consist of three parts: 1.) heat transfer from the two pipes in the borehole through the pipes and into the well seal material (shown in Figure 5.2a), 2.) heat transfer between the fluid circulated in the pipe and the grout in the geothermal borehole and well as the heat transfer between the grouting material and the surrounding native soil (shown in Figure 5.2b and c) , and 3.) heat interference between two or more geothermal boreholes in the field (shown in Figure 5.2e).

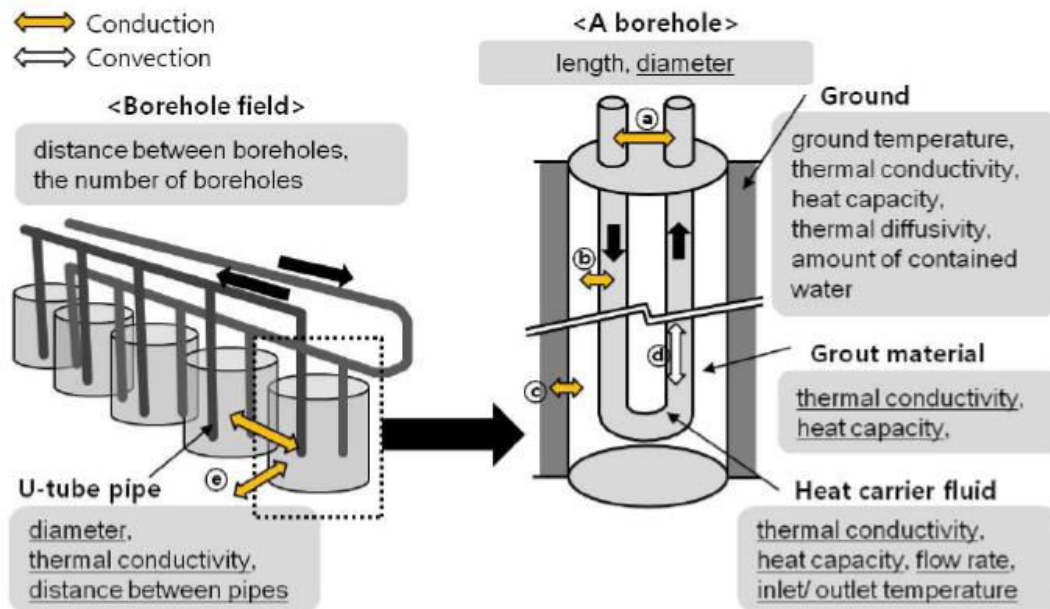


Figure 5.2 Heat transfer mechanisms and thermal influence factors of GHX
[Source: Choi *et al.* (2011)]

Figure 5.2b and c illustrate heat transfer between the fluid in the pipe and the ground by means of conduction. Conduction is the main heat transfer mechanism in a GHX, where the heat is transferred through the pipe and the grout material. Figure 5.2d illustrates the fluid movement inside the pipe, where the heat carrier fluid absorbs/releases heat from/to the ground at the same time in the borehole. This form of heat transfer that occurs within the heat carrier fluid is convection. This research project only focused on the modeling of conduction and convection of heat in a single borehole and not the heat interference of multiple boreholes. However, the modeling of the heat interference between boreholes is important especially when performing a thermal performance analysis for a geothermal system that has multiple boreholes. According to Choi *et al.* (2011), the short distance between the adjacent boreholes allows a small section of the ground to exchange heat for each borehole, and the adjacent boreholes thus affect each other thermally so that heat exchange between the fluid and the ground becomes insufficient. These heat interferences between boreholes are influenced not only by the distance between the boreholes but also by the ground's thermal characteristics.

5.1.1 Heat Transfer by Conduction and Convection

The first law of thermodynamics, also known as the conservation of energy, is the fundamental law that governs all heat transfer. The governing equation used by COMSOL for heat conduction and given in terms of temperature, T , is as follows:

$$\rho C_p \left(\frac{\partial T}{\partial t} + (\mathbf{u} \cdot \nabla) T \right) = -(\nabla \cdot \mathbf{q}) + \boldsymbol{\tau} \cdot \mathbf{S} - \left. \frac{T \partial \rho}{\rho \partial T} \right|_p \left(\frac{\partial p}{\partial t} + (\mathbf{u} \cdot \nabla) p \right) + Q \quad (7)$$

where ρ is the density (in kg/m³), C_p is the specific heat capacity at constant pressure (in J/kg-K), T is the absolute temperature (in K), u is the velocity vector (in m/s), q is the heat flux by conduction (in W/m²), p is the pressure (in Pa), τ is the viscous stress tensor (in Pa), S is the strain-rate tensor (in 1/s) and is given as: $\mathbf{S} = 0.5(\nabla \mathbf{u} + (\nabla \mathbf{u})^T)$, and Q contains heat sources other than viscous heating (in W/m³). The derivation of Equation 7 assumes mass is always conserved, which means that the relationship between density and velocity is as follows: $\partial \rho / \partial t + \nabla \cdot (\rho \mathbf{v}) = 0$. The heat transfer interfaces use Fourier's law of heat conduction, which states that the conductive heat flux, q , is proportional to the temperature gradient:

$$q_i = -k \frac{\partial T}{\partial x_i} \quad (8)$$

From Equation 7, the second term on the right represents viscous heating of a fluid. The third term represents pressure work and is responsible for the heating of a fluid under adiabatic compression and for some thermo acoustic effects. Inserting Equation 8 into 7 and ignoring viscous heating and pressure work yields the heat equation in the following form:

$$\rho C_p \frac{\partial T}{\partial t} + \rho C_p \mathbf{u} \cdot \nabla T = \nabla \cdot (k \nabla T) + Q \quad (9)$$

The heat equation as shown in Equation 9 was the default equation used in COMSOL to model both conduction and convection heat transfer. The two different heat mechanisms were differentiated by allocating different boundary and initial conditions for each.

5.2 Boundary and Initial Conditions

In order to solve the partial differential equation that models the transient heat transfer in a geothermal borehole, the problem was solved as being a boundary value problem (BVP) as well as being an initial value problem (IVP). The modeling performed in this chapter fits the criteria of a BVP and IVP because COMSOL solves the heat conduction differential equation based on the specified constraints at R_1 and R_2 together with the initial temperature of the geothermal borehole. The selected boundary and initial conditions for the convection and conduction heat transfer have been explained below.

5.2.1. Convection Heat Transfer

When considering the plan view of the geothermal model as shown in Figure 5.1, the inner radius, R_1 , was denoted as a forced convection boundary because fluid flows through the one inch diameter pipe while being pumped by a peristaltic pump. The convective cooling method assumes the heat transfer rate as being proportional to the temperature difference across a fictitious thermal boundary layer. The aforementioned heat flux is mathematically described as follows:

$$-\mathbf{n} \cdot (-k\nabla T) = h(T_{\text{ext}} - T) \quad (10)$$

where h is the convective heat transfer coefficient and T_{ext} is the temperature of the external fluid far from the boundary. Equation 10 is the default equation used by COMSOL, where the h term is the user defined input.

The Reynolds number was calculated to be 1969 for a heating cycle using the following relationship: $Re = \rho VL/\mu$, where ρ is the density of the fluid, V is the fluid velocity, L is the traveled length of the fluid, and μ is the dynamic viscosity. Following the same procedure, the Reynold's number for a cooling cycle was calculated to be 782.6. The first step in determining the heat transfer coefficient associated with the forced convection was to determine the Nusselt number (Nu). Since the Reynold's number for both the heating and cooling cycle was less than 10,000, the Nusslet number was then independent of Reynolds number and the Prandtl number. Hence, the value used was an empirical constant (Nu = 3.66). The empirical constant was used on the bases that the pipe was characterized by laminar flow and a constant surface temperature, which assumes negligible axial conduction (Incropera and DeWitt, 1996). Thereafter, the Nusselt number was then used to calculate the heat transfer coefficient as shown in Equation 11:

$$h = \frac{k}{D} \text{Nu} \quad (11)$$

where D is the diameter of the pipe and k is the thermal conductivity of water. Using Equation 11, the heat transfer coefficient was calculated to be 88 W/m²K. The typical

heat transfer coefficients for forced convections in liquids range from 50-20,000 W/m²K (Incropera and DeWitt, 1996). Therefore the calculated h value was within the expected heat transfer coefficient values. The initial condition that was specified for convective heat transfer during a heating cycle was an initial temperature of 48°C (321 K) and this was the average fluid temperature during a heating cycle. For a cooling cycle, the initial temperature used at the inner boundary was 5 °C (278 K). Additionally, it was assumed that the surfaces in contact with the fluid were isothermal; that is they retained a constant temperature along the fluid boundary.

The outer boundary, R_2 , of the geothermal model as show in Figure 5.1 was modeled as a free (or natural) convection boundary. At this boundary, the transition of the free convection depended on the relative magnitude of the buoyancy and viscous forces hence this correlation is given in terms of the Rayleigh number in the following form (Incropera and DeWitt, 1996):

$$Ra_L = \frac{g\beta(T_s - T_\infty)L^3}{\nu\alpha} \quad (12)$$

where g is the gravitational acceleration, β is the thermal expansion coefficient equal to $1/T$ and T is the absolute temperature, T_s is the surface temperature of the geothermal model, T_∞ is the temperature far from the surface of the object (quiescent temperature), L is the height of the geothermal model, ν is the kinematic viscosity of air, and α is the thermal diffusivity of air. Once the Rayleigh number was calculated for each of the three scenarios that were modeled, the Nusselt number was calculated using the following

relationship: $\overline{Nu}_L = Ra_L^n$, where $n=1/4$ and $n=1/3$ for laminar and turbulent flows, respectively. Since the flow of air was assumed to be lamina, $n=1/4$ was used in the calculations. Thereafter, the Nusselt values were used in Equation 11 in a similar manner as the forced convection boundary. The calculated convective heat transfer coefficient values associated with the free convection boundary are shown in Table 5.1.

Table 5.1 Convective heat transfer coefficient values associated with the free convection boundary for the three cases that were modeled in COMSOL Multiphysics

Scenario	Heating Cycle	Cooling Cycle
	Convective Heat Transfer coefficient, h (W/m ² .K)	Convective Heat Transfer coefficient, h (W/m ² .K)
Case 1: experimental thermal conductivity values in the lab geometry	92.64	13.32
Case 2: standard design thermal conductivity values in field geometry	107	107
Case 3: experimental thermal conductivity in field geometry	92.31	13.13

5.2.2. Conduction Heat Transfer

The boundary condition used for modeling heat transfer by conduction was Equation 7, with k , C_p , and ρ as the user defined inputs on COMSOL. These user defined inputs were based on the properties of the bentonite grout and were 1250 J/kg-K and 1140 kg/m³ for C_p , and ρ , respectively. The k value was 0.64 W/m-K for case one and case three for a heating cycle and 0.092 W/m-K for a cooling cycle. The thermal conductivity was 0.74 W/m-K for case two. The k values specified for case one and case three were the experimental thermal conductivity whereas the k value for case two was obtained from a technical specification as published by the manufacturer of the bentonite grout. Since the bentonite grout would be in contact with the native soil when considering a geothermal borehole in the field, the outside boundary of the grout, R_2 , was given an initial temperature equal to the expected ground temperature in Pennsylvania. According to the United States Geological Survey (USGS), the average ground temperature in Pennsylvania is approximately 12°C and this was the temperature value allocated to that boundary.

5.3 Finite Element Mesh

Figure 5.3 illustrates the finite element mesh that was discretized in COMSOL to model a geothermal borehole. The selected mesh was constructed in a two dimensional (2-D) rather than a three dimensional (3-D) cross section to reduce computational time. The 2-D approach was reasonable since the modeling of the geothermal borehole assumes a “slice” was considered at a certain depth.

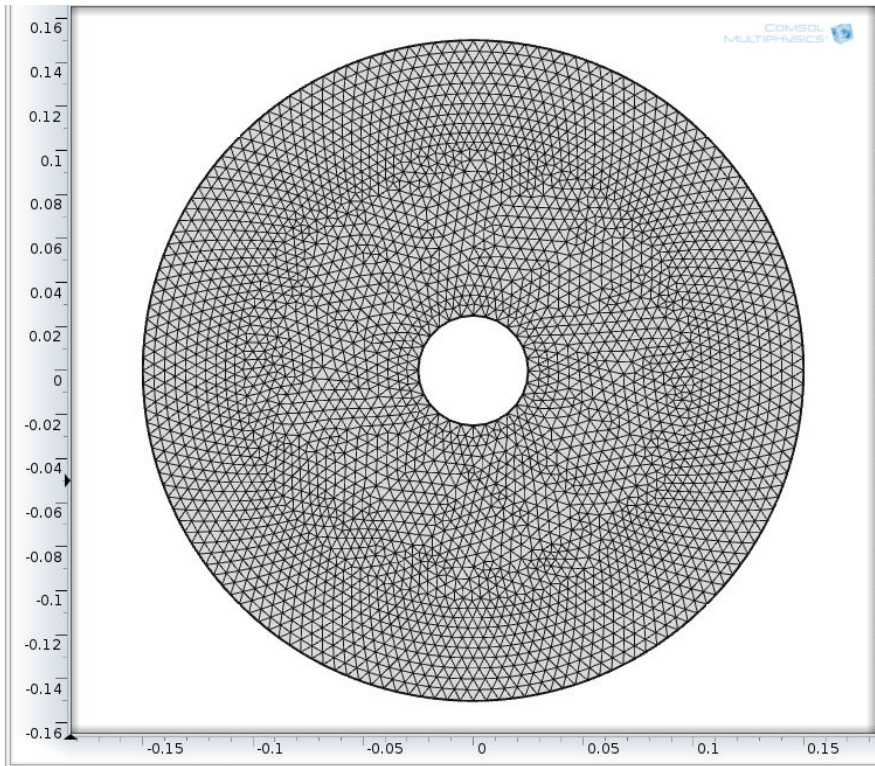


Figure 5.3 Two dimensional finite element mesh as modeled in COMSOL

A relatively fine mesh was selected to ensure that even with the circular geometry, the modeling was

performed with a high level of accuracy. A refinement study was also conducted by selecting a finer mesh than the one shown in Figure 5.3 to ensure that the results were independent of the selected mesh. The results of the refinement study showed no changed and so the initially selected mesh was used for the modeling. As shown in Figure 5.3, the number of boundary elements consisted of 188 elements and a total number of elements for the domain modeled added up to 6330 elements.

5.4 Results and Discussion

After the computation on COMSOL, the results that were of interest for this research project were to determine the time when the system reached steady state; that is the point where the temperature of the outer boundary, R_2 , was not significantly changing. Figures 5.4 to 5.7 illustrate the results obtained from COMSOL. Similar plots for case two and case three have been attached in the Appendix C. As can be seen in Figures 5.4 to 5.7, from a time dependent study the radial heat pattern that is formed during the cyclic heating and cooling tests can be easily visualized. During a heating cycle, the heat conducts outward from the inner boundary to the outer boundary because the temperature of the fluid in the one inch pipe is higher than the temperature of the grout and the surrounding medium. The opposite is true for a cooling cycle because the fluid temperature will be lower than the grout and the heat will conduct from the outer boundary inward. For case one, which was the experimental setup in the laboratory, steady state was reached in 13 hours. However, for case two and case three, where both scenarios considered a system that would be in the field, steady state was reached in 33 hours.

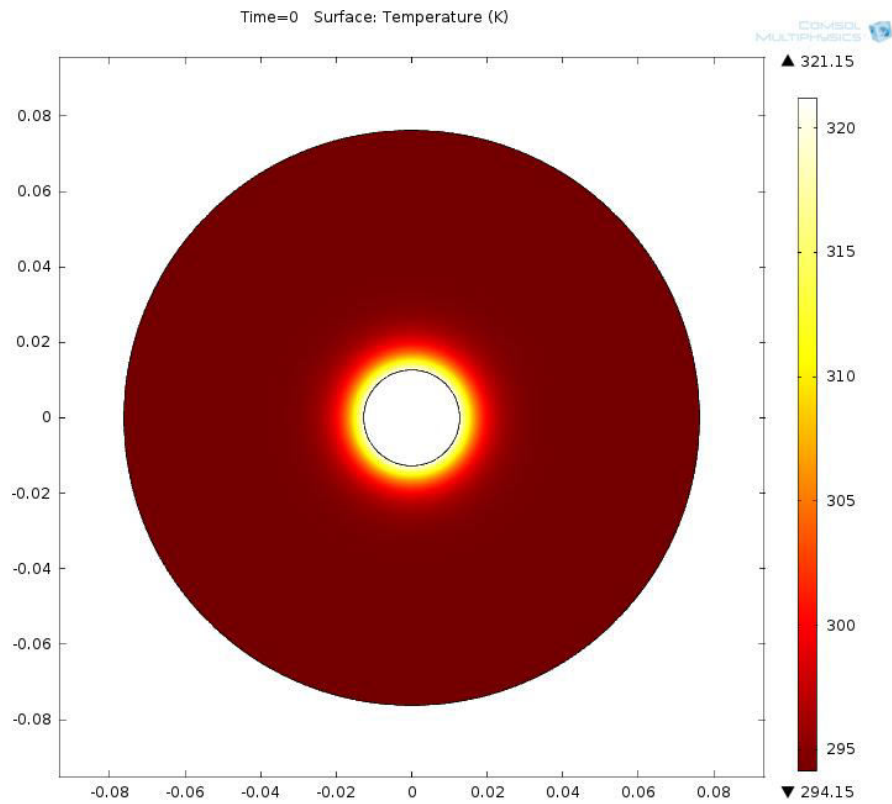


Figure 5.4 Case 1 temperature distribution for a heating cycle in the geometry modeled in COMSOL at zero hours

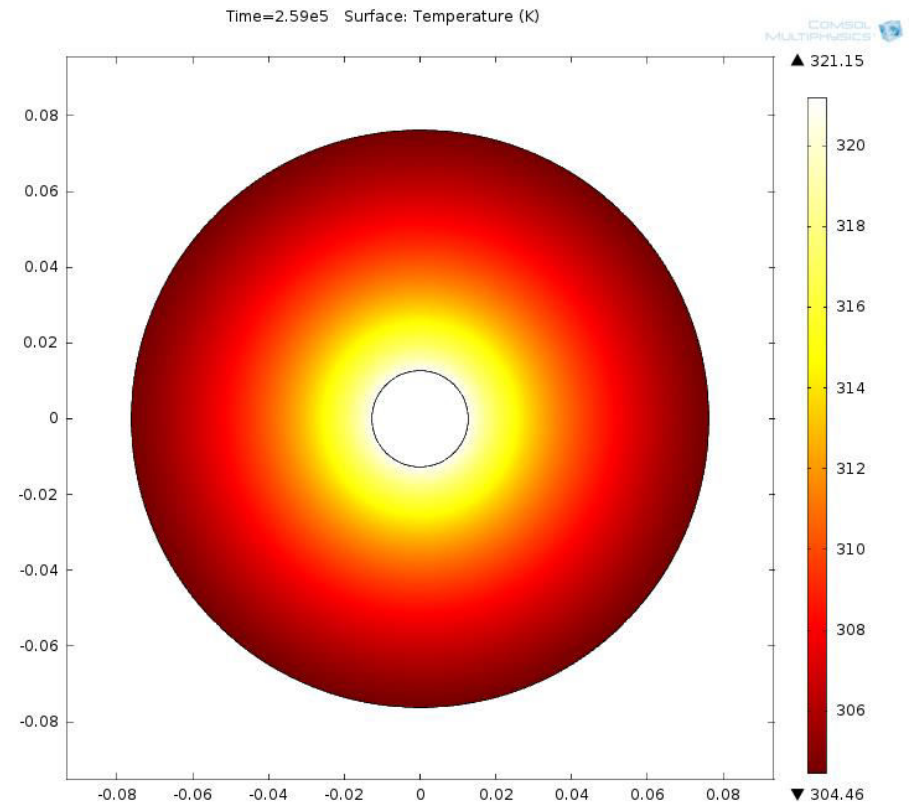


Figure 5.5 Case 1 temperature distribution for a heating cycle in the geometry modeled in COMSOL at 72 hours

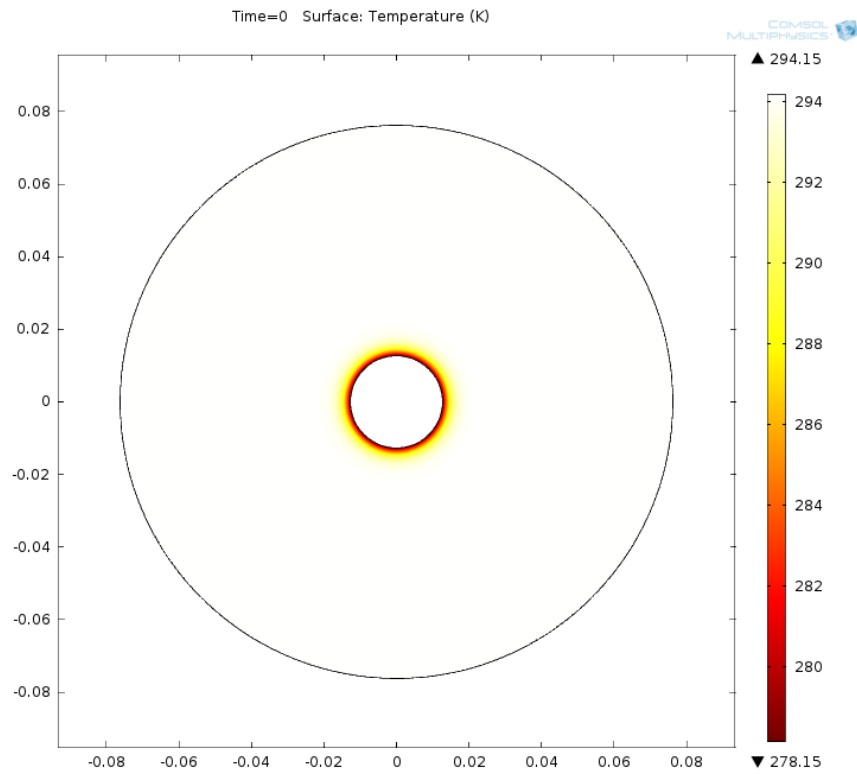


Figure 5.6 Case 1 temperature distribution for a cooling cycle in the geometry modeled in COMSOL at zero hours

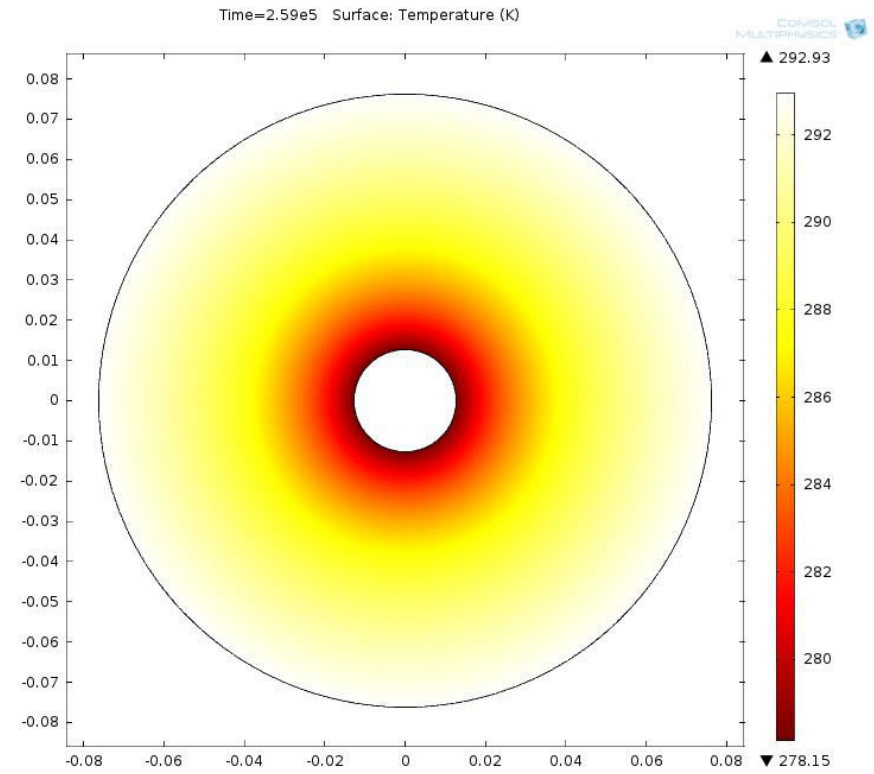


Figure 5.7 Case 1 temperature distribution for a cooling cycle in the geometry modeled in COMSOL at 72 hours

The results of the steady temperature at the outer boundary of the geothermal borehole, R_2 , have been tabulated in Table 5.2. The values shown in Table 5.2 are the steady state temperature values after 72 hours after the geothermal system had been operating.

Table 5.2 Results from COMSOL of the steady state temperatures at the outer boundary of the geothermal borehole

	Heating Cycle	Cooling Cycle
Scenario	Results from COMSOL: Steady Temperature ($^{\circ}\text{C}$)	Results from COMSOL: Steady Temperature ($^{\circ}\text{C}$)
Case 1: experimental thermal conductivity values in the lab geometry	31	19
Case 2: standard design thermal conductivity values in a field geometry	14	11
Case 3: experimental thermal conductivity in a field geometry	13	10

For case one, the values obtained from COMSOL were in close proximity to the temperature values recorded by the thermocouples in the geothermal well model. After 72 hours, the thermocouples at the outer boundary of the geothermal well model had temperatures of 32°C for a heating cycle and 17°C for a cooling cycle. By having the temperature solutions from COMSOL match the laboratory solutions, this was a way of calibrating the thermal conductivity tests. It was important to determine the steady state temperature at the outer boundary of the geothermal borehole because these values were

used to calculate the heat transfer rate between the grout and the surrounding formation. Determining the heat transfer rate at the outer boundary was valuable knowledge because this provided information on the rate of heat transfer between the grout and the immediate surrounding (native soil or air temperature in the case of the experimental setup in the laboratory). A high heat transfer rate indicates that the heat exchanging process between the bentonite grout and the ground was occurring with high efficiency. The heat transfer rate values that were obtained from COMSOL have been plotted in Figures 5.8 to 5.10.

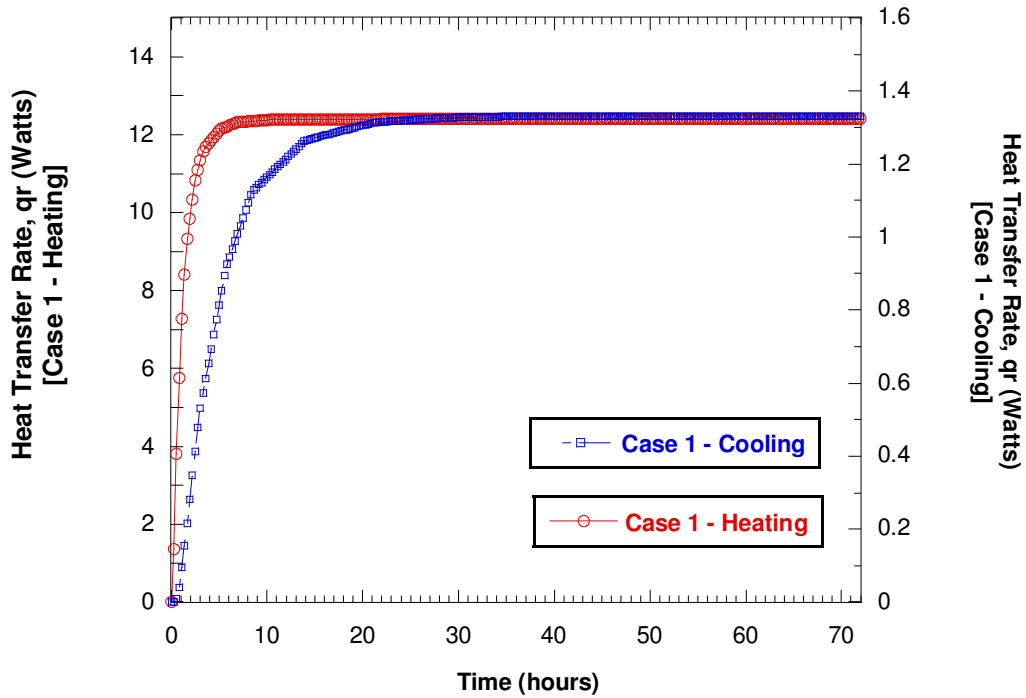


Figure 5.8 Plot of heat transfer rate with respect to time for case 1

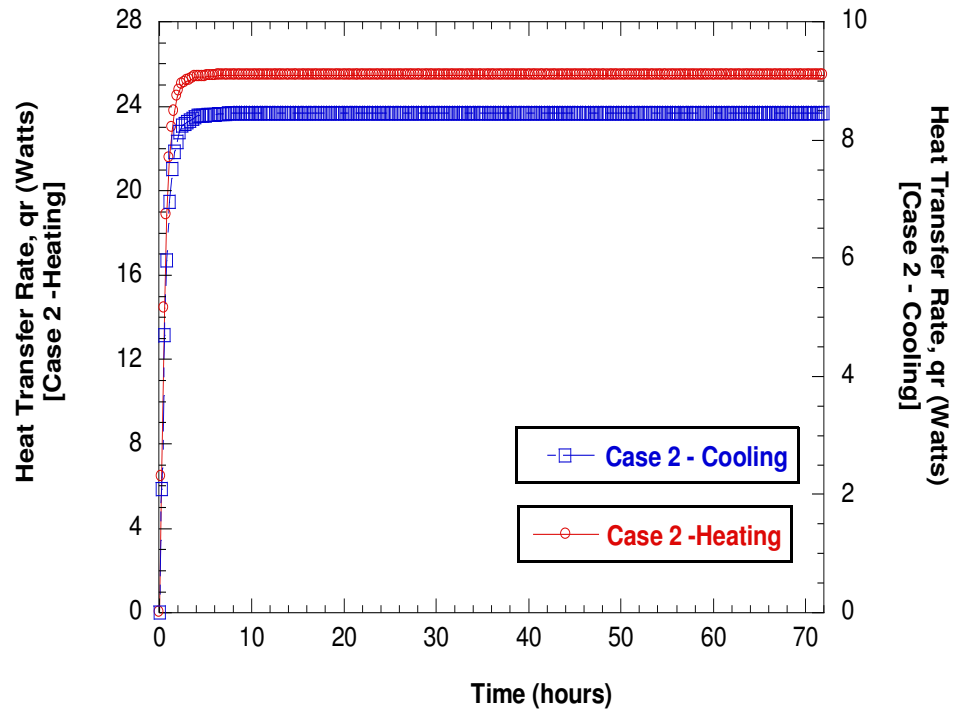


Figure 5.9 Plot of heat transfer rate with respect to time for case 2

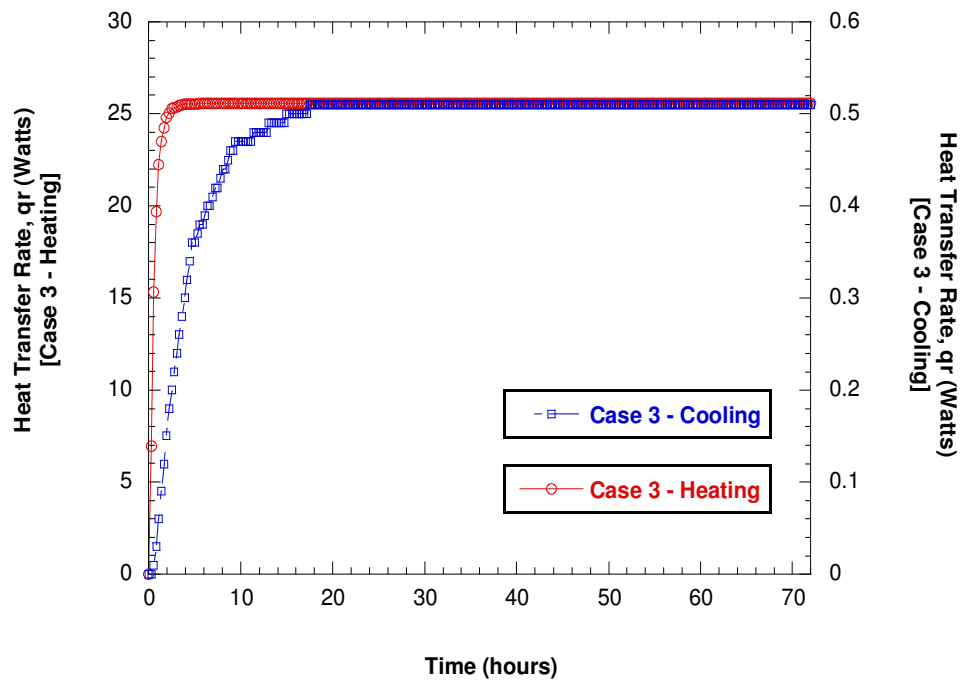


Figure 5.10 Plot of heat transfer rate with respect to time for case 3

As shown in Figures 5.8 to 5.9, there is a point during the cyclic heating and cooling test where a steady state heat flux was achieved in a similar manner as the temperature at the outer boundary. The steady state heat transfer rate values from these plots have been tabulated in Table 5.2. Hand calculations were also performed in order to verify the results obtained from COMSOL. The temperature distribution associated with radial conduction through a cylindrical wall is logarithmic and not linear. Therefore Fourier's law for expressing the heat transfer rate in a cylindrical geometry is given as:

$$q_r = \frac{2\pi L k(T_{s,1} - T_{s,2})}{\ln\left(\frac{R_2}{R_1}\right)} \quad (13)$$

where $T_{s,1}$ is the temperature of the inner boundary (R_1) and $T_{s,2}$ is the temperature of the outer boundary (R_2). The heat flux values as obtained from COMSOL as well as the hand calculated values using Equation 13 are shown in Table 5.3. The values shown in Table 5.3 are heat transfer rates at 72 hours. As can be seen from Table 5.3, case 2, which used the published expected published thermal conductivity, had the highest heat transfer rate for both heating and cooling cycles. However, the heat transfer rate for the cooling cycle in case 2 could have possibly over estimated the actual heat transfer rate because the published thermal conductivity does not vary with temperature. The steady state temperature and heat transfer rate values were used in chapter 6 to assess the performance and efficiency of the geothermal borehole.

Table 5.3 Steady state and hand calculated heat transfer values and values that were obtained from COMSOL at 72 hours

Scenario	Heating Cycle		Cooling Cycle	
	Results from COMSOL: Heat Transfer Rate, q_r (Watts)	Hand Calculated: Heat Transfer Rate, q_r (Watts)	Results from COMSOL: Heat Transfer Rate, q_r (Watts)	Hand Calculated: Heat Transfer Rate, q_r (Watts)
Case 1: experimental thermal conductivity values in the lab geometry	12.39	11.88	0.98	1.05
Case 2: standard design thermal conductivity values in a field geometry	25.99	26.1	8.45	8.7
Case 3: experimental thermal conductivity in a field geometry	25.58	27.41	0.52	0.46

CHAPTER 6: Performance of Geothermal Heat Pumps

In recent years, renewable and sustainable energy has been an emergent topic. The environmental status of the earth has become unstable as a result of the impacts of greenhouse gases and the depleting natural resources and this has required people to seek alternative energy as opposed to solely relying on burning fossil fuels. The Environmental Protection Agency (EPA) and the Department of Energy (DOE) have considered geothermal energy as a clean, green, and renewable resource because energy can be extracted without burning a fossil fuel. The main benefit of using geothermal energy is that the temperature of the subsurface is not subject to large variations experienced by air. Although technological advances are pushing geothermal energy to new depths, the greatest limitation of these systems is the extremely high initial costs compared to alternative Heating Ventilation and Air Conditioning (HVAC) systems. However, the high initial costs of a geothermal system can be compensated by the low maintenance costs. The high installation costs of geothermal heat pumps are due to the high cost of borehole drilling and vary depending on the desired loop and on the subsurface conditions (Dooley, 2001). Vertical closed-loop systems are the most expensive and the thermal conductivity of the grouting material used play a major role as significant reductions in bore length may be achievable through the use of high conductivity grouts. According to Cane and Forgas (1991), the length of geothermal heat exchangers is usually oversized by 10% to 30% in the North American market. Therefore, this chapter presents the evaluation of the efficiency and performance of

geothermal heat pumps with respect to thermal and hydraulic conductivity. This evaluation was accomplished by comparing the standard design thermal and hydraulic conductivity values as published by the manufacturer versus the experimental thermal and hydraulic conductivity values that was obtained in this research project.

6.1 Thermal performance and Efficiency of Geothermal Heat Pump

In the United States, the DOE set standards for the minimum performance of residential and commercial central air conditioners and heat pumps. The performance of a geothermal heat pump is influenced by all components of the installed system, including the soil conditions, the ground-coupled heat exchanger, the heat pump appliance, and the building distribution. However, geothermal systems are mainly evaluated by the "lift" between the input temperature and the output temperature. Geothermal heat pumps as well as other HVAC system have efficiencies rated according to their heating and cooling performance. The heating efficiency is determined by calculating a coefficient of performance (COP). A COP is the ratio of the coefficient of the rate of heat removal (in Watts) from or delivered to the conditioned space to the rate of energy (in Watts) input for a heat pump. The COP_R (which is the COP of the refrigeration) and the COP_{HP} (which is the COP of the heat pump) are calculated using Equations 14 and 15:

$$COP_R = \frac{\text{Rate of heat removal}}{\text{Rate of energy input}} = \frac{Q_L}{W} \quad (14)$$

$$\text{COP}_{\text{HP}} = \frac{\text{Rate of heat delivered}}{\text{Rate of energy input}} = \frac{Q_{\text{H}}}{W} \quad (15)$$

The COP is a quantitative way of determining how much energy the system produces versus how much it uses. A conventional electric heating system typically has a COP of one, meaning it takes one watt of electricity to deliver the heat equivalent of one Watt. In comparison, the COP of a geothermal heat pump (vertical closed loop) is approximately three to four for an indirect heating system and three to five for a direct heating system (Omar, 2008). This means that for every unit of energy used to power geothermal systems, three to five units are supplied as heat. Conversely, the cooling efficiency is measured by calculating the energy efficiency ratio (EER), which is the ratio of the heat removed (in Btu/hr) to the electricity required (in Watts) to run the system. Given that 1Watt = 3.412 Btu/h, the EER can be derived in terms of the following relationship: $\text{EER} = \text{Net cooling (Btu/hr)} / (\text{Total rate of electric input (Watts)})$; therefore the EER is calculated as:

$$\text{EER} = \frac{Q_{\text{L}} \left(\frac{\text{Btu}}{\text{hr}} \right)}{W \left(\frac{\text{Btu}}{\text{hr}} \right)} \times \frac{3.412 \frac{\text{Btu}}{\text{hr}}}{1 \text{ Watt}} = 3.412 \text{ COP}_{\text{R}} \quad (16)$$

The higher the EER (greater than 13 is desirable), the more efficient the cooling equipment is because this implies that less electricity is consumed in an air conditioner for the same cooling output. A geothermal heat pump (vertical closed loop) typically has an EER rating between 13 and 20 (Omar, 2008). The Air-Conditioning, Heating, and Refrigeration Institute (AHRI) have set a minimum EER rating of 13 on all air

conditioning systems. The EER only evaluates the efficiency during the peak usage of the air conditioning system. Therefore, a more accurate way of analyzing the efficiency of an air conditioning system is to calculate the seasonal energy efficiency ratio (SEER). The SEER is a ratio of the total cooling output of an air conditioner during its normal annual usage period for cooling (in Btu) to the total electric energy input (in Watt-hour). The SEER determines the energy efficiency of air conditioners over a seasonal period rather than just during peak usage. Similarly to the EER, a high SEER indicates less electricity consumption during the considered season.

The actual performances of refrigeration and heat pump cycles could be different from the ideal cycles that yield the abovementioned COP and EER values. This is because the efficiency of a geothermal system can be lowered due to the type of grouting material used. According to the ARHI, the efficiency of a fossil fuel furnace is typically 78% to 90% efficient whereas a geothermal heat pump is typically 300% to 400% efficient. When considering the efficiency of a geothermal system, very little attention is paid to the performance of the borehole as result of the type of the grouting material used. Hence the temperature efficiency of the borehole was calculated for a heating and cooling cycle. The two cases that were considered were 1.) the standard design thermal conductivity values as published by the manufacturer (case 2), and 2.) the experimental thermal conductivity values obtained in this research project (case 3). The temperature values that were used were obtained from temperature distribution that was modeled using

COMSOL in Chapter 5. These values were the steady state temperatures after 72 hours. The equation used to calculate the temperature efficiency is shown in Equation 17:

$$\eta = \frac{T_1 - T_2}{T_1 - T_g} \quad (17)$$

T_1 is the temperature of the inner boundary of the geothermal well model (R_1), T_2 is the temperature of the outer boundary of the geothermal well (R_2) after 72 hours of operating the system, and T_g is the ground temperature after 72 hours of operating the system. The standard design thermal conductivity is 0.74 W/m-K (0.43 Btu/hr.ft.°F) as published by the manufacturer and the thermal conductivity and the experimental thermal conductivity was determined to be 0.64W/m-K (0.39 Btu/hr.ft.°F) for a heating cycle and 0.092 W/m-K (0.053 Btu/hr.ft.°F) for a cooling cycle. The analysis performed with these thermal conductivity values yielded 94% efficiency for a heating cycle and 69% efficiency for a cooling cycle when considering the standard design thermal conductivity. For the experimental thermal conductivity, a heating cycle was calculated to have 98% efficiency and 69% for a cooling cycle. From the temperature efficiency results, it was observed that it is important to have a grouting material that has a high enough thermal conductivity to efficiently perform as a heat exchange pathway. Also, the temperature at the outer boundary (R_2) of the geothermal borehole has to be higher but still in close proximity than the surrounding ground temperature for optimal efficiency. Hence, based on the performance of the bentonite grout, it is more efficient to use the geothermal heat pump for heating rather than cooling. This is a great benefit for states like Pennsylvania, where the annualized demand for heating is higher than the demand for cooling.

6.2 Hydraulic Performance of Geothermal Borehole

For vertical closed loop geothermal piping in colder climates, antifreeze solutions are used to prevent the circulating fluid from freezing. A potential negative effect of geothermal systems is the unintended release of the antifreeze solution to the surrounding subsurface of the borehole especially in areas where there could be an aquifer. These antifreeze solutions include methanol, ethanol, potassium acetate, urea, propylene glycol, and calcium magnesium acetate (CMA). These chemicals are generally mixed with water when used as a heat exchange fluid. Antifreeze solutions can be released to the environment via spills or corrosion of system components. Heinonen *et al.* (1996) evaluated geothermal heat pumps for single family residence and the antifreeze solutions for the geothermal systems. The researchers evaluated the total energy consumption, corrosion due to the antifreeze, and the operational and environmental effects of six antifreeze solutions (methanol, ethanol, potassium acetate, propylene glycol, CMA, and urea). The conclusion made by Heinonen *et al.* (1996) was that the differences in total energy consumption for these antifreezes were considered minimal. The researchers recommended that propylene glycol was a better choice due to its low health, fire, and environmental risks. However, Heinonen *et al.* (1996) did not evaluate the leak potential in the geothermal borehole.

In order to evaluate the leak potential in a geothermal borehole, a cross section of the subsurface shown in Figure 6.1 was considered. The cross section of the subsurface shown in Figure 6.1, shows an aquitard layer in between an aquifer with some total hydraulic head.

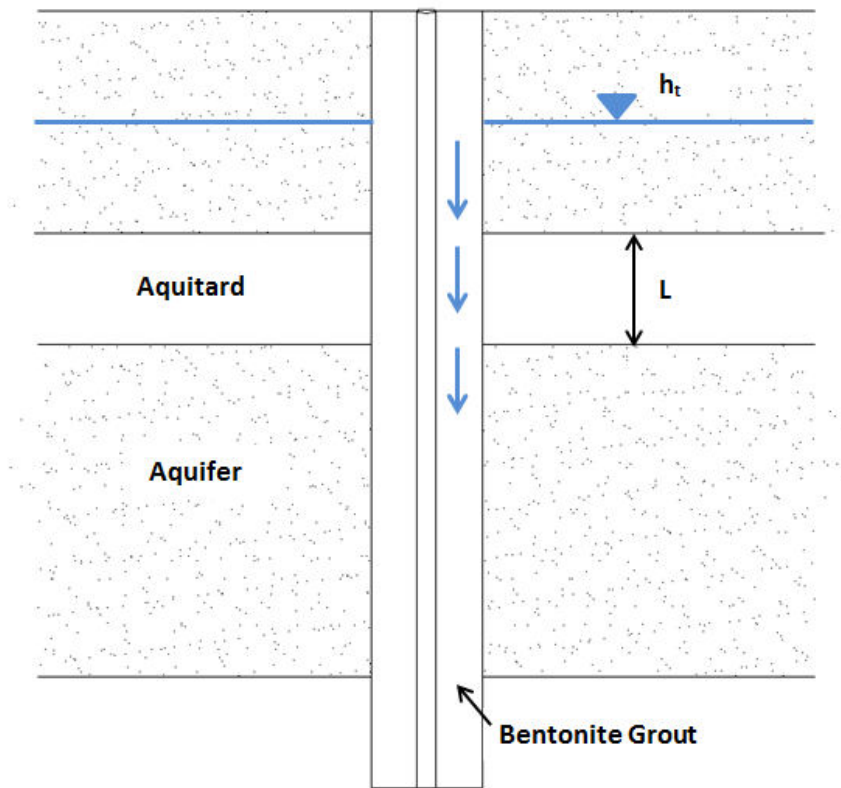


Figure 6.1 Cross section of a geothermal borehole with different soil layers

The amount of downward seepage (shown by the arrows) that could be experienced in a geothermal borehole was assessed by generating hydraulic conductivity curves using the hydraulic conductivity values obtained from the laboratory tests as well as the published expected hydraulic conductivity. Four hydraulic conductivity curves were generated, namely: 1.) initial hydraulic conductivity before the start of the cyclic heating and cooling test (k_{initial}), 2.) final hydraulic conductivity for a heating cycle (k_{heating}), 3.) final hydraulic conductivity for a cooling cycle (k_{cooling}), and 4.) hydraulic conductivity as published by the manufacture of the bentonite grout ($k_{\text{literature}}$). The amount of downward

seepage largely depends on the hydraulic gradient, which is calculated using the following relationship: $i = \Delta h_t / L$, where Δh_t is the change in total head and L is the thickness of the aquitard. The range of hydraulic gradient values that was selected was 0.01 to 10. The range of values for the Darcy flow rate was obtained by using Darcy's law in the following form: $q = kiA$, where k is the hydraulic conductivity, i is the hydraulic gradient, and A is the area of the grouted borehole. Figure 6.2 illustrates the curves used to assess the leakage potential in a geothermal borehole. As shown in Figure 6.2, the published hydraulic conductivity ($k_{\text{literature}}$) had very little to no downward seepage across the entire range of hydraulic gradient values because the $k_{\text{literature}}$ curve had a flow rate of 0.2 cm³/day as the worst case scenario in the system. A flow rate of 0.2 cm³/day would be equivalent to a few droplets and is not a significant amount of flow. However, from Figure 6.2, the worst case scenario that could happen in a geothermal borehole during cyclic heating and cooling is to have a hydraulic gradient of 10. At a hydraulic gradient of 10, switching from a cooling cycle (where there would be a leakage potential of 0.32 cm³/day) to a heating cycle would increase the leakage potential to 0.51 cm³/day. As shown on Figure 6.2, with an increasing hydraulic gradient the potential for downward seepage also increases. Using the assumed subsurface conditions and the laboratory measured values of hydraulic conductivity, the potential for leakage is the highest during a heating cycle in comparison to a cooling cycle but the quantity of flow is, under all conditions evaluated, rather small.

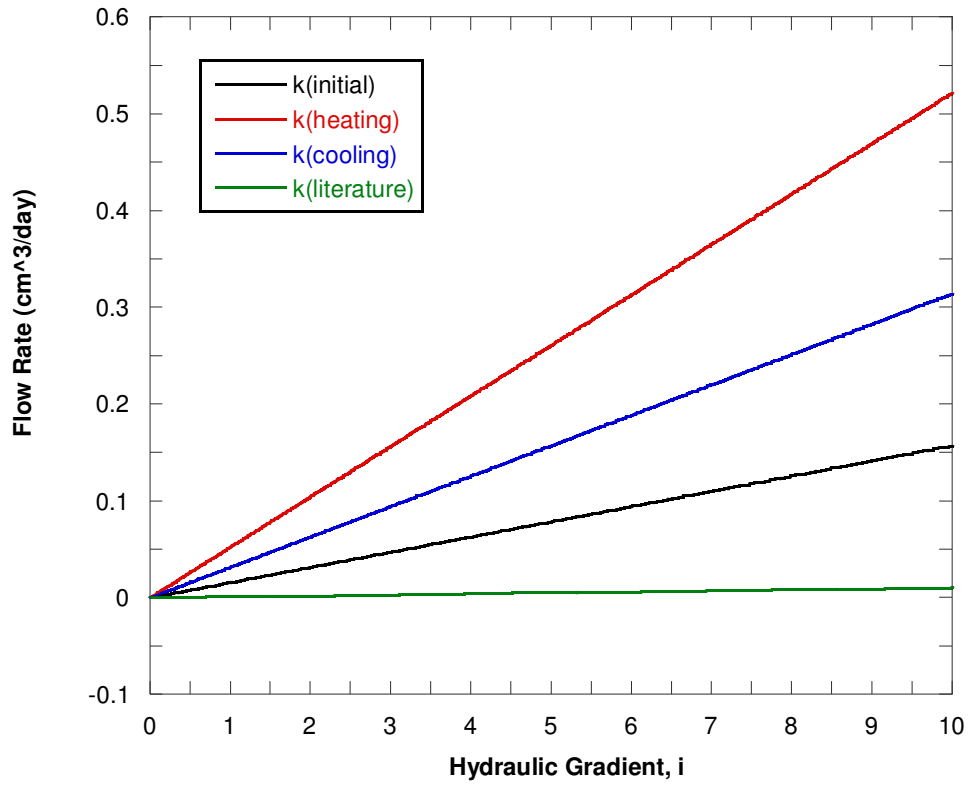


Figure 6.2 Plot of Darcy flow rate with respect to hydraulic gradient

CHAPTER 7: Conclusions and Recommendations

7.1 Thermal and Hydraulic Properties of Bentonite Grout

The principal goals of this research were to evaluate the thermal and hydraulic conductivity properties of bentonite grouts used in geothermal boreholes when subjected to cyclic heating and cooling. As mentioned in Chapter 1, the functions of the grout in a geothermal borehole are twofold: 1.) to perform as a heat exchange pathway between the circulating fluid and the earth, and 2.) to perform as a sealant to prevent the flow of groundwater along the borehole. Hence laboratory thermal and hydraulic conductivity tests were conducted in order to determine the performance of the bentonite grout while being subjected to heating and cooling cycles. Modeling was also undertaken to extend the laboratory results to field conditions. The results of these studies and recommendations for future studies are summarized below:

7.1.1 Thermal Conductivity Results

The obtained experimental thermal conductivity values for a heating and cooling cycle were 0.64 W/m-K and 0.092 W/m-K, respectively. The aforementioned thermal conductivity values were average values from 18 heating and cooling cycles. When comparing the experimental thermal conductivity values to the thermal conductivity published by the manufacturer (0.74 W.m-K), both experimental values obtained in the laboratory were lower. The average thermal conductivity of a cooling cycle was seven

times smaller than the average thermal conductivity of a heating cycle and can be explained by either of two hypotheses: 1.) the thermal conductivity of the bentonite grout is highly influenced by the change in temperature (from a heating to a cooling cycle), and 2.) the cyclic heating and cooling introduces a partial air gap during the cooling cycles. Further investigations need to be conducted regarding the above hypotheses and, in particular, whether the same observed patterns from the laboratory tests would yield similar results for a geothermal borehole in the field. A sevenfold drop in thermal conductivity or the formations of gaps at the grout/pipe interface would result in a geothermal system that would not perform as efficiently as expected using literature values for the grout. The numerical modeling performed using COMSOL helped in the understanding of the laboratory thermal conductivity tests and extending these results to field conditions. Additionally, heat flux numerical solutions were used to compare the thermal performance using the thermal conductivity values as published by the manufacturer of the grout compared with using the experimental thermal conductivity values. The solutions from COMSOL showed that for a heating cycle, the published expected thermal conductivity had a heat transfer rate of approximately 27 Watts, which is higher than the experimental thermal conductivity that yielded a heat transfer rate of approximately 24 Watts. For a cooling cycle, the heat transfer rate for the thermal conductivity was approximately nine Watts whereas the heat transfer rate for the experimental thermal conductivity was approximately one Watt. The conclusion made from the numerical heat flux solutions and analytical solutions was that it is more efficient to use the ground heat exchanging technique for heating rather than cooling.

7.1.2 Hydraulic Conductivity Results

The results of the flow pump permeability tests were used to assess the capability of the bentonite grout in performing as an efficient sealant. According to grouting standards and regulations, a seal with a hydraulic conductivity of 10^{-7} cm/s or less may be used as a sealant (Skouby, 2010). After 17 heating and cooling cycles, the average hydraulic conductivity (all values for each cycle) for a heating and cooling cycle was 2.6×10^{-6} cm/s and 1.29×10^{-6} cm/s, respectively. The hydraulic conductivity for both heating and cooling cycles had a fluctuating trend between 10^{-7} cm/s and 10^{-6} cm/s. From the heating cycles, there were three cycles where the hydraulic conductivity was greater than 10^{-7} cm/s indicating that the grout was not performing as an efficient sealant. Similarly, two cycles from the cooling cycles had hydraulic conductivity values that were greater than 10^{-7} cm/s. The intrinsic permeability data had a similar fluctuating trend as the hydraulic conductivity. The intrinsic permeability data illustrated that the cooling cycles had a larger increase in intrinsic permeability in comparison to the heating cycles whereas the opposite was true for the hydraulic conductivity data. The average intrinsic permeability for a heating and cooling cycle was 1.25×10^{-11} cm² and 1.84×10^{-11} cm², respectively. The experimental hydraulic conductivity values were also assessed to determine whether the possibility of debonding on the grout/pipe interface had been compromised. The hypothesis suggested by the data is that the formation of an air gap on the grout/pipe interface increases the hydraulic conductivity of the bentonite grout from $\sim 10^{-7}$ cm/s to $\sim 10^{-6}$ cm/s. Further investigation is needed to assess this hypothesis and the implications imposed on the hydraulic conductivity of the grout as a result of a formed air gap.

7.2 Experimental Limitations

Having reported thermal and hydraulic conductivity results, it was important to also identify the limitations of the experimental setup, which are as follows:

1. During the laboratory thermal conductivity tests, the geothermal well model was vacuumed sealed, which allowed net minimal change in the moisture content of the grout. In the field, once the geothermal borehole has been grout it is simply covered with the surrounding native soil and moisture in the seal can migrate into or out of the surrounding formation materials. Therefore, the effects of the changing moisture content of the grout could not be evaluated as it was kept constant. Lambe (1954) Mitchell *et. al* (1900) have identified change in water content as one of the factors that affect hydraulic conductivity. Additionally, moisture content of the soil has the most prominent effect on thermal conductivity (Salomone *et al.*, 1984). Hence, possible thermal and hydraulic conductivity changes that could happen in a field geothermal well were not observed in the laboratory tests.
2. This research project was more specific to geothermal boreholes in Pennsylvania and locations with similar borehole sealing regulations because parameters such as ground temperature and type of soil were assumed to be conditions that would be experienced in Pennsylvania. Also, the research only focused on vertical

closed loops and did not consider other geothermal configurations such as horizontal looped geothermal system.

7.3 Recommendations for Future Research

The steady state thermal and hydraulic conductivity in a geothermal borehole was evaluated in this research while considering the effect of cyclic heating and cooling. Although the steady state assumption may be appropriate for design condition and consideration, additional research should be conducted to investigate the effect of thermal and hydraulic properties during the transient phase of heating and cooling. Additional suggestions for further research on the performance of bentonite grouts used in geothermal boreholes while subjected to cyclic heating and cooling are as follows:

1. Allan (1997), Allan and Kavanaugh (1999), and Lee *et al.* (2010) have investigated the optimization of the thermal conductivity of bentonite grout by the addition of additives such as silica sand, graphite, alumina grit, silicon carbide grit, and steel grit. The addition of silica sand would be a more feasible alternative since its price is relatively cheap in comparison to the other additives. However, it would not be recommended to directly add silica sand to the BENSEAL/EZ-MUD® slurry that was used in this research because this grout has not been designed to have sand as an additive and therefore could possibly not perform as desired. The manufacturer of the BENSEAL/EZ-MUD® slurry, Bariod, also manufactures a bentonite grout that has already been thermally enhanced using silica sand. The name of the thermally enhanced bentonite grout is

BAROTHERM® GOLD and has an expected thermal conductivity range of 0.69 to 2.08 W/m-K and an expected hydraulic conductivity that is less than 10^{-7} cm/s. Future cyclic heating and cooling thermal and hydraulic conductivity test could be performed using the BAROTHERM® GOLD slurry.

2. The thermal conductivity setup could be modified by creating a sand box, where the bentonite grout would be placed instead of using the PVC piping as the outer boundary of the geothermal borehole (formation). By using a sandbox, the interaction of the bentonite grout and soil would provide a better estimate of the heat transfer rate between the grout and the formation.
3. The COMSOL modeling could also be modified by possibly performing a 3D analysis instead of the 2D analysis. Additionally, the modeling could also evaluate the vertical variation of the temperature distribution within the geothermal borehole. Modeling of the transient case could be used in conjunction with the observed laboratory data to further investigate the formation of air gaps (debonding).
4. Typically for large commercial buildings, the installed geothermal system consists of a number of geothermal boreholes. Therefore, an evaluation of the heat interaction of multiple boreholes with different temperatures to assess the efficiency of the system as a whole could be performed. This knowledge could be

useful in the design process when determining the spacing and layout of a geothermal system with numerous boreholes.

5. Since the results of the thermal conductivity of the cooling cycles rose suspicion that debonding between the pipe/grout interface occurs as a result of the drop in temperature. Therefore, further investigation on the likelihood of debonding at the pipe/grout interface is recommended and possible ways in which the debonding could be minimized. This investigation could be performed by conducting similar thermal conductivity tests that were conducted in this research project, but the transient phase of the geothermal system would also need to be considered to determine the point where the thermal conductivity of the cooling cycles starts to dramatically decrease.

REFERENCES

- Allan, M. L. (1997). *Thermal conductivity of cementitious grouts for geothermal heat pumps. Progress report FY 1997* (No. BNL--65129). Brookhaven National Lab., Upton, NY (United States).
- Allan, M. L. and Philippacopoulos, A.J. (1999). *PROPERTIES AND PERFORMANCE OF CEMENT-BASED GROUTS FOR GEOTHERMAL HEAT PUMP APPLICATIONS* (No. BNL--67006; EB4001). Brookhaven National Lab., Upton, NY (US).
- Allan, M. L., and Kavanaugh, S. P. (1999). Thermal conductivity of cementitious grouts and impact on heat exchanger length design for ground source heat pumps. *HVAC&R Research*, 5(2), 85-96.
- Beziat, A., Dardaine, M., and Mouche, E. (1992). Measurements of the thermal conductivity of clay-sand and clay-graphite mixtures used as engineered barriers for high-level radioactive waste disposal. *Applied clay science*, 6(4), 245-263.
- Bjerrum , L., and Huder, J. (1957). Measurement of the Permeability of Compacted Clays. *Proceedings, Fourth International Conference on Soil Mechanics and Foundation Engineering, Vol . London, England.* pg 6-10.
- Bradley, W.F and Grim, R.E. (1951). High Temperature Thermal Effects and Related Materials. *American Mineralogist*, 36, pg 182-201.
- Brandon, T. L., and Mitchell, J. K. (1989). Factors influencing thermal resistivity of sands. *Journal of Geotechnical Engineering*, 115(12), 1683-1698.
- Bristow, K. L. (1998). Measurement of thermal properties and water content of unsaturated sandy soil using dual-probe heat-pulse probes. *Agricultural and forest meteorology*, 89(2), 75-84.

- Campbell, G. S., Jungbauer Jr, J. D., Bidlake, W. R., and Hungerford, R. D. (1994). Predicting the effect of temperature on soil thermal conductivity. *Soil Science*, 158(5), 307-313.
- Cane, R. L. D., and Forgas, D. A. (1991). Modeling of ground source heat pump performance. *ASHRAE transactions*, 97(1), 909-925.
- Chapman, D. L. (1913). LI. A contribution to the theory of electrocapillarity. *The London, Edinburgh, and Dublin Philosophical Magazine and Journal of Science*, 25(148), 475-481.
- Charoenvisal, K. (2008). *Energy Performance and Economic Evaluations of the Geothermal Heat Pump System used in the KnowledgeWorks I and II Buildings, Blacksburg, Virginia* (Doctoral dissertation, Virginia Polytechnic Institute and State University).
- Cho, W. J., Lee, J. O., & Chun, K. S. (1999). The temperature effects on hydraulic conductivity of compacted bentonite. *Applied Clay Science*, 14(1), 47-58.
- Choi, M., Baek, S., Yeo, M., and Kim, K. (2011). Modeling of Heat Transfer in Geothermal Heat Exchanger Using GHX Zonal Model Method. *Proceedings of Building Simulation: 12th Conference of International Building Performance Simulation Association, Sydney*.
- Ctori, P. (1989). The effects of temperature on the physical properties of cohesive soil. *Ground engineering*, 22(5).
- Daniel, D.E. (1984). Predicting the Hydraulic Conductivity of Compacted Clays. *Journal of Geotechnical Engineering. ASCE*, 110(2). pg. 285-300.
- Das, B.M. (2010). *Fundamentals of Geotechnical Engineering*, 7th Edition. Cengage Learning, Inc., Stamford, CT.
- Demongodin, L., Pinoteau, B., Vasseur, G., & Gable, R. (1991). Thermal conductivity and well logs: a case study in the Paris basin. *Geophysical Journal International*, 105(3), 675-691.

- Dooley, R., Rafferty, K., and Shonder, J. (2001). Design of Commercial Ground Source Heat Pumps. *ASHRAE Short Course*.
- Evans, J. C., Fang, H. Y., and Kugelman, I. J. (1985). Influence of hazardous and toxic wastes on the engineering behavior of soils. *Management of Toxic and Hazardous Wastes*, Lewis Publishers, Inc., Chelsea Michigan. 1985. pg 237-264.
- Fang, H. Y., & Daniels, J. (2006). *Introductory geotechnical engineering: an environmental perspective*. CRC Press LLC.
- Fernandez, F., & Quigley, R. M. (1988). Viscosity and dielectric constant controls on the hydraulic conductivity of clayey soils permeated with water-soluble organics. *Canadian Geotechnical Journal*, 25(3), 582-589.
- Gouy, G. (1910). Constitution of the electric charge at the surface of an electrolyte. *J. phys*, 9(4), 457-467.
- Grim, R.E. (1963). *Clay Mineralogy*, 2nd Edition. McGraw-Hill, Inc., New York.
- Heinonen, E. W., Wildin, M. W., Beall, A. N., and Tapscott, R. E. (1997). Assessment of antifreeze solutions for ground-source heat pump systems. *Transaction-American Society of Heating Refrigerating and Air Conditioning Engineers*, 103, 747-756.
- Heller-Kallai, L. (2006). .2 Thermally Modified Clay Minerals. *Developments in Clay Science*, 1, 289-308.
- Hiraiwa, Y., and Kasubuchi, T. (2000). Temperature dependence of thermal conductivity of soil over a wide range of temperature (5–75 C). *European Journal of Soil Science*, 51(2), 211-218.
- Holtz, R. D., and Kovacs, W. D. (1981). *An introduction to geotechnical engineering* (No. Monograph).
- Hueckel, T., and Pellegrini, R. (1992). Effective stress and water pressure in saturated clays during heating-cooling cycles. *Canadian Geotechnical Journal*, 29(6), 1095-1102.

- Incropera, F. P., and DeWitt, D. P. Introduction to Heat Transfer (1996). *John WHey & Sons. New York. NY*
- Kaya, A., & Fang, H. Y. (2000). The effects of organic fluids on physicochemical parameters of fine-grained soils. *Canadian Geotechnical Journal*, 37(5), 943-950.
- Kersten, M. S. (1949). *LABORATORY RESEARCH FOR THE DETERMINATION OF THE THERMAL PROPERTIES OF SOILS*. MINNESOTA UNIV MINNEAPOLIS ENGINEERING EXPERIMENT STATION.
- Laguros, J. G. (1969). Effect of temperature on some engineering properties of clay soils. *Highway Research Board Special Report*, (103).
- Lambe, T. W. (1953). The structure of inorganic soil. In *Proc. ASCE* (Vol. 79, No. 1, pp. 1-49).
- Lambe, T. W. (1954). The permeability of compacted fine-grained soils. *Special Technical Publication*, 163, 55-67.
- Lambe, T. W. (1958). The structure of compacted clay. *Journal of the Soil Mechanics and Foundations Division, ASCE*, 84, 1-34.
- Lambe, T. W., and Whitman, R. V. (2008). *Soil mechanics SI version*. John Wiley & Sons Inc., New York.
- Lee, C., Lee, K., Choi, H., and Choi, H. P. (2010). Characteristics of thermally-enhanced bentonite grouts for geothermal heat exchanger in South Korea. *Science in China Series E: Technological Sciences*, 53(1), 123-128.
- Litvinov, I.M. (1960). Stabilization of Settling and Weak Clayey Soils by Thermal Treatment. *Special Report No. Highway Research Board*, Washington DC, 60: pg. 94-114.
- Low, P. F. (1987). Structural component of the swelling pressure of clays. *Langmuir*, 3(1), 18-25.

- McCray, K. B. (Ed.). (1997). *Guidelines for the construction of vertical boreholes for closed loop heat pump systems*. National Ground Water Association.
- Mesri, G., & Olson, R. E. (1971). Consolidation characteristics of montmorillonite. *Geotechnique*, 21(4), 341-352.
- Middtømme, K., & Roaldset, E. (1999). Thermal conductivity of sedimentary rocks: uncertainties in measurement and modelling. *Geological Society, London, Special Publications*, 158(1), 45-60.
- Mindess, S., & Young, J. F. (1981). Concrete, Prentice Hall. *Englewood Cliffs, NJ*, 481.
- Mitchell, J. K., Hooper, D. R., & Campanella, R. G. (1900). Permeability of compacted clay. *Journal of Soil Mechanics & Foundations Div*, 92(SM5, Proc Paper 490).
- Mitchell, J.K and Soga K. (2005). *Fundamentals of Soil Behavior*, 3rd Edition. John-Wiley and Sons Inc, New York.
- Mitchell, J.K. (1993). *Fundamentals of Soil Behavior*, 2nd Edition. John-Wiley and Sons Inc., New York.
- Mustafa Omer, A. (2008). Ground-source heat pumps systems and applications. *Renewable and Sustainable Energy Reviews*, 12(2), 344-371.
- Mustafa Omer, A. (2008). Ground-source heat pumps systems and applications. *Renewable and Sustainable Energy Reviews*, 12(2), 344-371.
- Nassar, I. N., and Horton, R. (1997). Heat, Water, and Solution Transfer in Unsaturated Porous Media: I--Theory Development and Transport Coefficient Evaluation. *Transport in porous media*, 27(1), 17-38.
- Olsen, H.W. (1962). Hydraulic Flow through Saturated Clays. *Clays and Clay Minerals*. Vol 9, pg. 131-161

- Olson, R.E. and Daniel, D.E. (1981) Measurement of the Hydraulic Conductivity of Fined-Grained Soils. *ASTM Special Technical Publication No.746*, Philadelphia, PA. pg 18-64.
- Park, M., Min, S., Lim, J., Choi, J. M., and Choi, H. (2011). Applicability of cement-based grout for ground heat exchanger considering heating-cooling cycles. *Science China Technological Sciences*, 54(7), 1661-1667.
- Philippacopoulos, A. J., & Berndt, M. L. (2001). Influence of debonding in ground heat exchangers used with geothermal heat pumps. *Geothermics*, 30(5), 527-545.
- Reeves, G. M., Sims, I., & Cripps, J. C. (Eds.). (2006). *Clay materials used in construction* (Vol. 21). Geological Society Publishing House.
- Roth, P., Georgiev, A., Busso, A., and Barraza, E. (2004). First in situ determination of ground and borehole thermal properties in Latin America. *Renewable Energy*, 29(12), 1947-1963.
- Salomone, L. and Kovacs, W, and Kusuda, T. (1984). Thermal Performance of Fined-Grained Soils. *Journal of Geotechnical Engineering*. 110(3), pg 359-374.
- Salomone, L. and Kovacs, W. (1984). Thermal Resistivity of Soils. *Journal of Geotechnical Engineering*. 110(3), pg 375–389.
- Salomone, L. and Marlowe, J. (1989). Soil and Rock Classification According to Thermal Conductivity: Design of Ground-Coupled Heat Pump Systems. *Report to Electric Power Research Institute, Report No. EPRI CU-6482*. Chantilly, VA.
- Sanyal, S. K. (2009). Future of geothermal energy. In *Proceedings, CanGEA Conference, Vancouver, BC, Canada*.
- Schackelford, C. D. (1994). Waste-soil interactions that alter hydraulic conductivity. *ASTM Special Technical Publication, 1142*, 111-111.
- Sepaskhah, A. R., and Boersma, L. (1979). Thermal conductivity of soils as a function of temperature and water content. *Soil Science Society of America Journal*, 43(3), 439-444.

Skouby, A. (Ed.). (2010). *Closed-loop/geothermal Heat Pump Systems: Design and Installation Standards*. International Ground Source Heat Pump Association.

Stern, O. (1924). The theory of the electrolytic double-layer. *Zeit. Elektrochem*, 30, 508-516.

Stitchman, R.W. (1990). *Methods of Borehole Stabilization to Avoid Groundwater Contamination*. Ontario HAZTECH/CANADA Conference, Toronto, Canada.

Tarnawski, V. R., & Gori, F. (2002). Enhancement of the cubic cell soil thermal conductivity model. *International journal of energy research*, 26(2), 143-157.

Van Olphen, H. (1963). *Introduction to Clay Colloid Chemistry*. Interscience Publishers.

Van Olphen, H. (1977). *An introduction to clay colloid chemistry: for clay technologists, geologists, and soil scientists*. John-Wiley & Sons Inc., New York.

Yilmaz, G. (2011). The Effects of Temperature on the Characteristics of Kaolinite and Bentonite. *Scientific Research and Essays*, Vol 6(9). Pg 1928-1939.

Ziman, J. (1967). The thermal properties of materials. In *Materials* (pp. 111-126). WH Freeman.

APPENDIX A

```

%conductivity.m
%Main program for calculating the thermal conductivity of a geothermal
%system

[m,n]=size(A);

btu = 0.003966; %Conversion factor from cal/hr to btu/hr
area=1.58; %ft^2
x=1; %ft
k=1; %
mass=6825; %Mass Flow Rate (g/hr)
Cp=1; %Specific Heat capacity, cal/(gram*degC)
R1=1.25; %in
R2=6; %in

%Calculate the thermal conductivity of each cell

%Thermal Conductivity for 110 and 111 thermocouples
T_w= A(:,1)-A(:,2); %Change in water temperature
T1=(A(:,4)-A(:,5)); %Change in grout temperature
q = (mass.*Cp.*T_w).*btu; %Heat flux (btu/hr)

T1_F=(T1.*1.8)+32; %Converting the grout temperature from celcius to Farenheit
k1=(q.*log(R2/R1))./(2.*3.14.*x.*T1_F); %Calculating Thermal Conductivity (Btu/(hr.
ft.degF))

disp(k1);

%Thermal Conductivity for 112 and 113 thermocouples
T2=(A(:,8)-A(:,7)); %Change in grout temperature

T2_F=(T2.*1.8)+32;
k2=(q.*log(R2/R1))./(2.*3.14.*x.*T2_F);%Calculating Thermal Conductivity (Btu/(hr.
ft.degF))

disp(k2);

%Thermal Conductivity for 106 and 107 thermocouples
T3=(A(:,10)-A(:,11)); %Change in grout temperature

T3_F=(T3.*1.8)+32;
k3=(q.*log(R2/R1))./(2.*3.14.*x.*T3_F);%Calculating Thermal Conductivity (Btu/(hr.ft.
degF))

disp(k3);

%Thermal Conductivity for 108 and 109 thermocouples
T4=(A(:,14)-A(:,13)); %Change in grout temperature

T2_F=(T2.*1.8)+32;

```

```

k4=(q.*log(R2/R1))./(2.*3.14.*x.*T4_F);%Calculating Thermal Conductivity (Btu/(hr.ft.
degF))

disp(k4);

%Thermal Conductivity for 102 and 103 thermocouples
T5=(A(:,16)-A(:,17)); %Change in grout temperature

T5_F=(T5.*1.8)+32;
k5=(q.*log(R2/R1))./(2.*3.14.*x.*T5_F);%Calculating Thermal Conductivity (Btu/(hr.
ft.degF))
disp(k5);

%Thermal Conductivity for 104 and 105 thermocouples
T6=(A(:,20)-A(:,19)); %Change in grout temperature

T6_F=(T6.*1.8)+32;
k6=(q.*log(R2/R1))./(2.*3.14.*x.*T6_F);%Calculating Thermal Conductivity (Btu/(hr.ft.
degF))
disp(k6)

time=(1:1:m)';
time_hr =time.*5/60;

%Plot the function

% x=time_hr;
%plot(x,k1,'b*',x,k2,'r*',x,k3,'y*',x,k4,'g*',x,k5,'k*',x,k6,'m*')
xlabel('Time (hours)')
ylabel('Thermal Conductivity(Btu/hr.ft.F)')

B=[k1;k3;k4;k5;k6]; %k2
mean(B)
plot(mean(B),'r*')
xlabel('Cycle Number')
ylabel('Thermal Conductivity(Btu/hr.ft.F)')

```

The following plots illustrate the temperature readings of the thermocouple for the thermal conductivity tests:

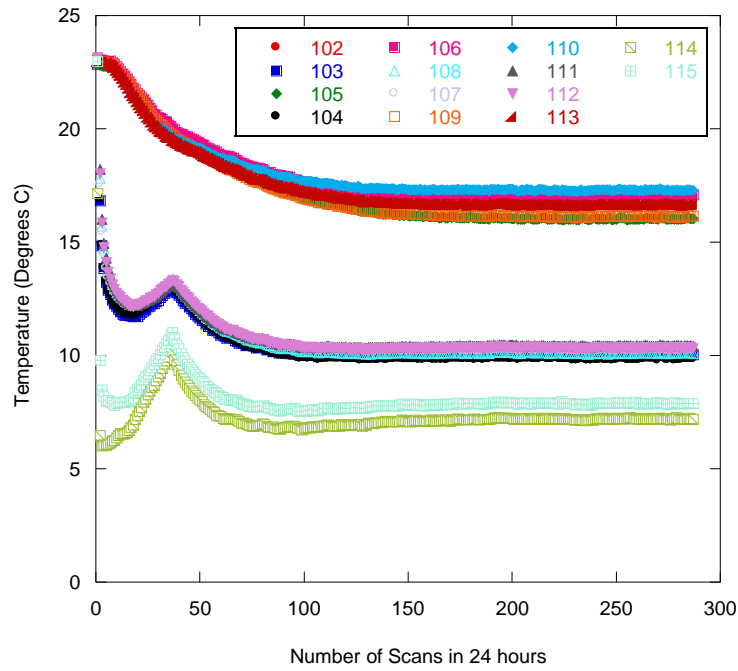


Figure A.1 Temperature data over a 24 hour period for cooling cycle 1 (test conducted in 2010)

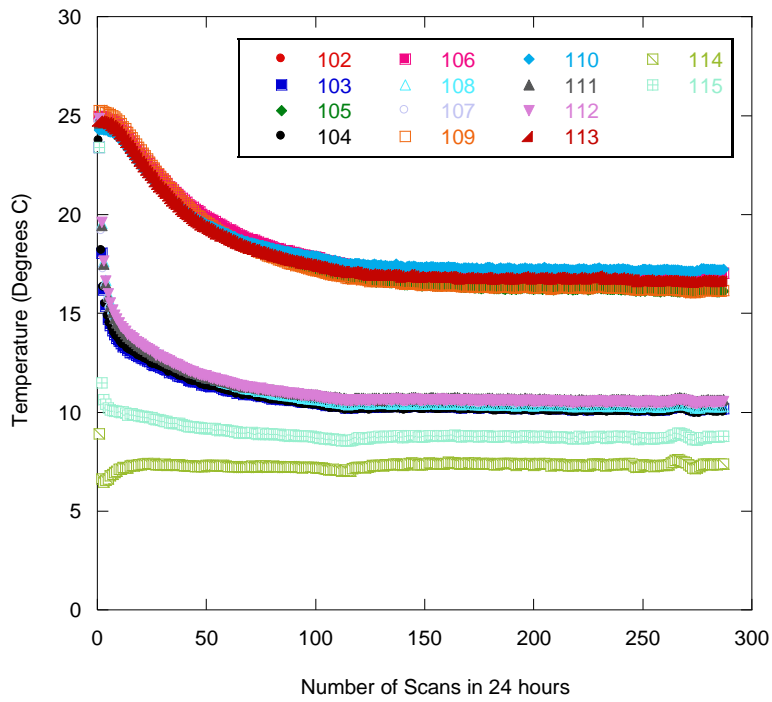


Figure A.2 Temperature data over a 24 hour period for cooling cycle 2 (test conducted in 2010)

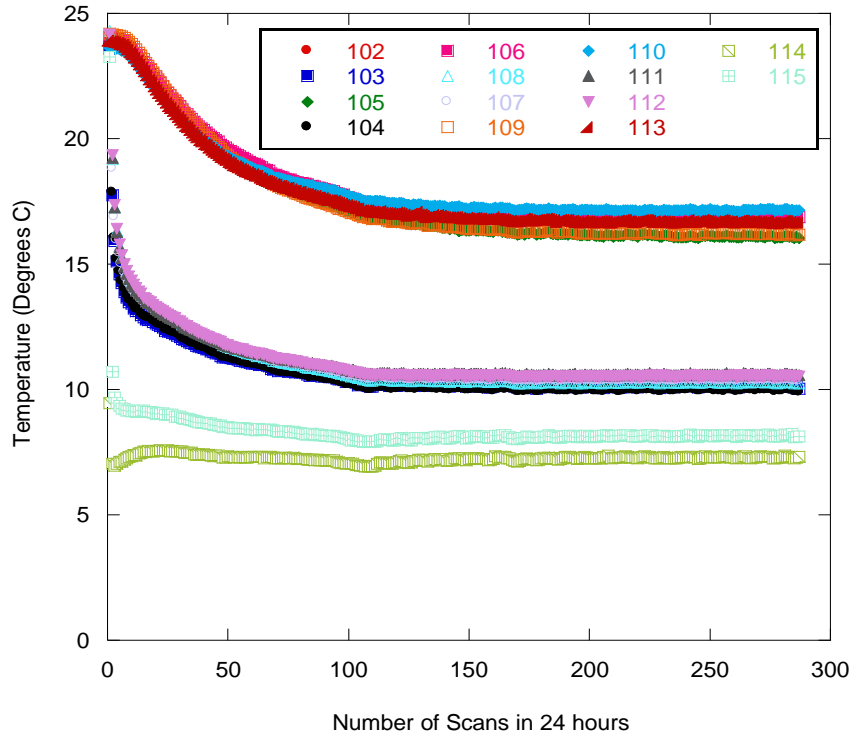


Figure A.3 Temperature data over a 24 hour period for cooling cycle 3 (test conducted in 2010)

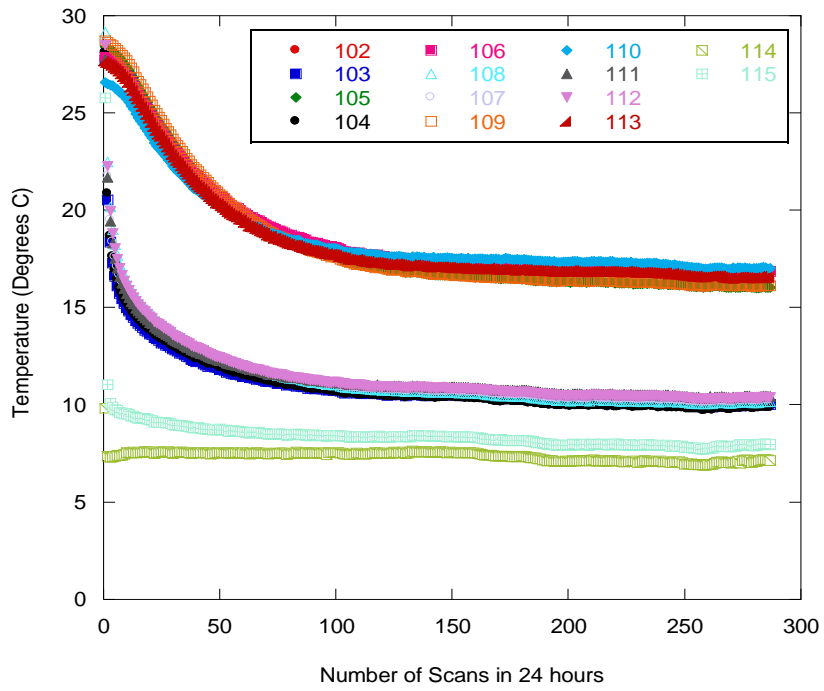


Figure A.4 Temperature data over a 24 hour period for cooling cycle 4 (test conducted in 2010)

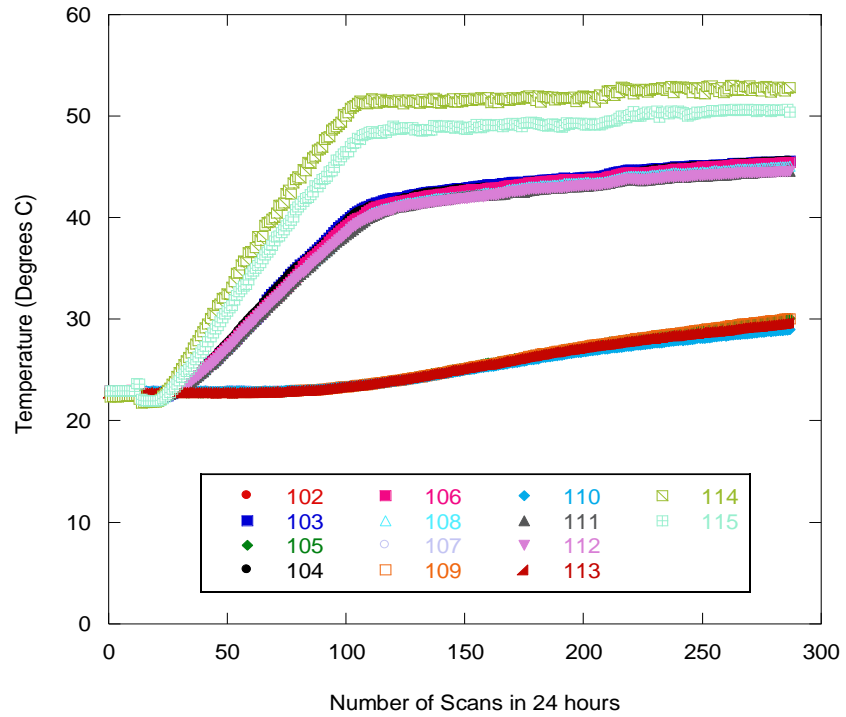


Figure A.5 Temperature data over a 24 hour period for heating cycle 1 (test conducted in 2010)

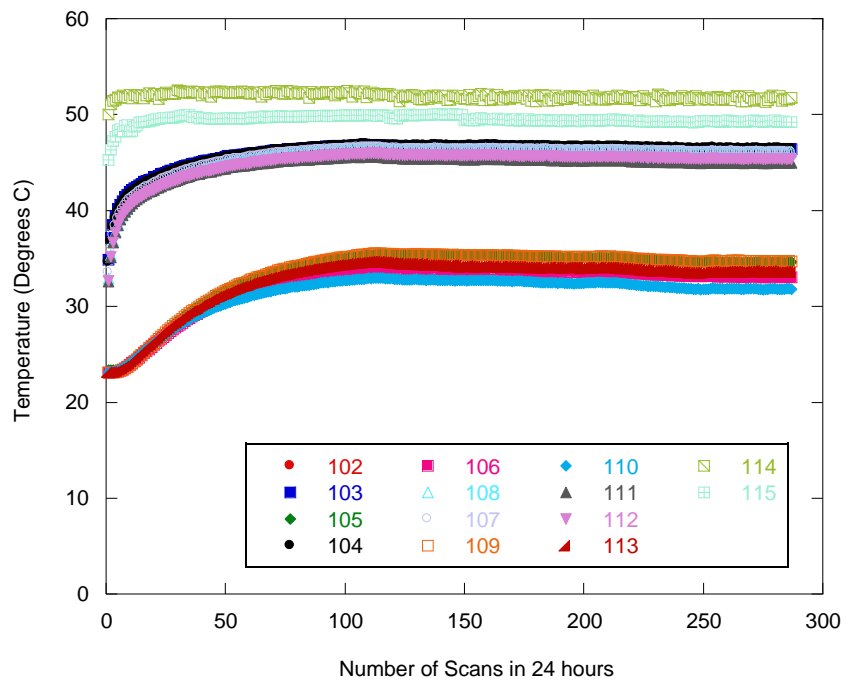


Figure A.6 Temperature data over a 24 hour period for heating cycle 2 (test conducted in 2010)

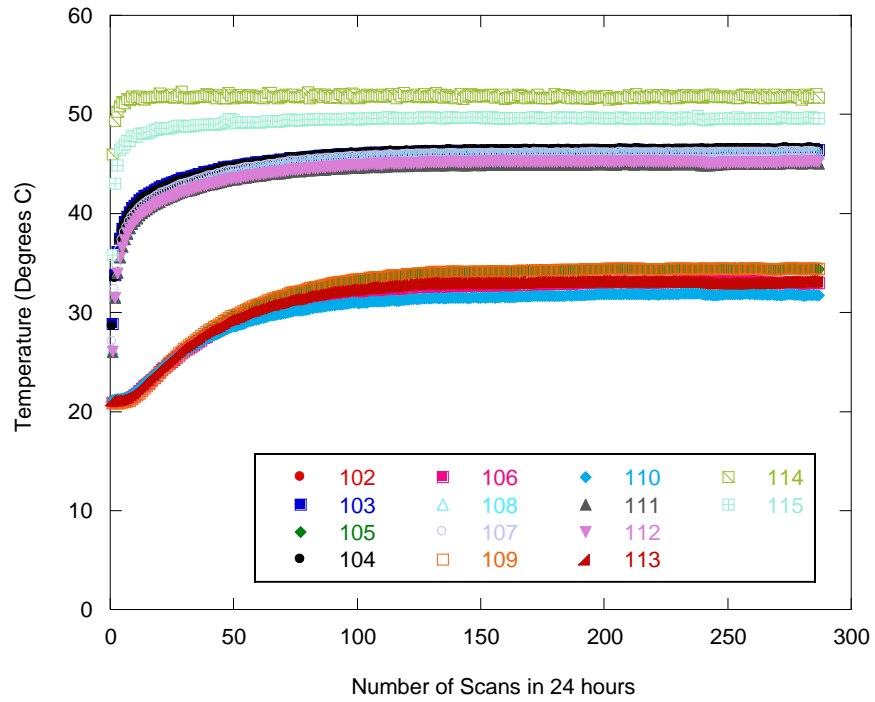


Figure A.7 Temperature data over a 24 hour period for heating cycle 3 (test conducted in 2010)

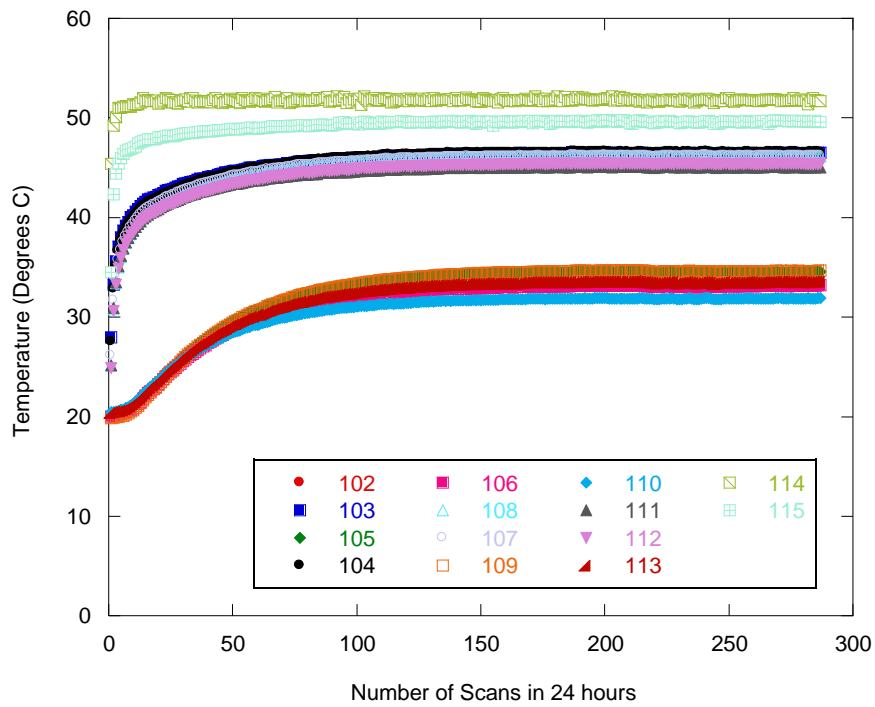


Figure A.8 Temperature data over a 24 hour period for heating cycle 4 (test conducted in 2010)

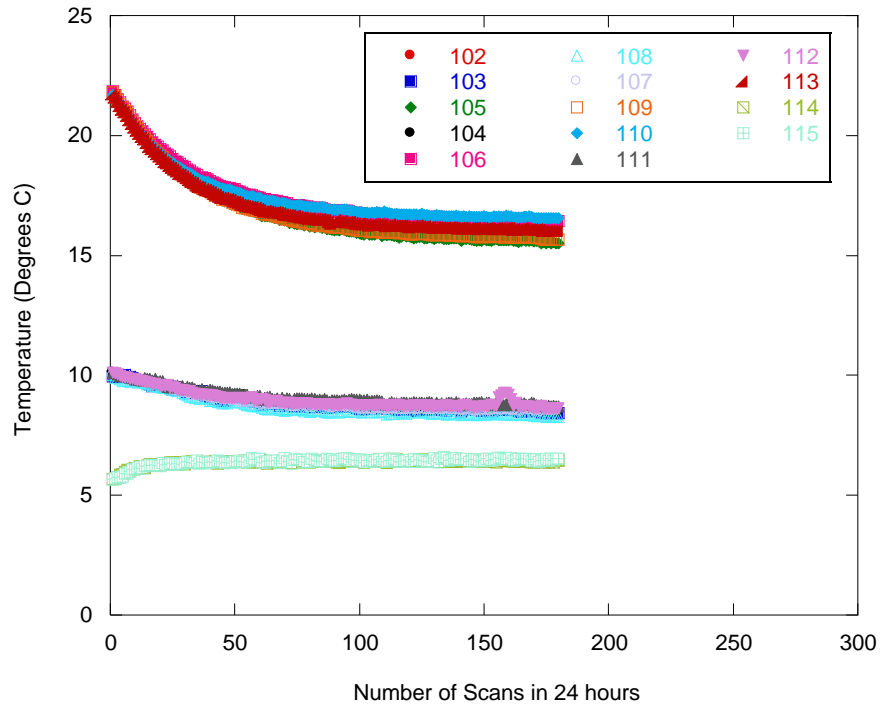


Figure A.9 Temperature data over a 24 hour period for cooling cycle 1 (test conducted in 2011)

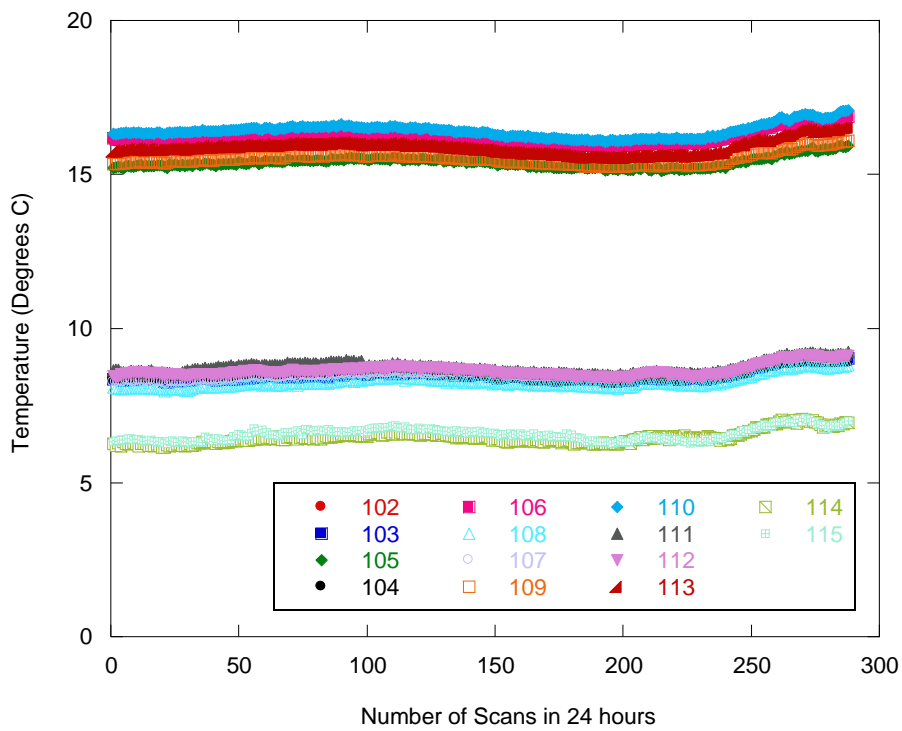


Figure A.10 Temperature data over a 24 hour period for cooling cycle 2 (test conducted in 2011)

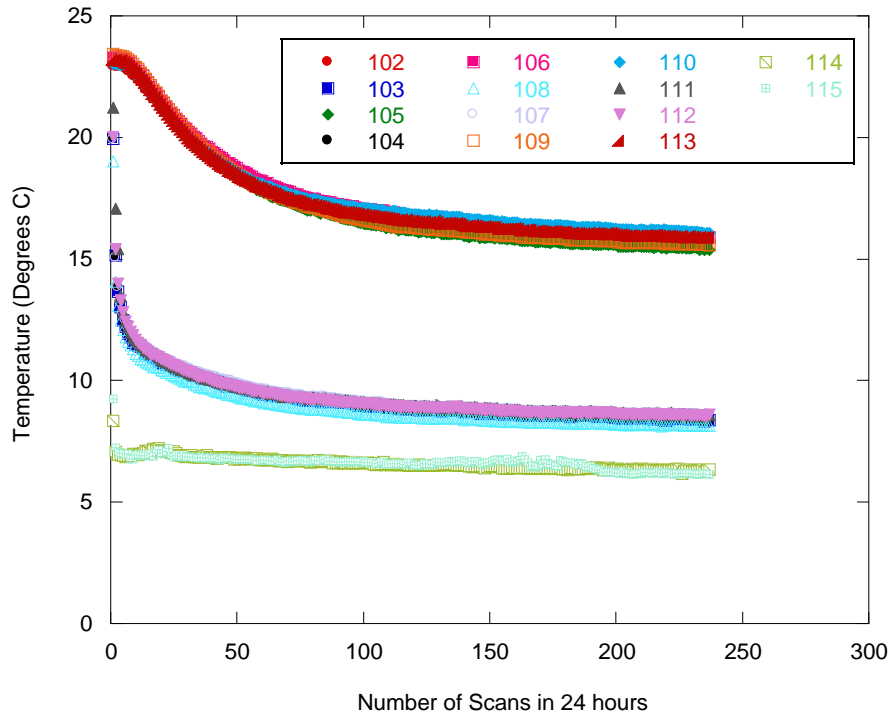


Figure A.11 Temperature data over a 24 hour period for cooling cycle 3 (test conducted in 2011)

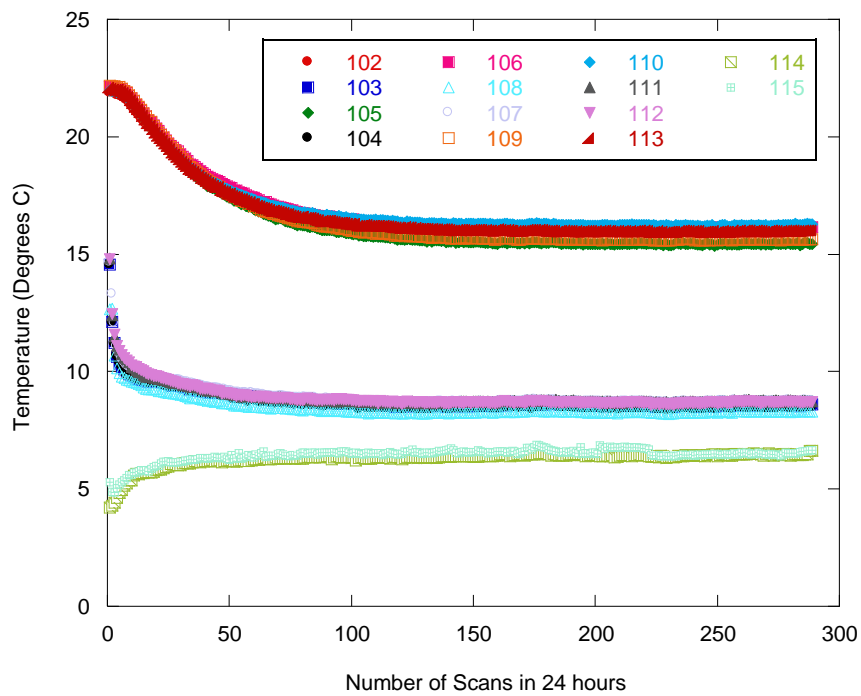


Figure A.12 Temperature data over a 24 hour period for cooling cycle 4 (test conducted in 2011)

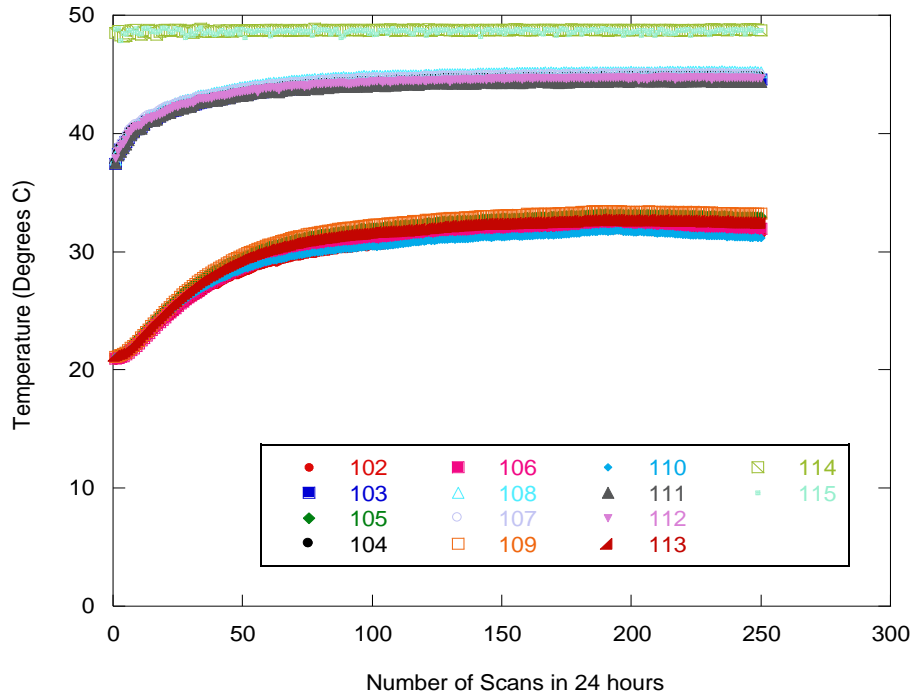


Figure A.13 Temperature data over a 24 hour period for heating cycle 1 (test conducted in 2011)

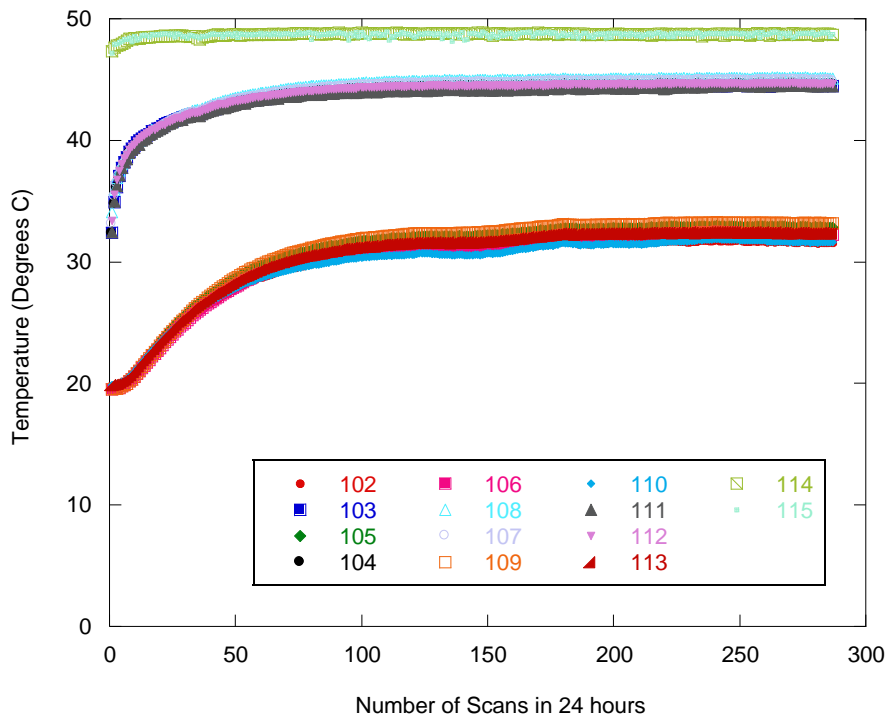


Figure A.14 Temperature data over a 24 hour period for heating cycle 2 (test conducted in 2011)

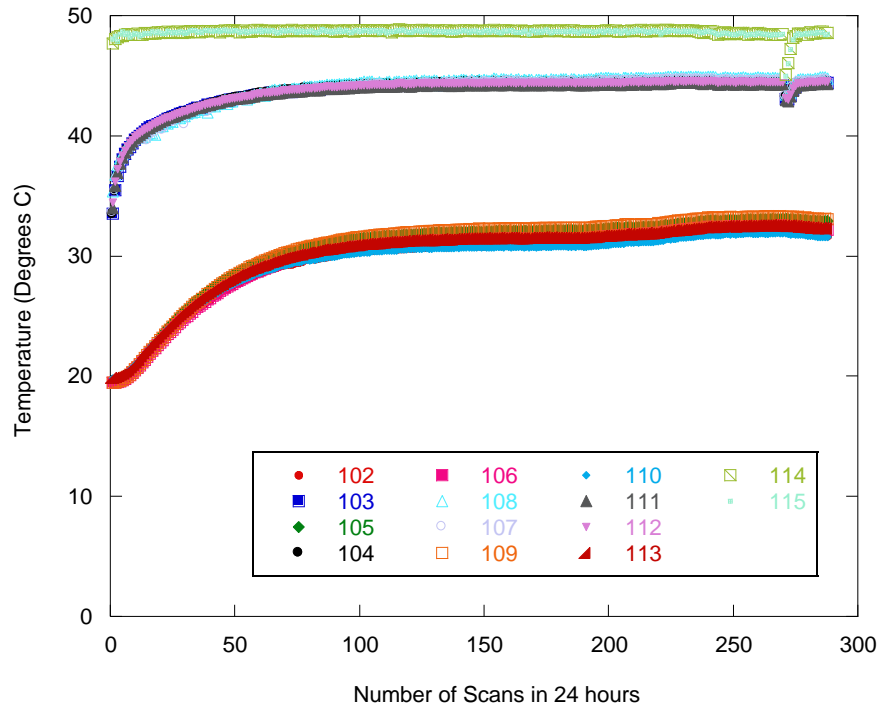


Figure A.15 Temperature data over a 24 hour period for heating cycle 3 (test conducted in 2011)

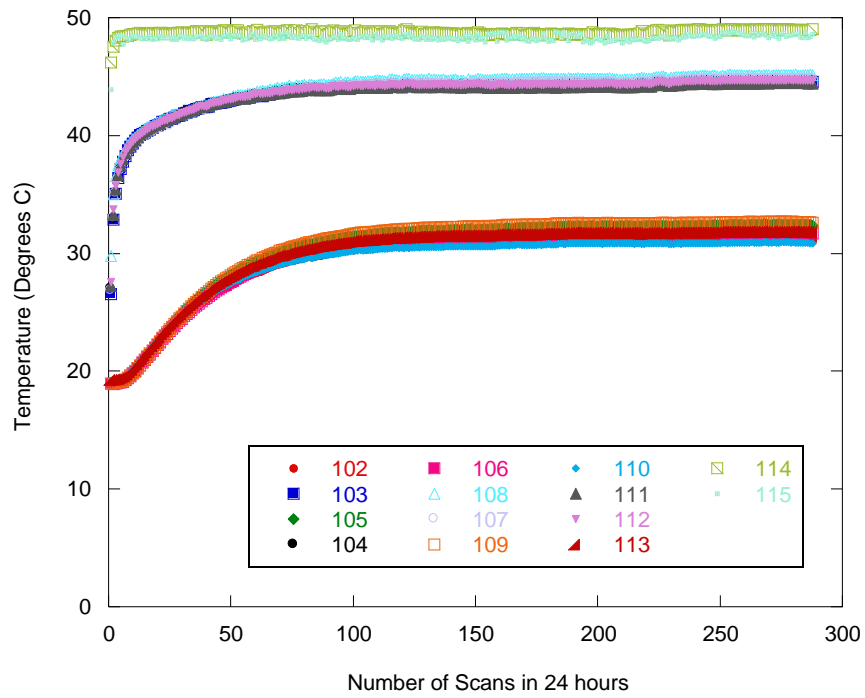


Figure A.16 Temperature data over a 24 hour period for heating cycle 4 (test conducted in 2011)

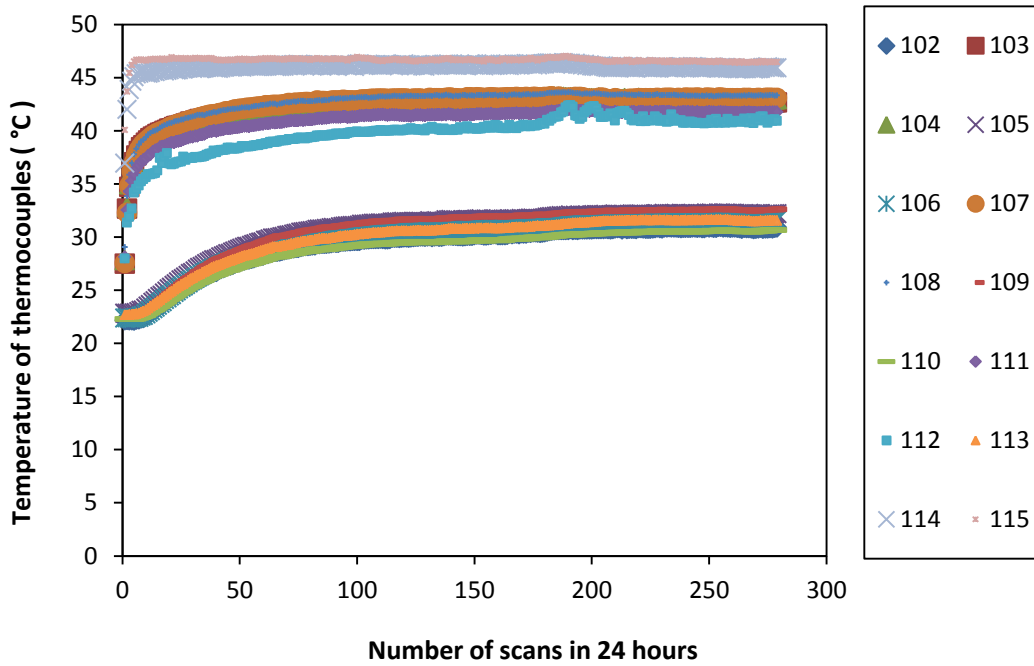


Figure A.17 Temperature data over a 24 hour period for heating cycle 1 (test conducted in 2012)

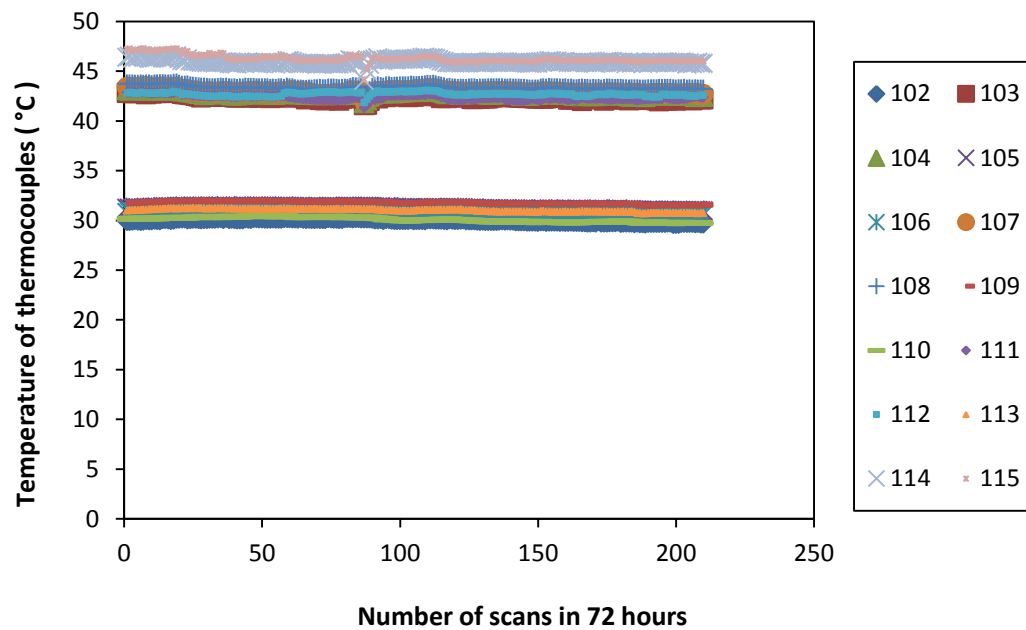


Figure A.18 Temperature data over a 24 hour period for heating cycle 2 (test conducted in 2012)

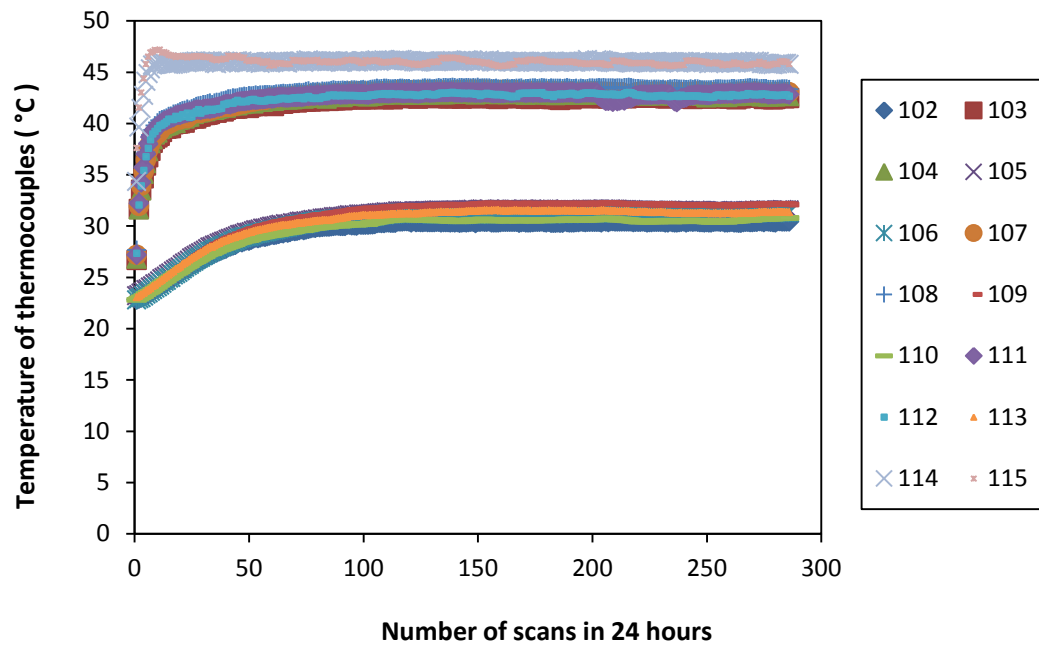


Figure A.19 Temperature data over a 24 hour period for heating cycle 3 (test conducted in 2012)

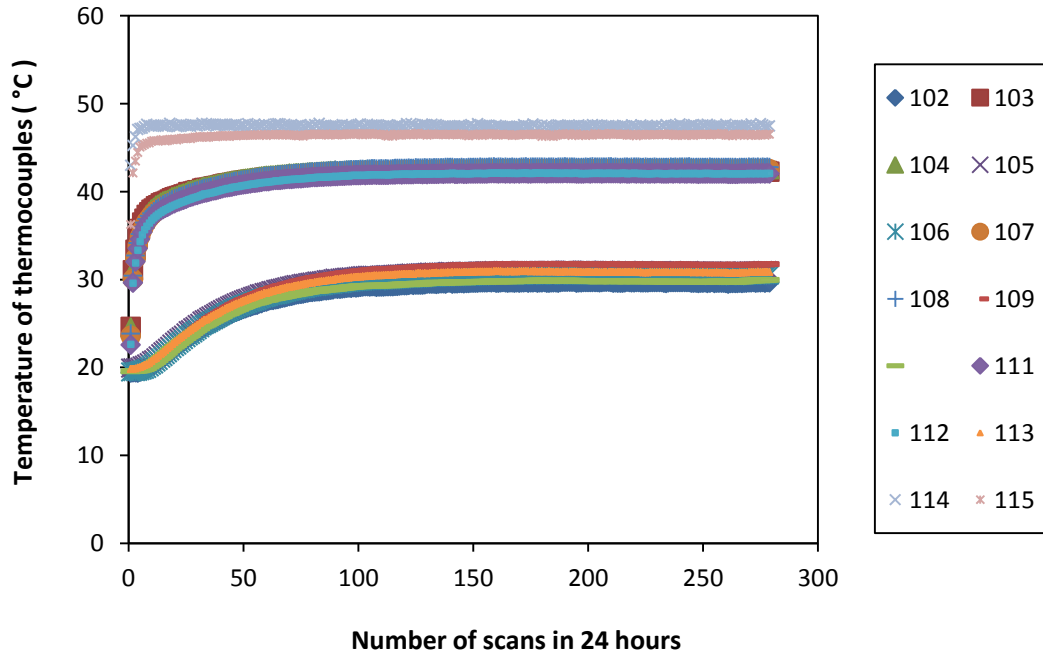


Figure A.20 Temperature data over a 24 hour period for heating cycle 4 (test conducted in 2012)

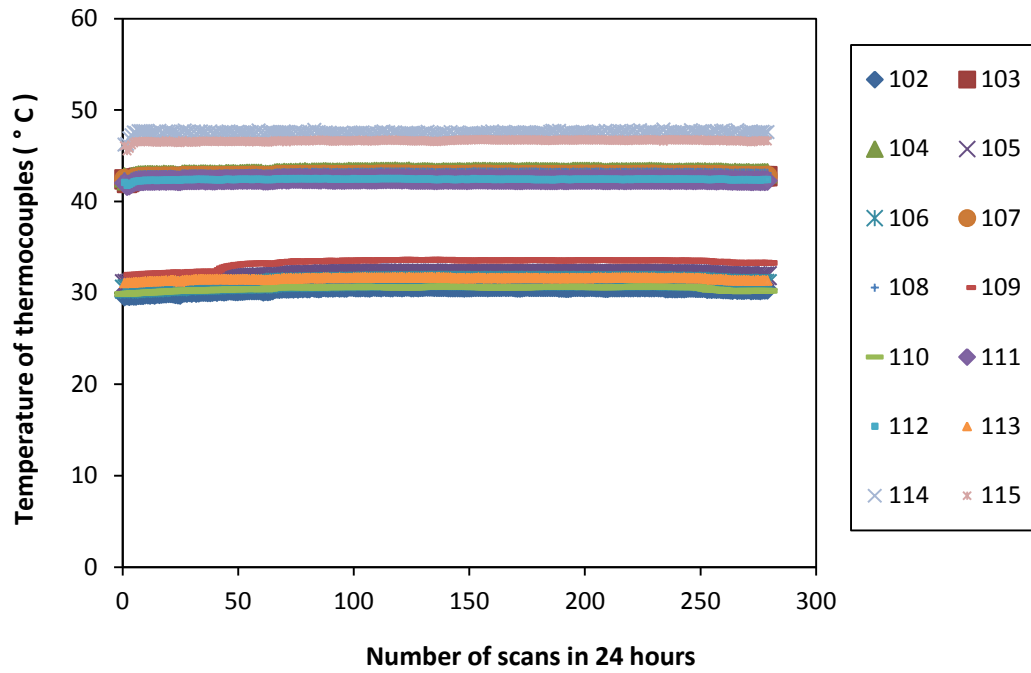


Figure A.21 Temperature data over a 24 hour period for heating cycle 5 (test conducted in 2012)

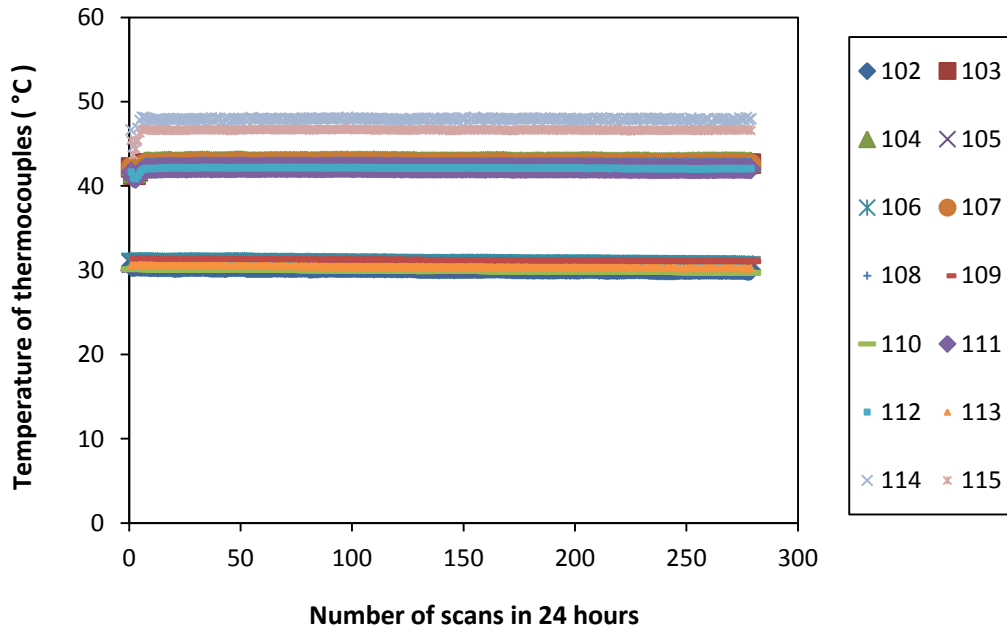


Figure A.22 Temperature data over a 24 hour period for heating cycle 6 (test conducted in 2012)

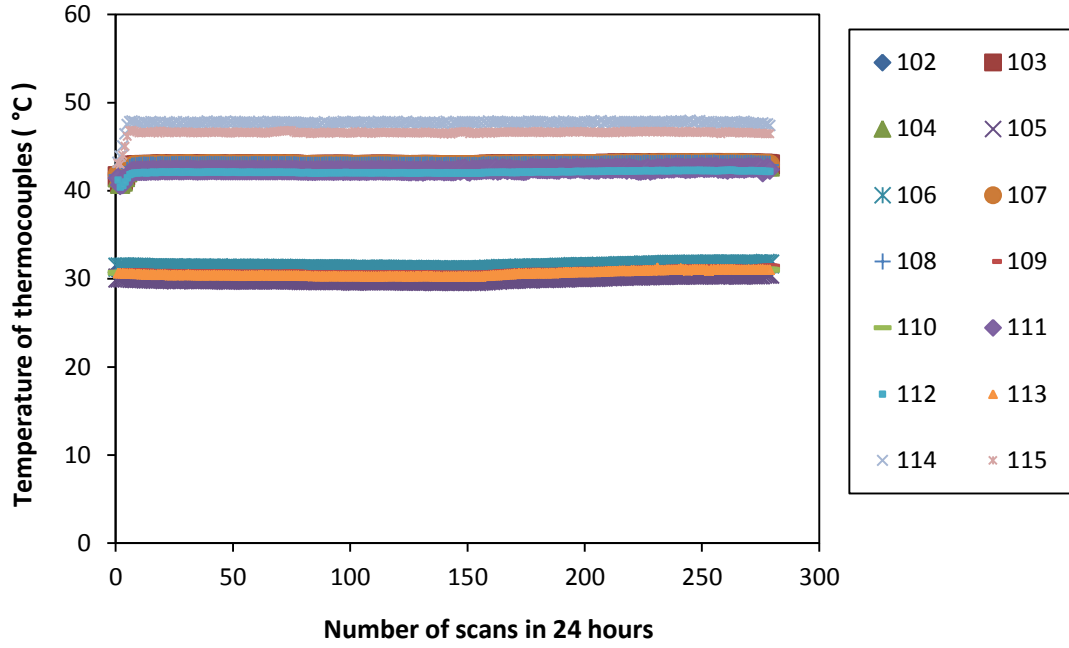


Figure A.23 Temperature data over a 24 hour period for heating cycle 7 (test conducted in 2012)

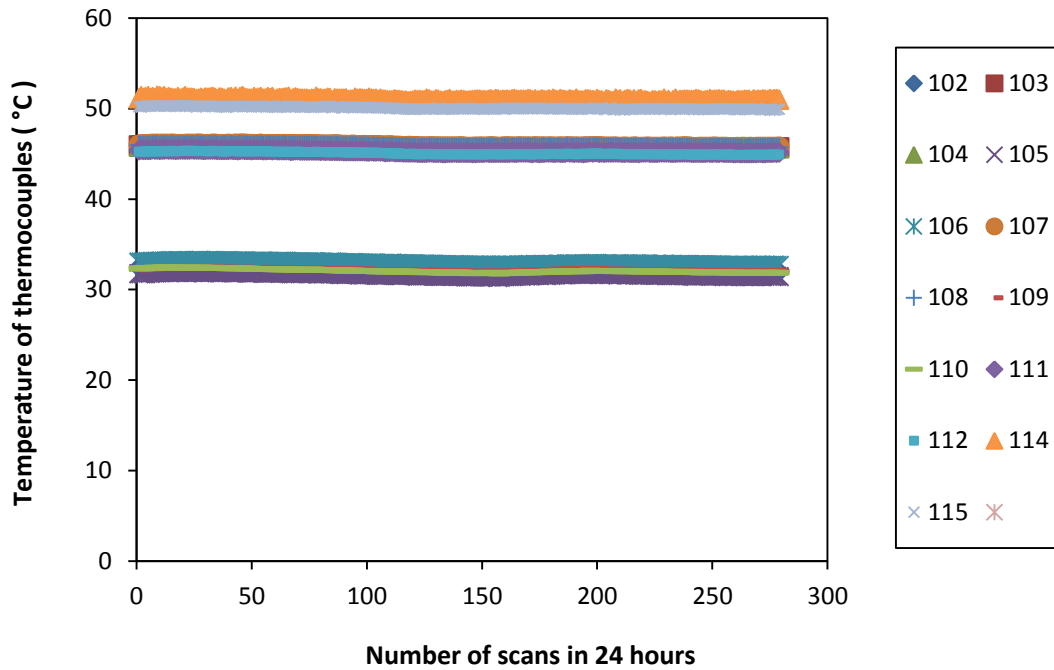


Figure A.24 Temperature data over a 24 hour period for heating cycle 8 (test conducted in 2012)

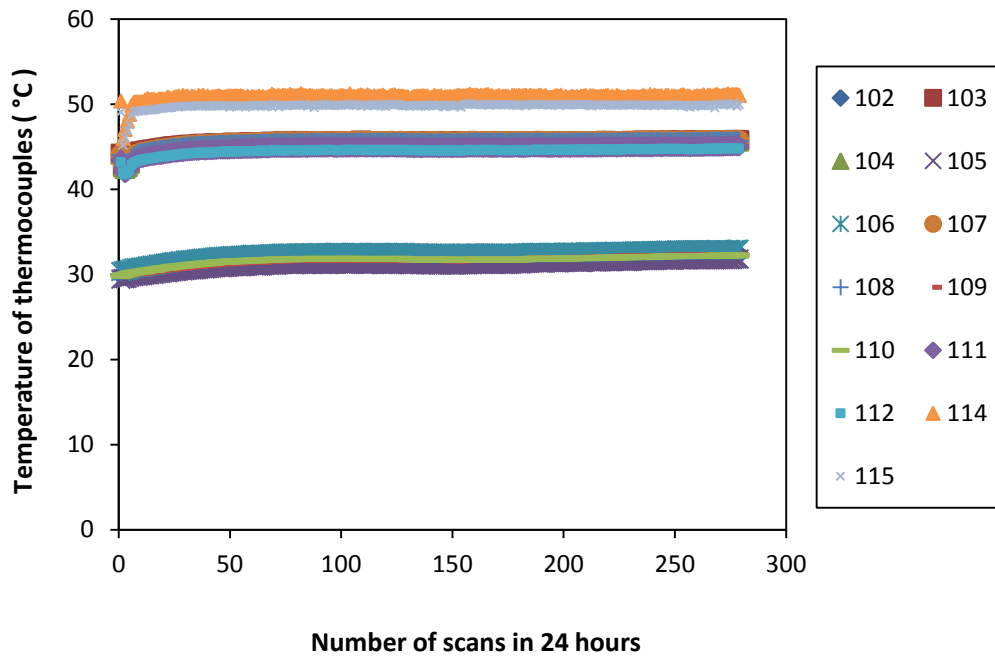


Figure A.25 Temperature data over a 24 hour period for heating cycle 9 (test conducted in 2012)

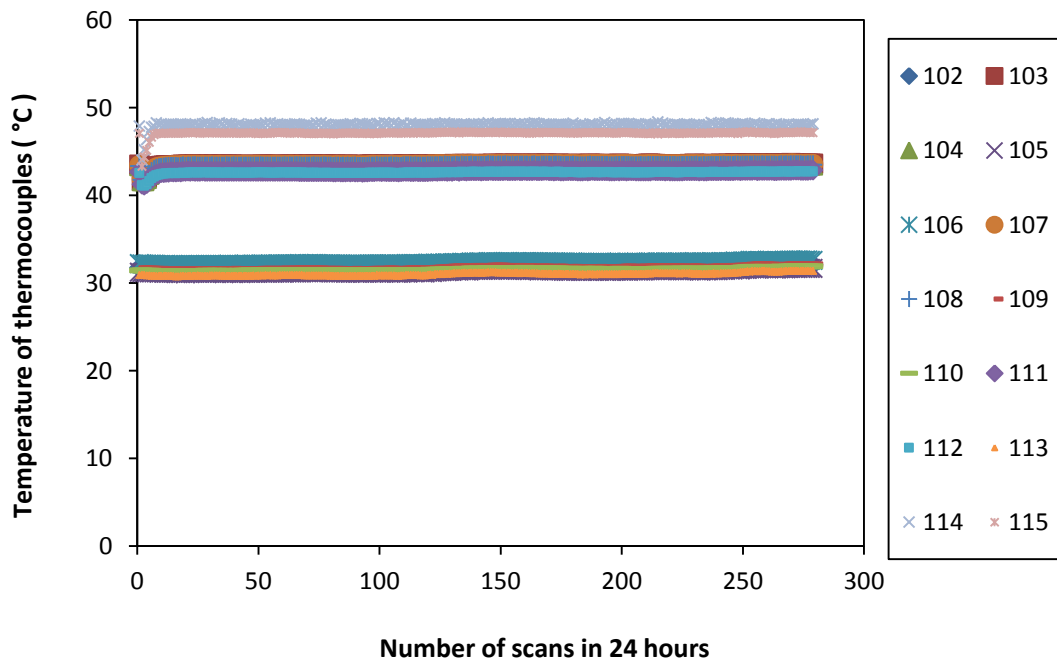


Figure A.26 Temperature data over a 24 hour period for heating cycle 10 (test conducted in 2012)

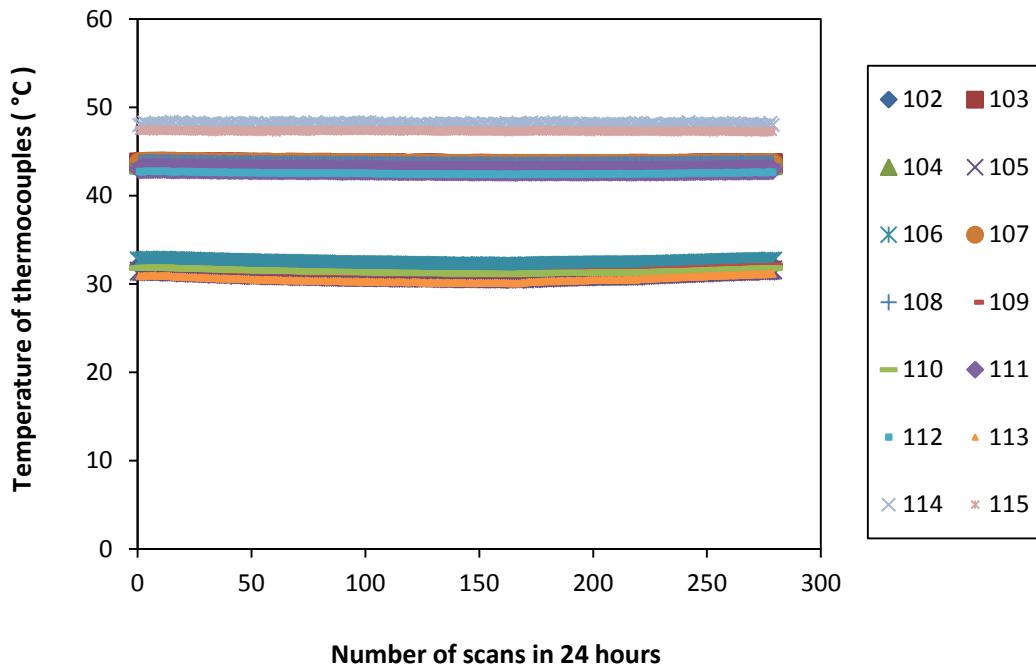


Figure A.27 Temperature data over a 24 hour period for heating cycle 11 (test conducted in 2012)

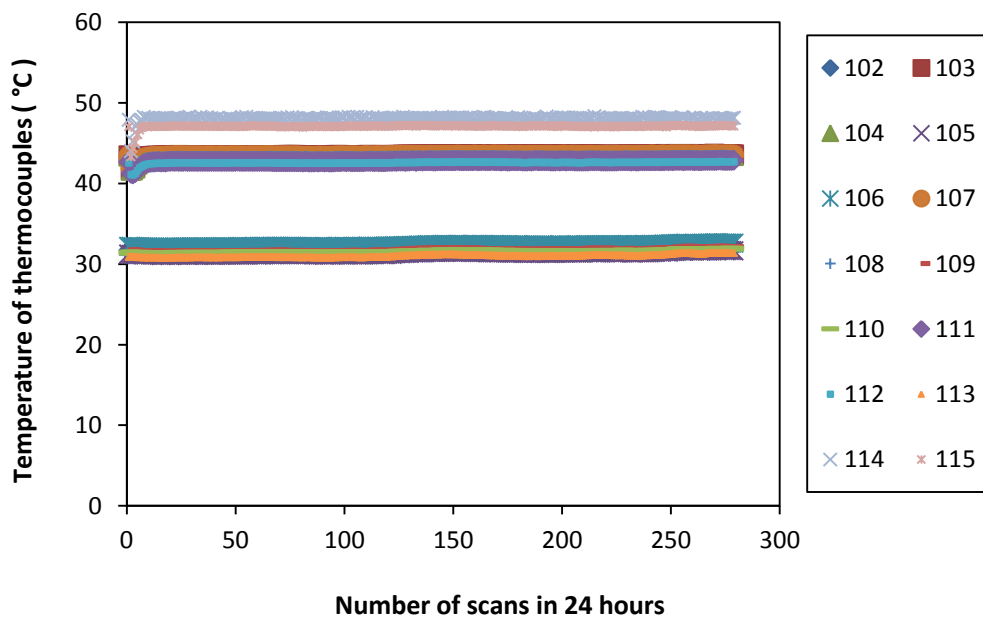


Figure A.28 Temperature data over a 24 hour period for heating cycle 12 (test conducted in 2012)

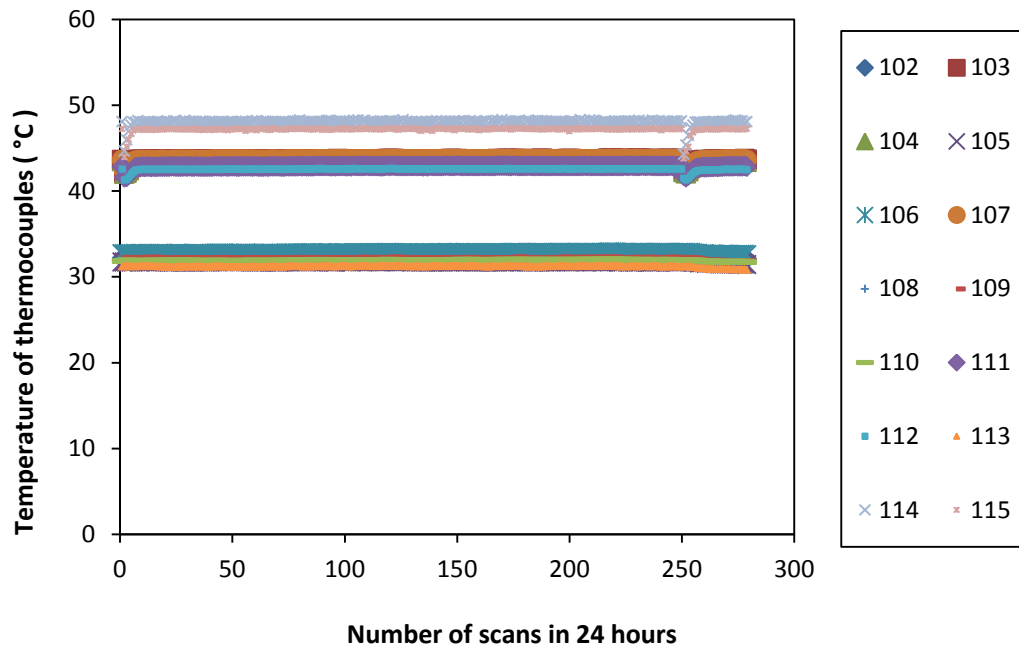


Figure A.29 Temperature data over a 24 hour period for heating cycle 13 (test conducted in 2012)

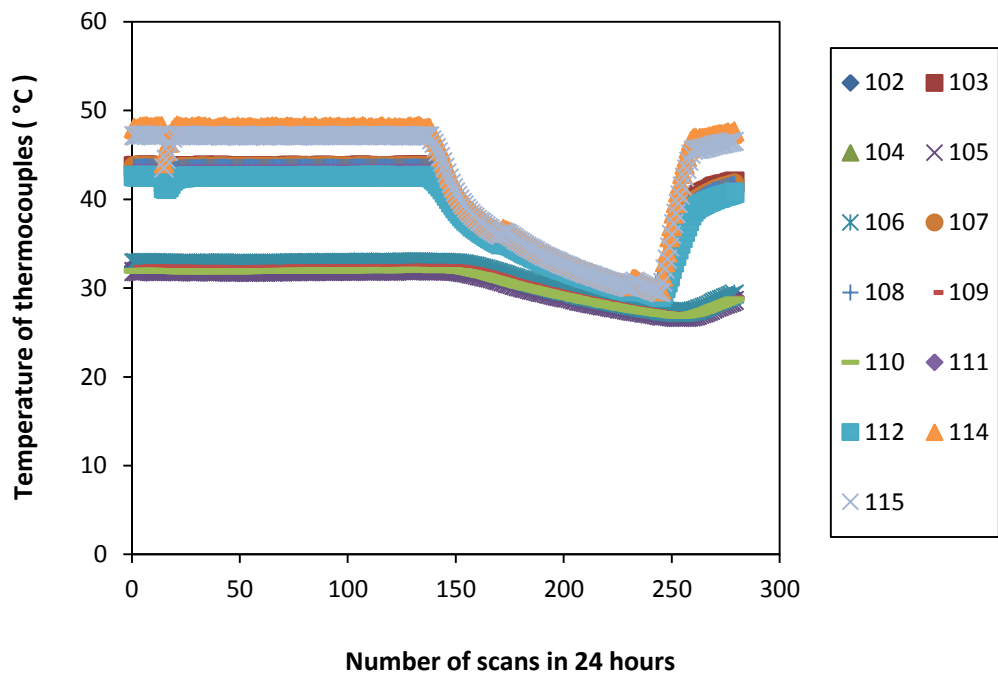


Figure A.30 Temperature data over a 24 hour period for heating cycle 14 (test conducted in 2012)

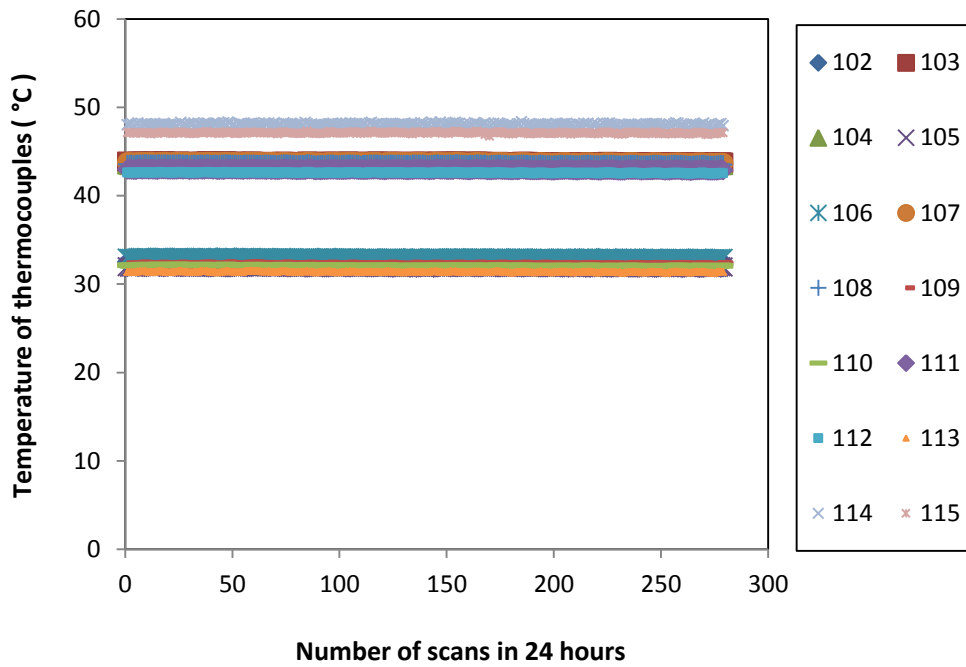


Figure A.31 Temperature data over a 24 hour period for heating cycle 15 (test conducted in 2012)

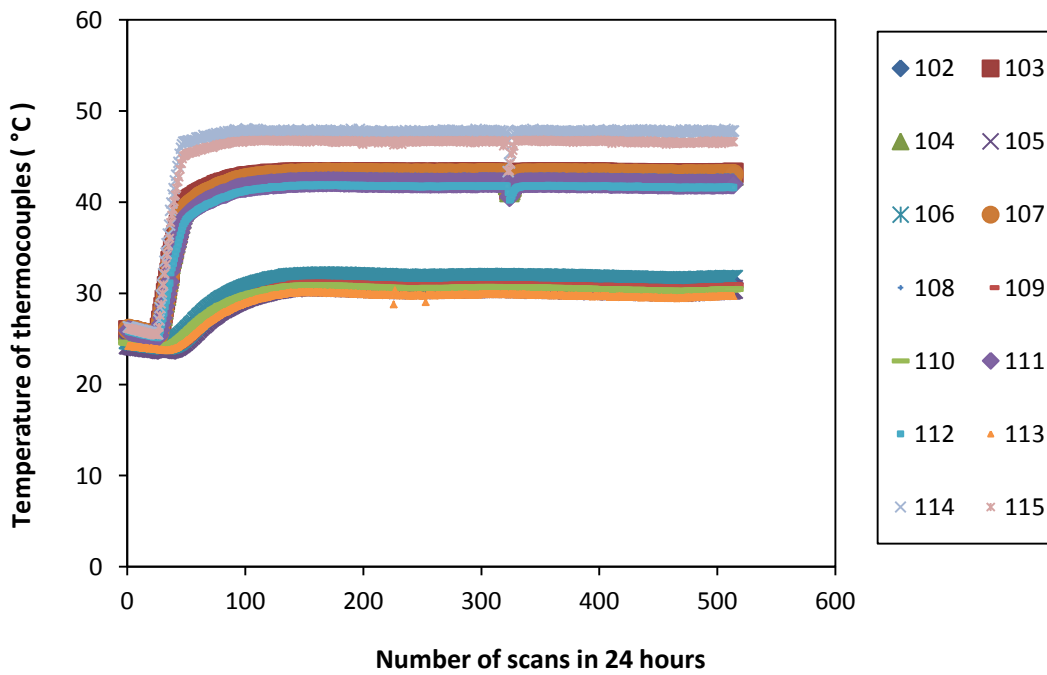


Figure A.32 Temperature data over a 24 hour period for heating cycle 16 (test conducted in 2012)

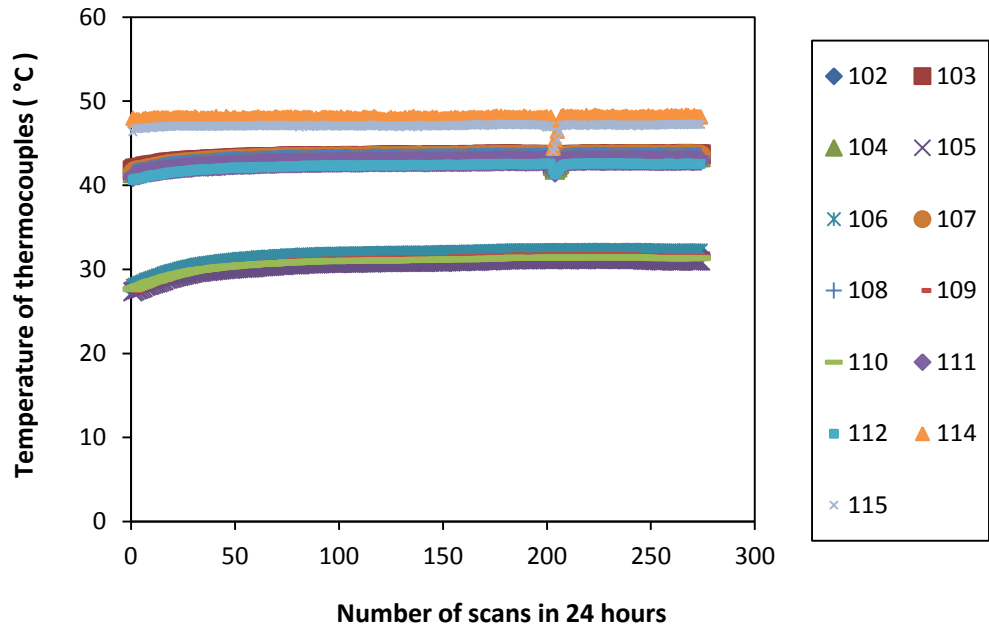


Figure A.33 Temperature data over a 24 hour period for heating cycle 17 (test conducted in 2012)

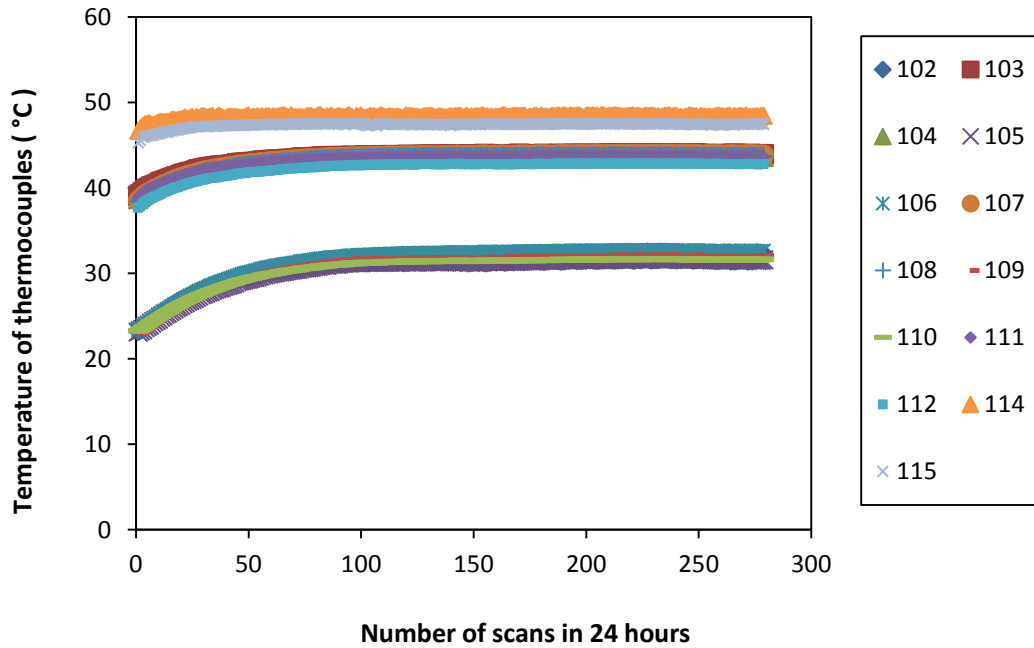


Figure A.33 Temperature data over a 24 hour period for heating cycle 17 (test conducted in 2012)

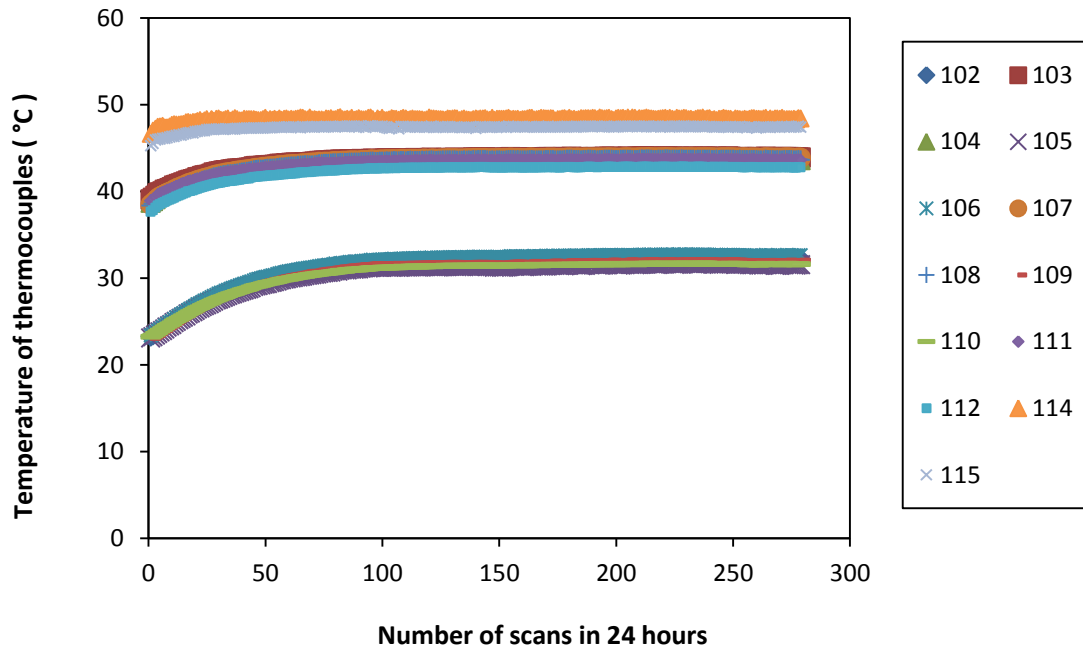


Figure A.34 Temperature data over a 24 hour period for heating cycle 18 (test conducted in 2012)

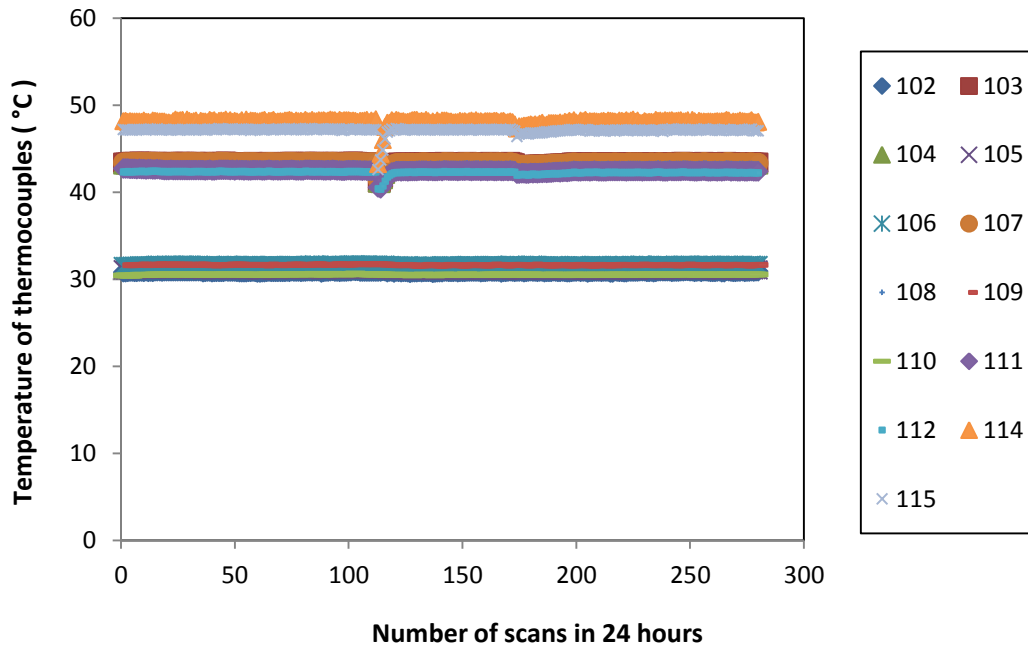


Figure A.35 Temperature data over a 24 hour period for heating cycle 19 (test conducted in 2012)

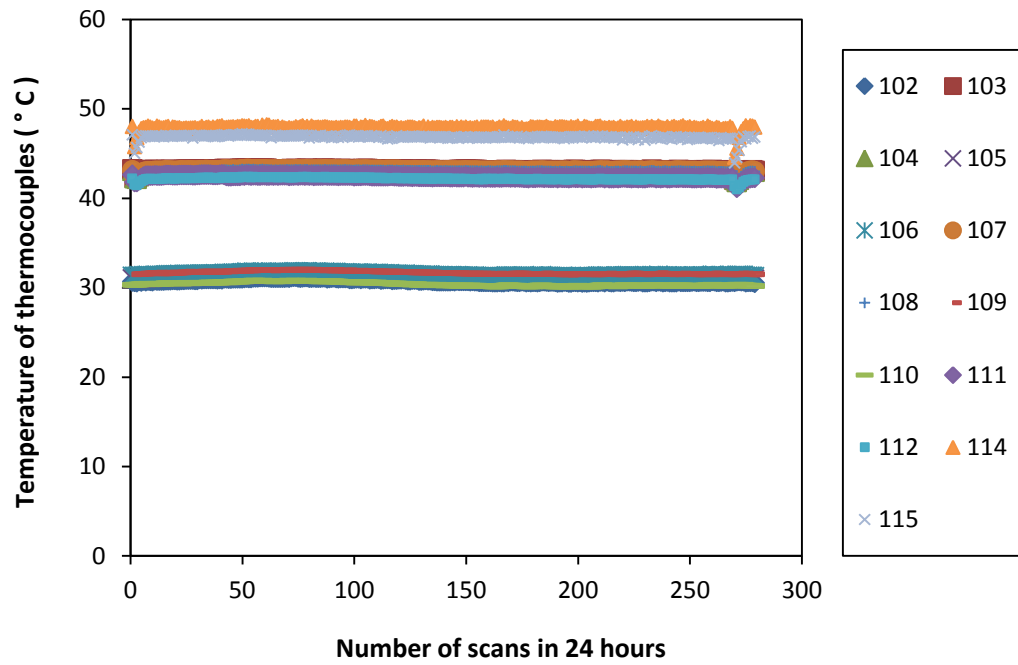


Figure A.36 Temperature data over a 24 hour period for heating cycle 20 (test conducted in 2012)

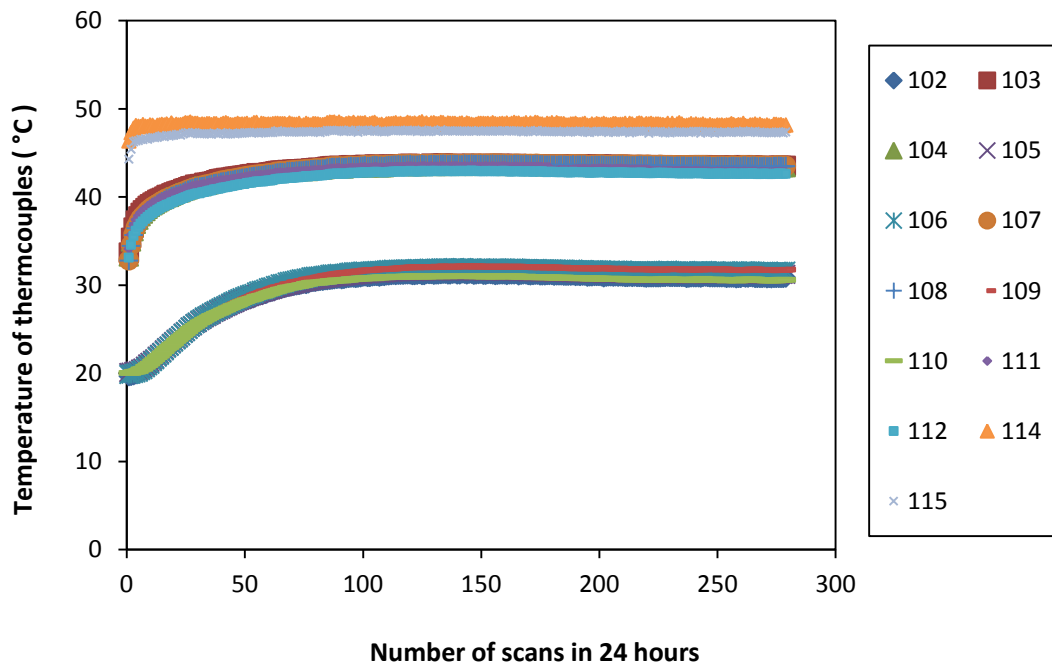


Figure A.37 Temperature data over a 24 hour period for heating cycle 21 (test conducted in 2012)

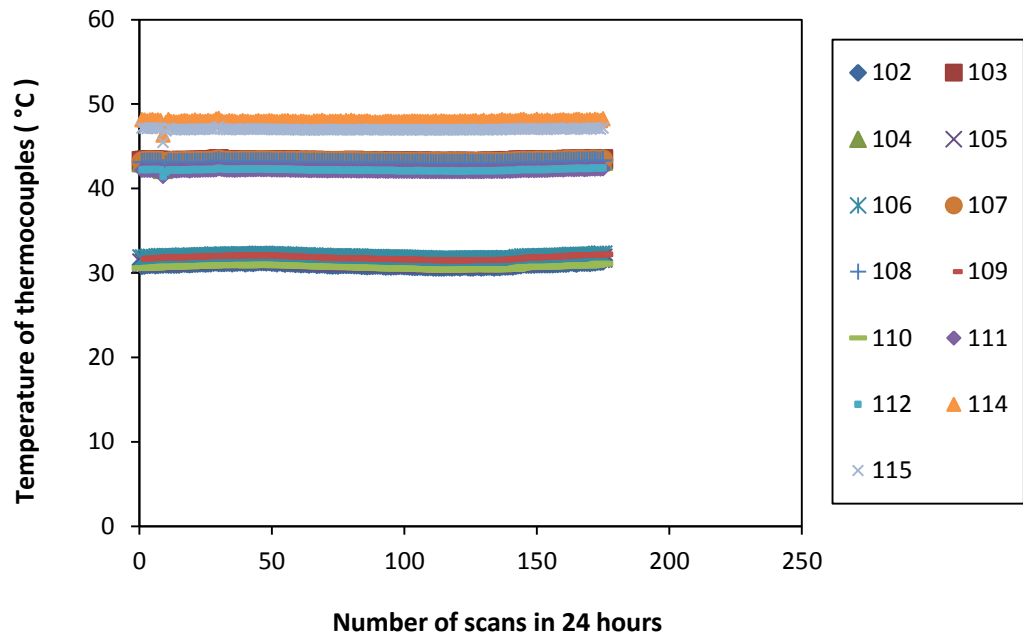


Figure A.38 Temperature data over a 24 hour period for heating cycle 22 (test conducted in 2012)

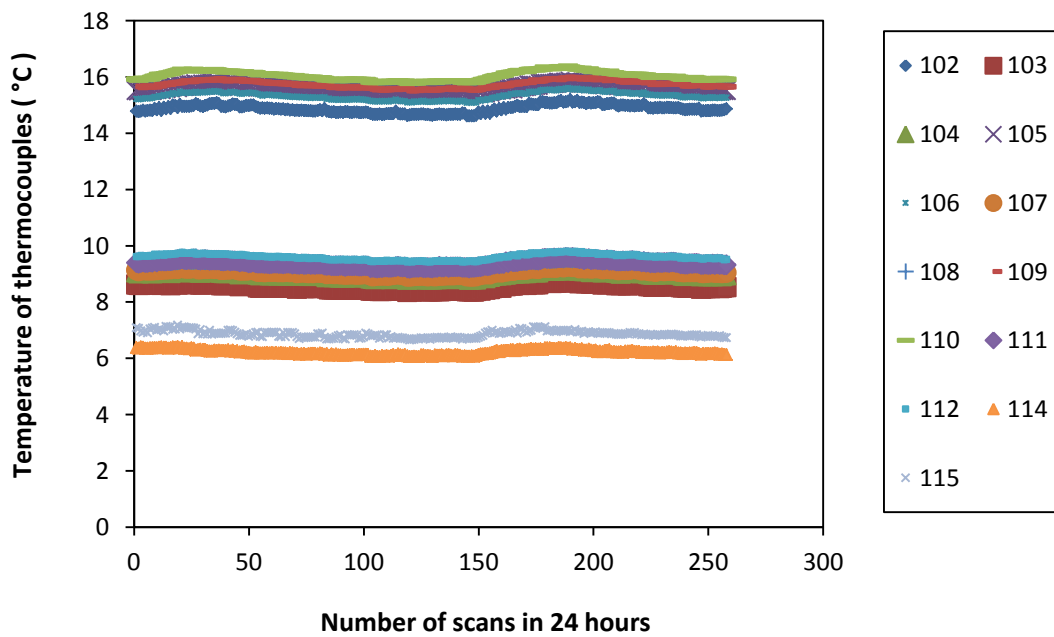


Figure A.39 Temperature data over a 24 hour period for heating cycle 23 (test conducted in 2012)

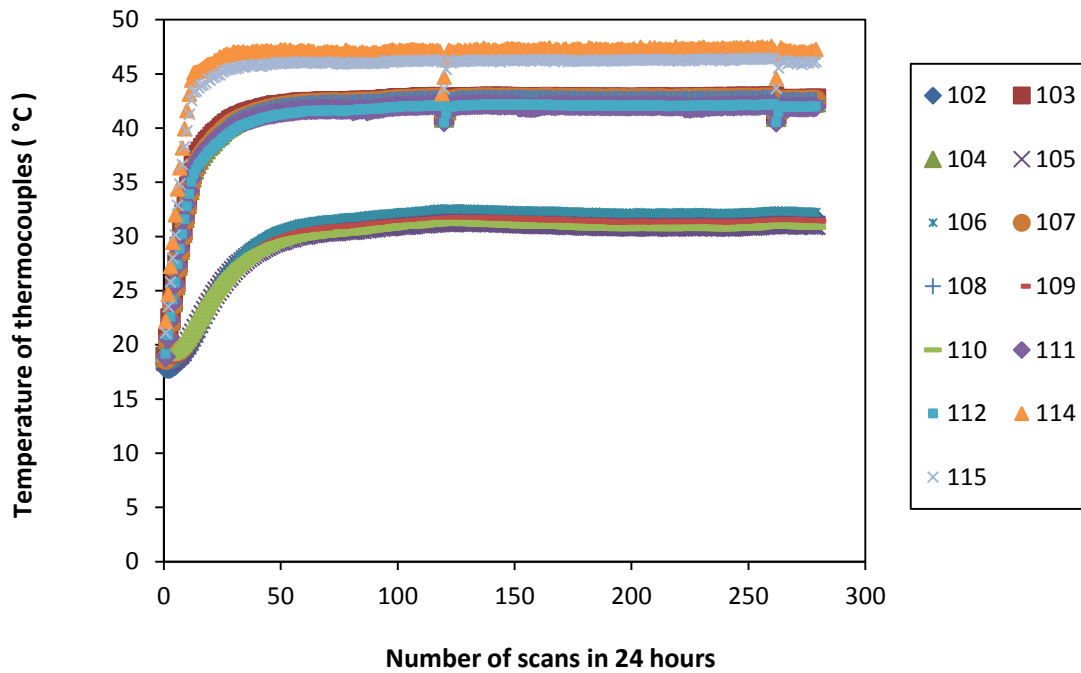


Figure A.40 Temperature data over a 24 hour period for heating cycle 24 (test conducted in 2012)

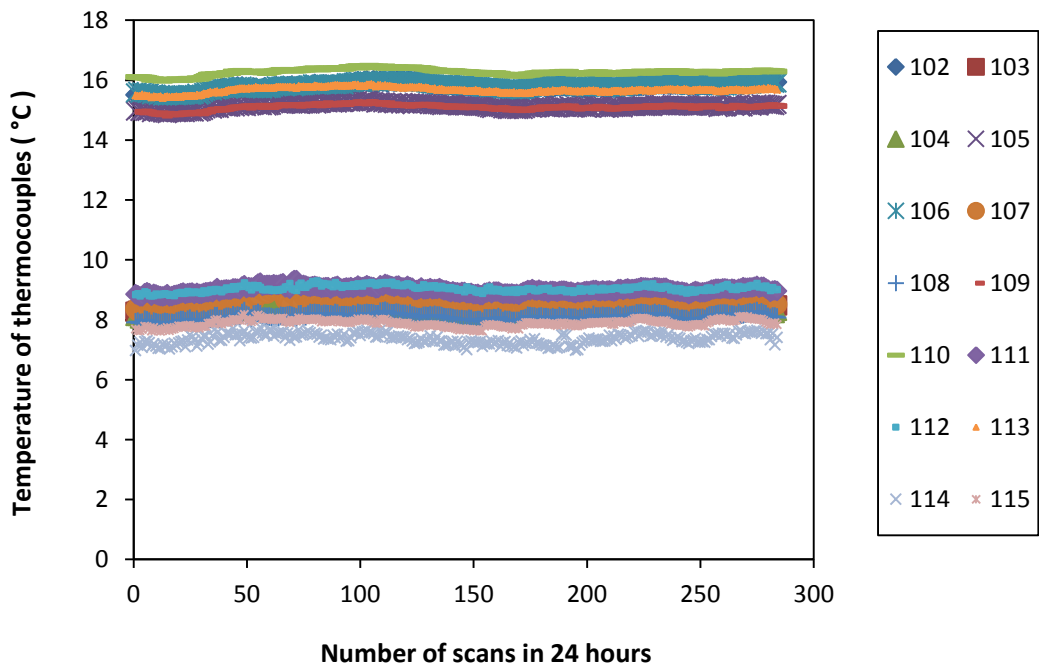


Figure A.41 Temperature data over a 24 hour period for cooling cycle 1 (test conducted in 2012)

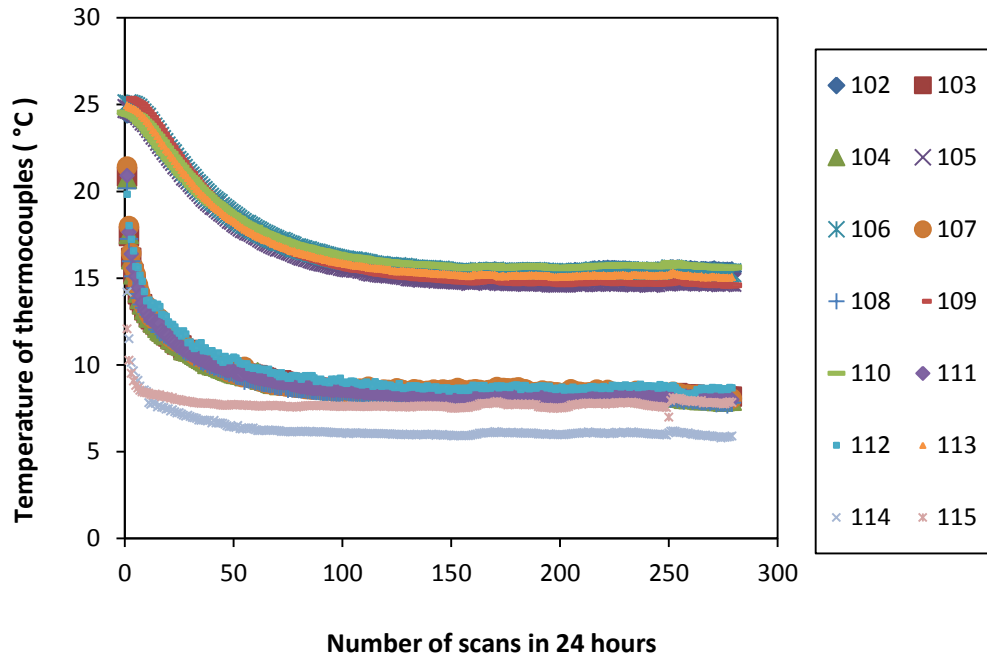


Figure A.41 Temperature data over a 24 hour period for cooling cycle 2 (test conducted in 2012)

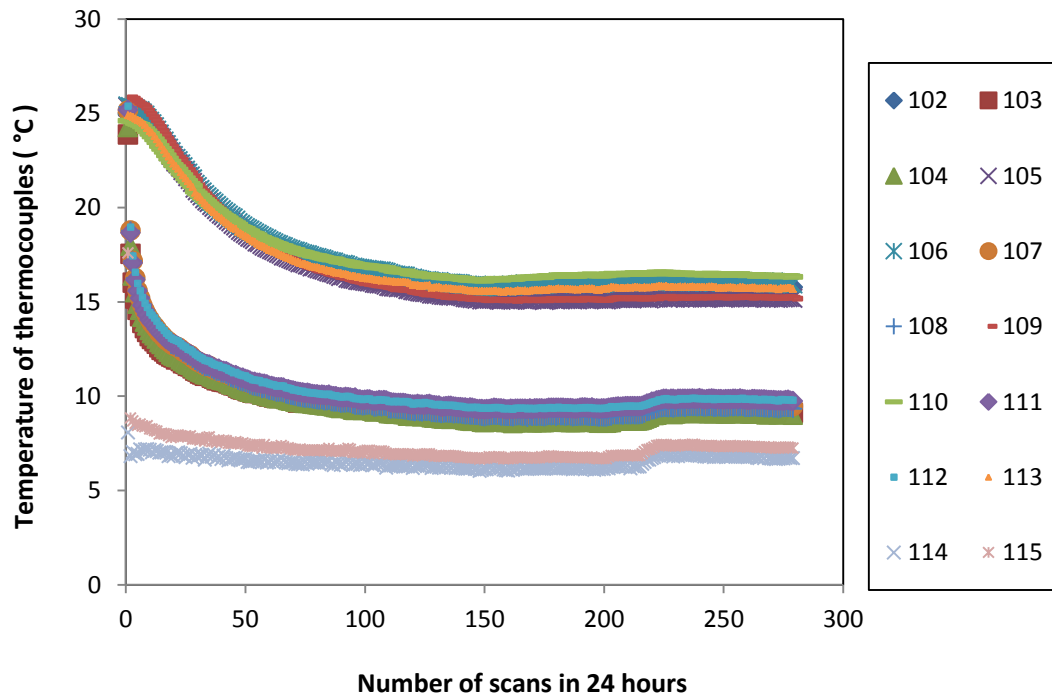


Figure A.42 Temperature data over a 24 hour period for cooling cycle 3 (test conducted in 2012)

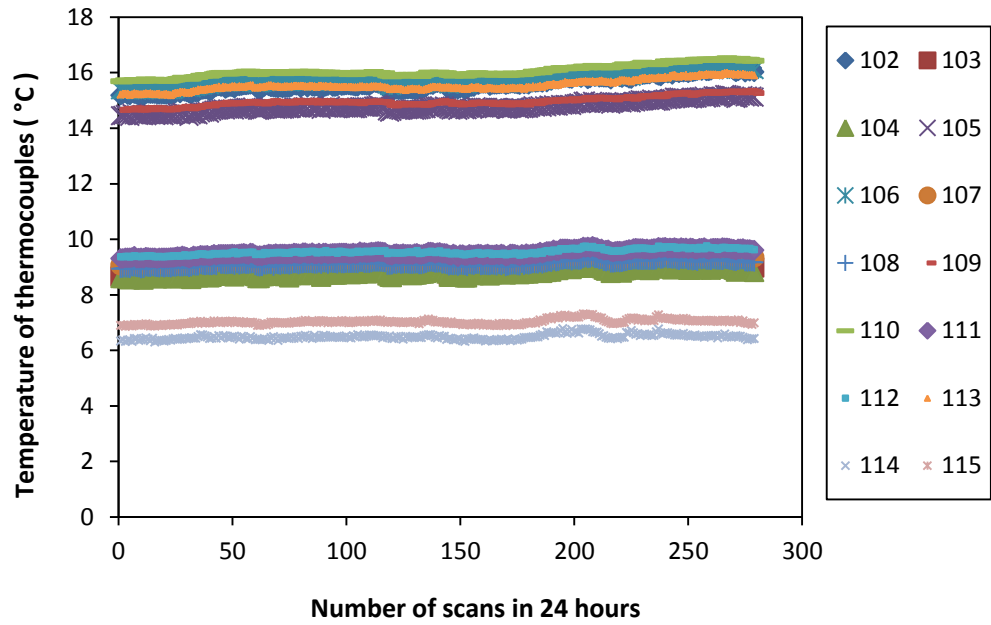


Figure A.43 Temperature data over a 24 hour period for cooling cycle 4 (test conducted in 2012)

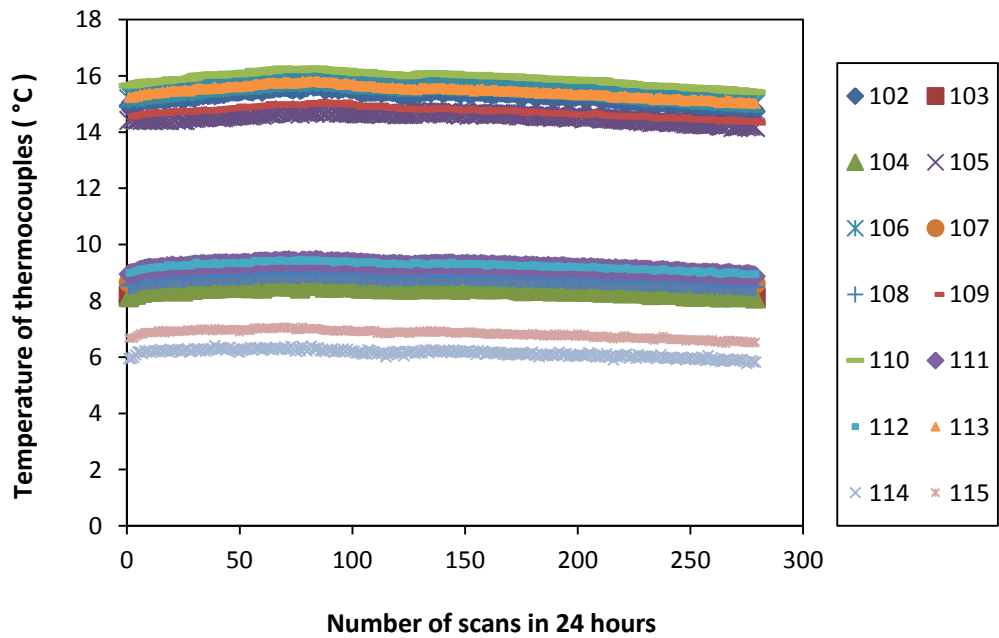


Figure A.44 Temperature data over a 24 hour period for cooling cycle 5 (test conducted in 2012)

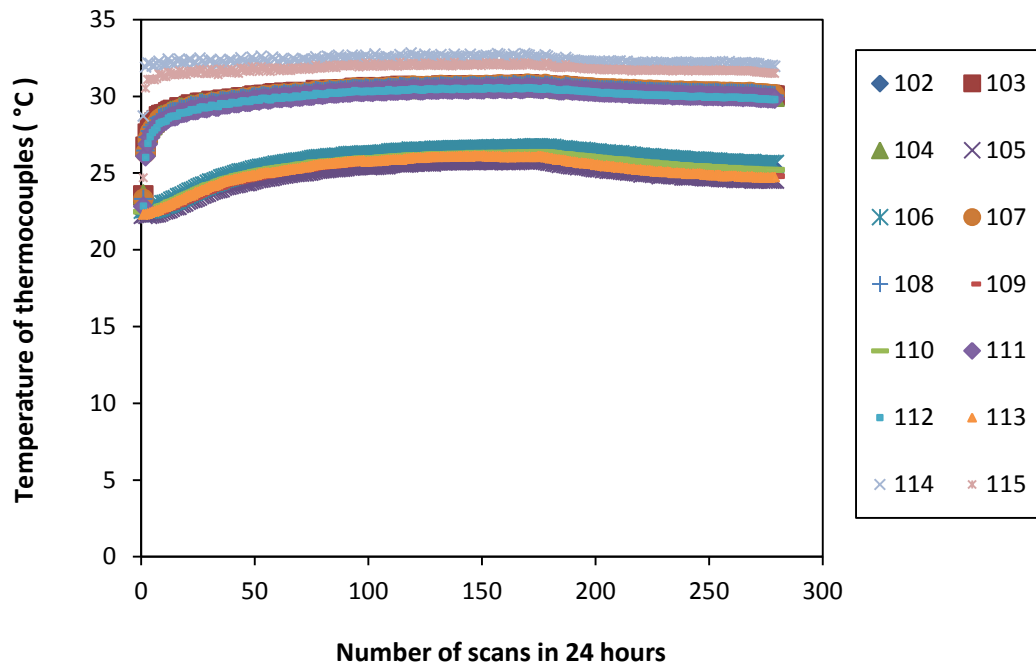


Figure A.45 Temperature data over a 24 hour period for cooling cycle 6 (test conducted in 2012)

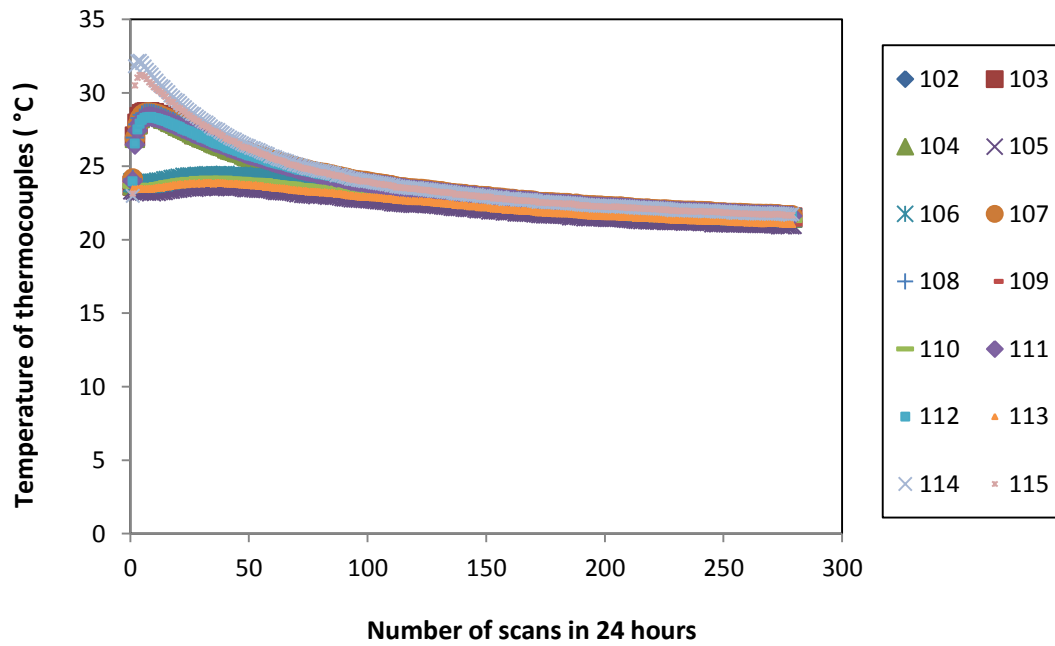


Figure A.46 Temperature data over a 24 hour period for cooling cycle 7 (test conducted in 2012)

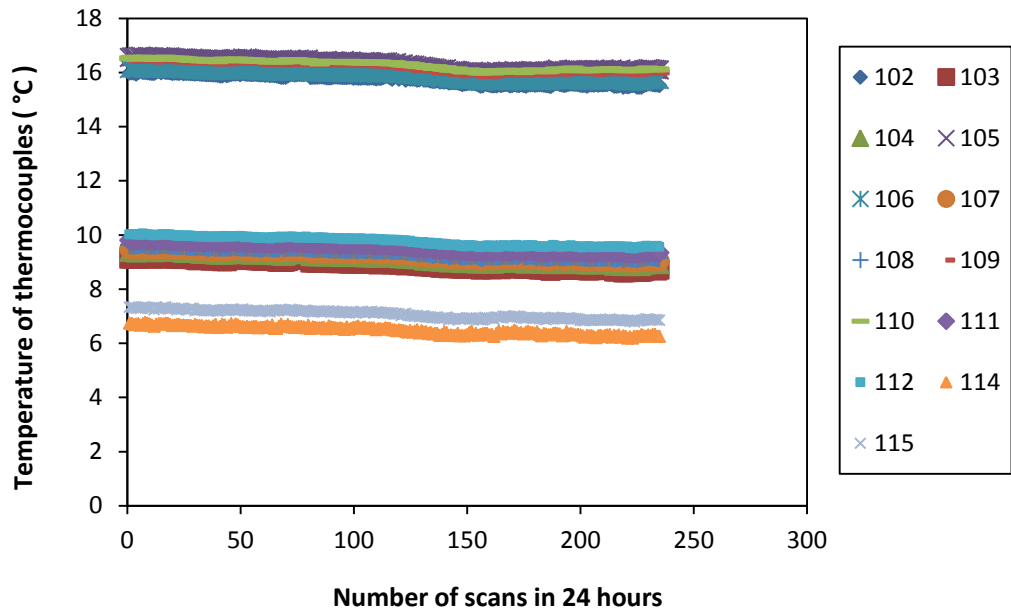


Figure A.47 Temperature data over a 24 hour period for cooling cycle 8 (test conducted in 2012)

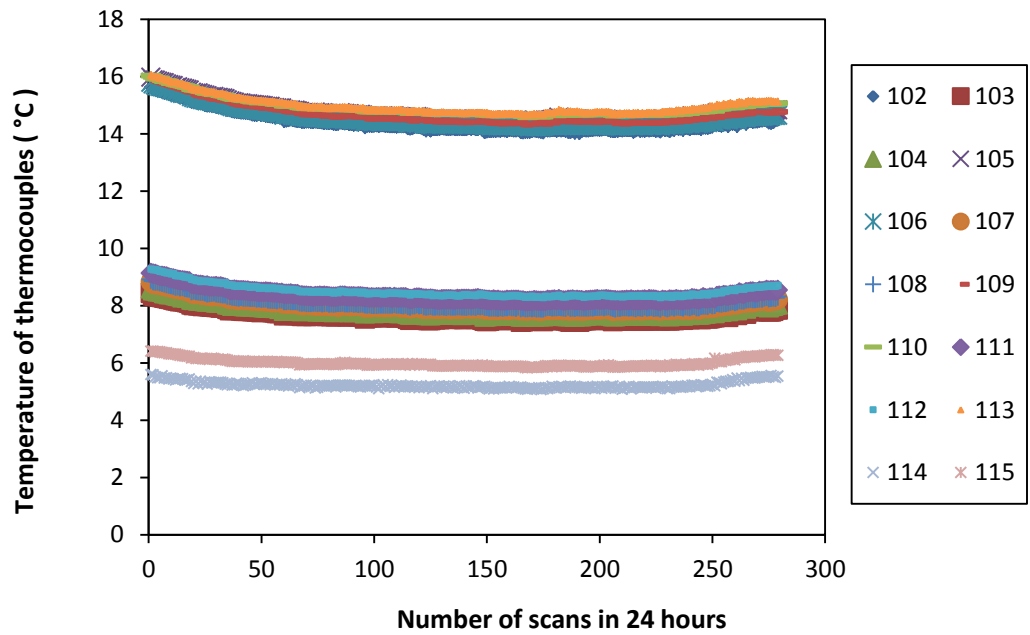


Figure A.48 Temperature data over a 24 hour period for cooling cycle 9 (test conducted in 2012)

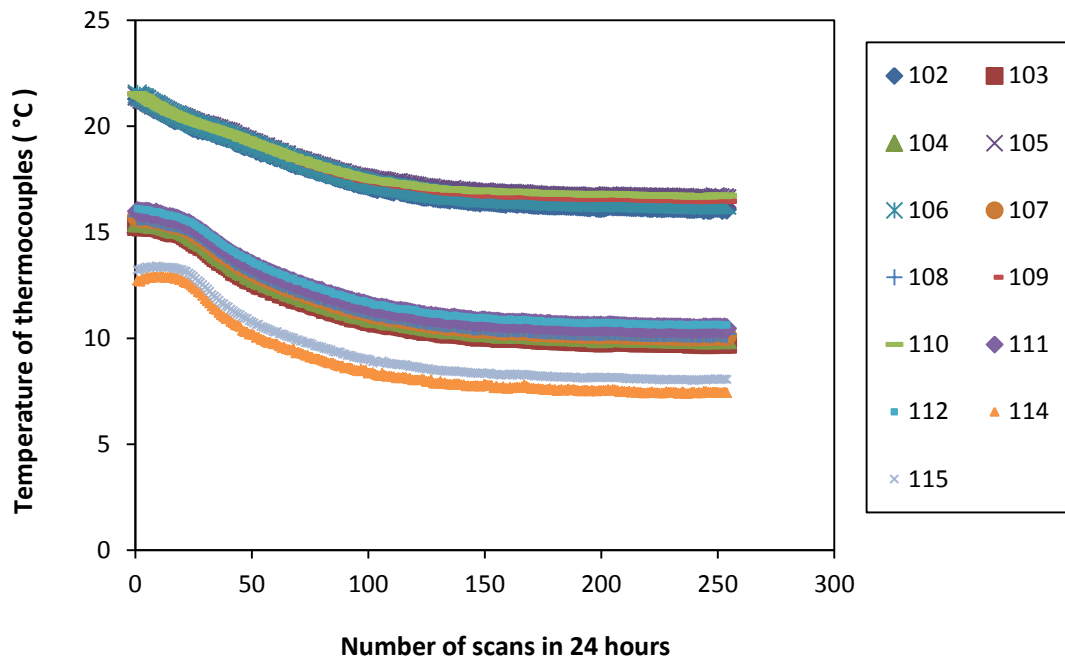


Figure A.49 Temperature data over a 24 hour period for cooling cycle 10 (test conducted in 2012)

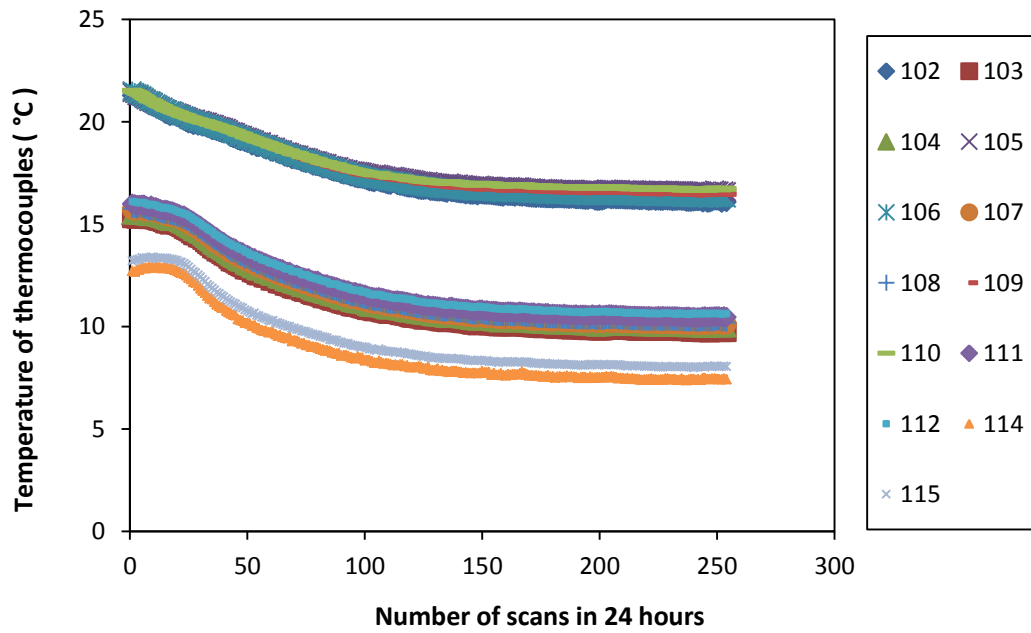


Figure A.50 Temperature data over a 24 hour period for cooling cycle 11 (test conducted in 2012)

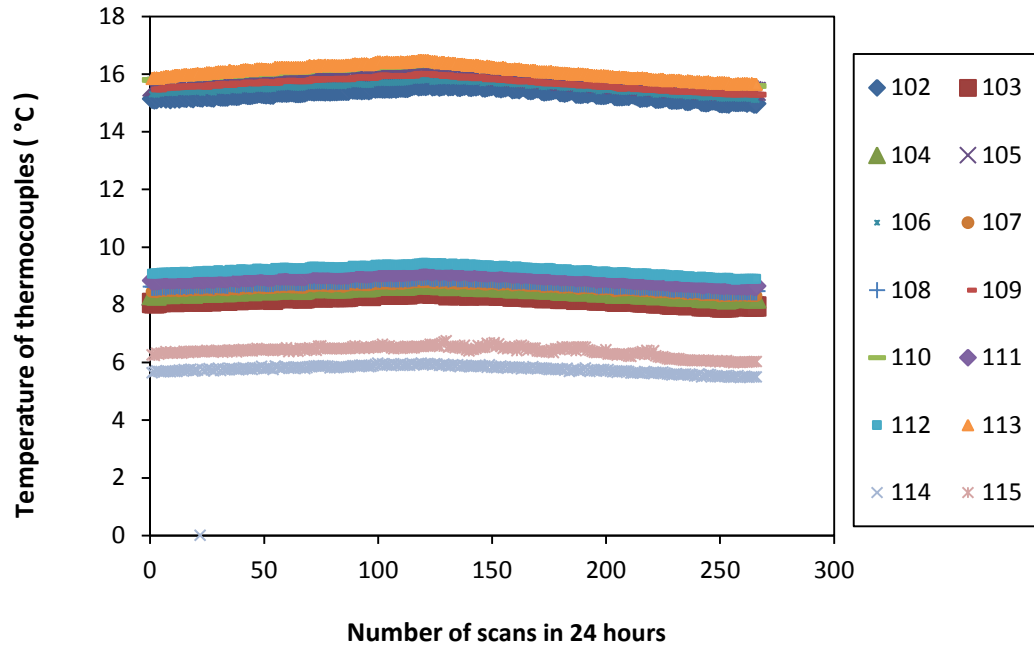


Figure A.51 Temperature data over a 24 hour period for cooling cycle 12 (test conducted in 2012)

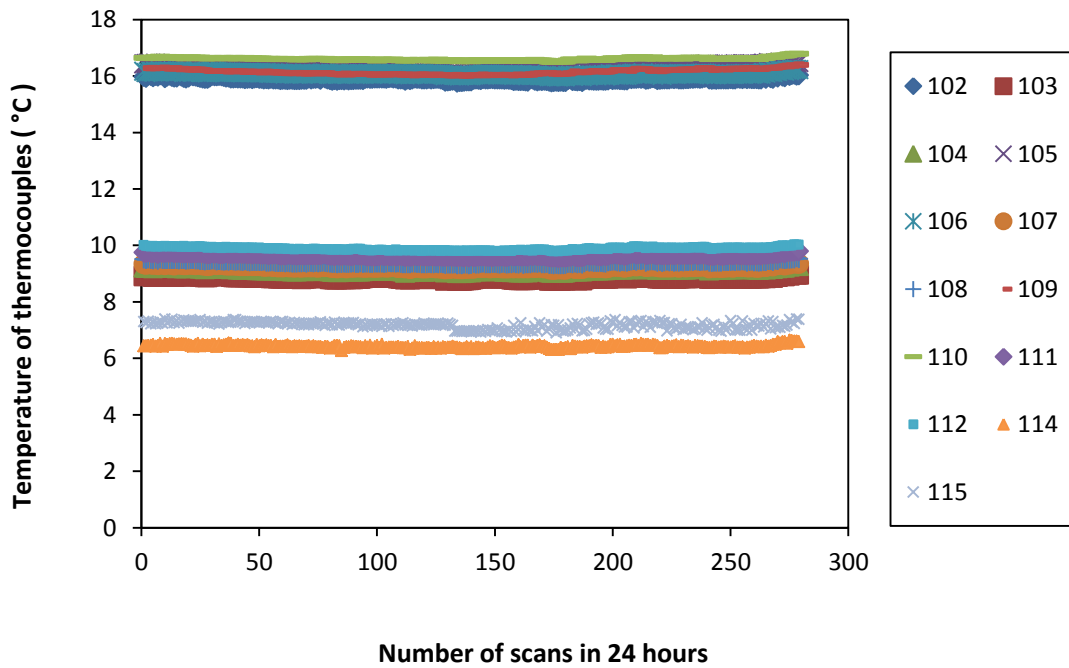


Figure A.52 Temperature data over a 24 hour period for cooling cycle 13 (test conducted in 2012)

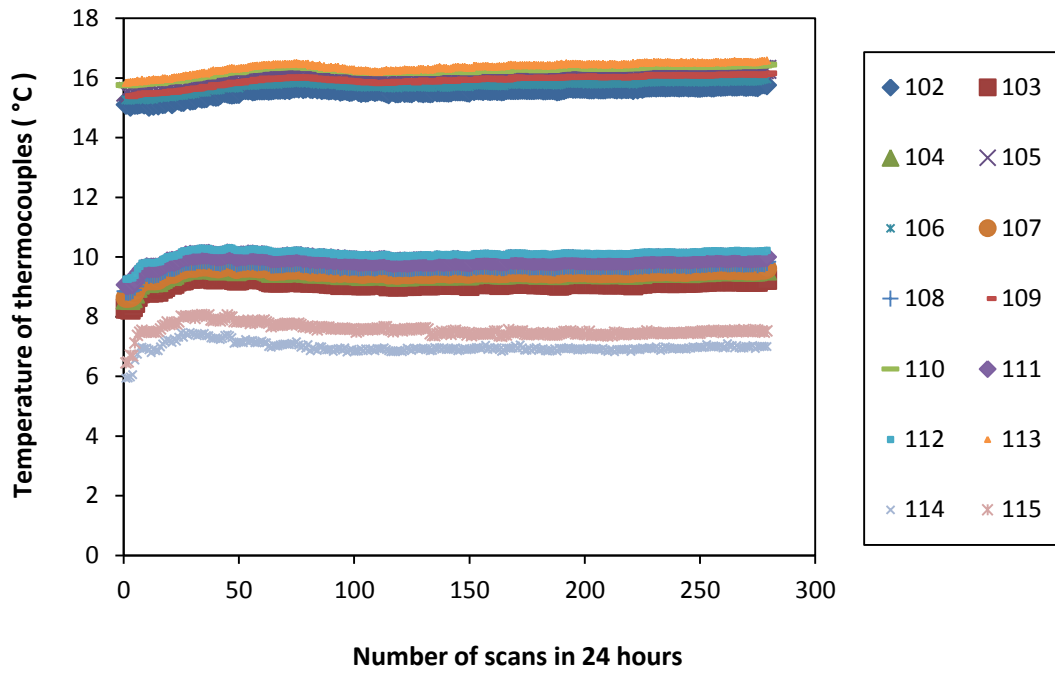


Figure A.53 Temperature data over a 24 hour period for cooling cycle 14 (test conducted in 2012)

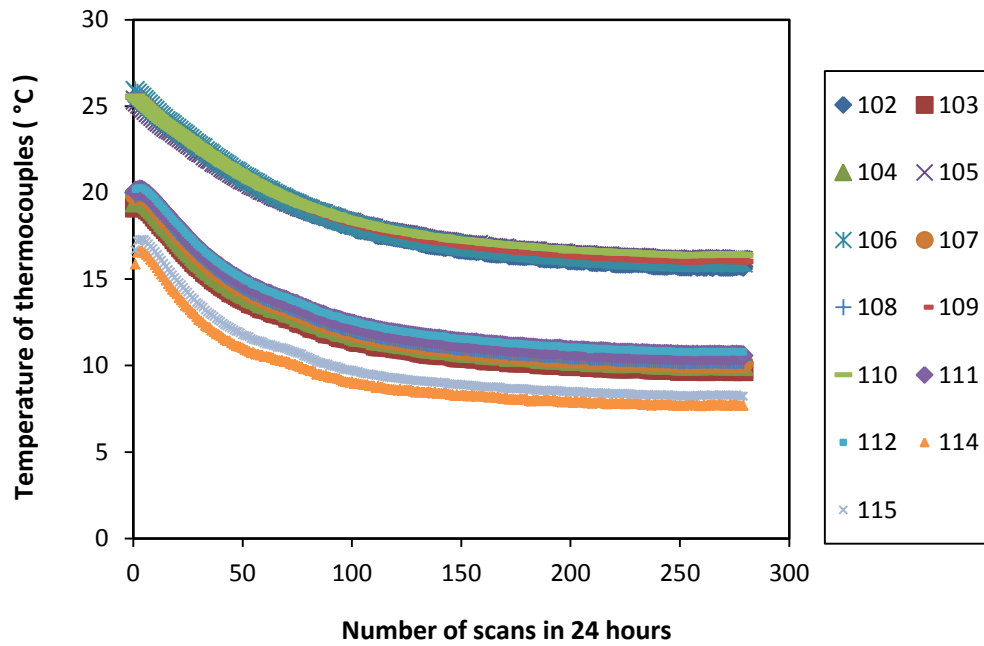


Figure A.54 Temperature data over a 24 hour period for cooling cycle 15 (test conducted in 2012)

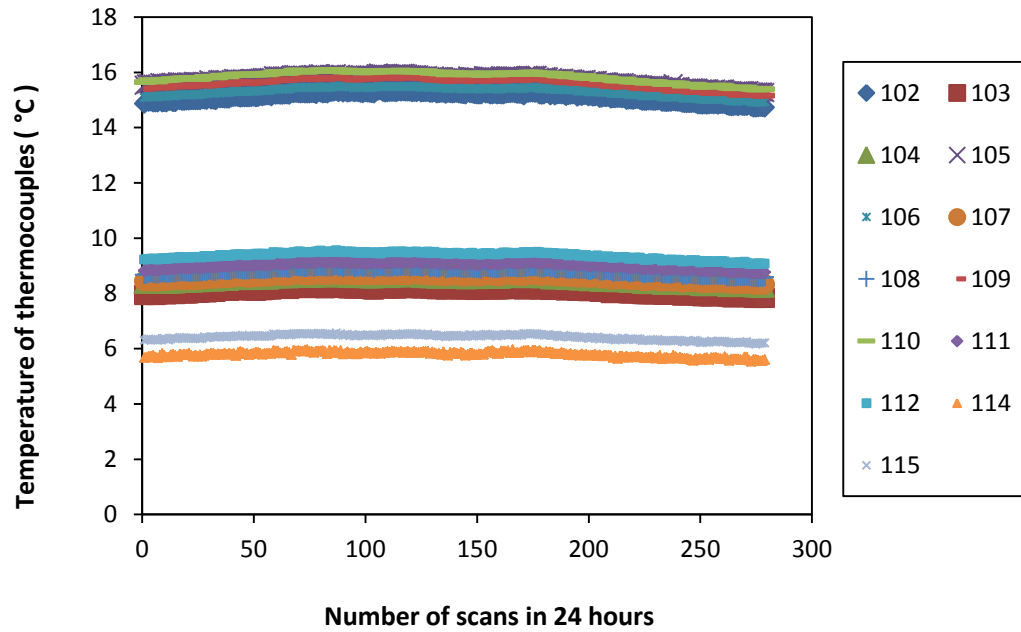


Figure A.55 Temperature data over a 24 hour period for cooling cycle 16 (test conducted in 2012)

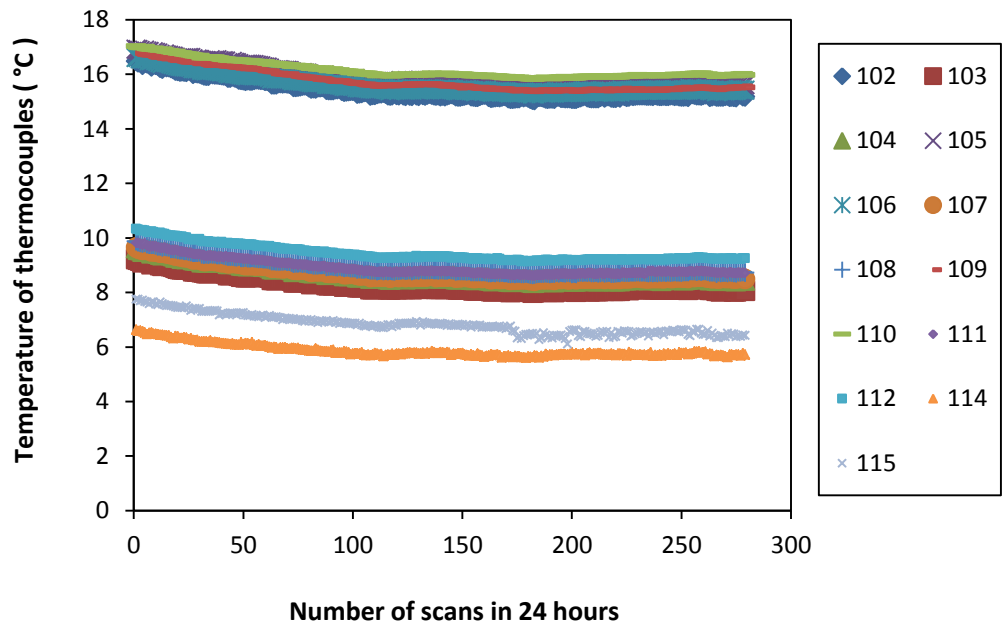


Figure A.56 Temperature data over a 24 hour period for cooling cycle 17 (test conducted in 2012)

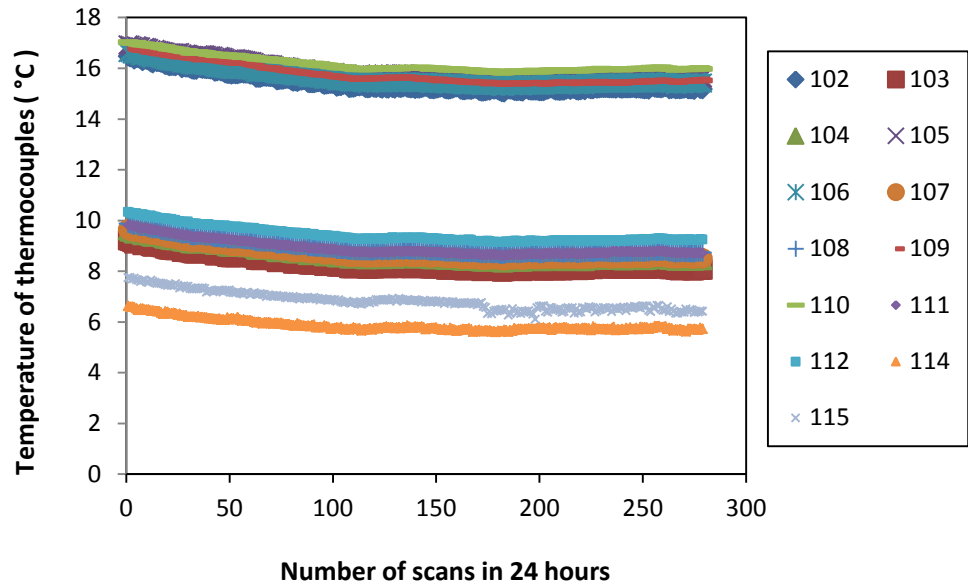


Figure A.57 Temperature data over a 24 hour period for cooling cycle 18 (test conducted in 2012)

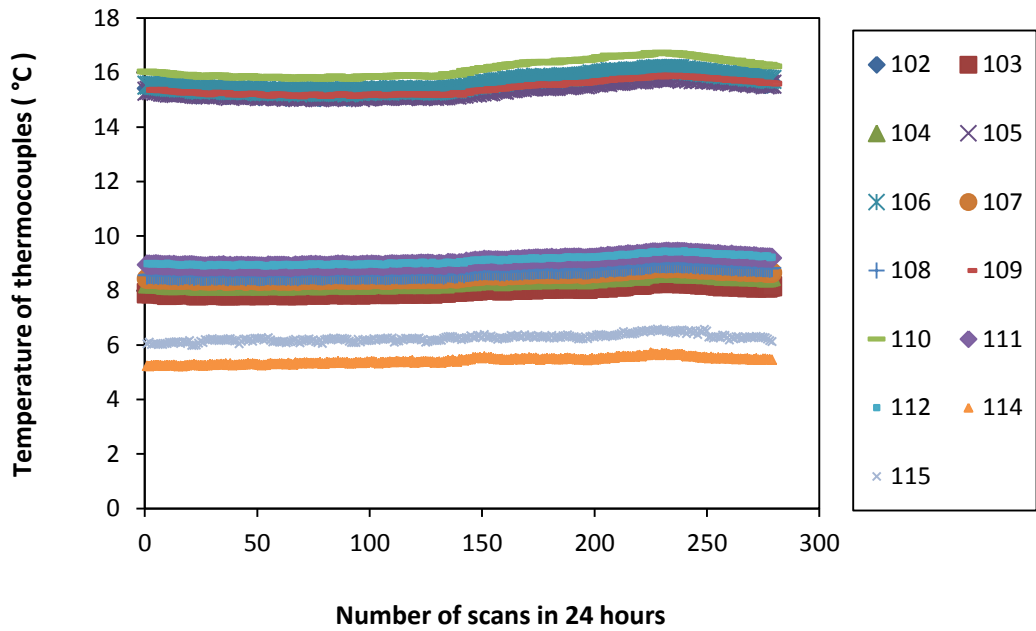


Figure A.58 Temperature data over a 24 hour period for cooling cycle 19 (test conducted in 2012)

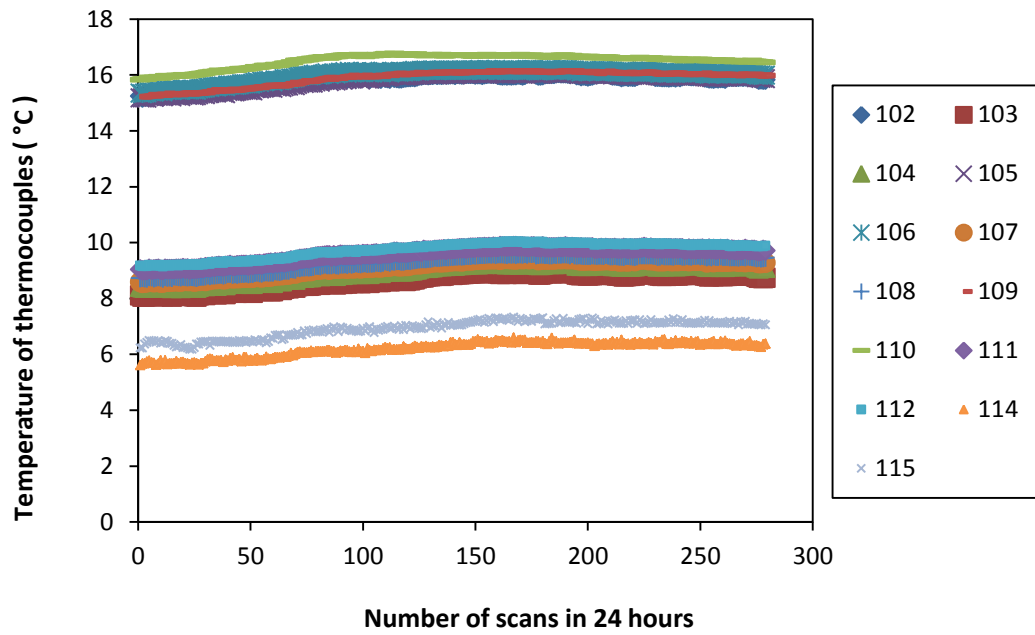


Figure A.60 Temperature data over a 24 hour period for cooling cycle 20 (test conducted in 2012)

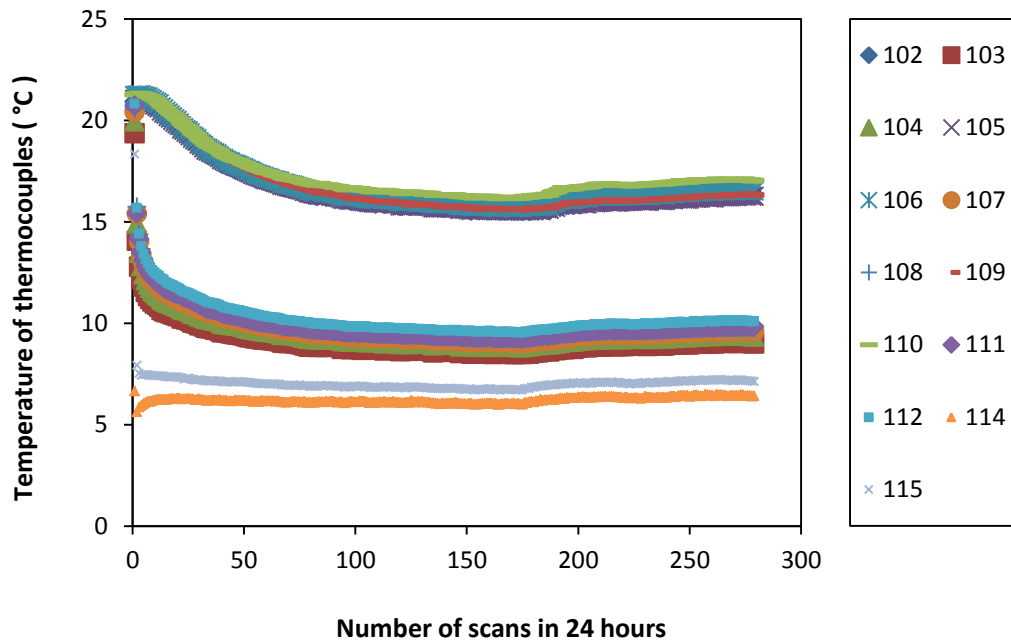


Figure A.61 Temperature data over a 24 hour period for cooling cycle 21 (test conducted in 2012)

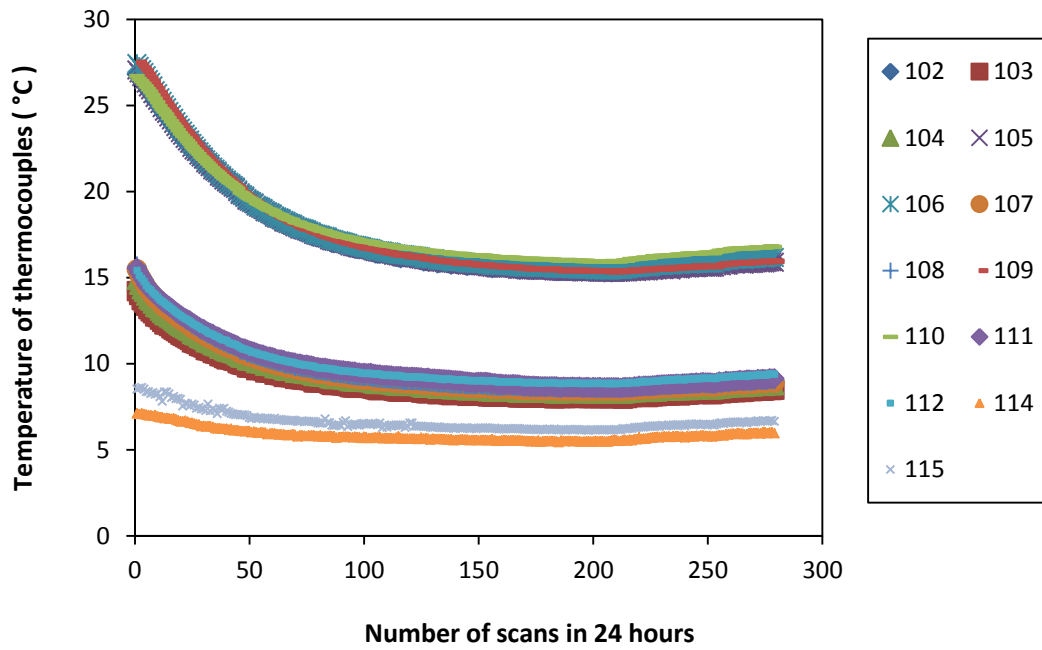


Figure A.62 Temperature data over a 24 hour period for cooling cycle 22 (test conducted in 2012)

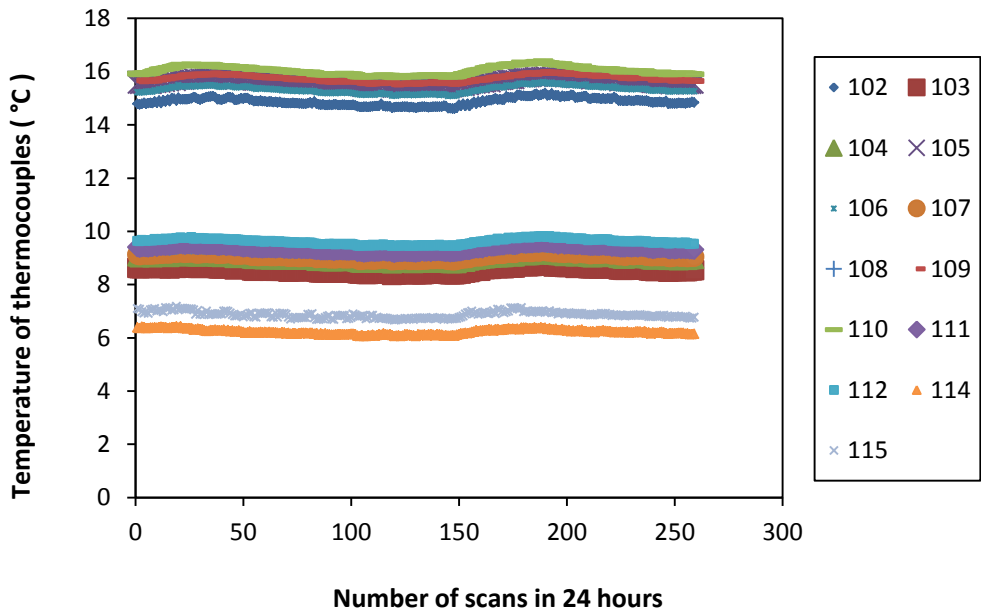


Figure A.63 Temperature data over a 24 hour period for cooling cycle 23 (test conducted in 2012)

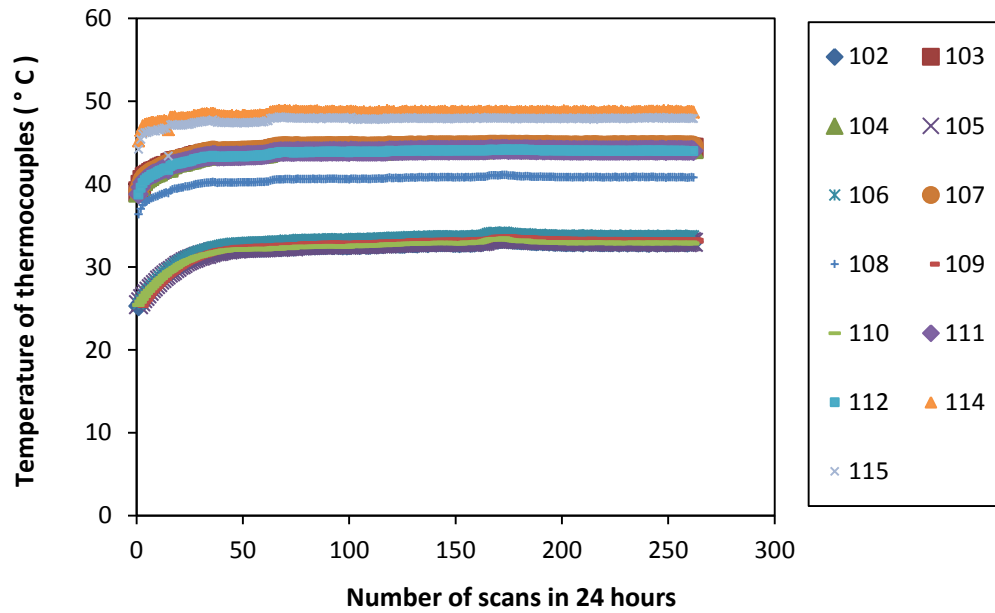


Figure A.64 Temperature data over a 24 hour period for heating cycle 1 (test conducted in 2013)

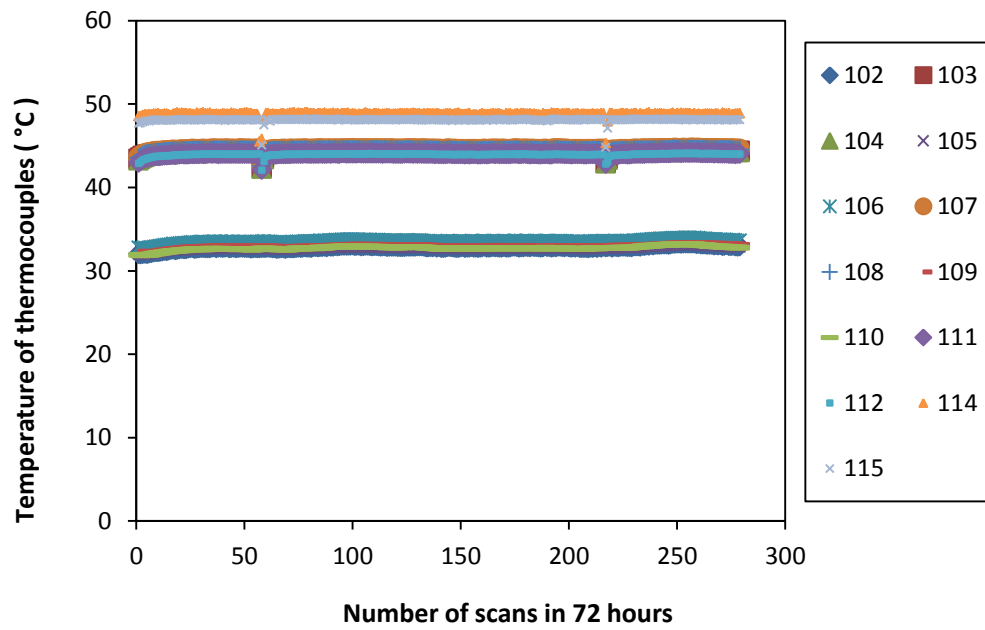


Figure A.65 Temperature data over a 72 hour period for heating cycle 2 (test conducted in 2013)

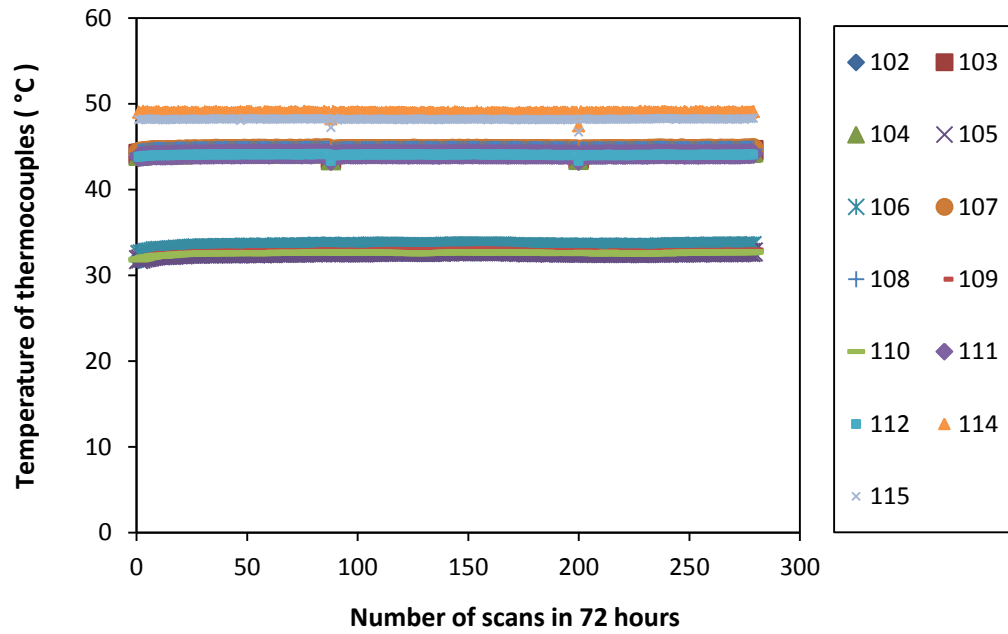


Figure A.66 Temperature data over a 72 hour period for heating cycle 3 (test conducted in 2013)

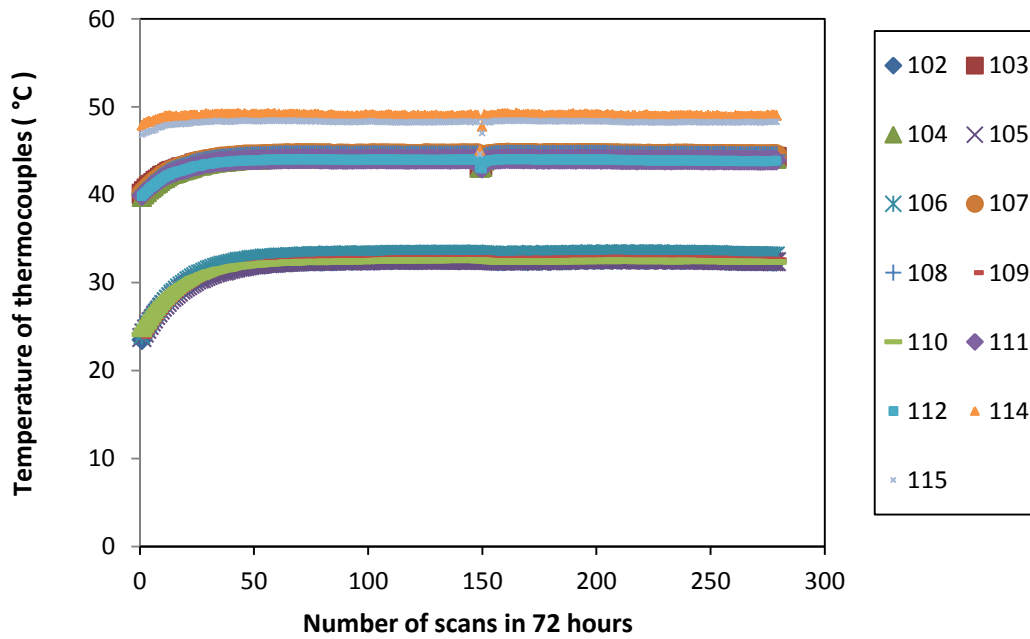


Figure A.67 Temperature data over a 72 hour period for heating cycle 4 (test conducted in 2013)

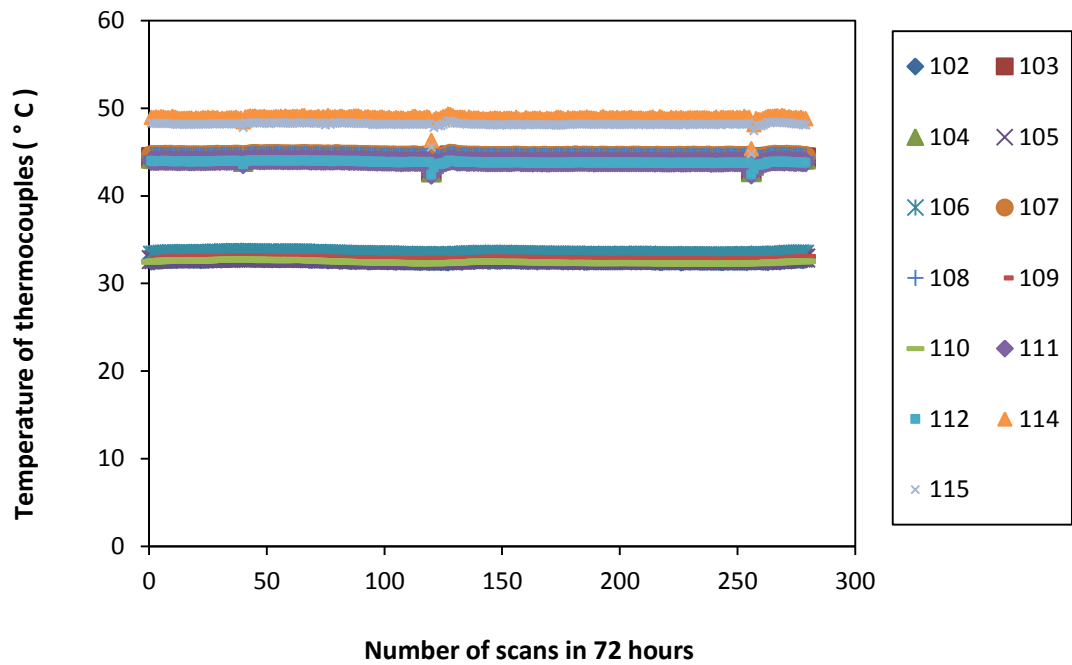


Figure A.68 Temperature data over a 72 hour period for heating cycle 5 (test conducted in 2013)

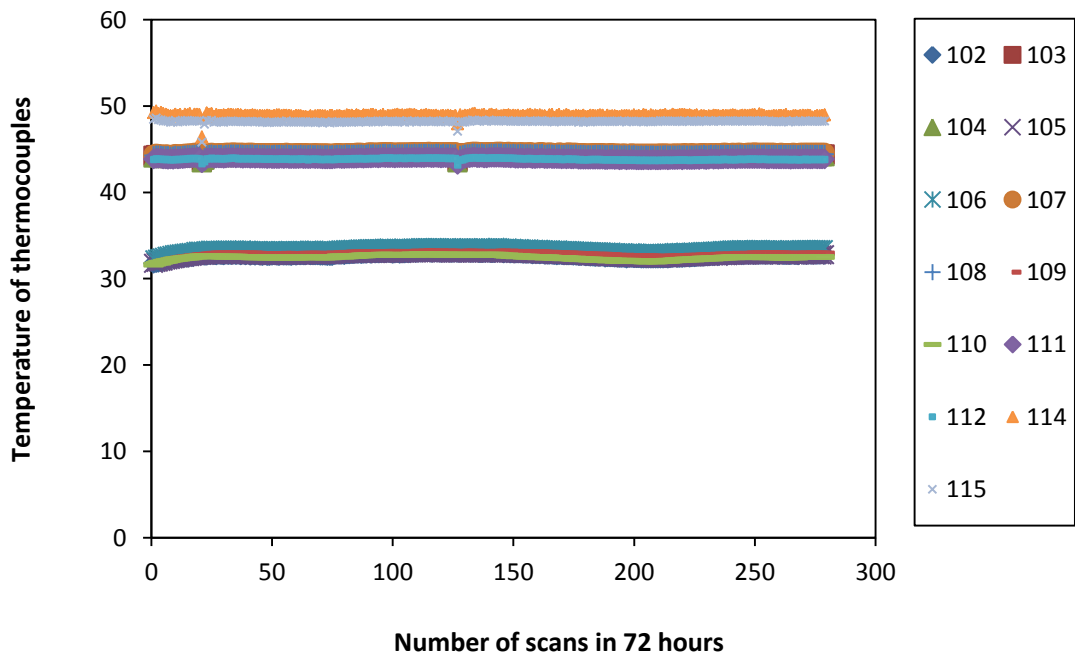


Figure A.69 Temperature data over a 72 hour period for heating cycle 6 (test conducted in 2013)

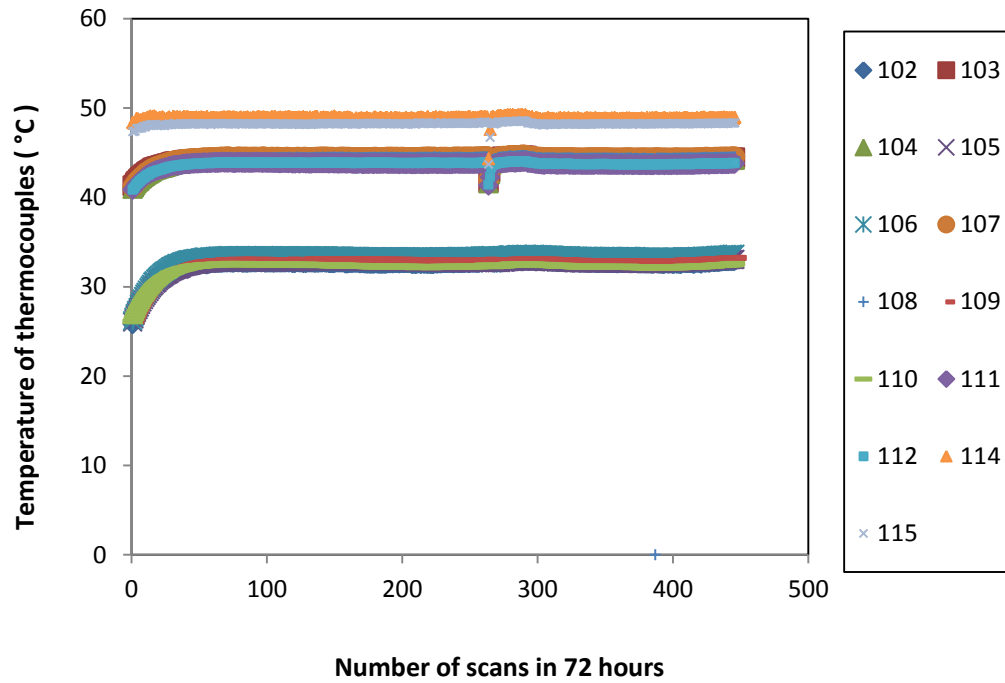


Figure A.70 Temperature data over a 72 hour period for heating cycle 7 (test conducted in 2013)

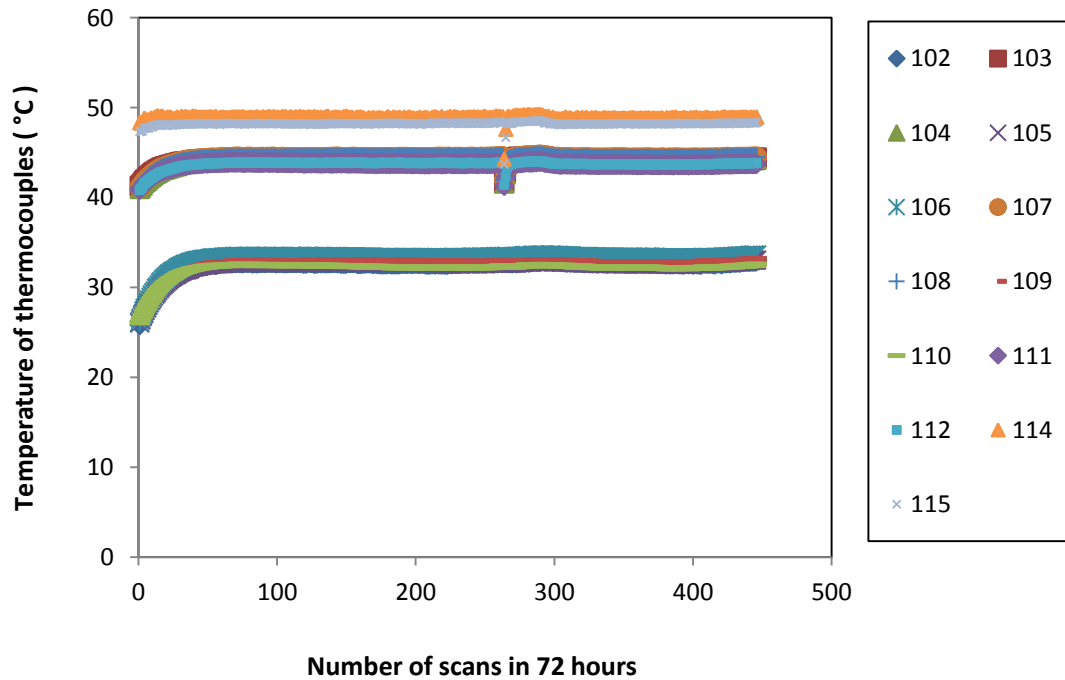


Figure A.71 Temperature data over a 72 hour period for heating cycle 8 (test conducted in 2013)

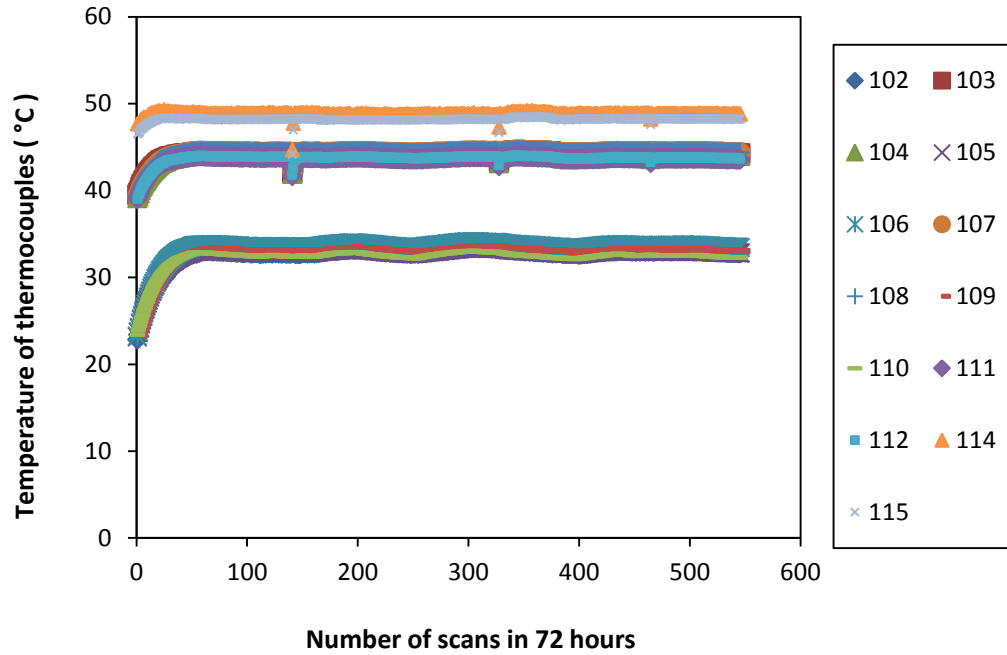


Figure A.72 Temperature data over a 72 hour period for heating cycle 9 (test conducted in 2013)

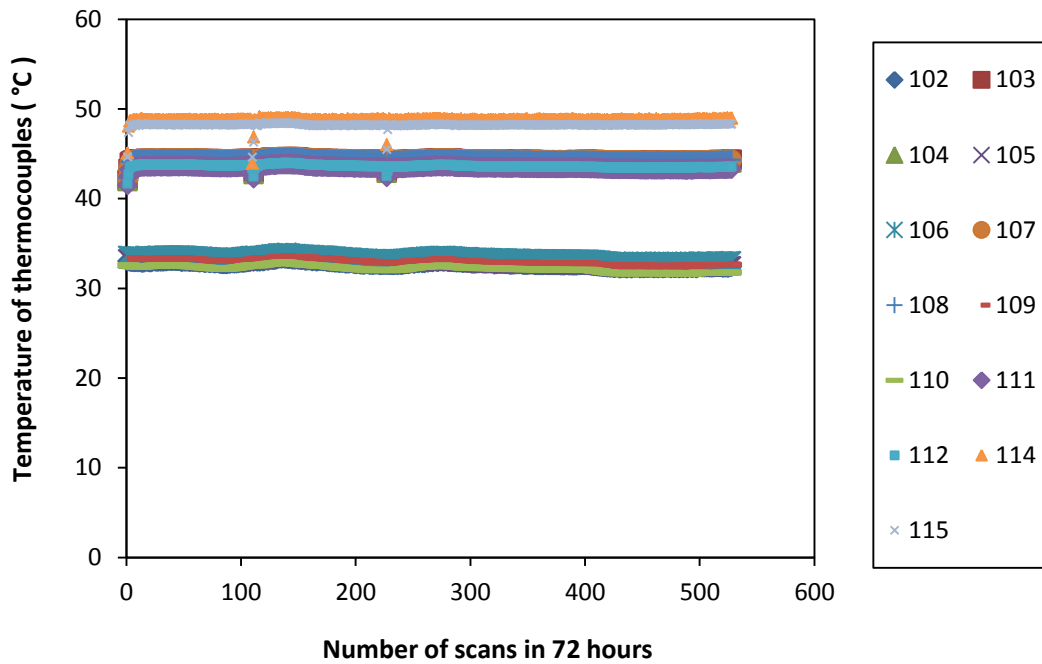


Figure A.73 Temperature data over a 72 hour period for heating cycle 10 (test conducted in 2013)

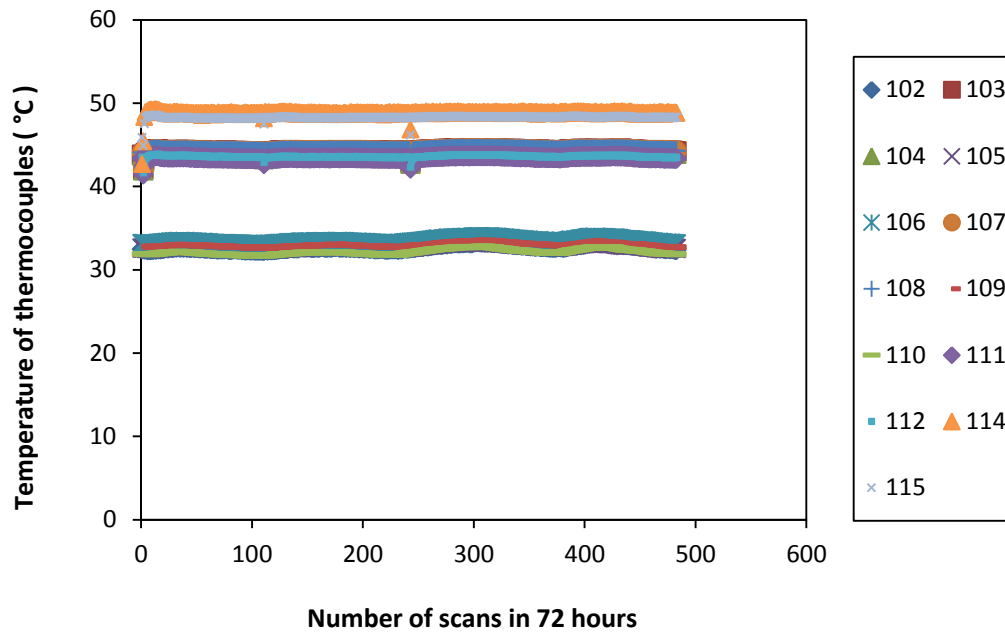


Figure A.74 Temperature data over a 72 hour period for heating cycle 11 (test conducted in 2013)

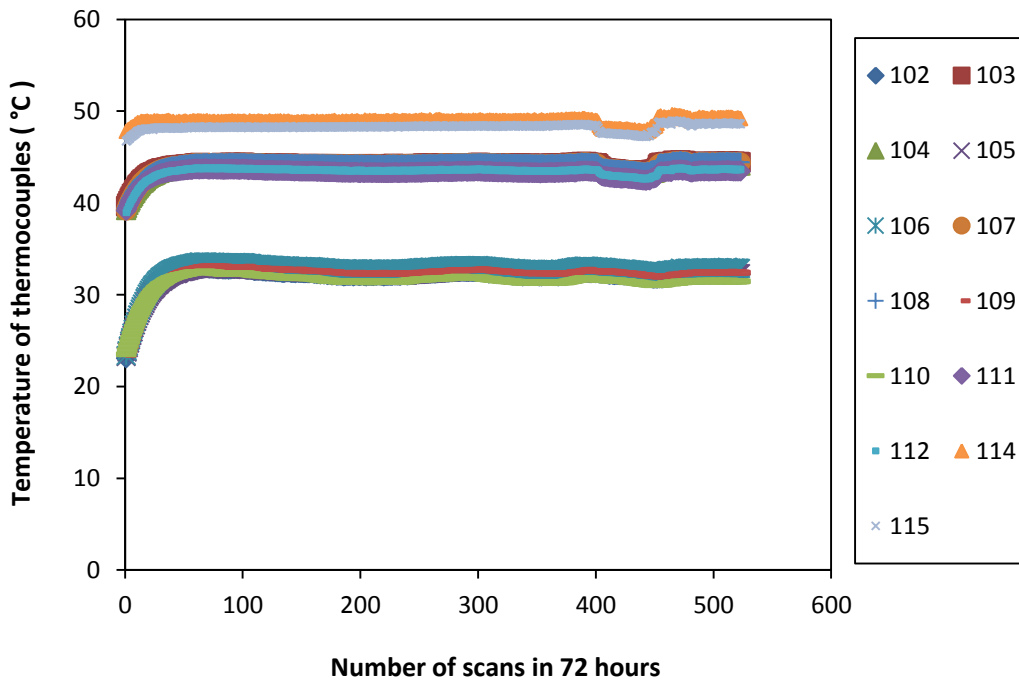


Figure A.75 Temperature data over a 72 hour period for heating cycle 12 (test conducted in 2013)

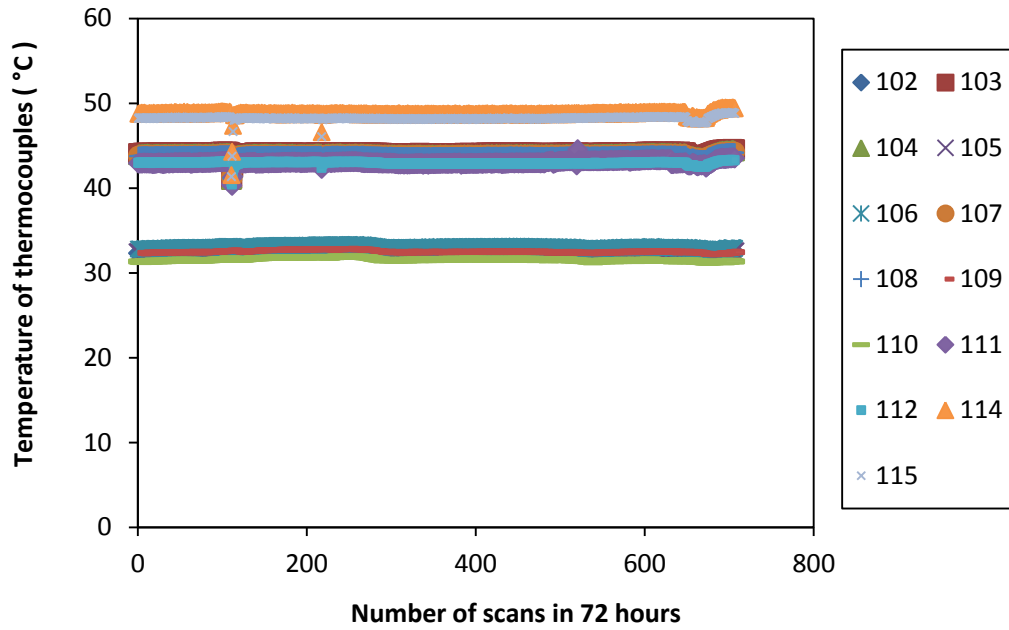


Figure A.76 Temperature data over a 72 hour period for heating cycle 13 (test conducted in 2013)

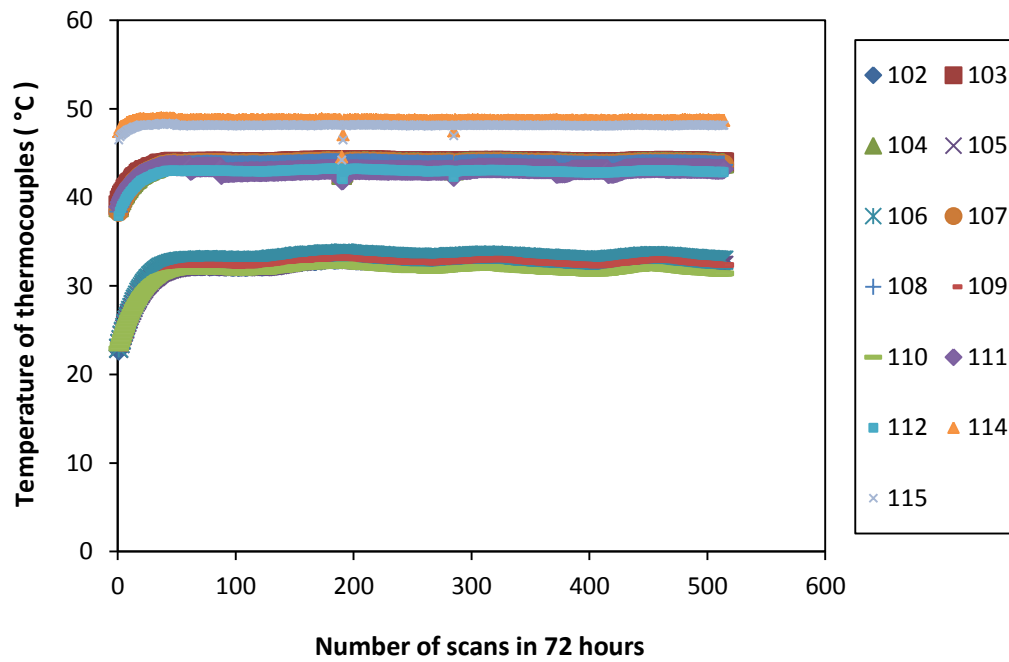


Figure A.77 Temperature data over a 72 hour period for heating cycle 14 (test conducted in 2013)

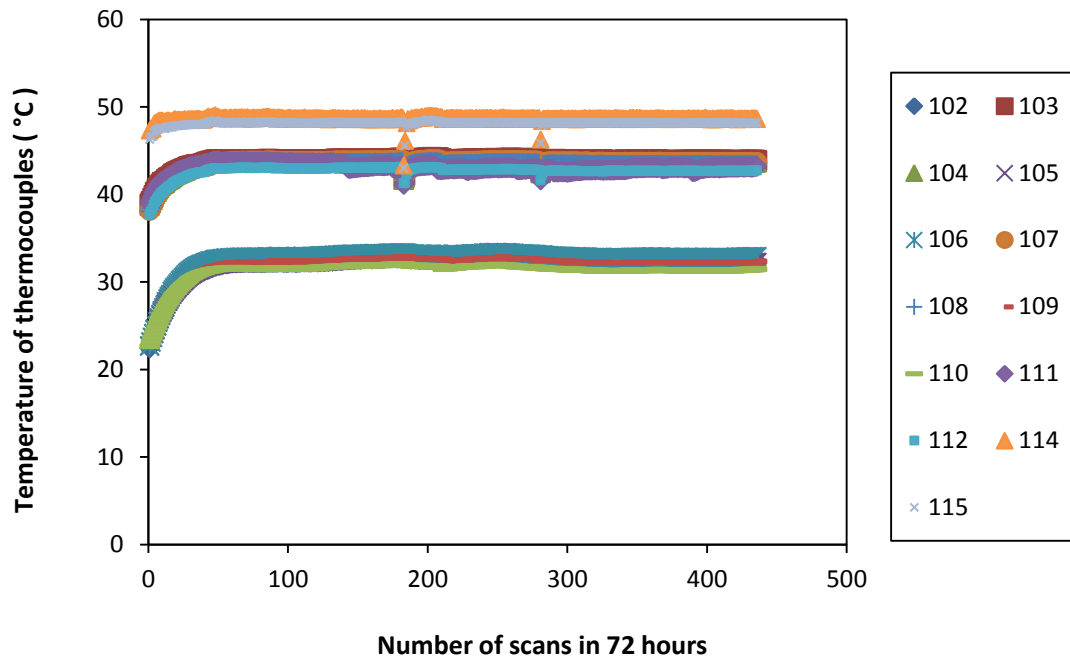


Figure A.78 Temperature data over a 72 hour period for heating cycle 15 (test conducted in 2013)

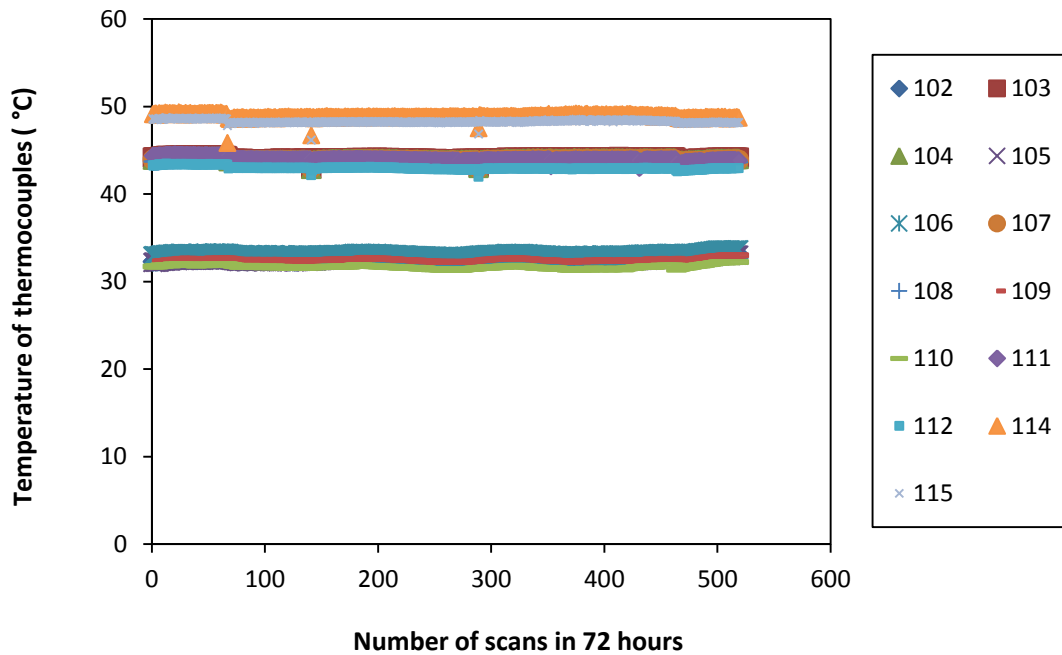


Figure A.79 Temperature data over a 72 hour period for heating cycle 16 (test conducted in 2013)

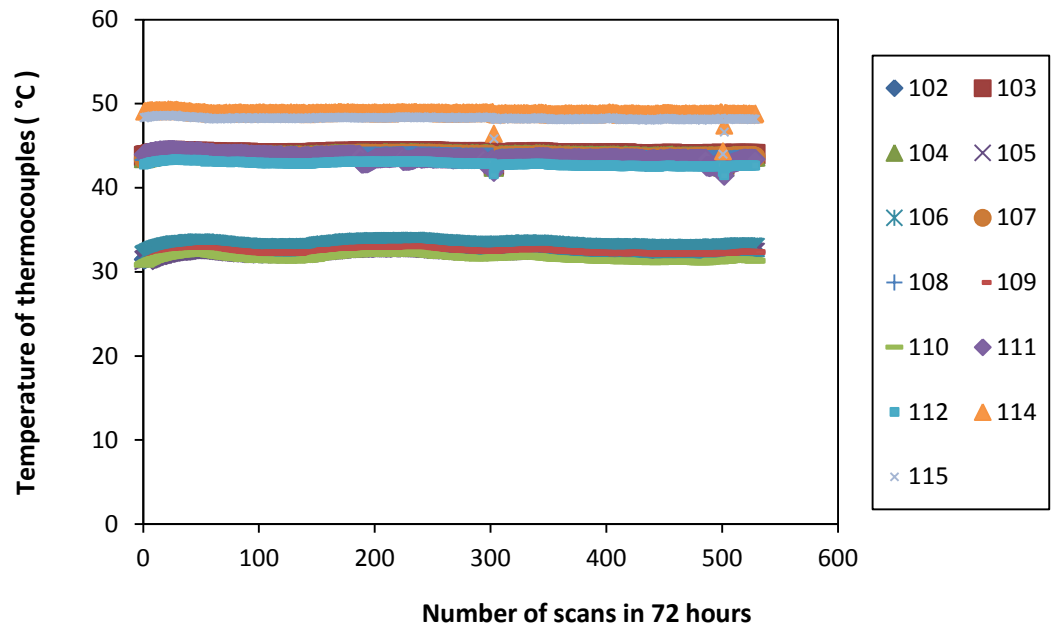


Figure A.80 Temperature data over a 72 hour period for heating cycle 17 (test conducted in 2013)

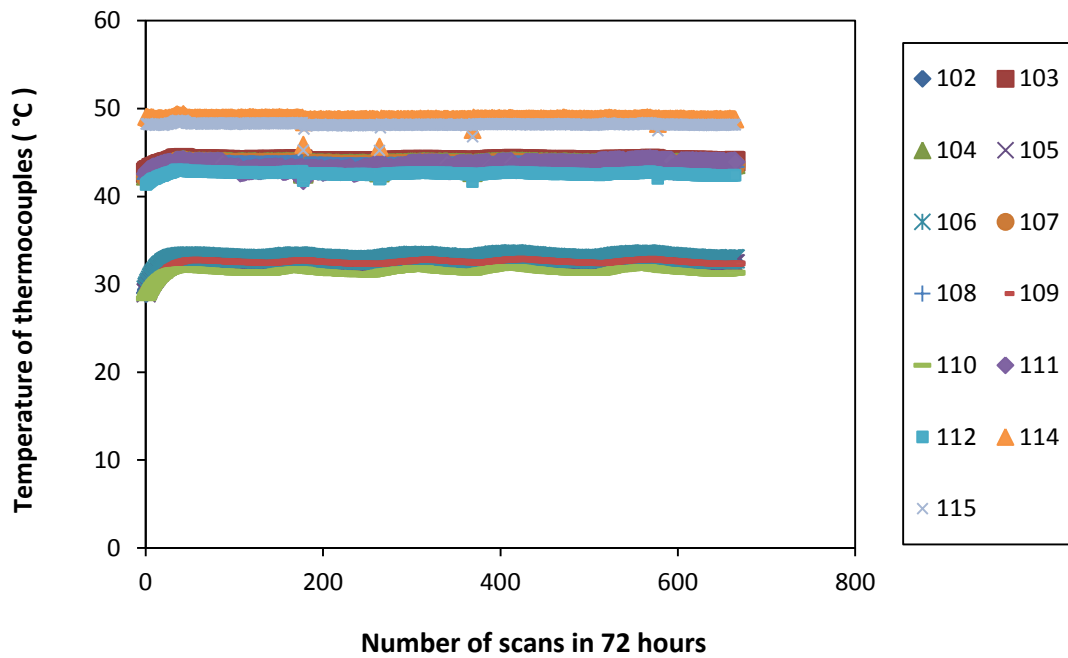


Figure A.81 Temperature data over a 72 hour period for heating cycle 18 (test conducted in 2013)

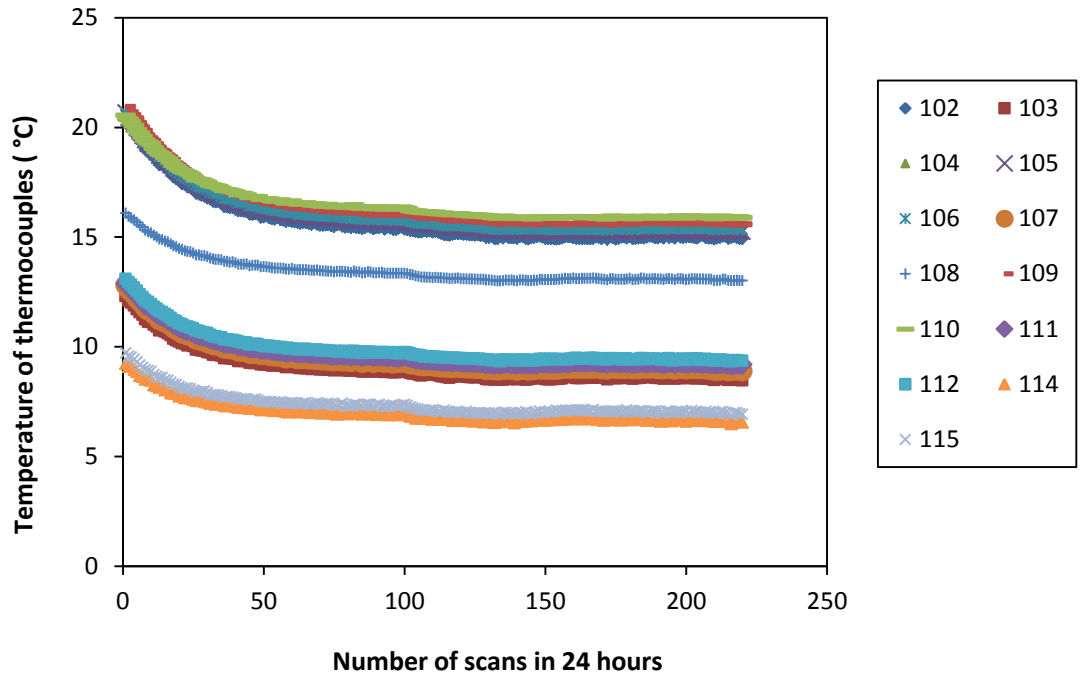


Figure A.82 Temperature data over a 24 hour period for cooling cycle 1 (test conducted in 2013)

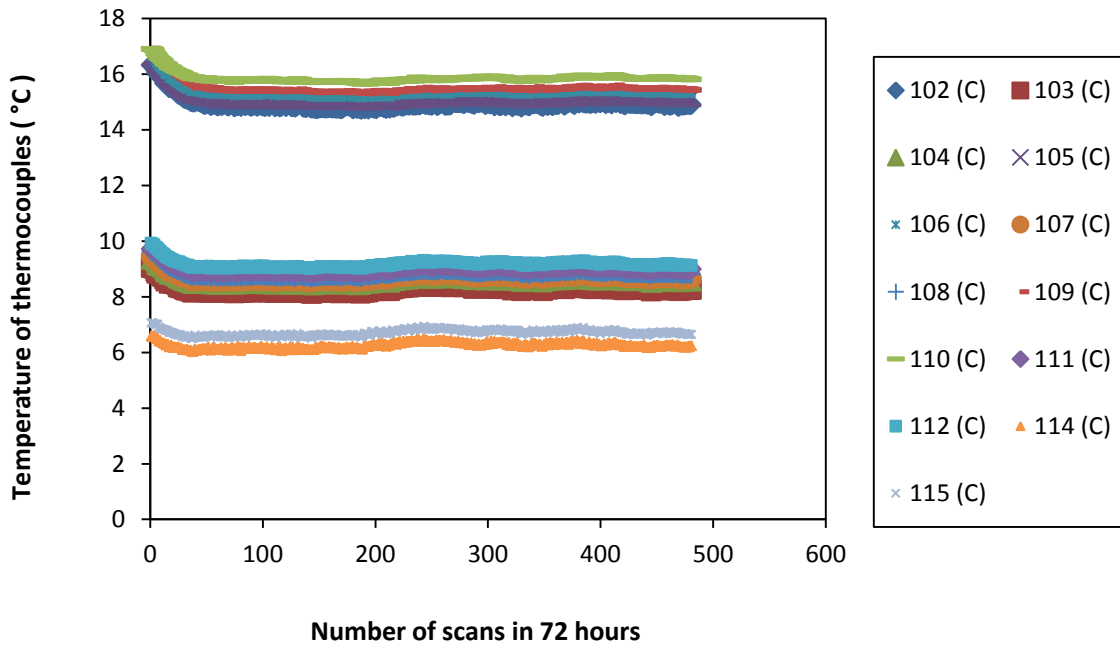


Figure A.83 Temperature data over a 72 hour period for cooling cycle 2 (test conducted in 2013)

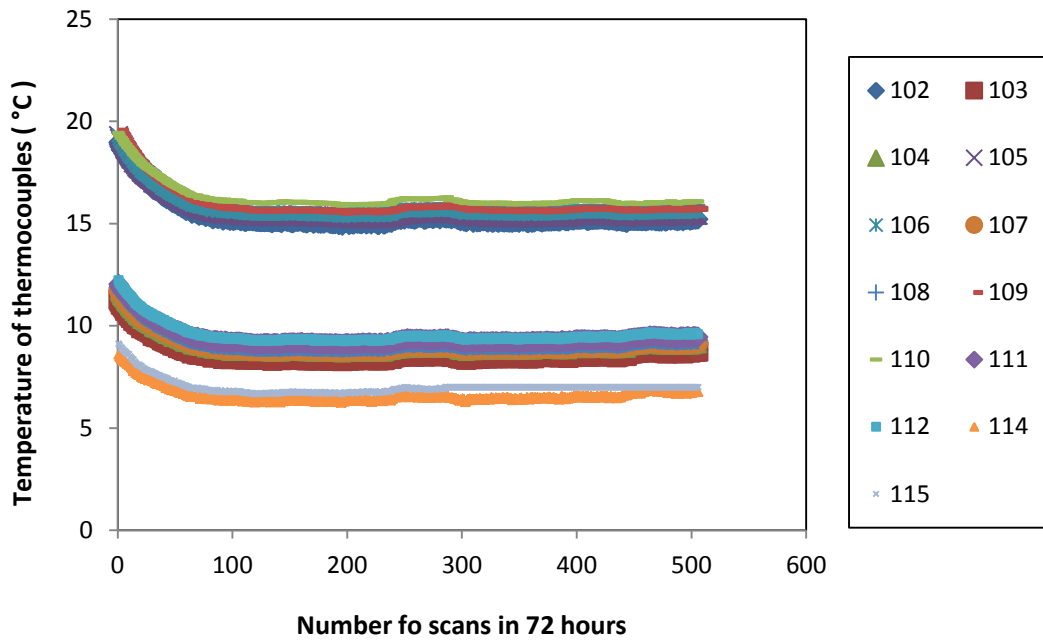


Figure A.84 Temperature data over a 72 hour period for cooling cycle 2 (test conducted in 2013)

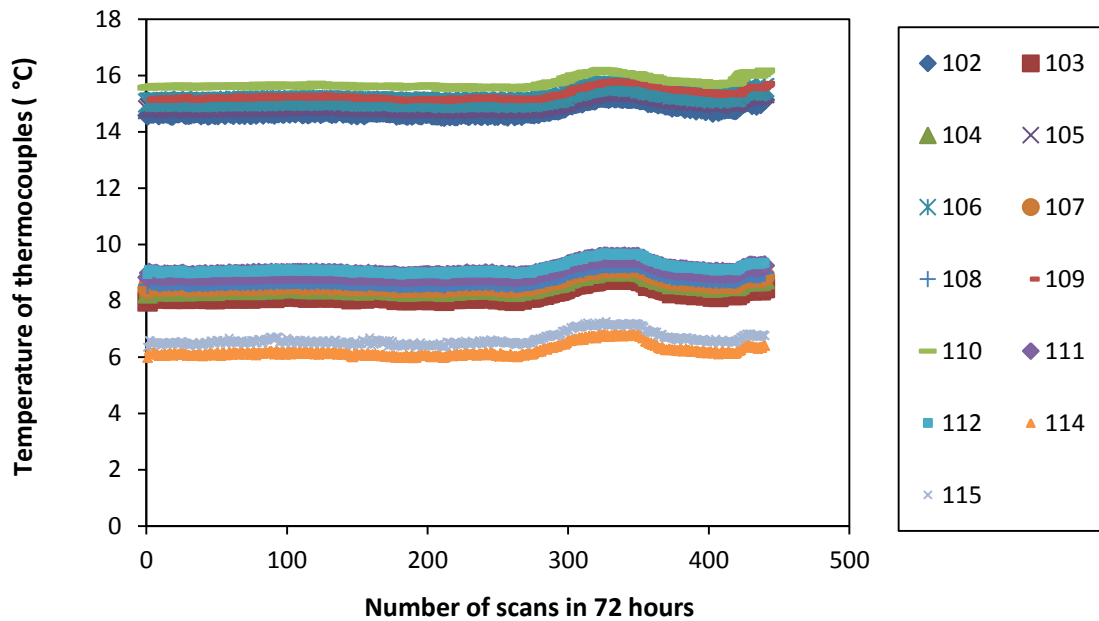


Figure A.85 Temperature data over a 72 hour period for cooling cycle 4 (test conducted in 2013)

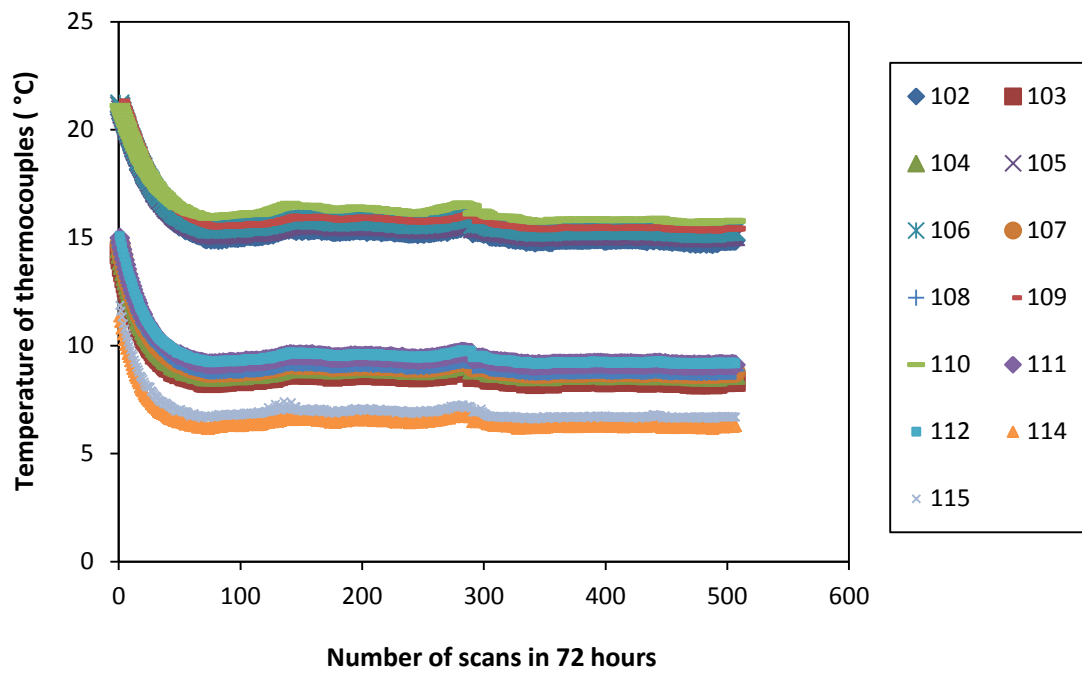


Figure A.86 Temperature data over a 72 hour period for cooling cycle 5 (test conducted in 2013)

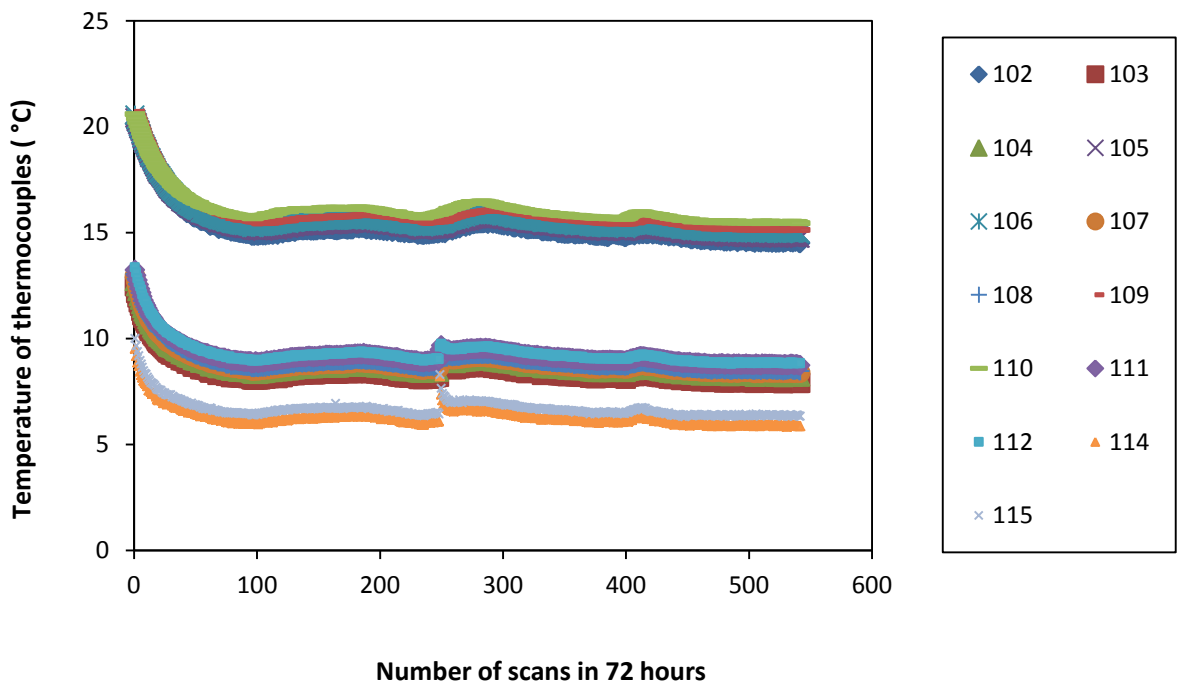


Figure A.87 Temperature data over a 72 hour period for cooling cycle 6 (test conducted in 2013)

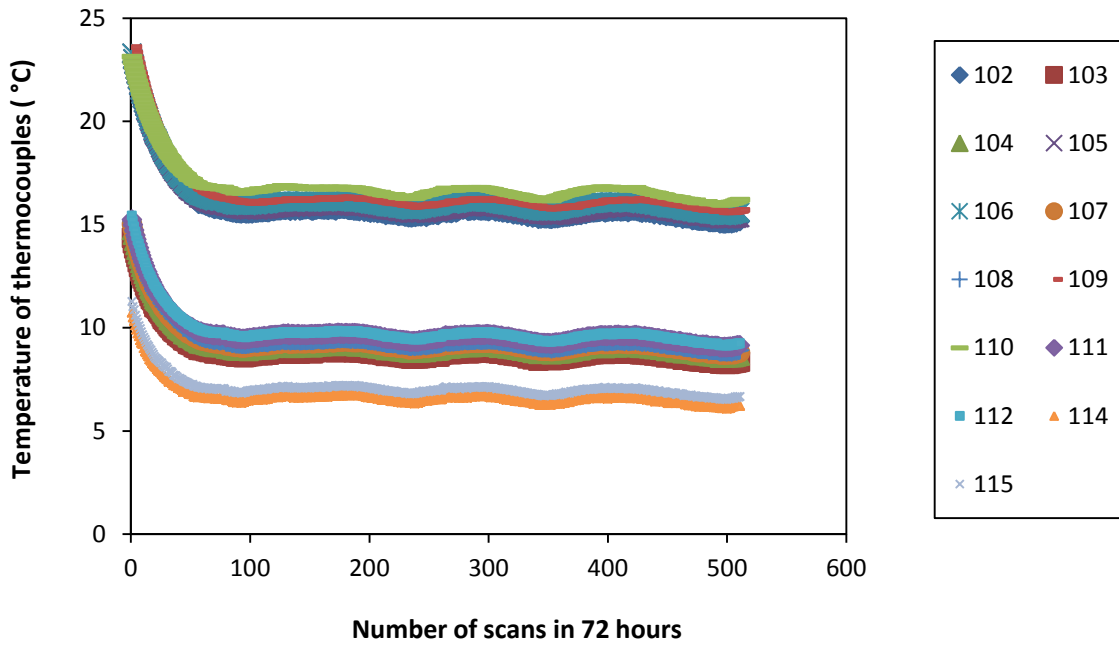


Figure A.88 Temperature data over a 72 hour period for cooling cycle 7 (test conducted in 2013)

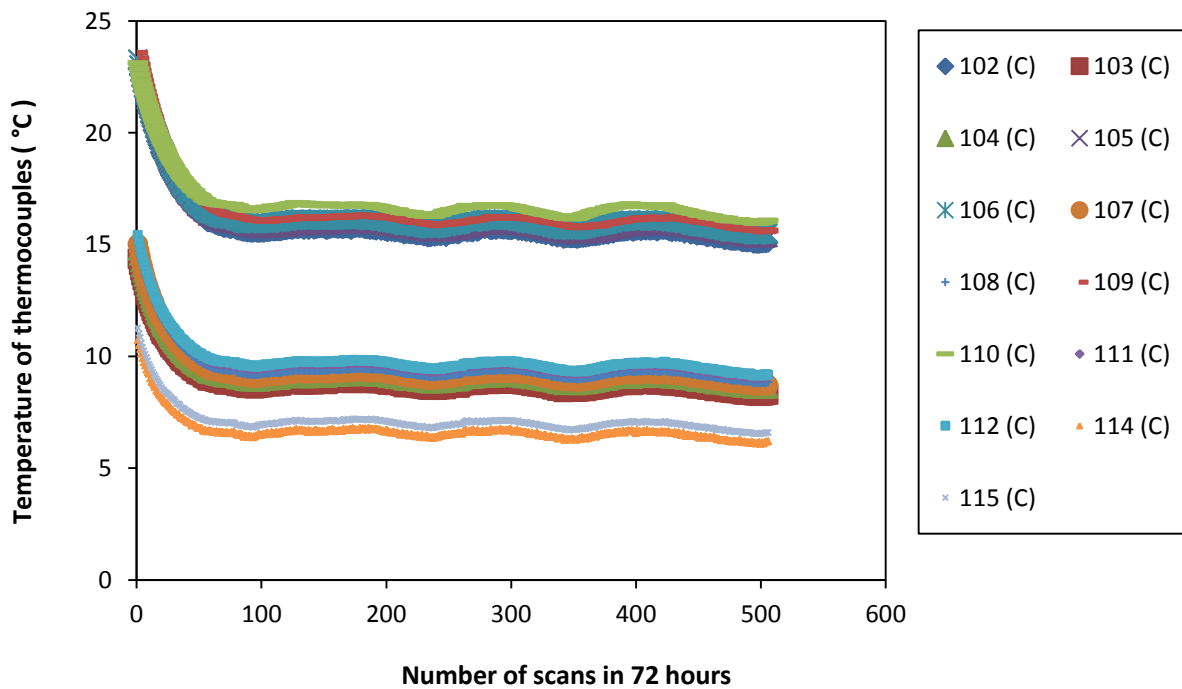


Figure A.89 Temperature data over a 72 hour period for cooling cycle 8 (test conducted in 2013)

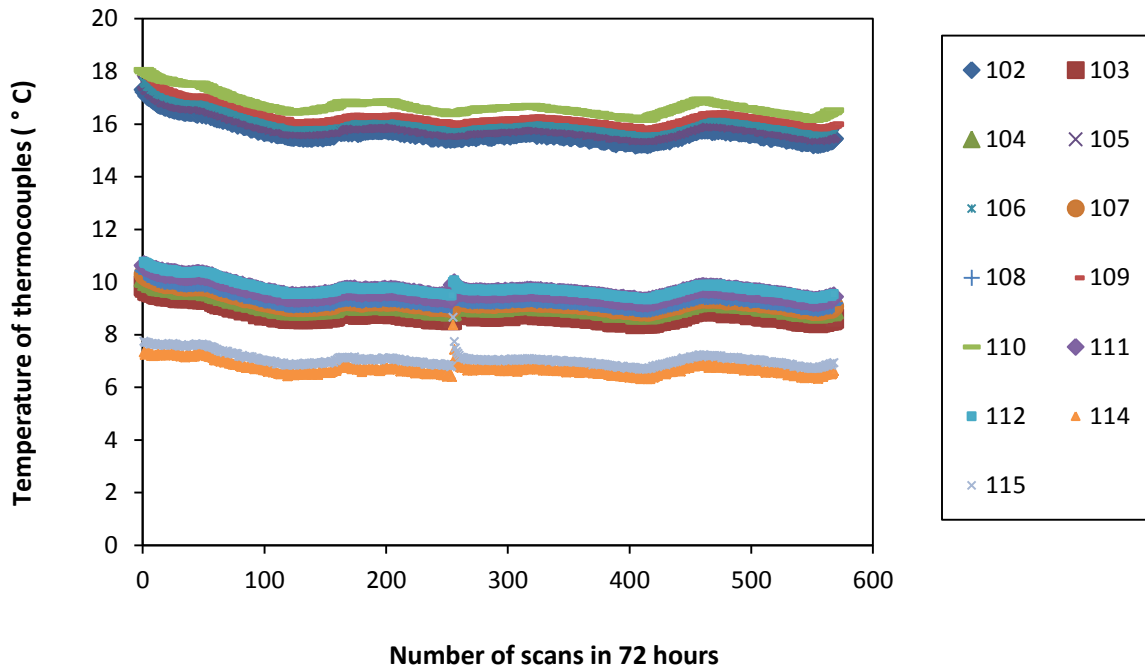


Figure A.90 Temperature data over a 72 hour period for cooling cycle 9 (test conducted in 2013)

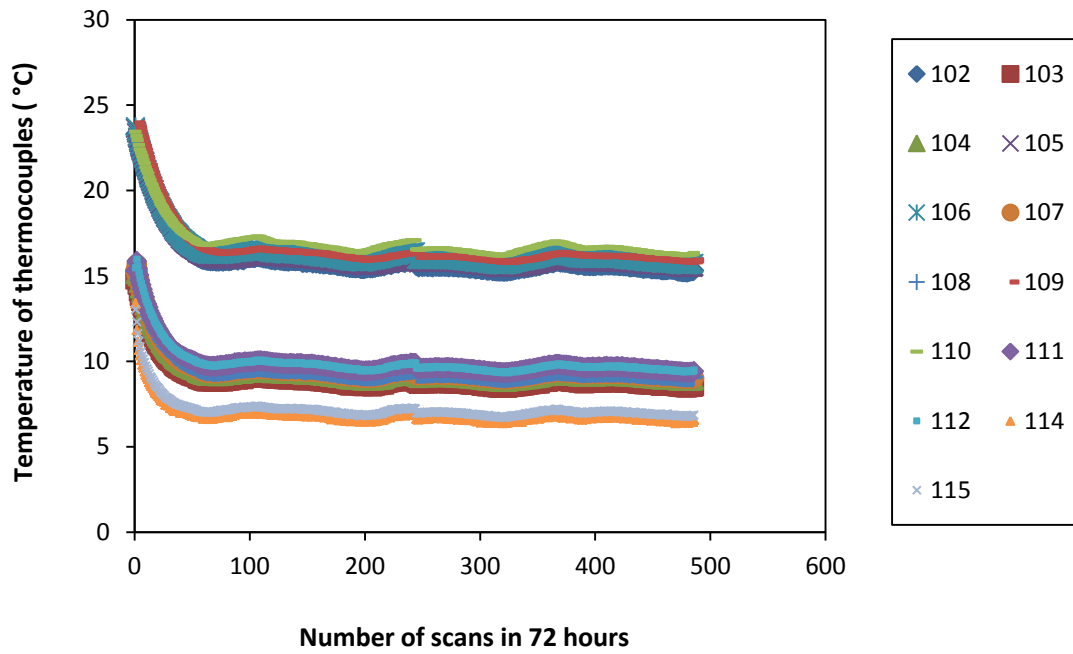


Figure A.91 Temperature data over a 72 hour period for cooling cycle 10 (test conducted in 2013)

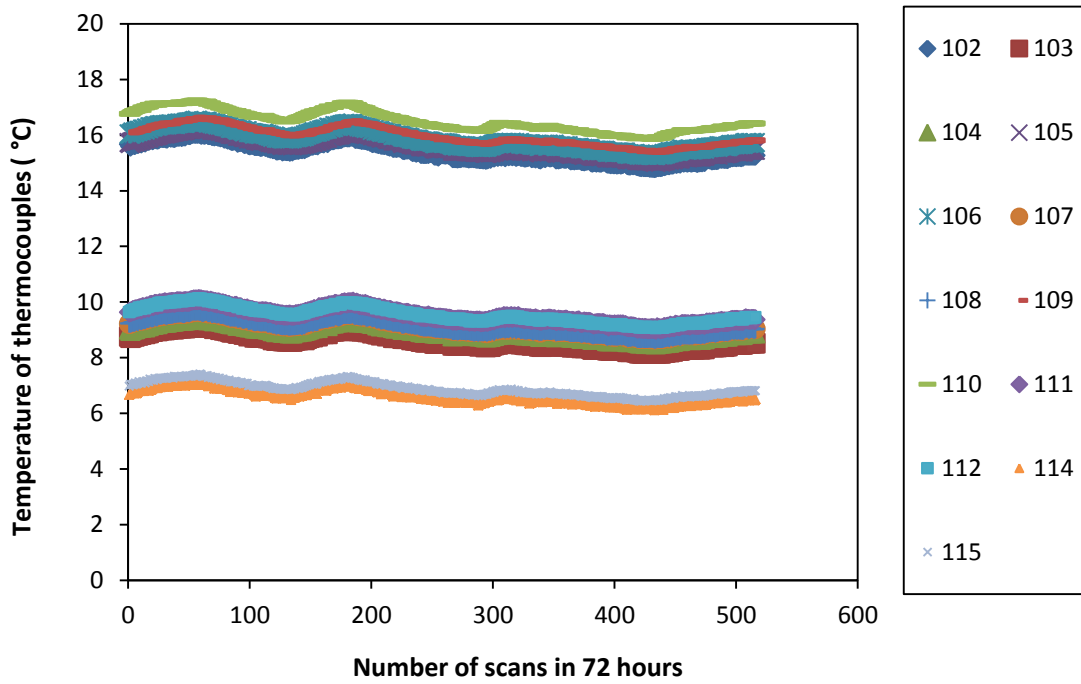


Figure A.92 Temperature data over a 72 hour period for cooling cycle 11 (test conducted in 2013)

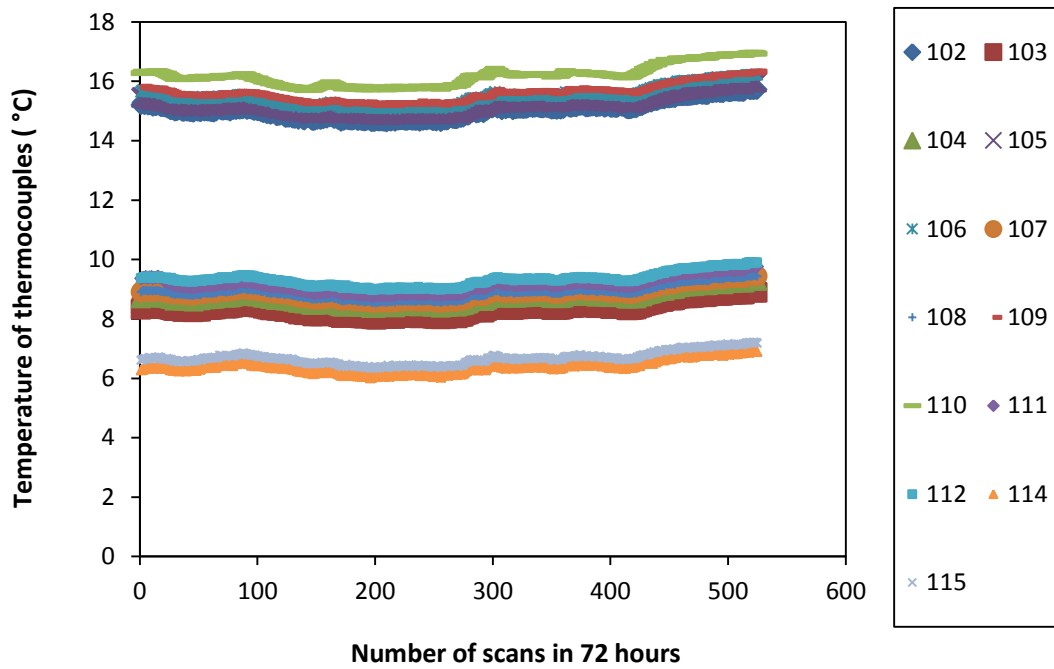


Figure A.93 Temperature data over a 72 hour period for cooling cycle 12 (test conducted in 2013)

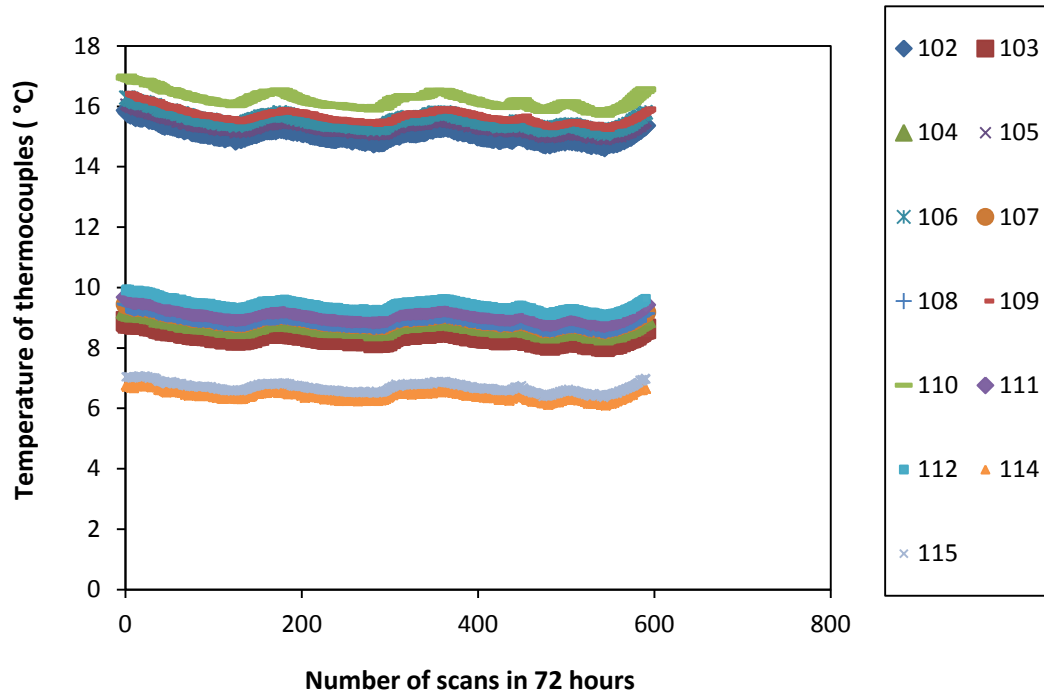


Figure A.94 Temperature data over a 72 hour period for cooling cycle 13 (test conducted in 2013)

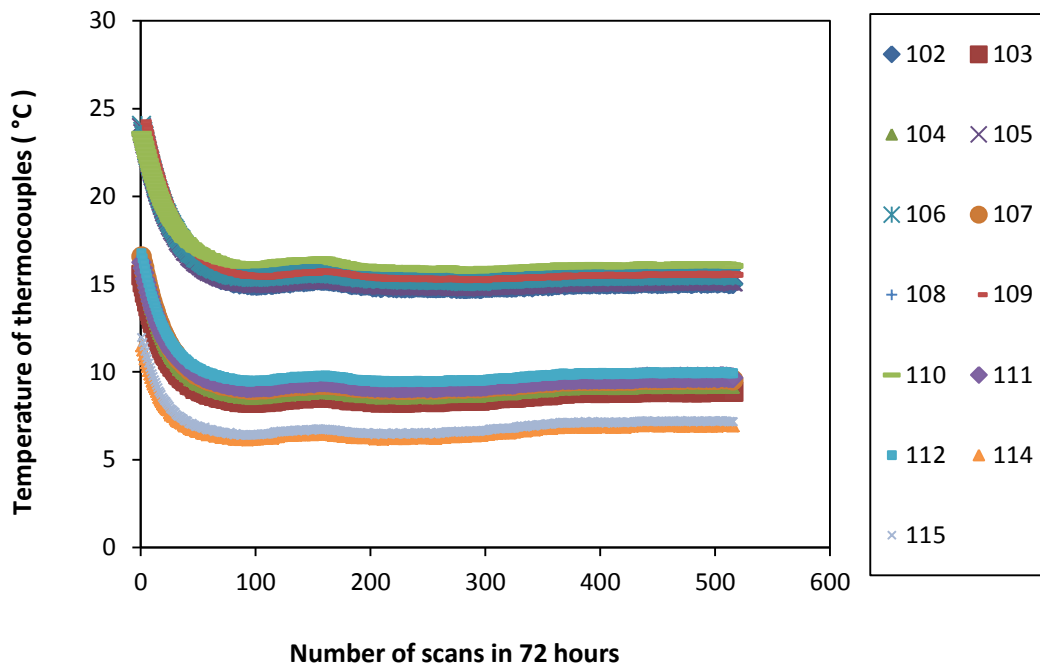


Figure A.95 Temperature data over a 72 hour period for cooling cycle 14 (test conducted in 2013)

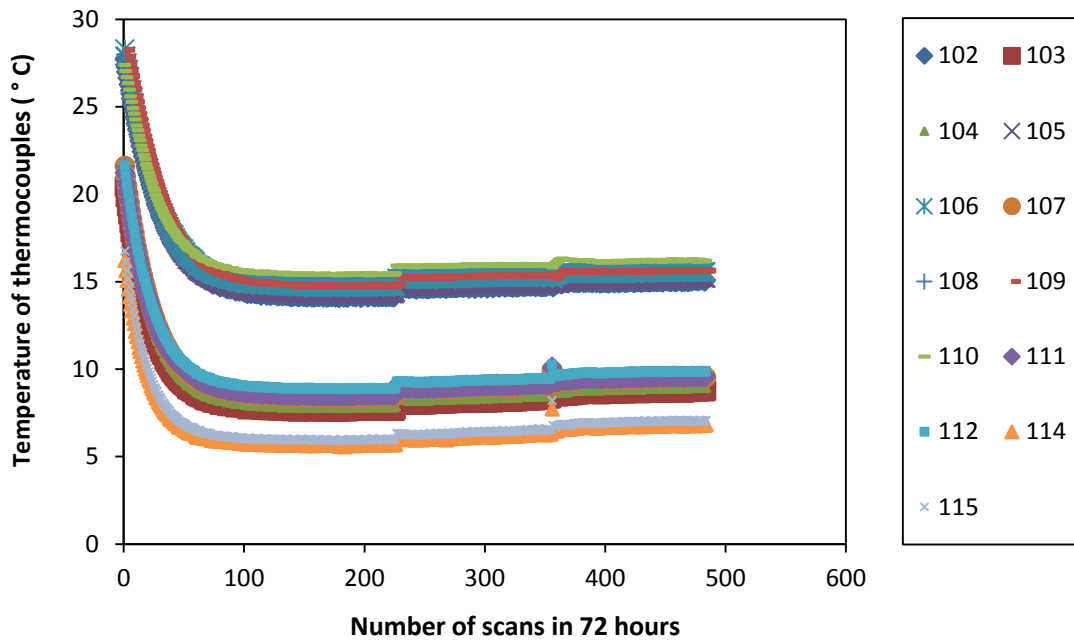


Figure A.96 Temperature data over a 72 hour period for cooling cycle 15 (test conducted in 2013)

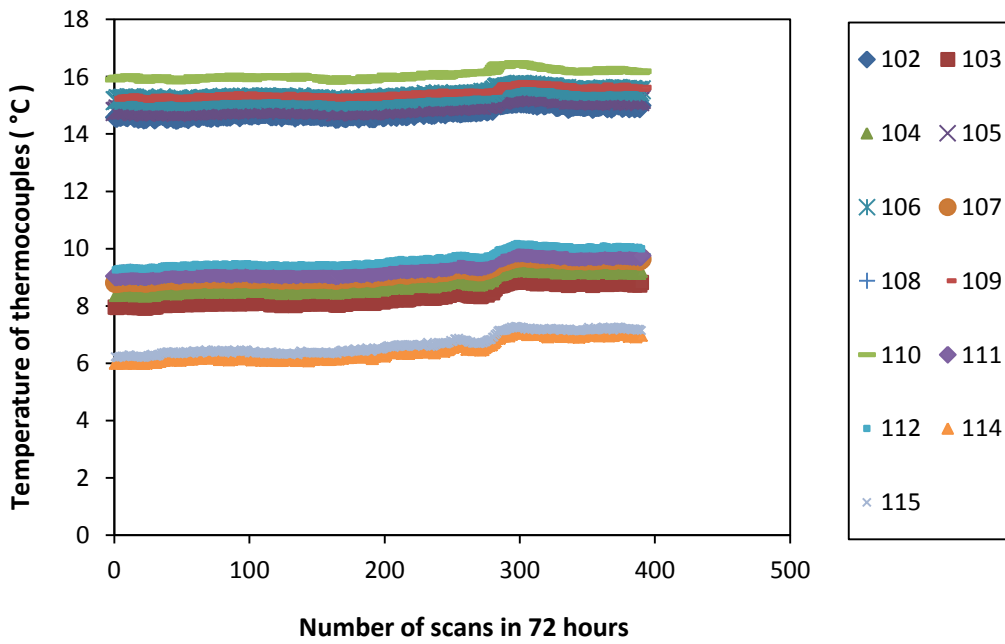


Figure A.97 Temperature data over a 72 hour period for cooling cycle 16 (test conducted in 2013)

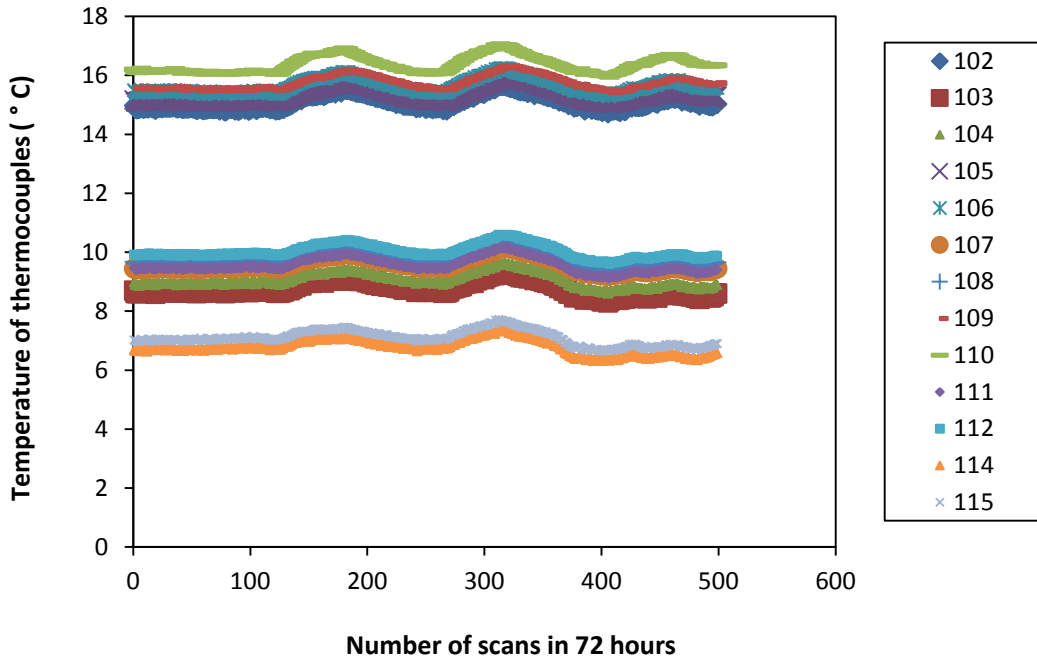


Figure A.98 Temperature data over a 72 hour period for cooling cycle 17 (test conducted in 2013)

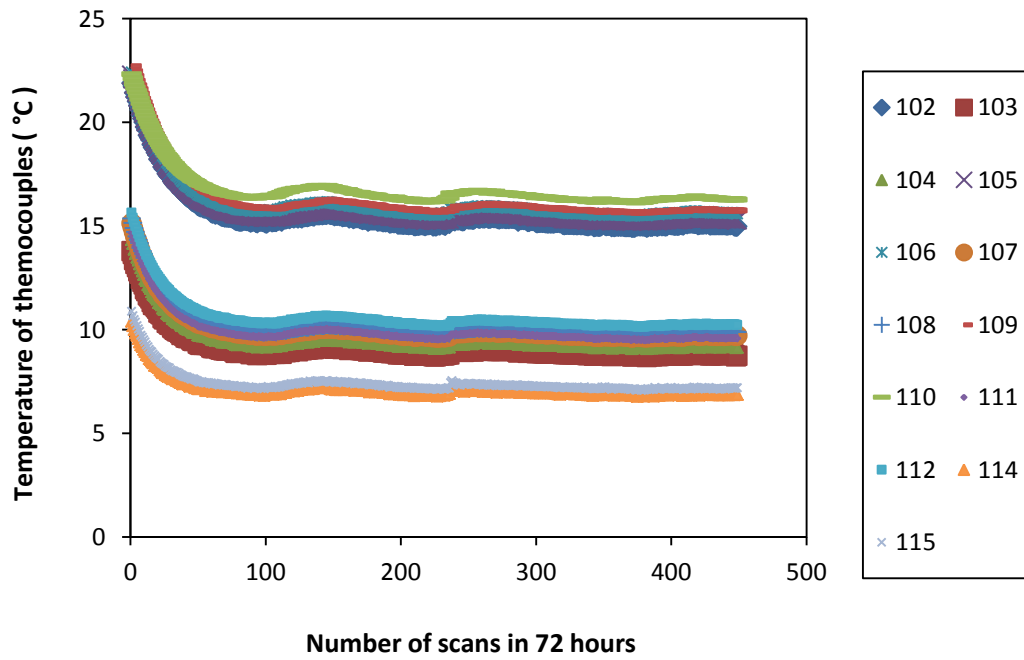


Figure A.99 Temperature data over a 72 hour period for cooling cycle 18 (test conducted in 2013)

Thermal conductivity sample calculations:

The following are sample calculations for a heating and cooling thermal conductivity tests. The heating and cooling systems shown in Figures A.100 and A.101 have temperature values of the grout and water after 72 hours.

Sample calculation for thermocouples 110 and 111 for a heating cycle:

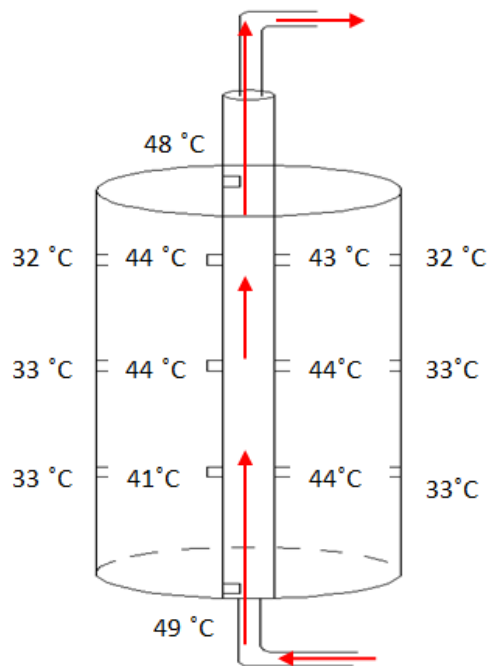


Figure A.100 Temperature distribution of a heating cycle after 72 hours

$$Q = \dot{m}c_p\Delta T_w$$

$$Q = \left(6825 \frac{\text{g}}{\text{hr}}\right) \left(1 \frac{\text{cal}}{\text{g}^\circ\text{C}}\right) (49 - 48^\circ\text{C})$$

$$Q = \left(6825 \frac{\text{cal}}{\text{hr}}\right) \frac{1.16 \times 10^{-3} \text{ Watts}}{\left(1 \frac{\text{cal}}{\text{hr}}\right)}$$

$$Q = 7.9 \text{ Watts}$$

$$k_t = \frac{Q \ln\left(\frac{R_2}{R_1}\right)}{2 \pi L \Delta T_g}$$

$$k_t = \frac{(7.9 \text{ Watts}) \ln\left(\frac{0.152 \text{ m}}{0.0254 \text{ m}}\right)}{2 \pi (0.3048 \text{ m})(44 - 32^\circ\text{C})}$$

$$k_t = 0.62 \text{ W/m} \cdot ^\circ\text{C}$$

Sample calculation for thermocouples 110 and 111 for a cooling cycle:

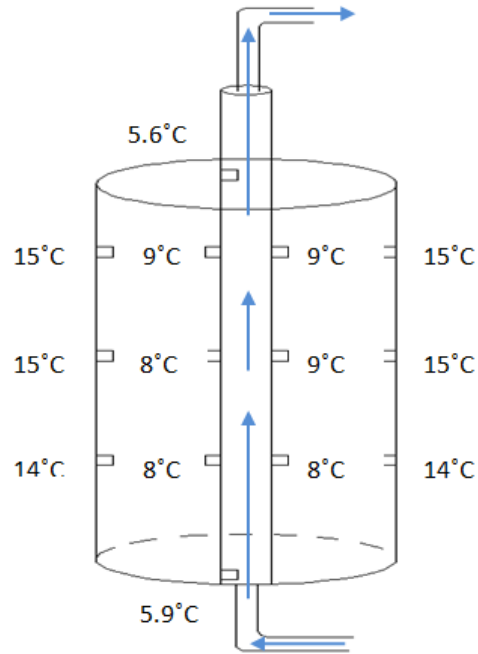


Figure A.101 Temperature distribution of a cooling cycle after 72 hours

$$Q = \dot{m}c_p\Delta T_w$$

$$Q = \left(6825 \frac{\text{g}}{\text{hr}}\right) \left(1 \frac{\text{cal}}{\text{g}^\circ\text{C}}\right) (5.9 - 5.6 \text{ }^\circ\text{C})$$

$$Q = \left(2048 \frac{\text{cal}}{\text{hr}}\right) \frac{1.16 \times 10^{-3} \text{ Watts}}{\left(1 \frac{\text{cal}}{\text{hr}}\right)}$$

$$Q = 2.4 \text{ Watts}$$

$$k_t = \frac{Q \ln\left(\frac{R_2}{R_1}\right)}{2 \pi L \Delta T_g}$$

$$k_t = \frac{(2.4 \text{ Watts}) \ln\left(\frac{0.152 \text{ m}}{0.0254 \text{ m}}\right)}{2 \pi (0.3048 \text{ m})(15 - 9 \text{ }^\circ\text{C})}$$

$$k_t = 0.37 \text{ W/m} \cdot ^\circ\text{C}$$

APPENDIX B

Table B.1 Raw data from consolidometer permeability test for sample 1

Date	Time	Min	Sec	Dial Reading (in)	Volume (ml)	Height (cm)	k (cm/s) x 10 ⁻⁸	Change in Dial Reading (in)
7-Jul-10	9:05pm	0	0	0.3131	7.6	47.6	4.05	0
8-Jul-10	10:00am	785	47100	0.3046	8.2	47.3	4.03	0.0085
8-Jul-10	8:00pm	1385	83100	0.3023	8.8	47	2.90	0.0108
9-Jul-10	10:00am	2198	131880	0.3012	9.2	46.9	2.58	0.0119
9-Jul-10	7:45pm	2783	166980	0.3006	9.4	46.8	2.16	0.0125
10-Jul-10	10:55am	3693	221580	0.3002	9.6	46.7	2.06	0.0129
10-Jul-10	8:30pm	4268	256080	0.2999	9.8	46.6	1.70	0.0132
11-Jul-10	11:30am	5168	310080	0.2995	9.8	46.6	1.53	0.0136

Table B.2 Raw data from consolidometer permeability test for sample 2

Date	Time	min	sec	Dial Reading (in)	Volume (ml)	Height (cm)	k (cm/s) x 10 ⁻⁸	Change in Dial Reading (in)
7-Jul-10	9:15pm	0	0	0.1306	6	48.5	1.01	0
8-Jul-10	10:00am	765	45900	0.1299	6.4	48.4	2.08	0.0007
8-Jul-10	8:10pm	1875	112500	0.1297	6.8	48	2.03	0.0009
9-Jul-10	10:00am	2705	162300	0.1298	7.2	47.8	1.66	0.0008
9-Jul-10	7:45pm	3290	197400	0.1298	7.2	47.8	1.49	0.0008
10-Jul-10	10:55am	4200	252000	0.1297	7.4	47.7	1.48	0.0009
10-Jul-10	8:35pm	4780	286800	0.1297	7.6	47.6	1.24	0.0009
11-Jul-10	11:30am	5675	340500	0.1295	7.6	47.6	1.26	0.0011

Table B.3 Raw data from consolidometer permeability test for sample 3

Date	Time	min	sec	Dial Reading (in)	Volume (ml)	Height (cm)	k (cm/s) x 10 ⁻⁸	Change in Dial Reading (in)
7-Jul-10	9:25pm	0	0	0.2484	4.6	50.9	3.92	0
8-Jul-10	10:05am	760	45600	0.2485	5.2	50.5	3.28	-1E-04
8-Jul-10	8:10pm	1365	81900	0.2486	5.4	50.3	3.40	-0.0002
9-Jul-10	10:05am	2200	132000	0.2487	6.2	49.9	2.69	-0.0003
9-Jul-10	7:45pm	2780	166800	0.2487	6.2	49.9	2.43	-0.0003
10-Jul-10	11:00am	3695	221700	0.2488	6.2	49.7	2.64	-0.0004
10-Jul-10	8:40pm	4275	256500	0.2471	6.4	49.4	2.48	0.0013
11-Jul-10	11:35am	5170	310200	0.2471	6.6	49.2	2.50	0.0013

Table B.5 Raw data for the triaxial permeability for Heating Cycle 1

porosity	n=																					
tube 2	area=	5.16	sq.cm	Average area=	5.185	sq.cm																
tube 3	area=	5.21	sq.cm																			
sample	area=	41.16	sq.cm																			
	length=	10.16	cm																			
Start time	Finish time	Elapsed time	Total elapsed	Pressure 1 (cell)	Pressure 2 (Inflow)	Pressure 3 (outflow)	Gradient	Burette Reading 1	Burette Reading 2	Burette Reading 3	Ho	Burette Reading 1	Burette Reading 2	Burette Reading 3	H1	Qin	Qout	K falling head (m/s)	K falling head (cm/s)	Qin-Qout	Qin/Qout	
[1] mm/dd/yy hh:mm	[2] mm/dd/yy hh:mm	(min)	ime (min)	(psi)	(psi)	(psi)		[1]	[1]	[1]	m	[2]	[2]	[2]	m	cc	cc	m/s	cm/s	cc		
10/18/2011 10:30	10/18/2011 19:33	543	543	45.5	43	40	20.75	7	13	19	2.177	8.5	13.1	18.3	2.168	0.52	3.65	8.29E-10	8.29E-08	-3.13	0.14	
10/18/2011 19:33	10/19/2011 9:55	862	1405	45.5	43	40	20.75	8.5	13.1	18.3	2.168	11.2	13.3	17.4	2.156	1.03	4.69	7.22E-10	7.22E-08	-3.66	0.22	
10/19/2011 9:55	10/19/2011 20:40	645	2050	45.5	43	40	20.75	11.2	13.3	17.4	2.156	13.2	13.3	16.9	2.150	0.00	2.61	4.40E-10	4.40E-08	-2.61	0.00	
10/19/2011 20:40	10/20/2011 11:55	915	2965	45.5	43	40	20.75	13.2	13.3	16.9	2.150	24.4	12.4	16.5	2.156	-4.64	2.08	□	□	-6.73	-2.23	
10/20/2011 11:55								24.4	12.4	16.5	0.047	0.0	0.0	0.0	0.000	-63.98	85.97			-149.95	-0.74	

Table B.9 Raw data for the triaxial permeability for Cooling Cycle 1

porosity	n=																					
tube 2	area=	5.16	sq.cm	Average area=	5.185	sq.cm																
tube 3	area=	5.21	sq.cm																			
sample	area=	41.16	sq.cm																			
	length=	10.16	cm																			
Start time	Finish time	Elapsed time (min)	Total elapsed time (min)	Pressure 1 (cell) (psi)	Pressure 2 (Inflow) (psi)	Pressure 3 (outflow) (psi)	Gradient	Burette Reading 1	Burette Reading 2	Burette Reading 3	Ho (m)	Burette Reading 1	Burette Reading 2	Burette Reading 3	H1 (m)	Qin (cc)	Qout (cc)	K falling head (m/s)	K falling head (cm/s)	Qin-Qout (cc)	Qin/Qout	
1] mm/dd/yy hh:mm	2] mm/dd/yy hh:mm	(min)	time (min)	(psi)	(psi)	(psi)		[1]	[1]	[1]	m	[2]	[2]	[2]	m	cc	cc	m/s	cm/s	cc		
10/20/2011 21:55	10/21/2011 8:30	635	635	45.5	43	40	20.75	4.7	16.5	22.5	2.177	10.6	16.5	22.3	2.175	0.00	1.04	1.77E-10	1.77E-08	-1.04	0.00	
10/21/2011 8:30	10/22/2011 10:00	1530	2165	45.5	43	40	20.75	10.6	16.5	22.3	2.175	14.2	17.1	22.1	2.166	3.10	1.04	2.94E-10	2.94E-08	2.05	2.97	
10/22/2011 10:00	10/22/2011 22:25	745	2910	45.5	43	40	20.75	14.2	17.1	22.1	2.166	15.7	17.5	22.1	2.161	2.06	0.00	3.03E-10	3.03E-08	2.06	#DIV/0!	
10/22/2011 22:25	10/23/2011 14:25	960	3870	45.5	43	40	20.75	15.7	17.5	22.1	2.161	17.4	18.0	22.0	2.154	2.58	0.52	3.54E-10	3.54E-08	2.06	4.95	
10/23/2011 14:25	10/23/2011 22:30	485	4355	45.5	43	40	20.75	17.4	18	22	2.154	18.2	18.2	22.0	2.152	1.03	0.00	2.34E-10	2.34E-08	1.03	#DIV/0!	
								18.2	18.2	22	0.044	0.0										

Table B.10 Raw data for the triaxial permeability for Cooling Cycle 2

porosity	n=																					
tube 2	area=	5.16	sq.cm	Average area=	5.185	sq.cm																
tube 3	area=	5.21	sq.cm																			
sample	area=	41.16	sq.cm																			
	length=	10.16	cm																			
Start time	Finish time	Elapsed time (min)	Total elapsed time (min)	Pressure 1 (cell) (psi)	Pressure 2 (Inflow) (psi)	Pressure 3 (outflow) (psi)	Gradient	Burette Reading 1	Burette Reading 2	Burette Reading 3	Ho (m)	Burette Reading 1	Burette Reading 2	Burette Reading 3	H1 (m)	Qin (cc)	Qout (cc)	K falling head (m/s)	K falling head (cm/s)	Qin-Qout (cc)	Qin/Qout	
1] mm/dd/yy hh:mm	2] mm/dd/yy hh:mm	(min)	time (min)	(psi)	(psi)	(psi)		[1]	[1]	[1]	m	[2]	[2]	[2]	m	cc	cc	m/s	cm/s	cc		
11/9/2011 12:30	11/9/2011 21:55	565	565	45.5	43	40	20.75	5	12.6	21.1	2.206	7.5	13.0	21.1	2.201	2.06	0.00	3.93E-10	3.93E-08	2.06	#DIV/0!	
11/9/2011 21:55	11/10/2011 14:35	1000	1565	45.5	43	40	20.75	7.5	13	21.1	2.201	9.4	13.4	21.1	2.197	2.06	0.00	2.22E-10	2.22E-08	2.06	#DIV/0!	
11/10/2011 14:35	11/11/2011 8:55	1100	2665	45.5	43	40	20.75	9.4	13.4	21.1	2.197	9.9	14.8	21.1	2.181	7.22	0.00	7.11E-10	7.11E-08	7.22	#DIV/0!	
11/11/2011 8:55	11/11/2011 22:45	830	3495	45.5	43	40	20.75	9.9	14.8	21.1	2.181	10.5	15.6	21.1	2.172	4.13	0.00	5.41E-10	5.41E-08	4.13	#DIV/0!	
11/11/2011 22:45	11/12/2011 10:40	715	4210	45.5	43	40	20.75	10.5	15.6	21.1	2.172	10.9	16.4	22.1	2.174	4.13	-5.21	□	□	9.34	-0.79	
11/12/2011 10:40	11/13/2011 10:57	1457	5667	45.5	43	40	20.75	10.9	16.4	22.1	2.174	0.0	0.0	0.0	2.109	-84.62	115.14	2.23E-09	2.23E-07	-199.77	-0.73	

The following is the raw data of the rigid wall/flow pump permeability tests (temperature readings of the water bath where the permeameter was submerged and the differential pressure readings). Also, the corresponding sample calculations for the conducted heating and cooling cycles are included

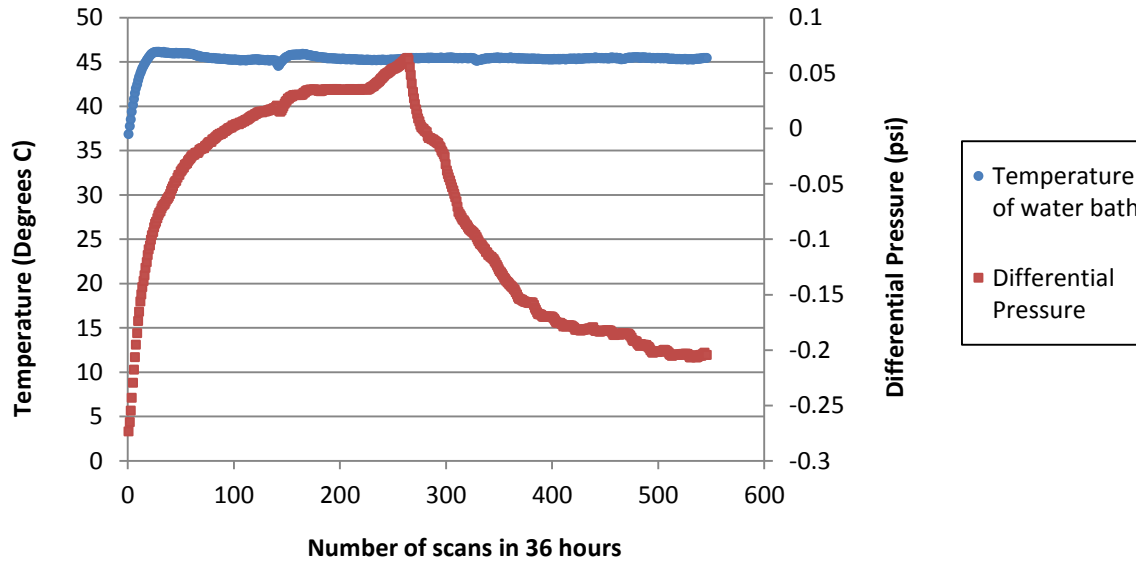


Figure B.1 Temperature of water bath and differential pressure readings for heating cycle 1

Sample calculations for heating cycle 1:

Area of sample, A	38.4	cm ²	density, ρ at 5 C (kg/m ³)	1000	μ at 5 C (N.s/m ²)	1.52E-03	g (m ² /s)	9.81	density, ρ at 49 C (kg/m ³)	988	μ at 49 C (N.s/m ²)	5.47E-04	
Length of sample, L	3.81	cm											
Flow Rate, q	0.000028	cm ³ /s											
Heating Cycle:		Infuse	Heating Cycle:					Refill					
Average Differential Pressure (psi)			Average Differential Pressure (psi)					Average Differential Pressure (psi)					
0.220			0.186					0.186					
h (cm)	15.52		h (cm)	14.96			h (cm)	14.96					
i	4.07		i	3.93			i	3.93					
k (cm/s)	1.79E-07		k (cm/s)	1.86E-07			k (cm/s)	1.86E-07					
k,intrinsic (m²)	1.01E-16		k,intrinsic (m²)	1.05E-16			k,intrinsic (m²)	1.05E-16					
k,intrinsic (cm²)	1.01E-12		k,intrinsic (cm²)	1.05E-12			k,intrinsic (cm²)	1.05E-12					
Average k	1.82E-07	cm/s											
Average ki	1.03E-12	cm ²											

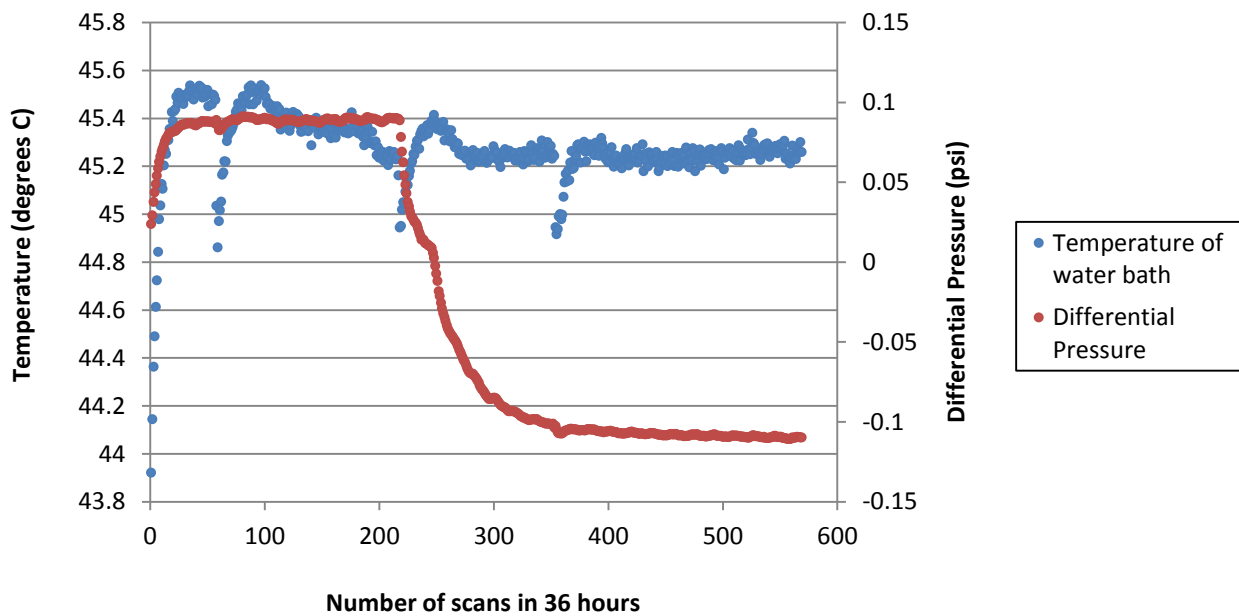


Figure B.2 Temperature of water bath and differential pressure readings for heating cycle 2

Sample calculations for heating cycle 2:

Area of sample, A	38.4	cm ²	density, ρ at 5 C (kg/m ³)	1000	μ at 5 C (N.s/m ²)	1.52E-03	g (m ² /s)	9.81	density, ρ at 49 C (kg/m ³)	988	μ at 49 C (N.s/m ²)	5.47E-04
Length of sample, L	3.81	cm										
Flow Rate, q	2.80E-05	cm ³ /s										
Heating Cycle : Infuse			Heating Cycle : Refill									
Average Differential Pressure (psi)			Average Differential Pressure (psi)									
0.090			0.110									
h (cm)	6.34		h (cm)	7.80								
i	1.66		i	2.05								
k (cm/s)	4.38E-07		k (cm/s)	3.56E-07								
k_i,intrinsic (m²)	2.47E-16		k_i,intrinsic (m²)	2.01E-16								
k_i,intrinsic (cm²)	2.47E-12		k_i,intrinsic (cm²)	2.01E-12								
Average k	3.97E-07	cm/s										
Average k_i	2.24E-12	cm ²										

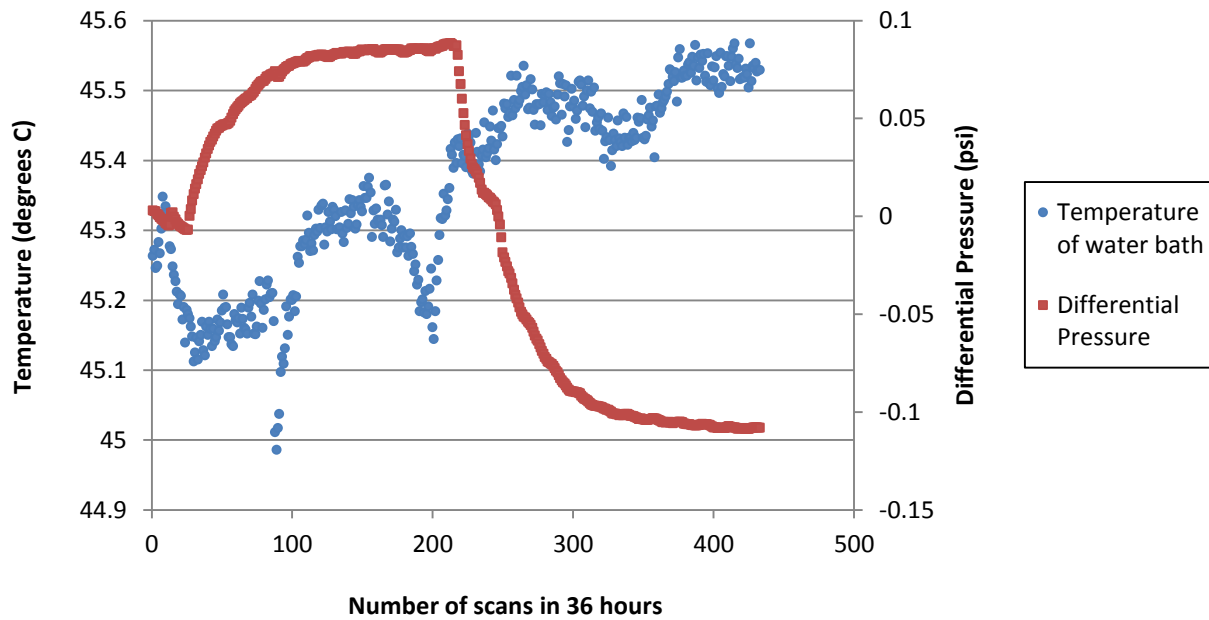


Figure B.3 Temperature of water bath and differential pressure readings for heating cycle 3

Sample calculations for heating cycle 3:

Area of sample, A	38.4	cm ²	density, ρ at 5 C (kg/m ³)	1000	μ at 5 C (N.s/m ²)	1.52E-03	g (m ² /s)	9.81	density, ρ at 49 C (kg/m ³)	988	μ at 49 C (N.s/m ²)	5.47E-04
Length of sample, L	3.81	cm										
Flow Rate, q	2.80E-05	cm ³ /s										
Heating Cycle : Infuse			Heating Cycle : Refill									
Average Differential Pressure (psi)	0.088		Average Differential Pressure (psi)									
			0.109									
h (cm)	6.19		h (cm)									
i	1.62		7.66									
k (cm/s)	4.49E-07		i									
k,intrinsic (m ²)	2.53E-16		2.01									
k,intrinsic (cm ²)	2.53E-12		k (cm/s)									
			3.63E-07									
Average k	4.06E-07	cm/s	k,intrinsic (m ²)									
Average ki	2.29E-12	cm ²	2.05E-16									
			k,intrinsic (cm ²)									
			2.05E-12									

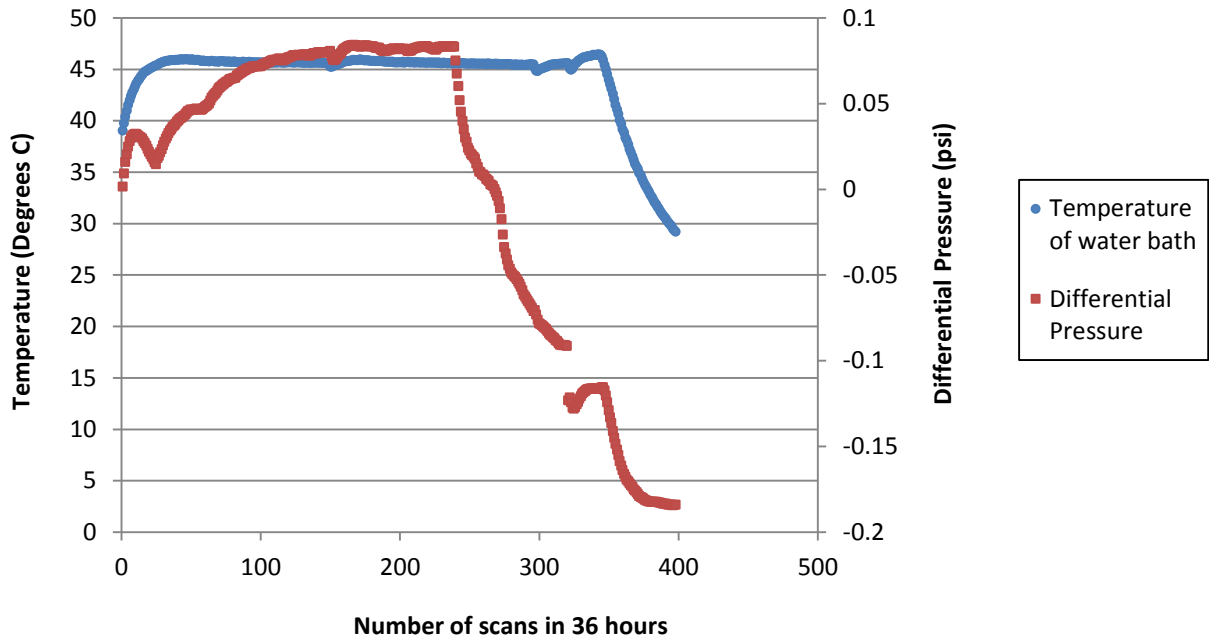


Figure B.4 Temperature of water bath and differential pressure readings for heating cycle 4

Sample calculations for heating cycle 4:

Area of sample, A	38.4	cm ²	density, ρ at 5 C (kg/m ³)	1000	μ at 5 C (N.s/m ²)	1.52E-03	g (m ² /s)	9.81	density, ρ at 49 C (kg/m ³)	988	μ at 49 C (N.s/m ²)	5.47E-04
Length of sample, L	3.81	cm										
Flow Rate, q	0.000028	cm ³ /s										
Heating Cycle : Infuse			Heating Cycle : Refill									
Average Differential Pressure (psi)			Average Differential Pressure (psi)									
0.065			0.082									
h (cm)			h (cm)									
4.57			5.80									
i			i									
1.20			1.52									
k (cm/s)			k (cm/s)									
6.08E-07			4.79E-07									
k,intrinsic (m ²)			k,intrinsic (m ²)									
3.43E-16			2.70E-16									
k,intrinsic (cm ²)			k,intrinsic (cm ²)									
3.43E-12			2.70E-12									
Average k	5.43E-07	cm/s										
Average ki	3.06E-12	cm ²										

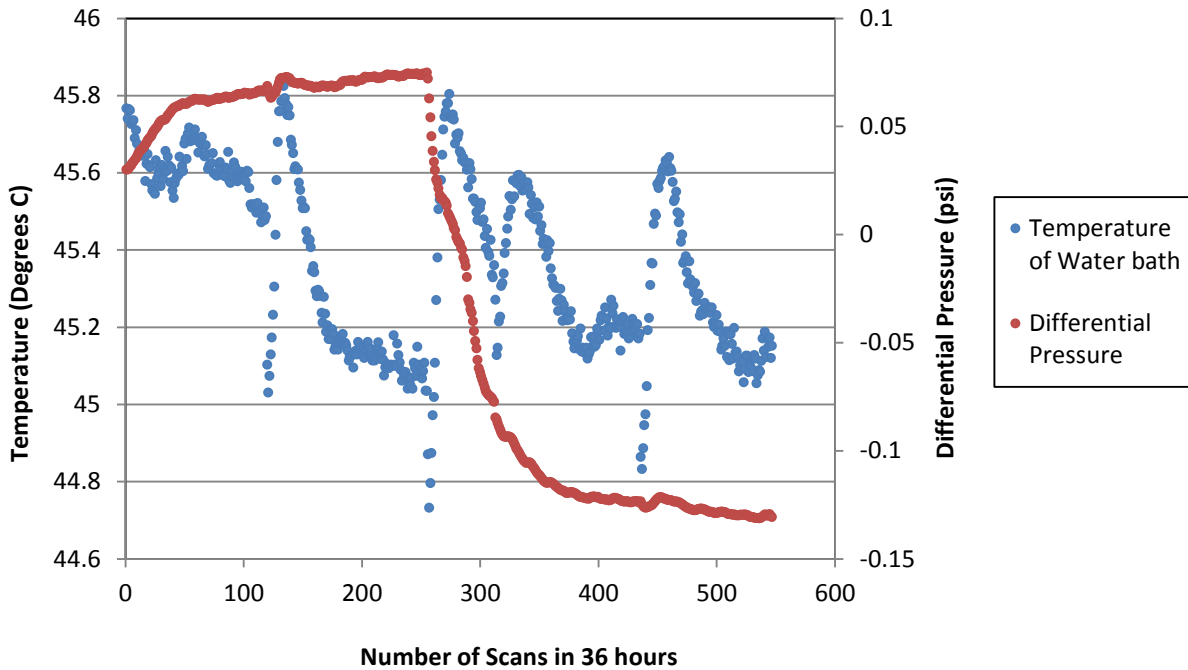


Figure B.5 Temperature of water bath and differential pressure readings for heating cycle 5

Sample calculations for heating cycle 5:

Area of sample, A	38.4	cm ²	density, ρ at 5 C (kg/m ³)	1000	μ at 5 C (N.s/m ²)	1.52E-03	g (m ² /s)	9.81	density, ρ at 49 C (kg/m ³)	988	μ at 49 C (N.s/m ²)	5.47E-04
Length of sample, L	3.81	cm										
Flow Rate, q	2.80E-05	cm ³ /s										
Heating Cycle : Infuse			Heating Cycle : Refill									
Average Differential Pressure (psi)			Average Differential Pressure (psi)									
0.064			0.095									
h (cm)	4.52		h (cm) 6.72									
i	1.19		i 1.76									
k (cm/s)	6.15E-07		k (cm/s) 4.13E-07									
k,intrinsic (m²)	3.47E-16		k,intrinsic (m²) 2.33E-16									
k,intrinsic (cm²)	3.47E-12		k,intrinsic (cm²) 2.33E-12									
Average k	5.14E-07	cm/s										
Average ki	2.90E-12	cm ²										

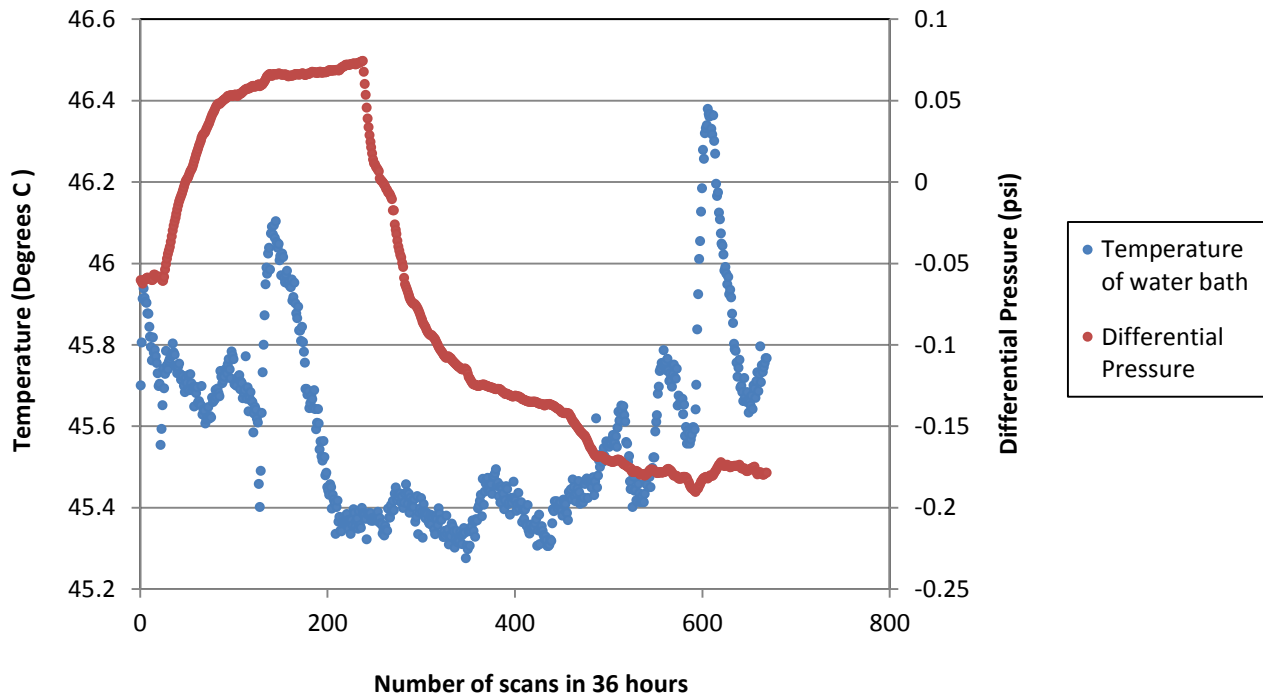


Figure B.6 Temperature of water bath and differential pressure readings for heating cycle 6

Sample calculations for heating cycle 6:

Area of sample, A	38.4	cm ²	density, ρ at 5 C (kg/m ³)	1000	μ at 5 C (N.s/m ²)	1.52E-03	g (m ² /s)	9.81	density, ρ at 49 C (kg/m ³)	988	μ at 49 C (N.s/m ²)	5.47E-04
Length of sample, L	3.81	cm										
Flow Rate, q	0.000028	cm ³ /s										
Heating Cycle : Infuse												
Average Differential Pressure (psi)												
0.035												
h (cm)	2.44											
i	0.64											
k (cm/s)	1.14E-06											
k,intrinsic (m ²)	6.43E-16											
k,intrinsic (cm ²)	6.43E-12											
Average k			7.23E-07	cm/s								
Average ki			4.08E-12	cm ²								
Heating Cycle : Refill												
Average Differential Pressure (psi)												
0.129												
h (cm)	9.08											
i	2.38											
k (cm/s)	3.06E-07											
k,intrinsic (m ²)	1.73E-16											
k,intrinsic (cm ²)	1.73E-12											

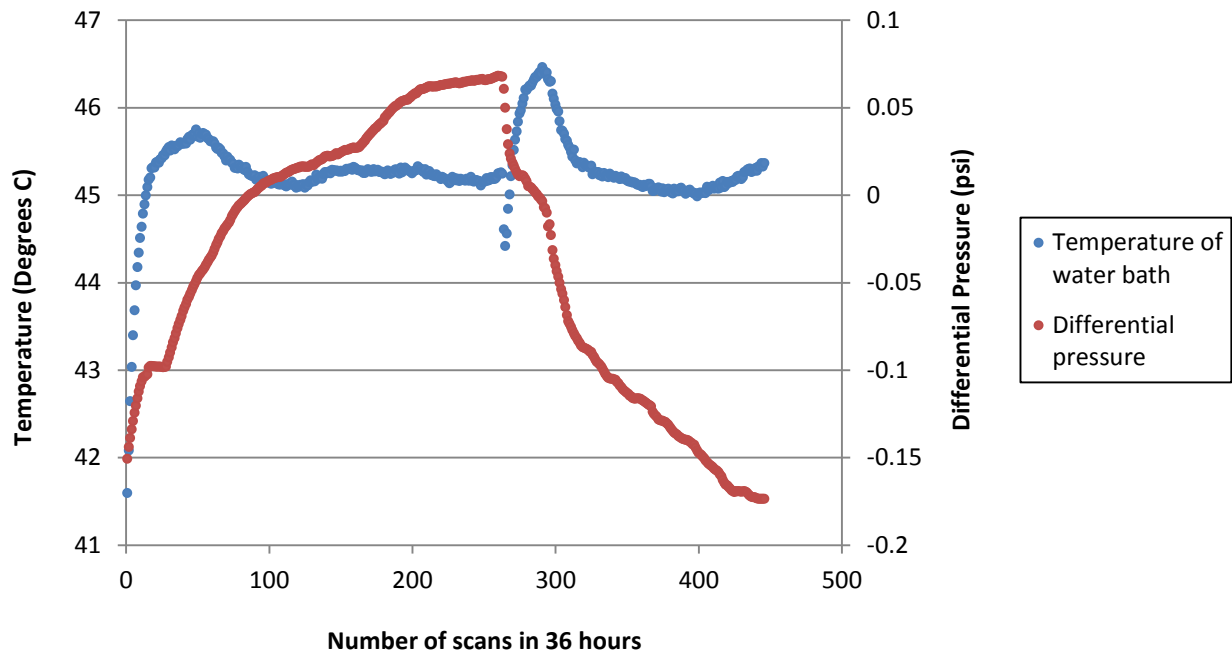


Figure B.7 Temperature of water bath and differential pressure readings for heating cycle 7

Sample calculations for heating cycle 7:

Area of sample, A	38.4	cm ²	density, ρ at 5 C (kg/m ³)	μ at 5 C (N.s/m ²)	g (m ² /s)	density, ρ at 49 C (kg/m ³)	μ at 49 C (N.s/m ²)
Length of sample, L	3.81	cm	1000	1.52E-03	9.81	988	5.47E-04
Flow Rate, q	0.000028	cm ³ /s					

Heating Cycle : Infuse	
Average Differential Pressure (psi)	
0.005	
h (cm)	0.32
i	0.09
k (cm/s)	8.55E-06
k_i,intrinsic (m²)	4.83E-15
k_i,intrinsic (cm²)	4.83E-11

Heating Cycle : Refill	
Average Differential Pressure (psi)	
0.095	
h (cm)	6.74
i	1.77
k (cm/s)	4.12E-07
k_i,intrinsic (m²)	2.33E-16
k_i,intrinsic (cm²)	2.33E-12

Average k	4.48E-06	cm/s
Average k_i	2.53E-11	cm ²

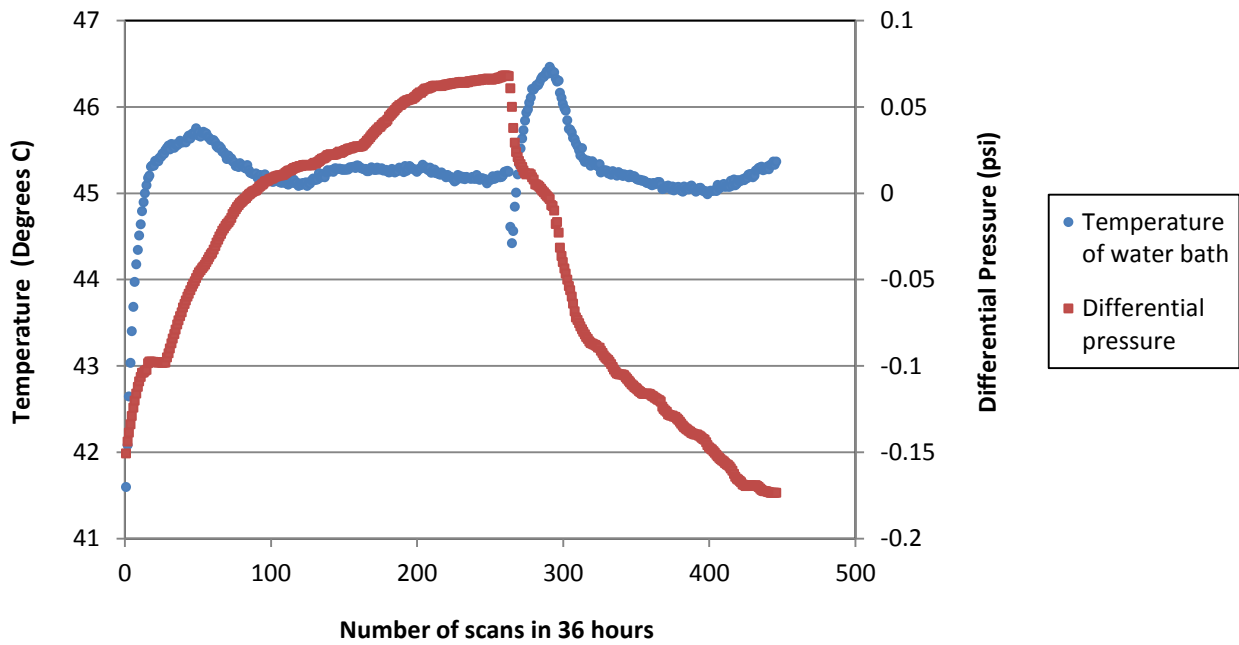


Figure B.8 Temperature of water bath and differential pressure readings for heating cycle 8

Sample calculations for heating cycle 8:

Area of sample, A	38.4	cm ²	density, ρ at 5 C (kg/m ³)	1000	μ at 5 C (N.s/m ²)	1.52E-03	g (m ² /s)	9.81	density, ρ at 49 C (kg/m ³)	988	μ at 49 C (N.s/m ²)	5.47E-04
Length of sample, L	3.81	cm										
Flow Rate, q	0.000028	cm ³ /s										
Heating Cycle : Infuse			Heating Cycle : Refill									
Average Differential Pressure (psi)			Average Differential Pressure (psi)									
0.005			0.095									
h (cm)	0.32		h (cm) 6.74									
i	0.09		i 1.77									
k (cm/s)	8.55E-06		k (cm/s) 4.12E-07									
k,intrinsic (m²)	4.83E-15		k,intrinsic (m²) 2.33E-16									
k,intrinsic (cm²)	4.83E-11		k,intrinsic (cm²) 2.33E-12									
Average k	4.48E-06	cm/s										
Average ki	2.53E-11	cm ²										

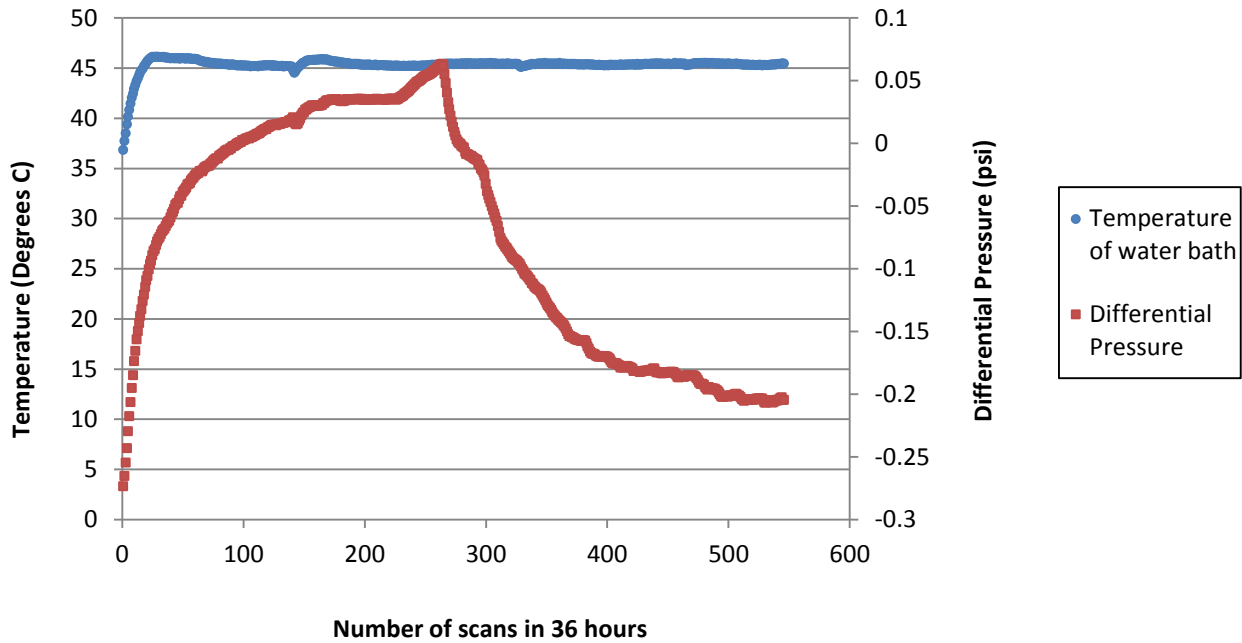


Figure B.9 Temperature of water bath and differential pressure readings for heating cycle 9

Sample calculations for heating cycle 9:

Area of sample, A	38.4	cm ²	density, ρ at 5 C (kg/m ³)	1000	μ at 5 C (N.s/m ²)	1.52E-03	g (m ² /s)	9.81	density, ρ at 49 C (kg/m ³)	988	μ at 49 C (N.s/m ²)	5.47E-04
Length of sample, L	3.81	cm										
Flow Rate, q	0.000028	cm ³ /s										
Heating Cycle : Infuse			Heating Cycle : Refill									
Average Differential Pressure (psi)	0.007		Average Differential Pressure (psi)									
			0.137									
h (cm)	0.49		h (cm)									
i	0.13		9.65									
k (cm/s)	5.64E-06		i									
k,intrinsic (m ²)	3.18E-15		2.53									
k,intrinsic (cm ²)	3.18E-11		k (cm/s)									
			2.88E-07									
Average k	2.96E-06	cm/s	k,intrinsic (m ²)									
Average ki	1.67E-11	cm ²	1.62E-16									
			k,intrinsic (cm ²)									
			1.62E-12									

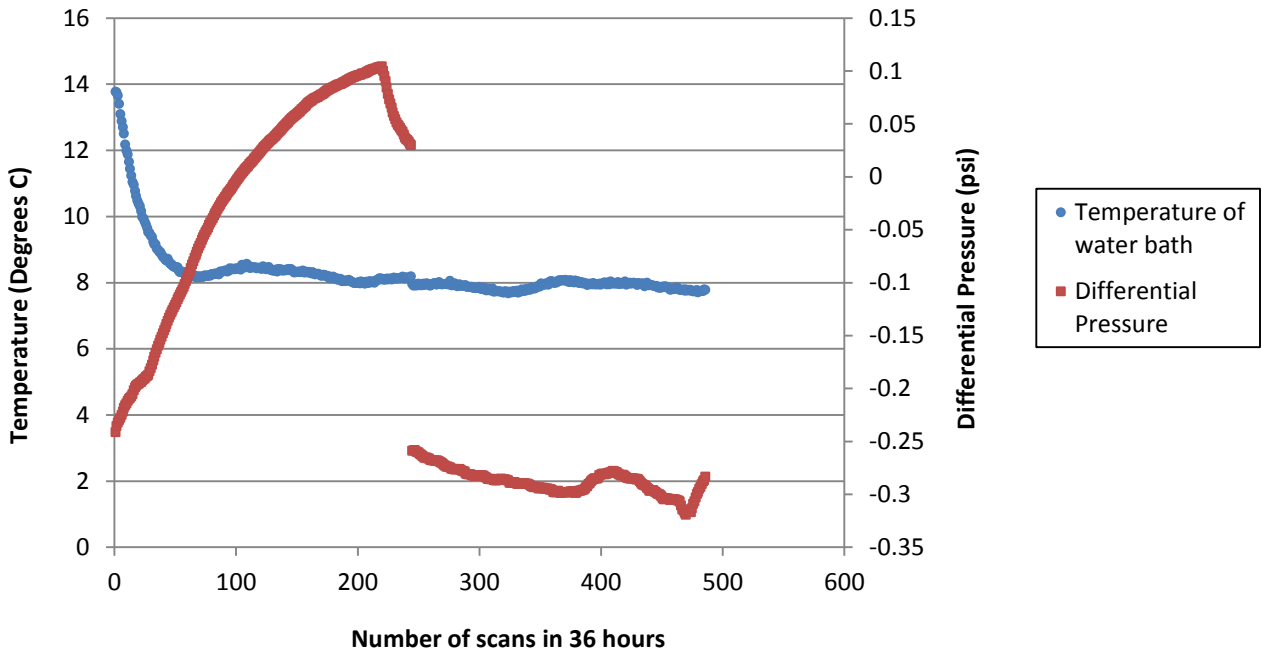


Figure B.10 Temperature of water bath and differential pressure readings for heating cycle 10

Sample calculations for heating cycle 10:

Area of sample, A	38.4	cm ²	density, ρ at 5 C (kg/m ³)	1000	μ at 5 C (N.s/m ²)	1.52E-03	g (m ² /s)	9.81	density, ρ at 49 C (kg/m ³)	988	μ at 49 C (N.s/m ²)	5.47E-04
Length of sample, L	3.81	cm										
Flow Rate, q	0.000028	cm ³ /s										
Heating Cycle : Infuse			Heating Cycle : Refill									
Average Differential Pressure (psi)			Average Differential Pressure (psi)									
0.001			-0.139									
h (cm)	0.08		h (cm)	-9.82								
i	0.02		i	-2.58								
k (cm/s)	3.52E-05		k (cm/s)	-2.83E-07								
k,intrinsic (m²)	1.99E-14		k,intrinsic (m²)	-1.60E-16								
k,intrinsic (cm²)	1.99E-10		k,intrinsic (cm²)	-1.60E-12								
Average k	1.75E-05	cm/s										
Average ki	9.86E-11	cm ²										

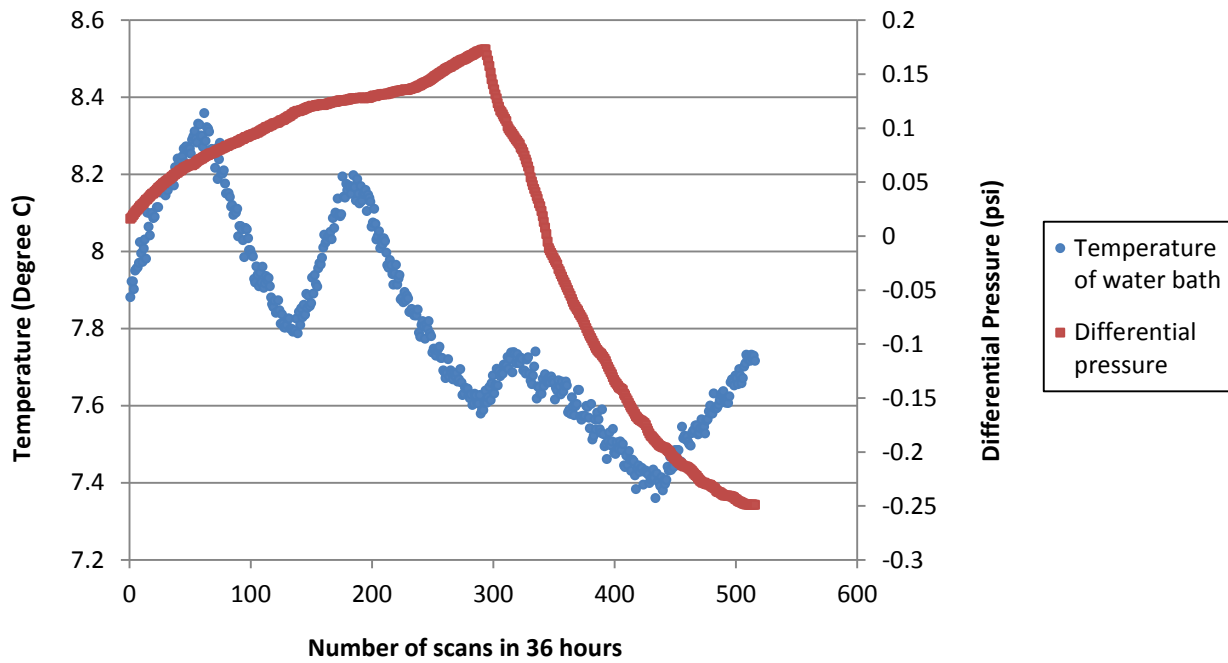


Figure B.11 Temperature of water bath and differential pressure readings for heating cycle 11

Sample calculations for heating cycle 11:

Area of sample, A	38.4	cm ²	density, ρ at 5 C (kg/m ³)	1000	μ at 5 C (N.s/m ²)	1.52E-03	g (m ² /s)	9.81	density, ρ at 49 C (kg/m ³)	988	μ at 49 C (N.s/m ²)	5.47E-04
Length of sample, L	3.81	cm										
Flow Rate, q	0.000028	cm ³ /s										
Heating Cycle : Infuse			Heating Cycle : Refill									
Average Differential Pressure (psi)			Average Differential Pressure (psi)									
0.066			0.108									
h (cm)	4.68		h (cm) 7.61									
i	1.23		i 2.00									
k (cm/s)	5.94E-07		k (cm/s) 3.65E-07									
k,intrinsic (m²)	3.35E-16		k,intrinsic (m²) 2.06E-16									
k,intrinsic (cm²)	3.35E-12		k,intrinsic (cm²) 2.06E-12									
Average k	4.79E-07	cm/s										
Average ki	2.71E-12	cm ²										

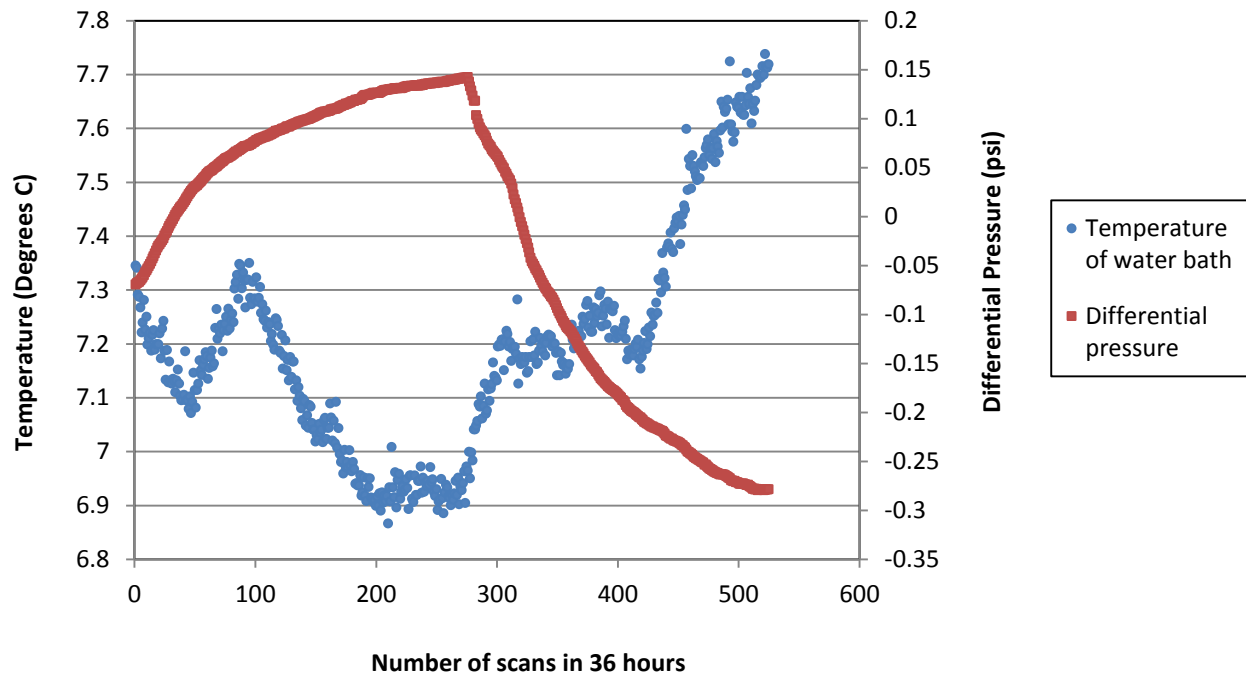


Figure B.12 Temperature of water bath and differential pressure readings for heating cycle 12

Sample calculations for heating cycle 12:

Area of sample, A	38.4	cm ²	density, ρ at 5 C (kg/m ³)	1000	μ at 5 C (N.s/m ²)	1.52E-03	g (m ² /s)	9.81	density, ρ at 49 C (kg/m ³)	988	μ at 49 C (N.s/m ²)	5.47E-04
Length of sample, L	3.81	cm										
Flow Rate, q	0.000028	cm ³ /s										
Heating Cycle : Infuse			Heating Cycle : Refill									
Average Differential Pressure (psi)	0.037		Average Differential Pressure (psi)	0.095								
h (cm)	2.59		h (cm)	6.71								
i	0.68		i	1.76								
k (cm/s)	1.07E-06		k (cm/s)	4.14E-07								
k,intrinsic (m²)	6.04E-16		k,intrinsic (m²)	2.34E-16								
k,intrinsic (cm²)	6.04E-12		k,intrinsic (cm²)	2.34E-12								
Average k	7.43E-07	cm/s										
Average ki	4.19E-12	cm ²										

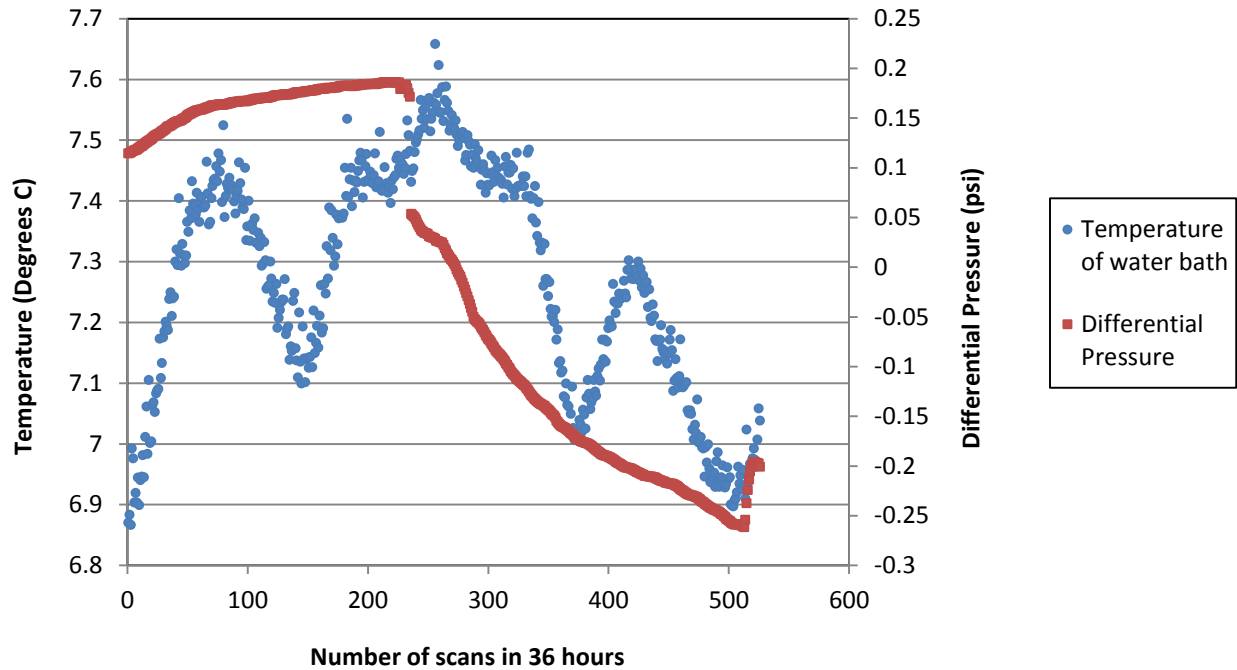


Figure B.13 Temperature of water bath and differential pressure readings for heating cycle 13

Sample calculations for heating cycle 13:

Area of sample, A	38.4	cm ²	density, ρ at 5 C (kg/m ³)	1000	μ at 5 C (N.s/m ²)	1.52E-03	g (m ² /s)	9.81	density, ρ at 49 C (kg/m ³)	988	μ at 49 C (N.s/m ²)	5.47E-04
Length of sample, L	3.81	cm										
Flow Rate, q	0.000028	cm ³ /s										
Heating Cycle : Infuse			Heating Cycle : Refill									
Average Differential Pressure (psi)	0.035		Average Differential Pressure (psi)	0.107								
h (cm)	2.46		h (cm)	7.53								
i	0.65		i	1.98								
k (cm/s)	1.13E-06		k (cm/s)	3.69E-07								
k,intrinsic (m²)	6.38E-16		k,intrinsic (m²)	2.08E-16								
k,intrinsic (cm²)	6.38E-12		k,intrinsic (cm²)	2.08E-12								
Average k	7.50E-07	cm/s										
Average ki	4.23E-12	cm ²										

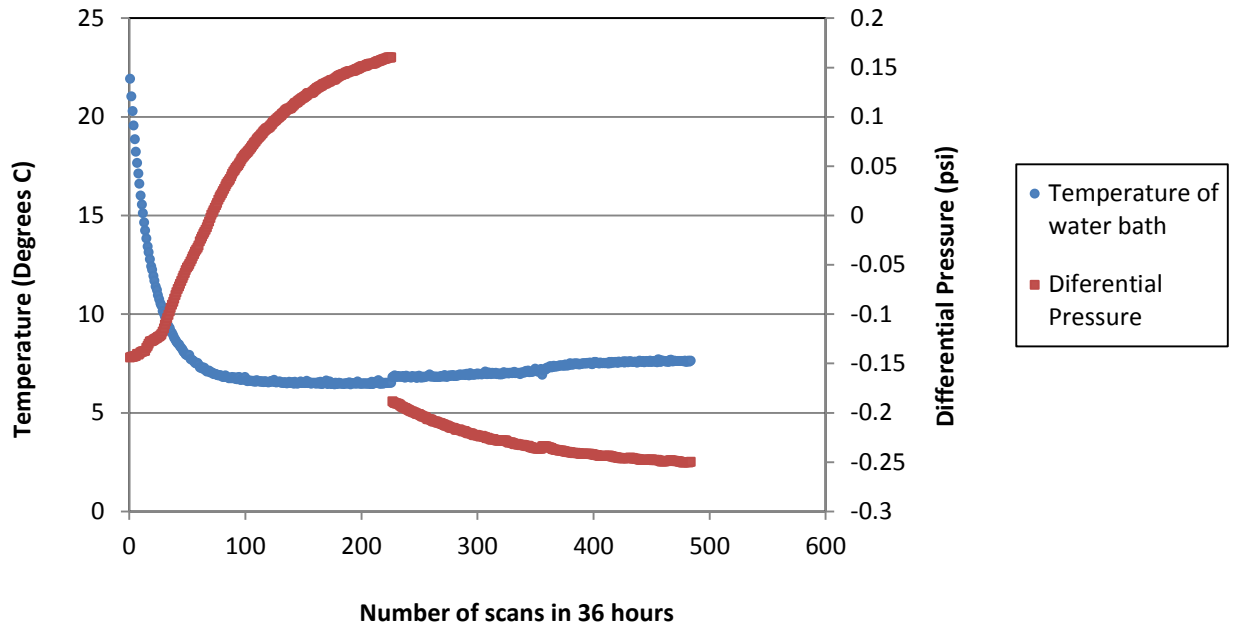


Figure B.14 Temperature of water bath and differential pressure readings for heating cycle 14

Sample calculations for heating cycle 14:

Area of sample, A	38.4	cm ²	density, ρ at 5 C (kg/m ³)	1000	μ at 5 C (N.s/m ²)	1.52E-03	g (m ² /s)	9.81	density, ρ at 49 C (kg/m ³)	988	μ at 49 C (N.s/m ²)	5.47E-04
Length of sample, L	3.81	cm										
Flow Rate, q	0.000028	cm ³ /s										
Heating Cycle : Infuse			Heating Cycle : Refill									
Average Differential Pressure (psi)			Average Differential Pressure (psi)									
0.041			0.102									
h (cm)			h (cm)									
2.90			7.19									
i			i									
0.76			1.89									
k (cm/s)			k (cm/s)									
9.58E-07			3.86E-07									
k,intrinsic (m²)			k,intrinsic (m²)									
5.41E-16			2.18E-16									
k,intrinsic (cm²)			k,intrinsic (cm²)									
5.41E-12			2.18E-12									
Average k			Average k									
6.72E-07			cm/s									
Average ki			Average ki									
3.79E-12			cm ²									

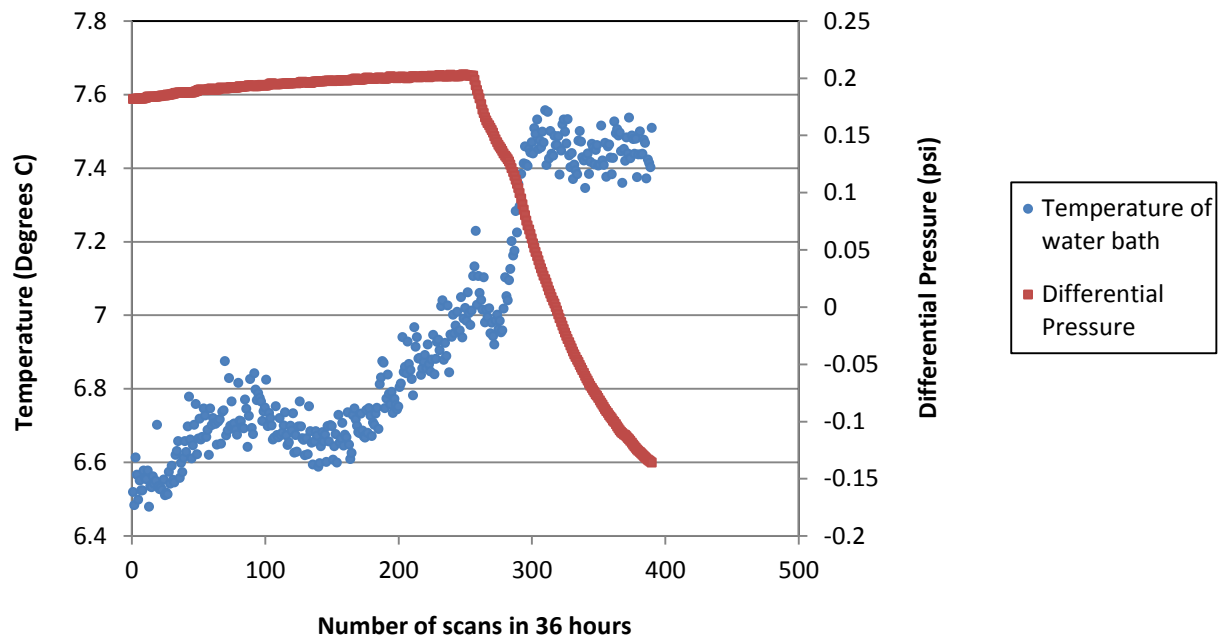


Figure B.15 Temperature of water bath and differential pressure readings for heating cycle 15

Sample calculations for heating cycle 15:

Area of sample, A	38.4	cm ²	density, ρ at 5 C (kg/m ³)	1000	μ at 5 C (N.s/m ²)	1.52E-03	g (m ² /s)	9.81	density, ρ at 49 C (kg/m ³)	988	μ at 49 C (N.s/m ²)	5.47E-04
Length of sample, L	3.81	cm										
Flow Rate, q	0.000028	cm ³ /s										
Heating Cycle : Infuse			Heating Cycle : Refill									
Average Differential Pressure (psi)	0.038		Average Differential Pressure (psi)									
	0.038		0.116									
h (cm)	2.67		h (cm)									
	2.67		8.20									
i	0.70		i									
	0.70		2.15									
k (cm/s)	1.04E-06		k (cm/s)									
	1.04E-06		3.39E-07									
k,intrinsic (m²)	5.88E-16		k,intrinsic (m²)									
	5.88E-16		1.91E-16									
k,intrinsic (cm²)	5.88E-12		k,intrinsic (cm²)									
	5.88E-12		1.91E-12									
Average k	6.90E-07	cm/s										
Average ki	3.90E-12	cm ²										

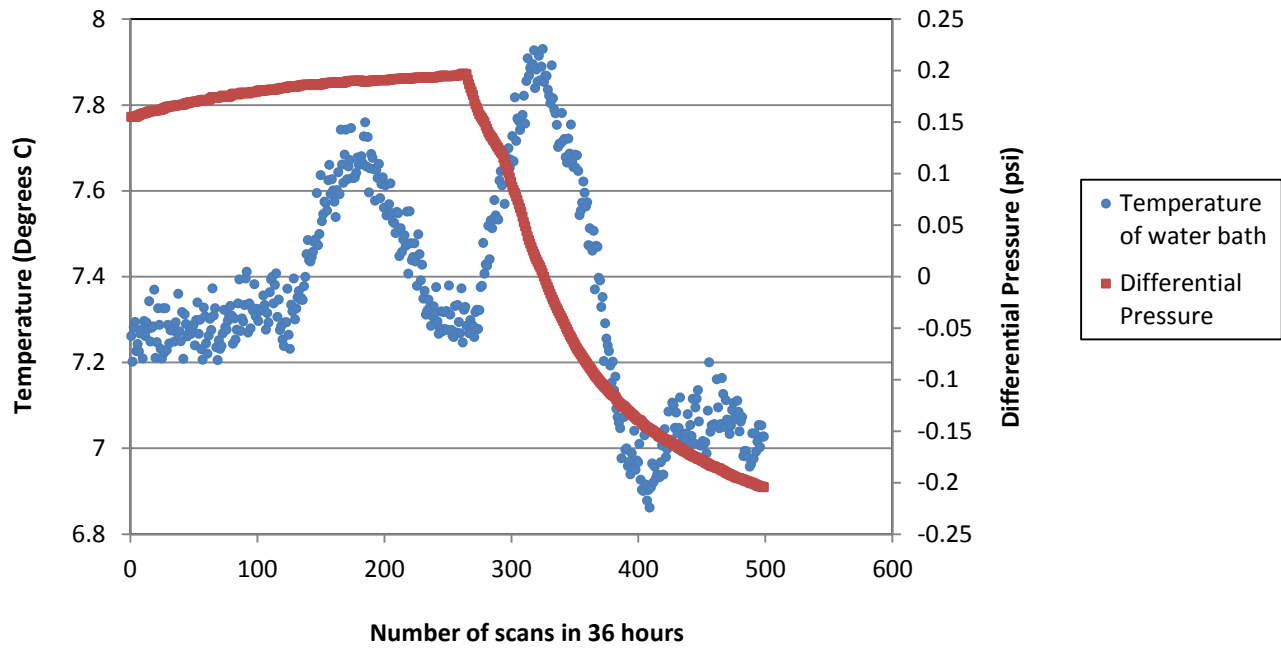


Figure B.16 Temperature of water bath and differential pressure readings for heating cycle 16

Sample calculations for heating cycle 16:

Area of sample, A	38.4	cm ²	density, ρ at 5 C (kg/m ³)	1000	μ at 5 C (N.s/m ²)	1.52E-03	g (m ² /s)	9.81	density, ρ at 49 C (kg/m ³)	988	μ at 49 C (N.s/m ²)	5.47E-04
Length of sample, L	3.81	cm										
Flow Rate, q	0.000028	cm ³ /s										
Heating Cycle : Infuse			Heating Cycle : Refill									
Average Differential Pressure (psi)	0.043		Average Differential Pressure (psi)									
			0.104									
h (cm)	3.04		h (cm)									
			7.31									
i	0.80		i									
			1.92									
k (cm/s)	9.15E-07		k (cm/s)									
			3.80E-07									
k,intrinsic (m²)	5.16E-16		k,intrinsic (m²)									
			2.15E-16									
k,intrinsic (cm²)	5.16E-12		k,intrinsic (cm²)									
			2.15E-12									
Average k	6.48E-07	cm/s										
Average ki	3.66E-12	cm ²										

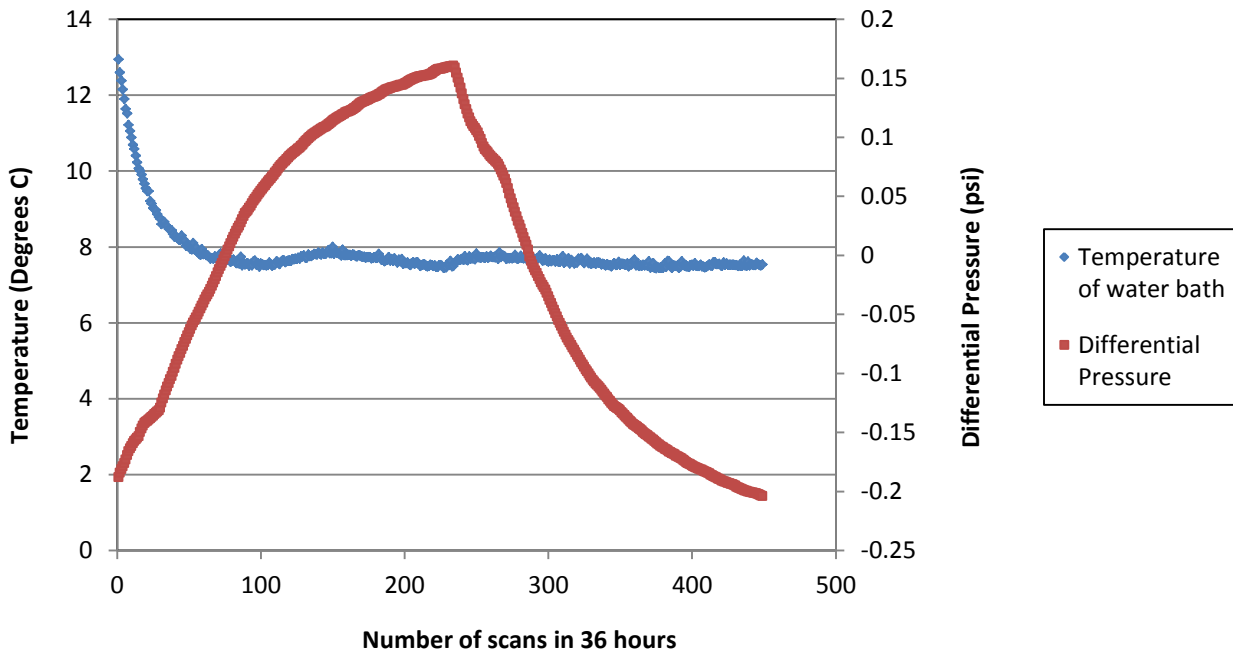


Figure B.17 Temperature of water bath and differential pressure readings for heating cycle 17

Sample calculations for heating cycle 17:

Area of sample, A	38.4	cm ²	density, ρ at 5 C (kg/m ³)	1000	μ at 5 C (N.s/m ²)	1.52E-03	g (m ² /s)	9.81	density, ρ at 49 C (kg/m ³)	988	μ at 49 C (N.s/m ²)	5.47E-04
Length of sample, L	3.81	cm										
Flow Rate, q	0.000028	cm ³ /s										
Heating Cycle : Infuse			Heating Cycle : Refill									
Average Differential Pressure (psi)			Average Differential Pressure (psi)									
0.044			0.127									
h (cm)			h (cm)									
3.10			8.93									
i			i									
0.81			2.34									
k (cm/s)			k (cm/s)									
8.97E-07			3.11E-07									
k,intrinsic (m²)			k,intrinsic (m²)									
5.07E-16			1.76E-16									
k,intrinsic (cm²)			k,intrinsic (cm²)									
5.07E-12			1.76E-12									
Average k			Average k									
6.04E-07 cm/s			6.04E-07 cm/s									
Average ki			Average ki									
3.41E-12 cm ²			3.41E-12 cm ²									

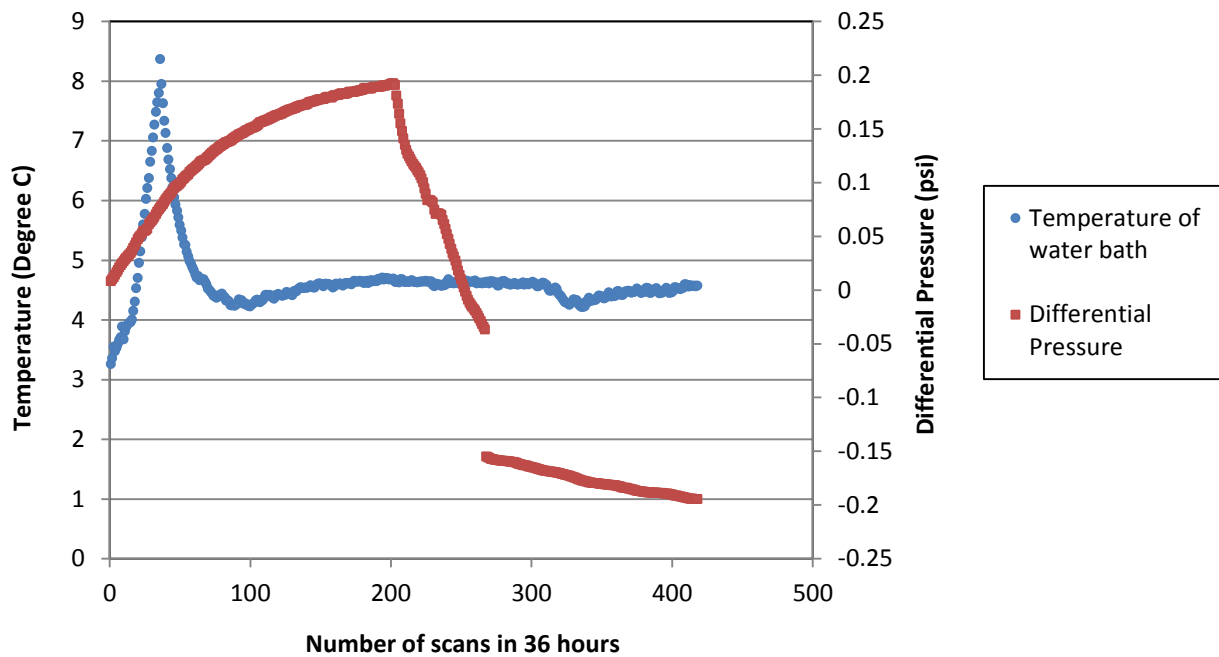


Figure B.18 Temperature of water bath and differential pressure readings for cooling cycle 1

Sample calculations for cooling cycle 1:

<u>Cooling Cycle :</u>		Infuse			<u>Cooling Cycle :</u>		Refill		
Average Differential Pressure (psi)					Average Differential Pressure (psi)				
0.212					0.219				
h (cm)		14.96			h (cm)		14.96		
i		3.93			i		3.93		
k (cm/s)		1.86E-07			k (cm/s)		1.86E-07		
k,intrinsic (m^2)		1.05E-16			k,intrinsic (m^2)		1.05E-16		
k,intrinsic (m^2)		1.05E-12			k,intrinsic (cm^2)		1.05E-12		
Average k		1.86E-07	cm/s						
Average ki		1.05E-12	cm^2						

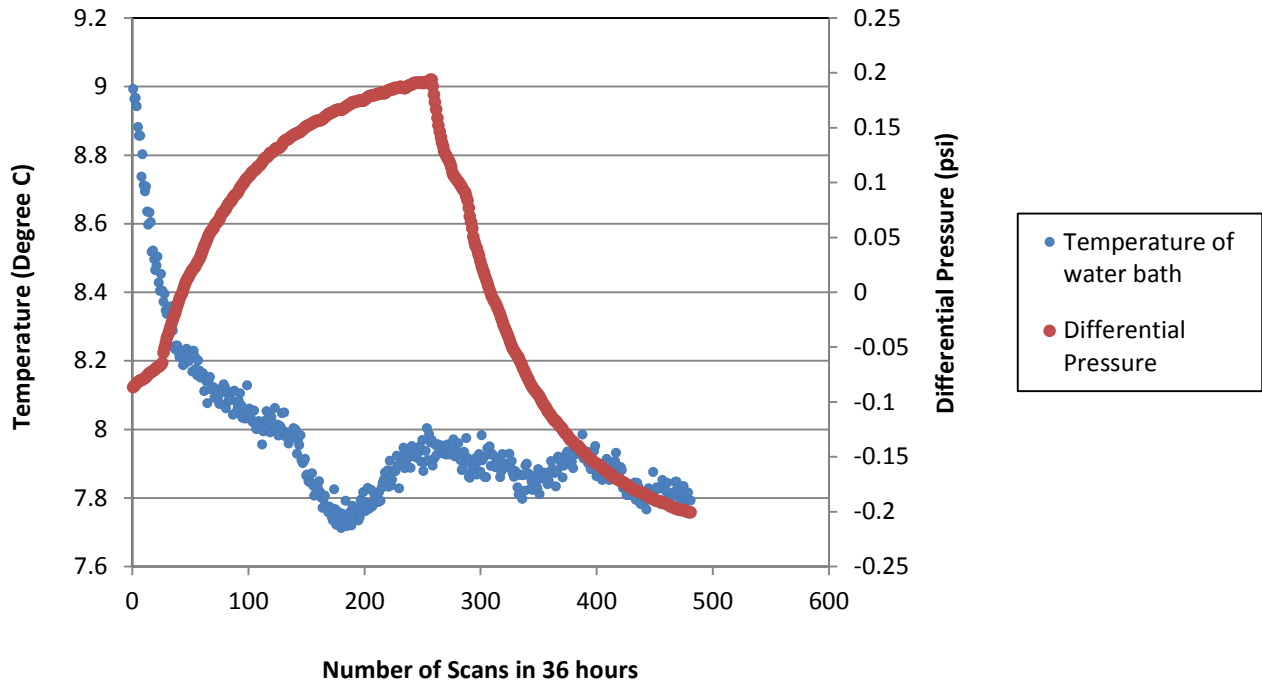


Figure B.19 Temperature of water bath and differential pressure readings for cooling cycle 2

Sample calculations for cooling cycle 2:

Area of sample, A	38.4	cm ²	density, ρ at 5 C (kg/m ³)	1000	μ at 5 C (N.s/m ²)	1.52E-03	density, ρ at 49 C (kg/m ³)	988	μ at 49 C (N.s/m ²)	5.47E-04
Length of sample, L	3.81	cm								
Flow Rate, q	2.80E-05	cm ³ /s								
Cooling Cycle : Infuse			Cooling Cycle : Refill							
Average Differential Pressure (psi)	0.190		Average Differential Pressure (psi)	0.200						
h (cm)	13.39		h (cm)	14.08						
i	3.51		i	3.70						
k (cm/s)	2.08E-07		k (cm/s)	1.97E-07						
k,intrinsic (m ²)	3.21E-16		k,intrinsic (m ²)	1.11E-16						
k,intrinsic (cm ²)	3.21E-12		k,intrinsic (cm ²)	1.11E-12						
Average k	2.02E-07	cm/s								
Average ki	2.16E-12	cm ²								

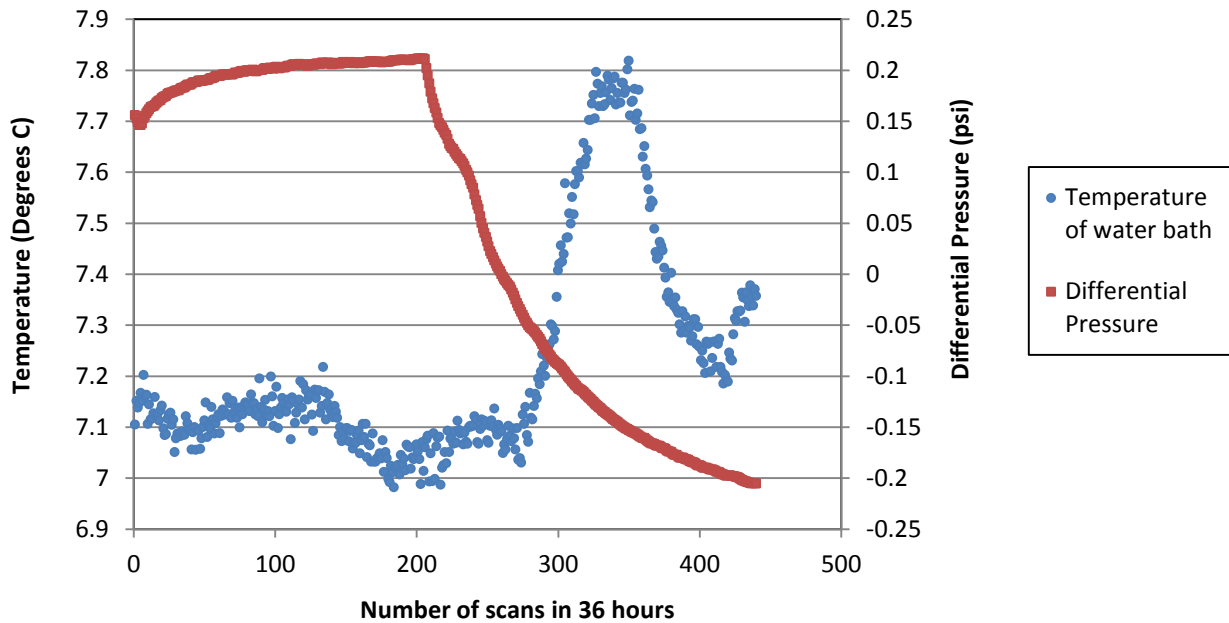


Figure B.21 Temperature of water bath and differential pressure readings for cooling cycle 4

Sample calculations for cooling cycle 4

Area of sample, A	38.4	cm ²	density, ρ at 5 C (kg/m ³)	1000	μ at 5 C (N.s/m ²)	1.52E-03	g (m ² /s)	9.81	density, ρ at 49 C (kg/m ³)	988	μ at 49 C (N.s/m ²)	5.47E-04
Length of sample, L	3.81	cm										
Flow Rate, q	0.000028	cm ³ /s										
Cooling Cycle : Infuse			Cooling Cycle : Refill									
Average Differential Pressure (psi)	0.196		Average Differential Pressure (psi)									
h (cm)	13.85		h (cm)									
i	3.64		i									
k (cm/s)	2.01E-07		k (cm/s)									
k,intrinsic (m ²)	3.11E-16		k,intrinsic (m ²)									
k,intrinsic (cm ²)	3.11E-12		k,intrinsic (cm ²)									
Average k	3.52E-07	cm/s	Average k									
Average ki	5.45E-12	cm ²	Average ki									

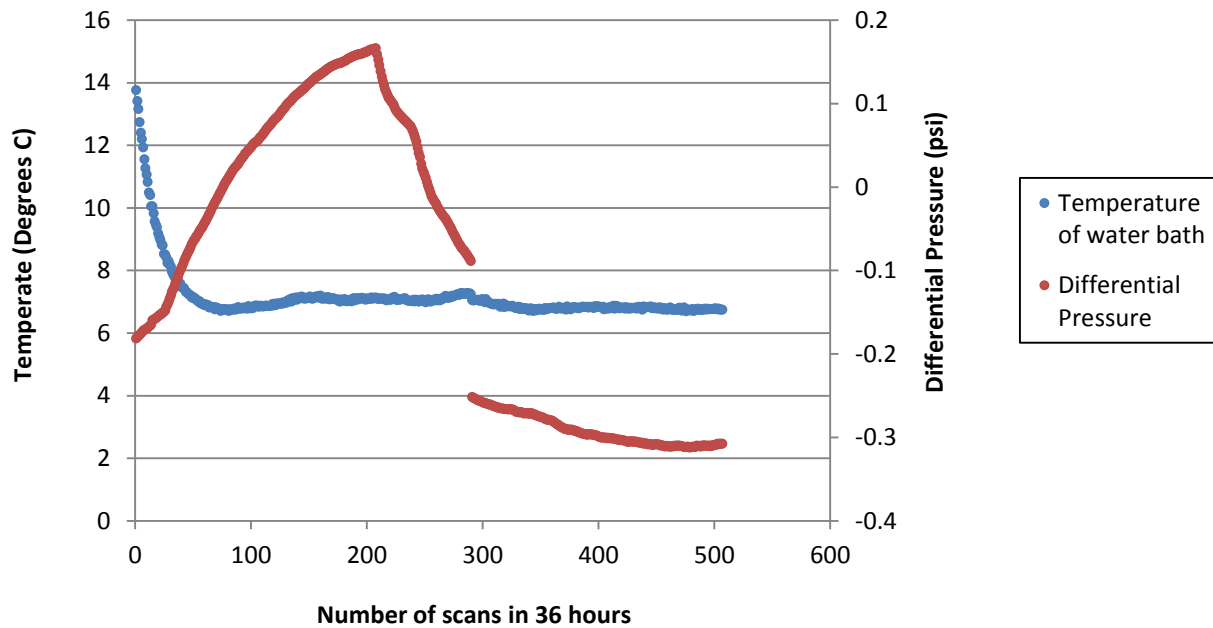


Figure B.22 Temperature of water bath and differential pressure readings for cooling cycle 5

Sample calculations for cooling cycle 5:

Area of sample, A	38.4	cm ²	density, ρ at 5 C (kg/m ³)	1000	μ at 5 C (N.s/m ²)	1.52E-03	g (m ² /s)	9.81	density, ρ at 49 C (kg/m ³)	988	μ at 49 C (N.s/m ²)	5.47E-04
Length of sample, L	3.81	cm										
Flow Rate, q	0.000028	cm ³ /s										
Cooling Cycle : Infuse			Cooling Cycle : Refill									
Average Differential Pressure (psi)	0.025		Average Differential Pressure (psi)	0.167								
h (cm)	1.76		h (cm)	11.78								
i	0.46		i	3.09								
k (cm/s)	1.58E-06		k (cm/s)	2.36E-07								
k,intrinsic (m ²)	2.44E-15		k,intrinsic (m ²)	3.65E-16								
k,intrinsic (cm ²)	2.44E-11		k,intrinsic (cm ²)	3.65E-12								
Average k	9.07E-07	cm/s										
Average ki	1.40E-11	cm ²										

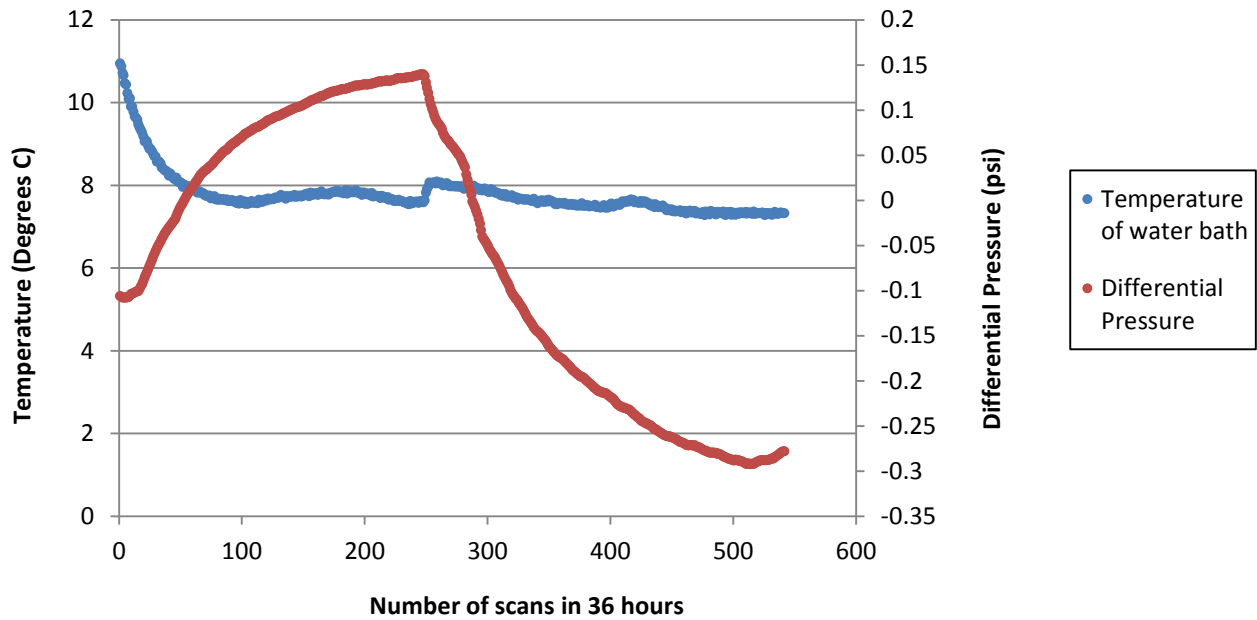


Figure B.23 Temperature of water bath and differential pressure readings for cooling cycle 6

Sample calculations for cooling cycle 6:

Area of sample, A	38.4	cm ²	density, ρ at 5 C (kg/m ³)	1000	μ at 5 C (N.s/m ²)	1.52E-03	g (m ² /s)	9.81	density, ρ at 49 C (kg/m ³)	988	μ at 49 C (N.s/m ²)	5.47E-04
Length of sample, L	3.81	cm										
Flow Rate, q	0.000028	cm ³ /s										
Cooling Cycle : Infuse			Cooling Cycle : Refill									
Average Differential Pressure (psi)	0.059		Average Differential Pressure (psi)	0.166								
h (cm)	4.19		h (cm)	11.70								
i	1.10		i	3.07								
k (cm/s)	6.63E-07		k (cm/s)	2.38E-07								
k,intrinsic (m ²)	1.03E-15		k,intrinsic (m ²)	3.68E-16								
k,intrinsic (cm ²)	1.03E-11		k,intrinsic (cm ²)	3.68E-12								
Average k	4.50E-07	cm/s										
Average ki	6.97E-12	cm ²										

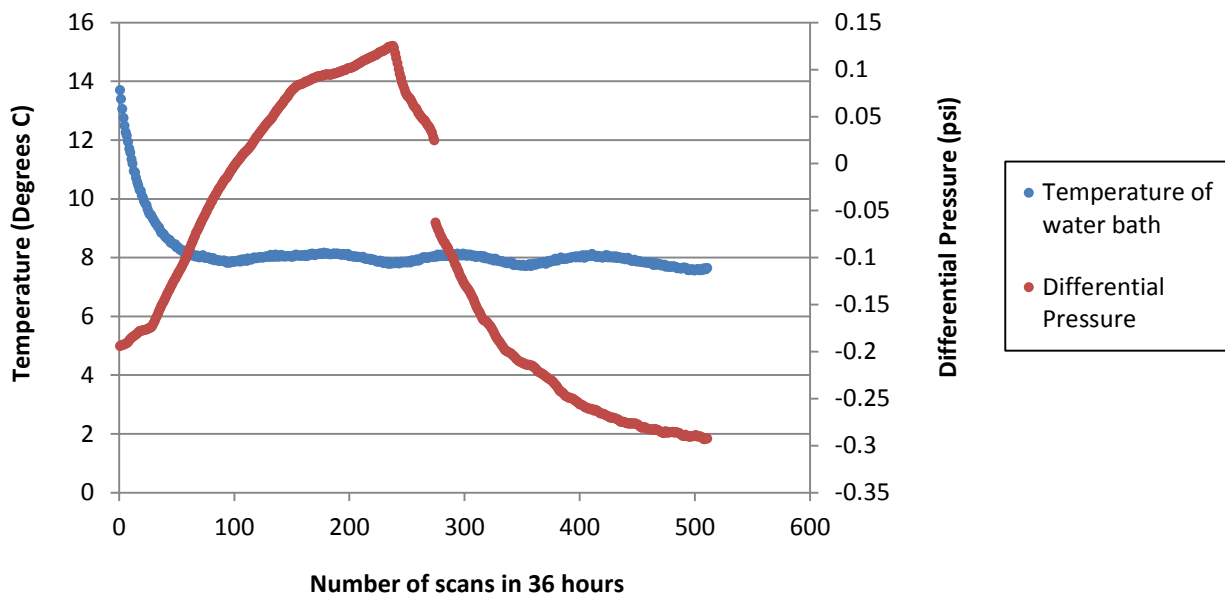


Figure B.24 Temperature of water bath and differential pressure readings for cooling cycle 7

Sample calculations for cooling cycle 7:

Area of sample, A	38.4	cm ²	density, ρ at 5 C (kg/m ³)	1000	μ at 5 C (N.s/m ²)	1.52E-03	g (m ² /s)	9.81	density, ρ at 49 C (kg/m ³)	988	μ at 49 C (N.s/m ²)	5.47E-04
Length of sample, L	3.81	cm										
Flow Rate, q	0.000028	cm ³ /s										
Cooling Cycle : Infuse			Cooling Cycle : Refill									
Average Differential Pressure (psi)	0.006		Average Differential Pressure (psi)	0.181								
h (cm)	0.39		h (cm)	12.78								
i	0.10		i	3.35								
k (cm/s)	7.07E-06		k (cm/s)	2.17E-07								
k,intrinsic (m ²)	1.09E-14		k,intrinsic (m ²)	3.37E-16								
k,intrinsic (cm ²)	1.09E-10		k,intrinsic (cm ²)	3.37E-12								
Average k	3.64E-06	cm/s										
Average ki	5.64E-11	cm ²										

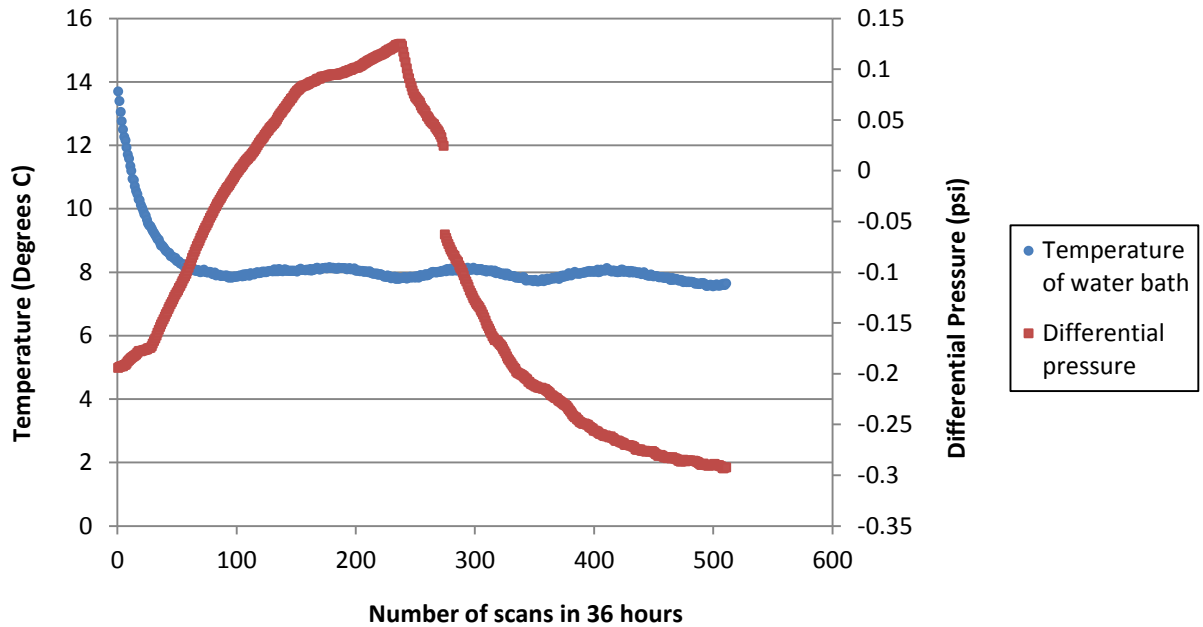


Figure B.25 Temperature of water bath and differential pressure readings for cooling cycle 8

Sample calculations for cooling cycle 8:

Area of sample, A	38.4	cm ²	density, ρ at 5 C (kg/m ³)	1000	μ at 5 C (N.s/m ²)	1.52E-03	g (m ² /s)	9.81	density, ρ at 49 C (kg/m ³)	988	μ at 49 C (N.s/m ²)	5.47E-04
Length of sample, L	3.81	cm										
Flow Rate, q	0.000028	cm ³ /s										
Cooling Cycle : Infuse			Cooling Cycle : Refill									
Average Differential Pressure (psi)			Average Differential Pressure (psi)									
0.008			0.175									
h (cm)			h (cm)									
0.59			12.33									
i			i									
0.15			3.24									
k (cm/s)			k (cm/s)									
4.72E-06			2.25E-07									
k,intrinsic (m²)			k,intrinsic (m²)									
7.31E-15			3.49E-16									
k,intrinsic (cm²)			k,intrinsic (cm²)									
7.31E-11			3.49E-12									
Average k			Average k									
2.47E-06			cm/s									
Average ki			Average ki									
3.83E-11			cm ²									

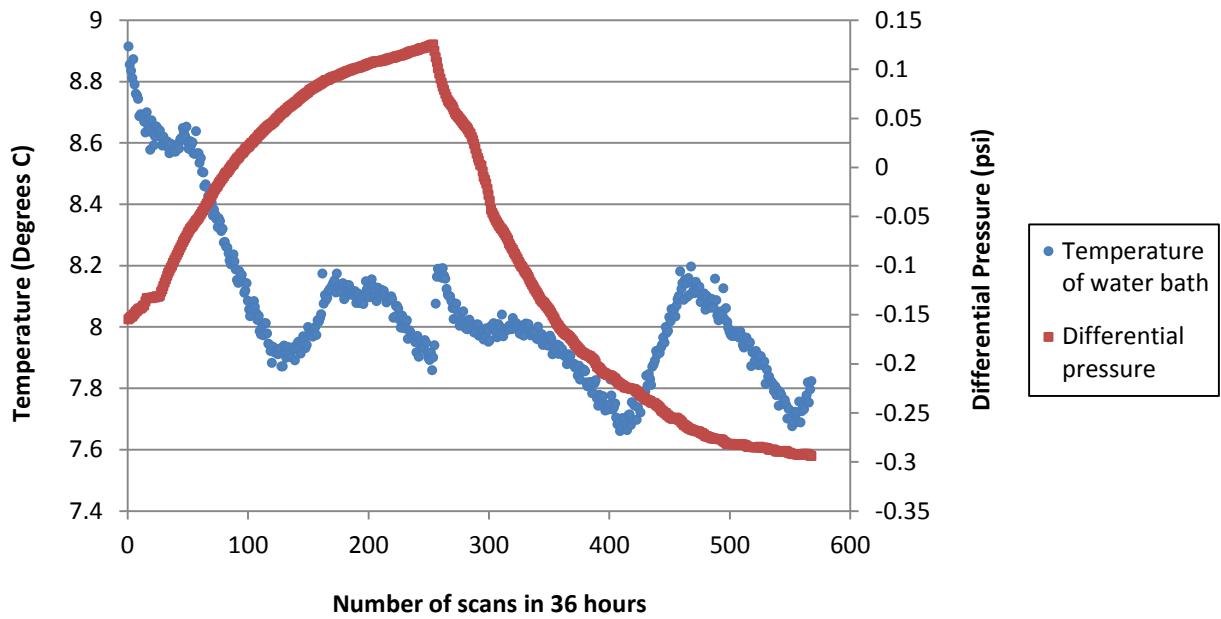


Figure B.26 Temperature of water bath and differential pressure readings for cooling cycle 9

Sample calculations for cooling cycle 9:

Area of sample, A	38.4	cm ²	density, ρ at 5 C (kg/m ³)	1000	μ at 5 C (N.s/m ²)	1.52E-03	g (m ² /s)	9.81	density, ρ at 49 C (kg/m ³)	988	μ at 49 C (N.s/m ²)	5.47E-04
Length of sample, L	3.81	cm										
Flow Rate, q	0.000028	cm ³ /s										
Cooling Cycle : Infuse			Cooling Cycle : Refill									
Average Differential Pressure (psi)	0.022		Average Differential Pressure (psi)									
			0.173									
h (cm)	1.58		h (cm)									
i	0.42		12.23									
k (cm/s)	1.75E-06		k (cm/s)									
k,intrinsic (m ²)	2.72E-15		2.27E-07									
k,intrinsic (cm ²)	2.72E-11		k,intrinsic (m ²)									
			3.52E-16									
			k,intrinsic (cm ²)									
			3.52E-12									
Average k	9.91E-07	cm/s										
Average ki	1.53E-11	cm ²										

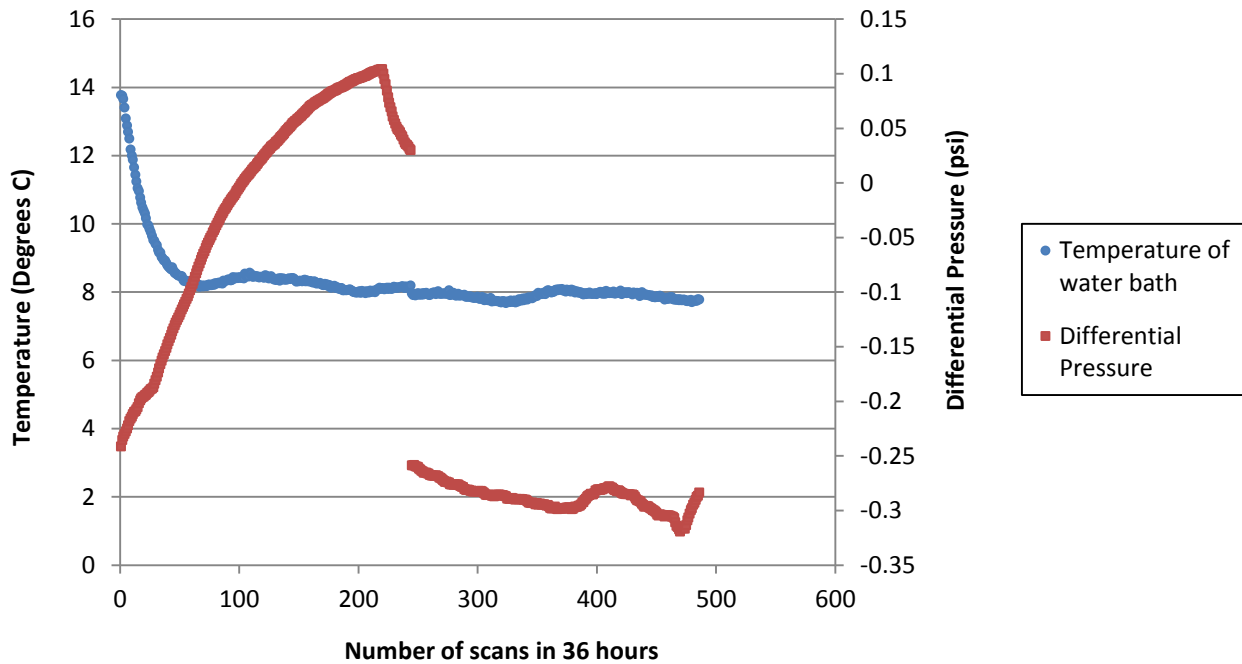


Figure B.27 Temperature of water bath and differential pressure readings for cooling cycle 10

Sample calculations for cooling cycle 10:

Area of sample, A	38.4	cm ²	density, ρ at 5 C (kg/m ³)	1000	μ at 5 C (N.s/m ²)	1.52E-03	g (m ² /s)	9.81	density, ρ at 49 C (kg/m ³)	988	μ at 49 C (N.s/m ²)	5.47E-04
Length of sample, L	3.81	cm										
Flow Rate, q	0.000028	cm ³ /s										
Cooling Cycle : Infuse			Cooling Cycle : Refill									
Average Differential Pressure (psi)			Average Differential Pressure (psi)									
0.016			0.288									
h (cm)			h (cm)									
1.10			20.35									
i			i									
0.29			5.34									
k (cm/s)			k (cm/s)									
2.53E-06			1.36E-07									
k,intrinsic (m²)			k,intrinsic (m²)									
3.91E-15			2.11E-16									
k,intrinsic (cm²)			k,intrinsic (cm²)									
3.91E-11			2.11E-12									
Average k			Average k									
1.33E-06			cm/s									
Average ki			Average ki									
2.06E-11			cm ²									

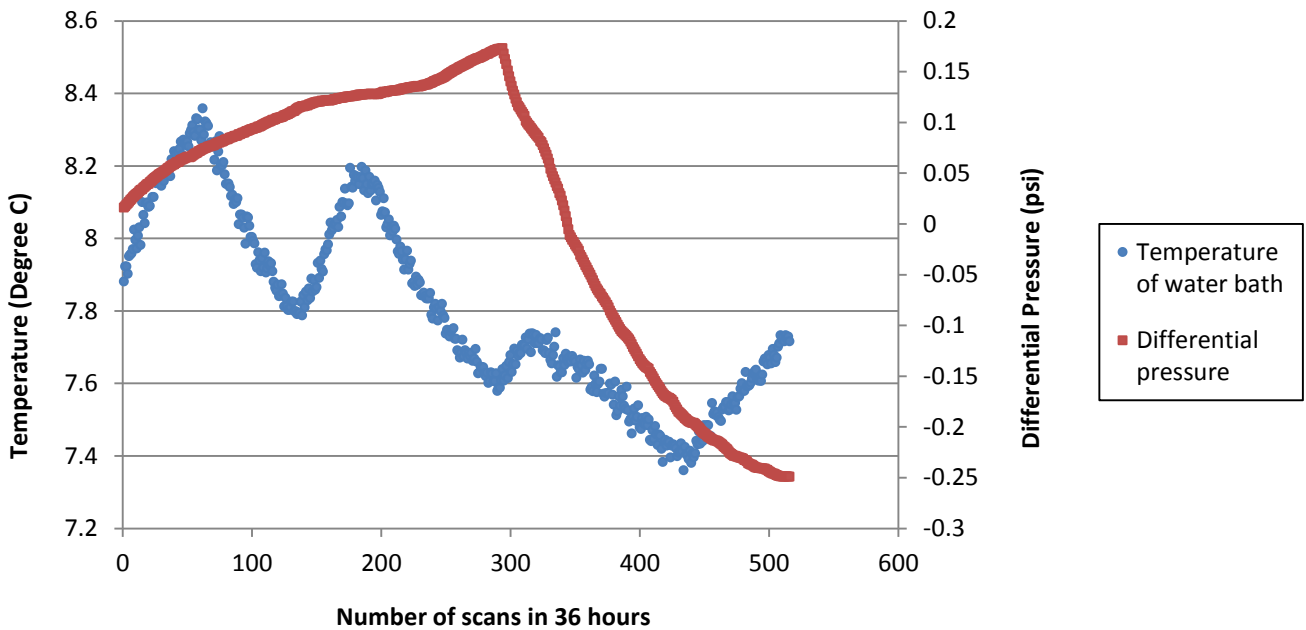


Figure B.28 Temperature of water bath and differential pressure readings for cooling cycle 11

Sample calculations for cooling cycle 11:

Area of sample, A	38.4	cm ²	density, ρ at 5 C (kg/m ³)	1000	μ at 5 C (N.s/m ²)	1.52E-03	g (m ² /s)	9.81	density, ρ at 49 C (kg/m ³)	988	μ at 49 C (N.s/m ²)	5.47E-04
Length of sample, L	3.81	cm										
Flow Rate, q	0.000028	cm ³ /s										
Cooling Cycle : Infuse			Cooling Cycle : Refill									
Average Differential Pressure (psi)	0.108		Average Differential Pressure (psi)									
h (cm)	7.59		h (cm)									
i	1.99		i									
k (cm/s)	3.66E-07		k (cm/s)									
k,intrinsic (m ²)	5.67E-16		k,intrinsic (m ²)									
k,intrinsic (cm ²)	5.67E-12		k,intrinsic (cm ²)									
Average k	3.68E-07	cm/s	Average k									
Average ki	5.70E-12	cm ²	Average ki									

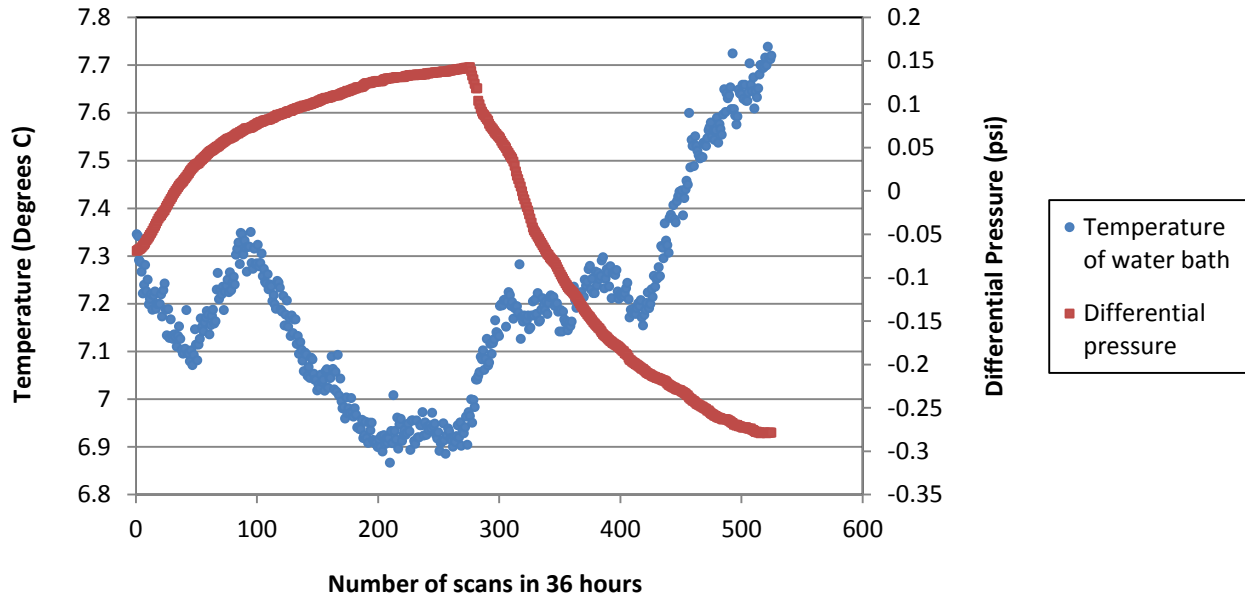


Figure B.29 Temperature of water bath and differential pressure readings for cooling cycle 12

Sample calculations for cooling cycle 12:

Area of sample, A	38.4	cm ²	density, ρ at 5 C (kg/m ³)	1000	μ at 5 C (N.s/m ²)	1.52E-03	g (m ² /s)	9.81	density, ρ at 49 C (kg/m ³)	988	μ at 49 C (N.s/m ²)	5.47E-04
Length of sample, L	3.81	cm										
Flow Rate, q	0.000028	cm ³ /s										
Cooling Cycle : Infuse			Cooling Cycle : Refill									
Average Differential Pressure (psi)			Average Differential Pressure (psi)									
0.081			0.146									
h (cm)	5.73		h (cm)		10.27							
i	1.50		i		2.70							
k (cm/s)	4.85E-07		k (cm/s)		2.70E-07							
k,intrinsic (m²)	7.51E-16		k,intrinsic (m²)		4.19E-16							
k,intrinsic (cm²)	7.51E-12		k,intrinsic (cm²)		4.19E-12							
Average k	3.78E-07	cm/s										
Average ki	5.85E-12	cm ²										

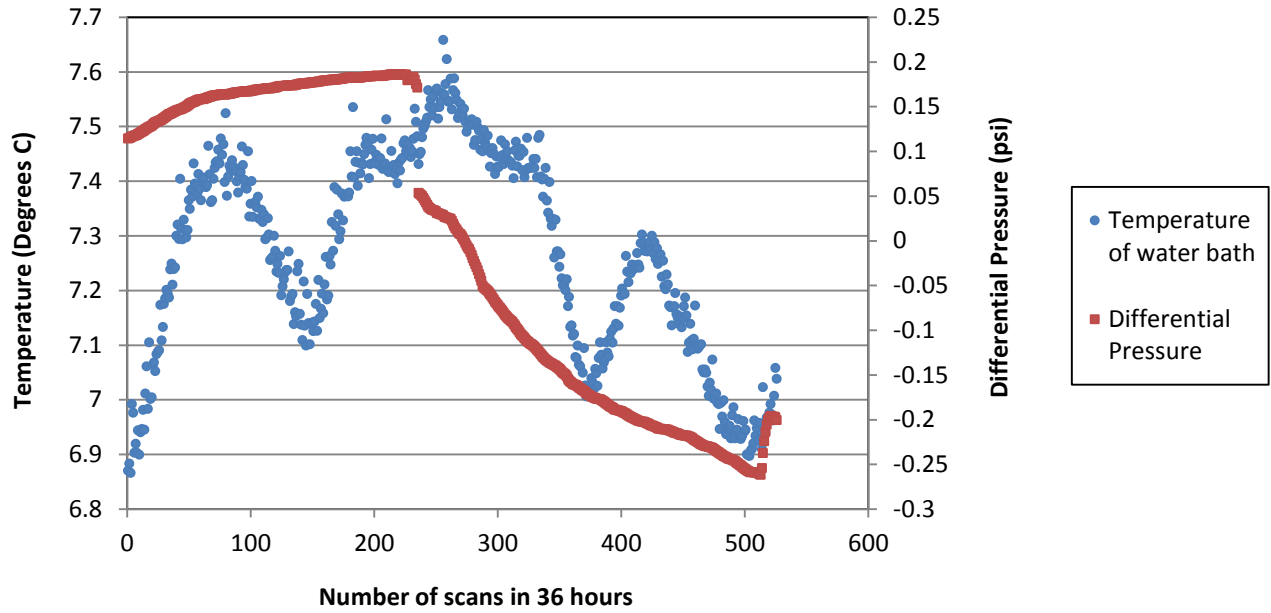


Figure B.30 Temperature of water bath and differential pressure readings for cooling cycle 13

Sample calculations for cooling cycle 13:

Area of sample, A	38.4	cm ²	density, ρ at 5 C (kg/m ³)	1000	μ at 5 C (N.s/m ²)	1.52E-03	g (m ² /s)	9.81	density, ρ at 49 C (kg/m ³)	988	μ at 49 C (N.s/m ²)	5.47E-04
Length of sample, L	3.81	cm										
Flow Rate, q	0.000028	cm ³ /s										
Cooling Cycle : Infuse			Cooling Cycle : Refill									
Average Differential Pressure (psi)	0.165		Average Differential Pressure (psi)	0.142								
h (cm)	11.66		h (cm)	10.03								
i	3.06		i	2.63								
k (cm/s)	2.38E-07		k (cm/s)	2.77E-07								
k,intrinsic (m²)	3.69E-16		k,intrinsic (m²)	4.29E-16								
k,intrinsic (cm²)	3.69E-12		k,intrinsic (cm²)	4.29E-12								
Average k	2.58E-07	cm/s										
Average ki	3.99E-12	cm ²										

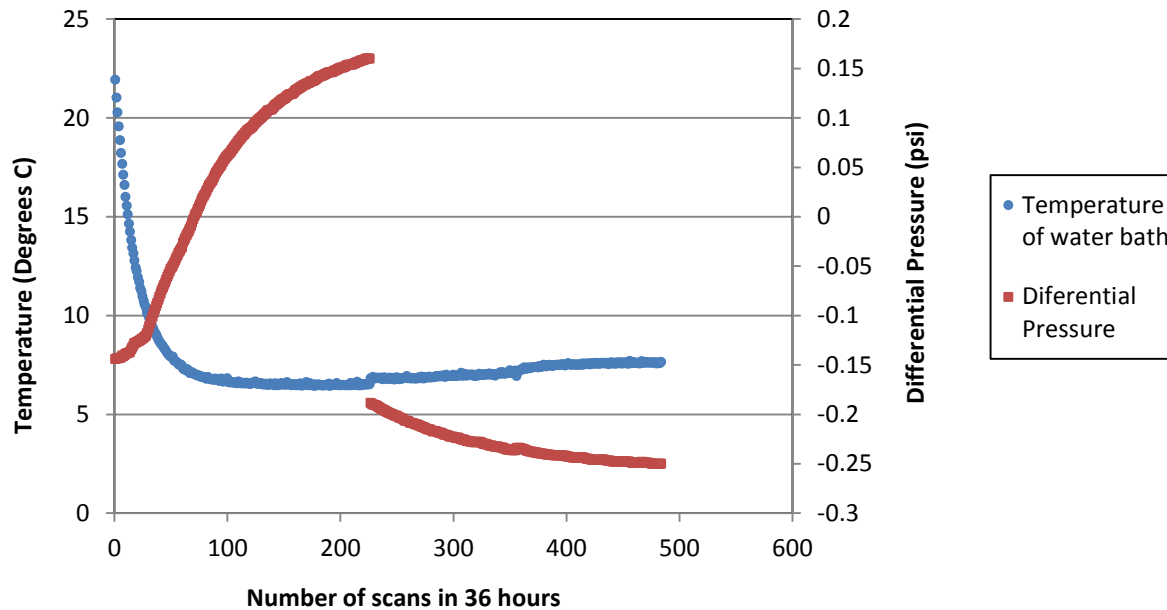


Figure B.31 Temperature of water bath and differential pressure readings for cooling cycle 14

Sample calculations for cooling cycle 14;

Area of sample, A	38.4	cm ²	density, ρ at 5 C (kg/m ³)	μ at 5 C (N.s/m ²)	g (m ² /s)	density, ρ at 49 C (kg/m ³)	μ at 49 C (N.s/m ²)
Length of sample, L	3.81	cm	1000	1.52E-03	9.81	988	5.47E-04
Flow Rate, q	0.000028	cm ³ /s					

Cooling Cycle :		Infuse	Cooling Cycle :		Refill
Average Differential Pressure (psi)			Average Differential Pressure (psi)		
0.046			0.231		
h (cm)	3.25		h (cm)	16.29	
i	0.85		i	4.28	
k (cm/s)	8.54E-07		k (cm/s)	1.71E-07	
k,intrinsic (m ²)	1.32E-15		k,intrinsic (m ²)	2.64E-16	
k,intrinsic (cm ²)	1.32E-11		k,intrinsic (cm ²)	2.64E-12	
Average k	5.12E-07	cm/s			
Average ki	7.93E-12	cm ²			

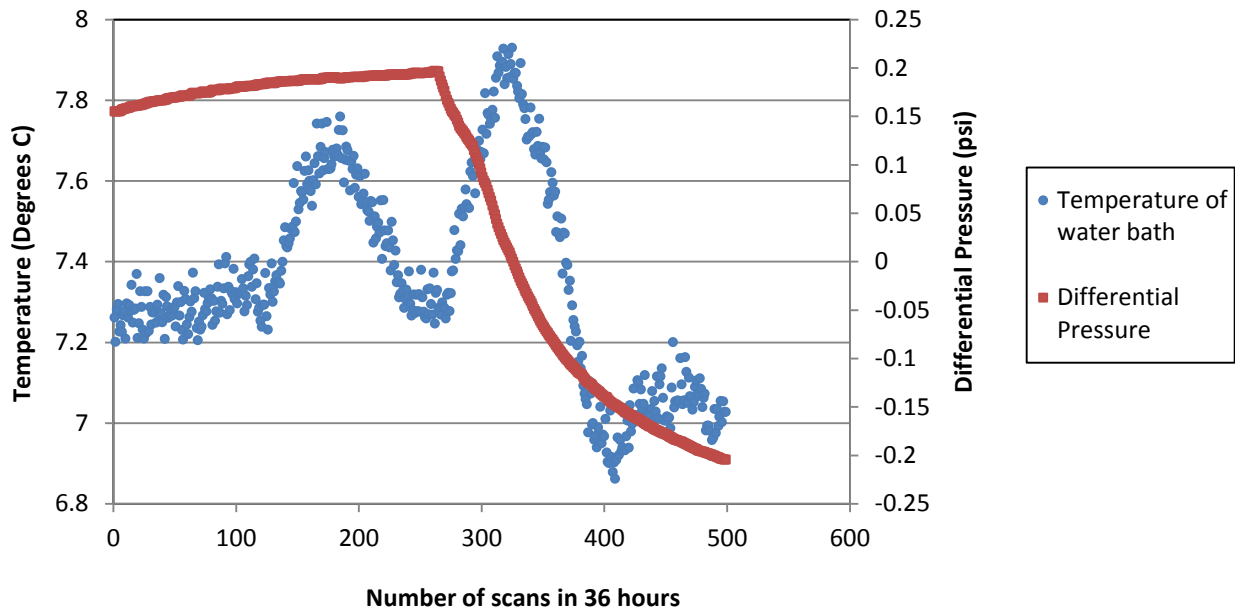


Figure B.33 Temperature of water bath and differential pressure readings for cooling cycle 16

Sample calculations for cooling cycle 16:

Area of sample, A	38.4	cm ²	density, ρ at 5 C (kg/m ³)	1000	μ at 5 C (N.s/m ²)	1.52E-03	g (m ² /s)	9.81	density, ρ at 49 C (kg/m ³)	988	μ at 49 C (N.s/m ²)	5.47E-04
Length of sample, L	3.81	cm										
Flow Rate, q	0.000028	cm ³ /s										
Heating Cycle : Infuse			Heating Cycle : Refill									
Average Differential Pressure (psi)			Average Differential Pressure (psi)									
0.043			0.104									
h (cm)	3.04		h (cm)	7.31								
i	0.80		i	1.92								
k (cm/s)	9.15E-07		k (cm/s)	3.80E-07								
k,intrinsic (m²)	5.16E-16		k,intrinsic (m²)	2.15E-16								
k,intrinsic (cm²)	5.16E-12		k,intrinsic (cm²)	2.15E-12								
Average k	6.48E-07	cm/s										
Average ki	3.66E-12	cm ²										

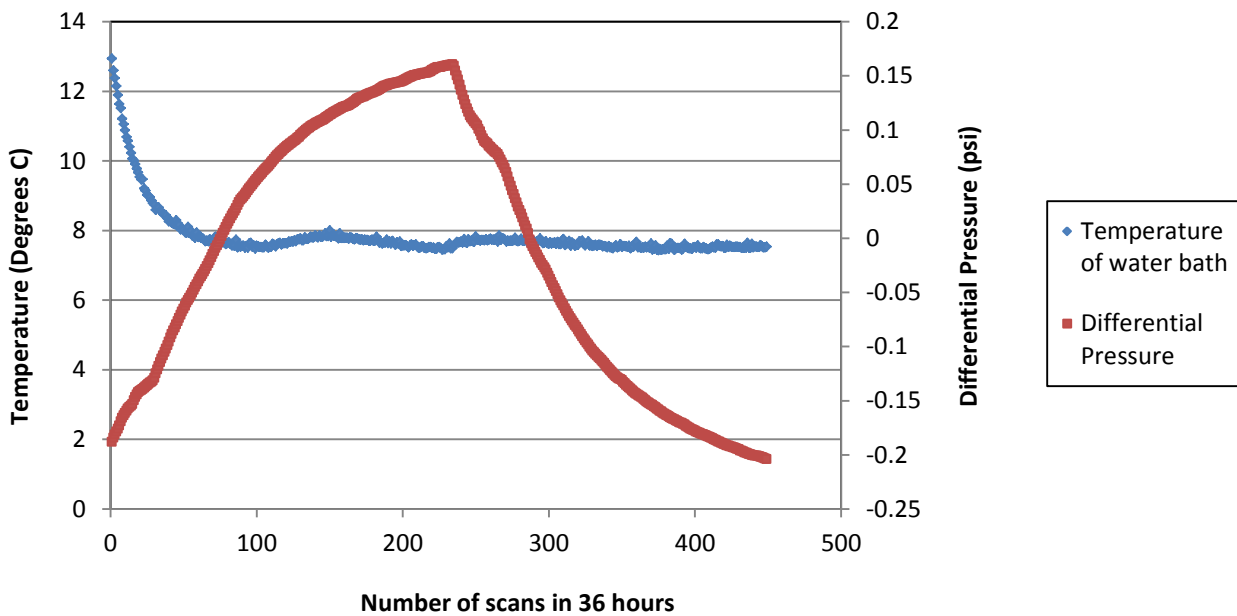


Figure B.34 Temperature of water bath and differential pressure readings for cooling cycle 17

Sample calculations for cooling cycle 17:

Area of sample, A	38.4	cm ²	density, ρ at 5 C (kg/m ³)	1000	μ at 5 C (N.s/m ²)	1.52E-03	g (m ² /s)	9.81	density, ρ at 49 C (kg/m ³)	988	μ at 49 C (N.s/m ²)	5.47E-04
Length of sample, L	3.81	cm										
Flow Rate, q	0.000028	cm ³ /s										
Heating Cycle : Infuse			Heating Cycle : Refill									
Average Differential Pressure (psi)			Average Differential Pressure (psi)									
0.044			0.127									
h (cm)			h (cm)									
3.10			8.93									
i			i									
0.81			2.34									
k (cm/s)			k (cm/s)									
8.97E-07			3.11E-07									
k,intrinsic (m²)			k,intrinsic (m²)									
5.07E-16			1.76E-16									
k,intrinsic (cm²)			k,intrinsic (cm²)									
5.07E-12			1.76E-12									
Average k			Average k									
6.04E-07			cm/s									
Average ki			Average ki									
3.41E-12			cm ²									

Table B.13 Raw data for the final moisture content test after for 18 bentonite samples

Sample Number	Weight of Tin (g)	Before Oven: Weight of Tin & Grout (g)	After Oven: Weight of Tin & Grout (g)	Total weight (g)	Weight of Solids (g)	Weight of Water (g)	Moisture Content, w (%)
1	1.03	13.77	3.07	12.74	2.04	10.70	524.51
2	1.01	10.29	2.52	9.28	1.51	7.77	514.57
3	1.04	16.05	3.70	15.01	2.66	12.35	464.29
4	1.03	9.16	2.78	8.13	1.75	6.38	364.57
5	1.02	11.26	2.70	10.24	1.68	8.56	509.52
6	1.04	14.18	3.10	13.14	2.06	11.08	537.86
7	1.02	16.84	3.46	15.82	2.44	13.38	548.36
8	1.01	10.99	2.58	9.98	1.57	8.41	535.67
9	1.03	7.7	2.10	6.67	1.07	5.60	523.36
10	1.04	10.42	2.52	9.38	1.48	7.90	533.78
11	1.04	11.05	2.58	10.01	1.54	8.47	550.00
12	1.01	25.67	3.24	24.66	2.23	22.43	1005.83
13	1.02	11.35	2.68	10.33	1.66	8.67	522.29
14	1.04	17.95	3.73	16.91	2.69	14.22	528.62
15	0.98	13.6	3.00	12.62	2.02	10.60	524.75
16	1.05	11.74	2.74	10.69	1.69	9.00	532.54
17	0.98	17.42	3.59	16.44	2.61	13.83	529.89
18	0.97	14.15	3.08	13.18	2.11	11.07	524.64
Average Final Moisture Content							543

APPENDIX C

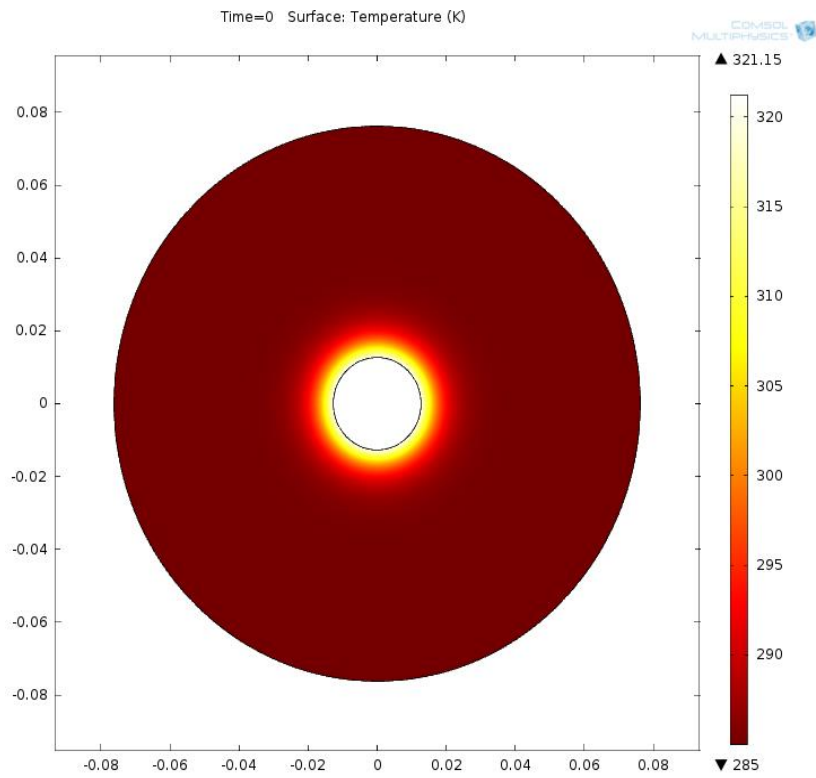


Figure C.1 Case 2 temperature distribution for a heating cycle in the geometry modeled in COMSOL at zero hours

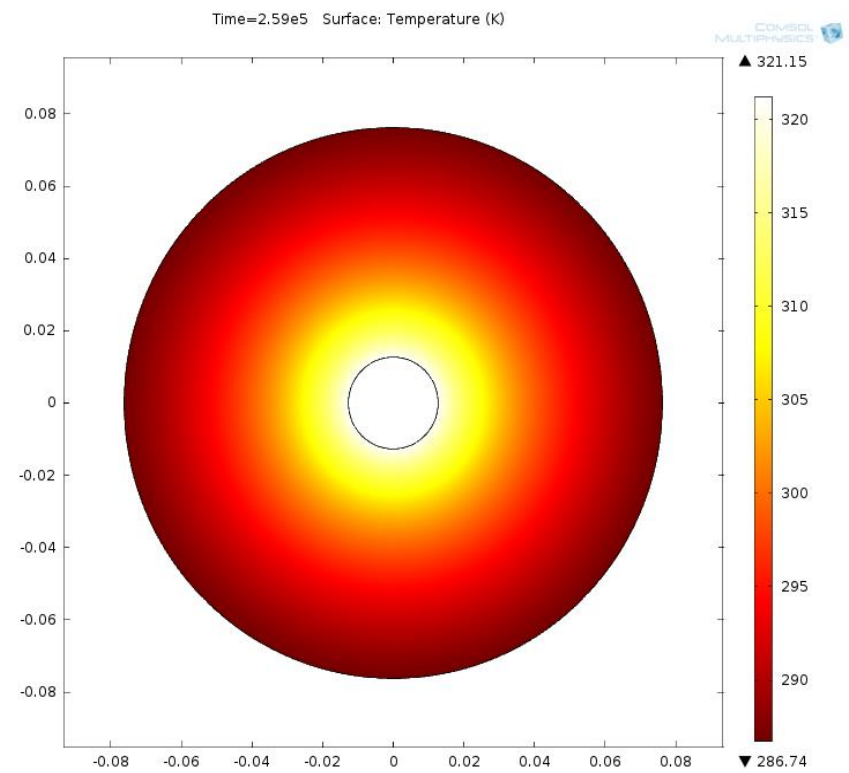


Figure C.2 Case 2 temperature distribution for a heating cycle in the geometry modeled in COMSOL at 72 hours

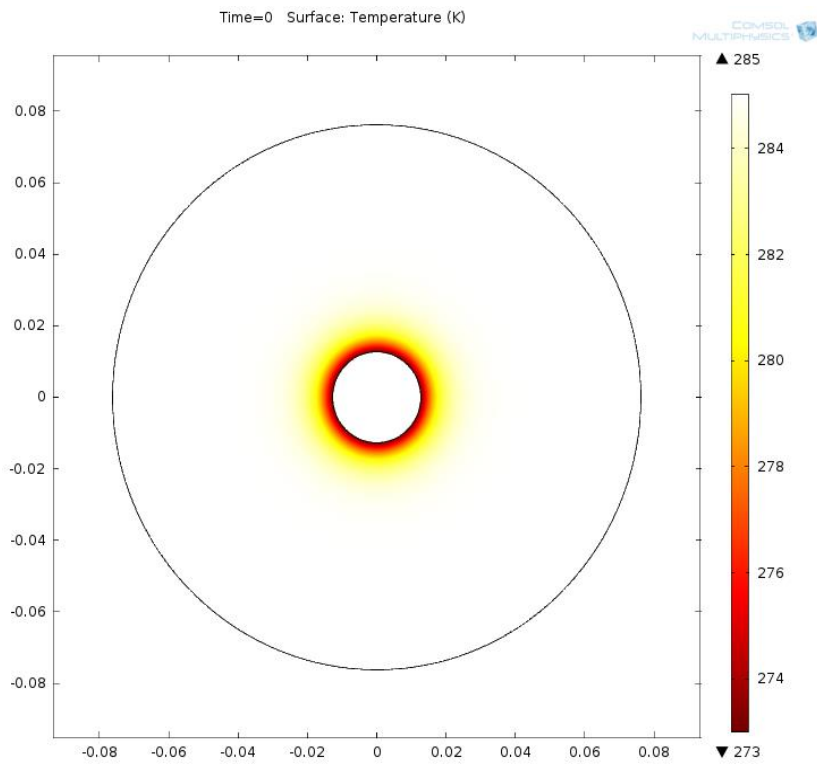


Figure C.3 Case 2 temperature distribution for a cooling cycle in the geometry modeled in COMSOL at zero hours

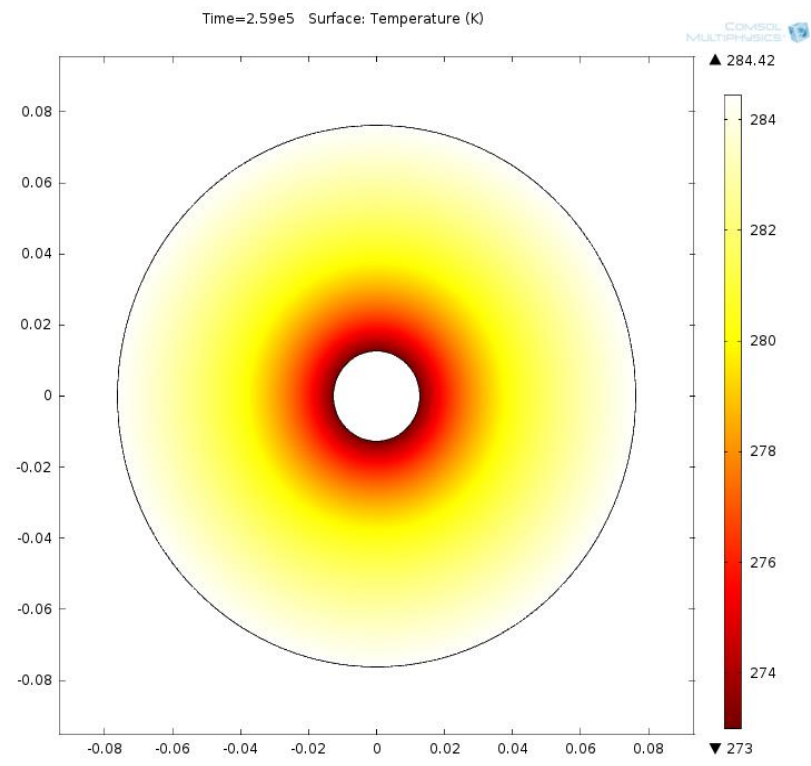


Figure C.4 Case 2 temperature distribution for a cooling cycle in the geometry modeled in COMSOL at 72 hours

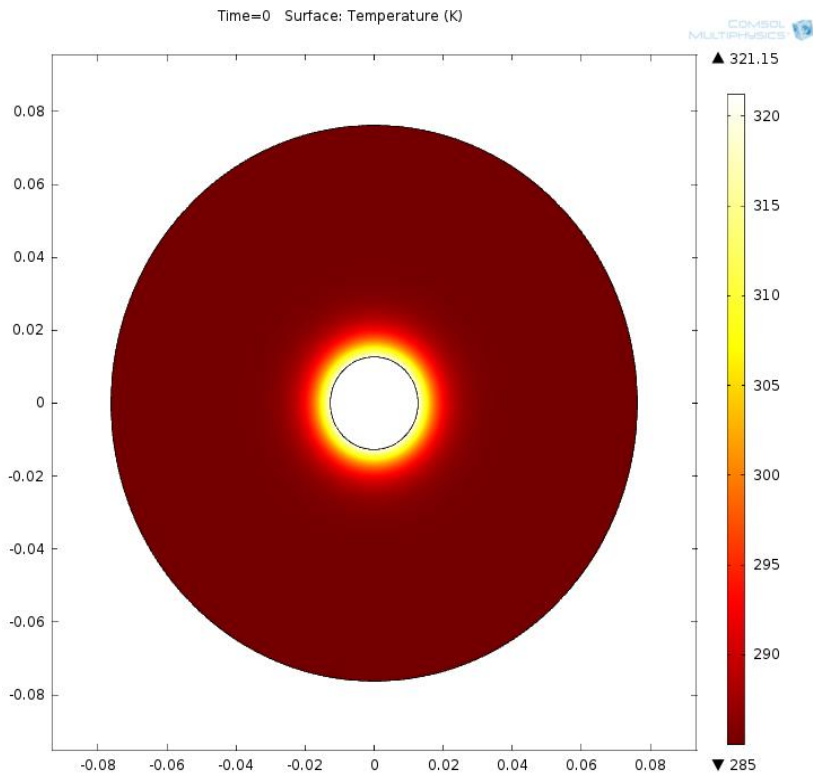


Figure C.5 Case 3 temperature distribution for a heating cycle in the geometry modeled in COMSOL at zero hours

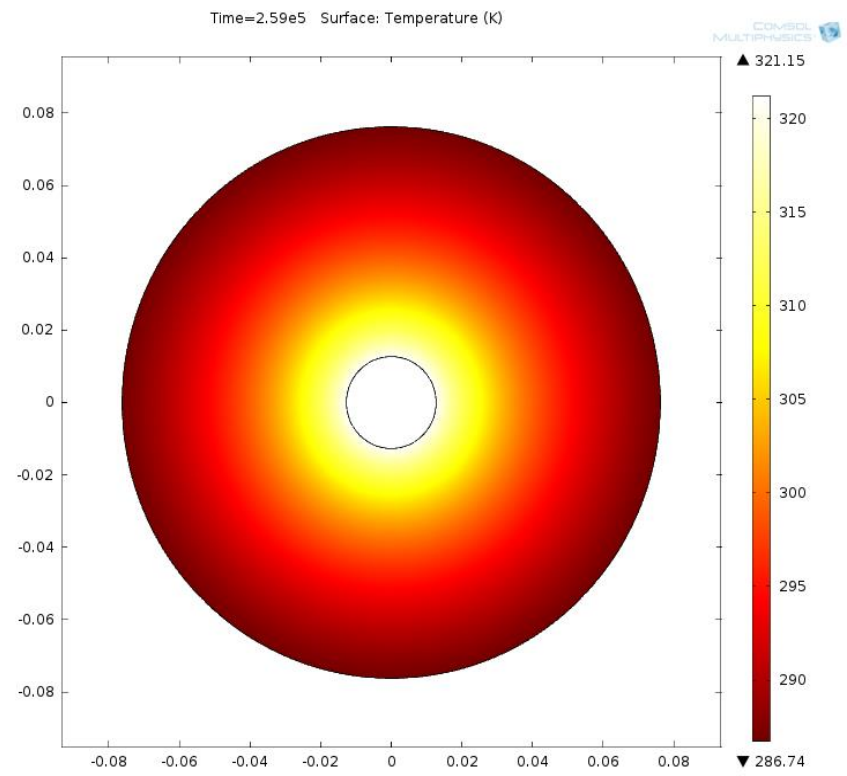


Figure C.6 Case 3 temperature distribution for a heating cycle in the geometry modeled in COMSOL at 72 hours

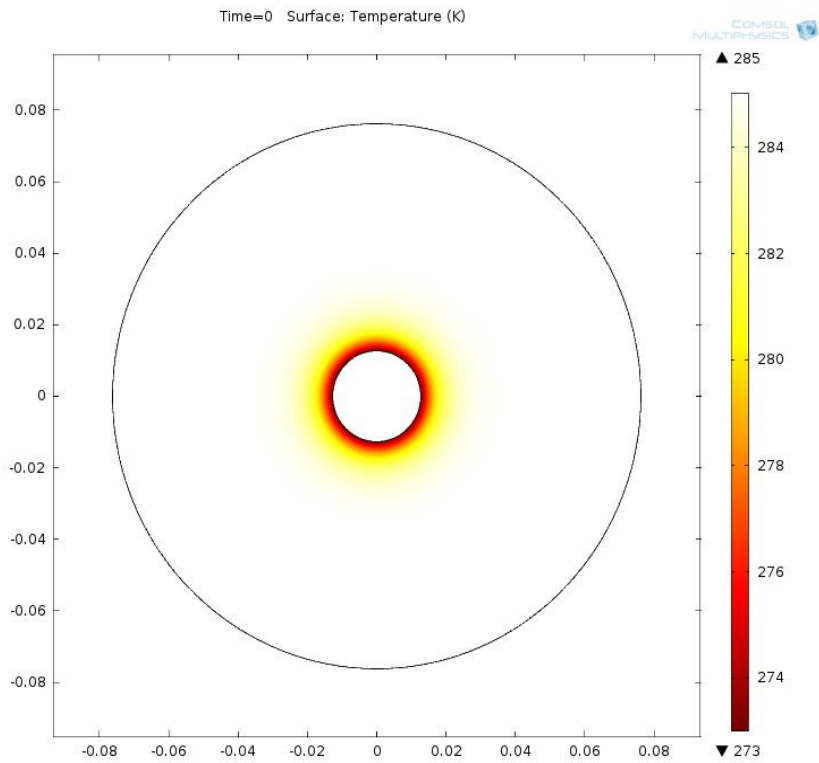


Figure C.7 Case 3 temperature distribution for a cooling cycle in the geometry modeled in COMSOL at zero hours

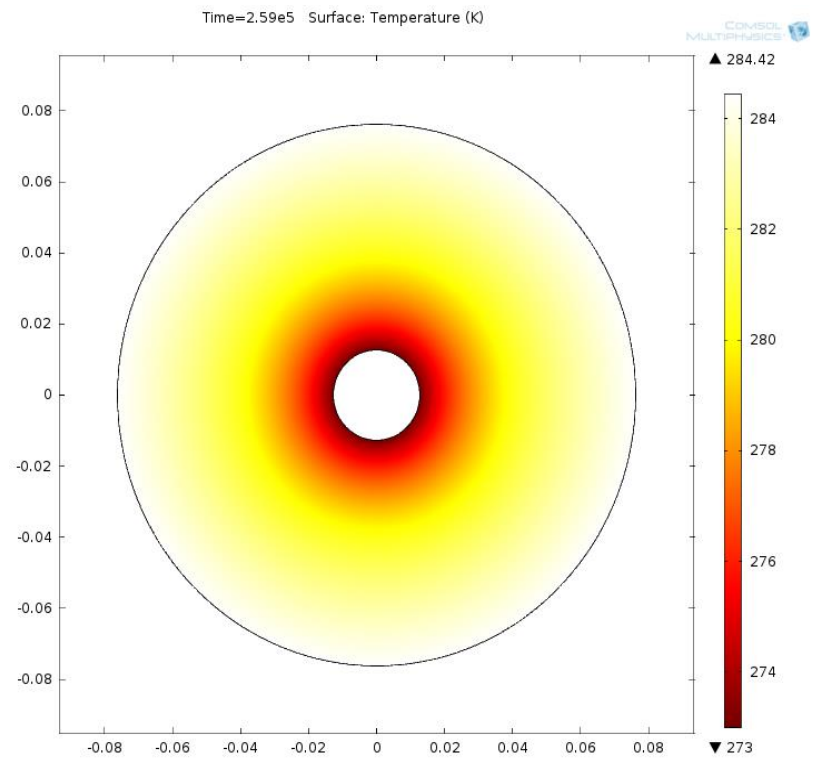


Figure C.8 Case 3 temperature distribution for a cooling cycle in the geometry modeled in COMSOL at 72 hours

